Universidad Politécnica de Valencia
DEPARTAMENTO DE INGENIERÍA ELECTRÓNICA

UNIVERSITAT
POLITÈCNICA
DE VALÈNCIA

Development of the Beam Position Monitors for the Diagnostics of the Test Beam Line in the CTF3 at CERN

TESIS DOCTORAL

Juan José García Garrigós

Mayo 2013

DIRECTORES

Dr. Ángeles Faus Golfe

Dr. Francisco J. Mora Más

A mis queridos Padres,
Juan y Fina,
por todo, y más.

A la memoria de mi Padre,
Juan García Segura (1942-2010).

Acknowledgments

I would like to express my gratitude to IFIC —*Instituto de Física Corpuscular, CSIC-Universidad de Valencia*— for giving me the opportunity to realize this work in the field of beam instrumentation for particle accelerators. Thanks to the CTF3 —*CLIC Test Facility 3*— collaboration from CERN —*European Organization for Nuclear Research*— for helping us with such a challenging task of developing the beam position monitors for the TBL —*Test Beam Line*— of CTF3.

I am sincerely grateful to Dr. Angeles Faus Golfe, not only my supervisor at IFIC but a mentor for me, with her always encouraging support and leadership; and also to my supervisor and tutor at the DIE-UPV —*Departamento de Ingeniería Electrónica-Universidad Politécnica de Valencia*— Dr. Francisco J. Mora Más for his really helpful advices, encouragement and constant support.

Also, I am pleased to thank Dr. Angel Sebastiá Cortés for his kind advices and support as one of the supervisors and UPV tutor of the master thesis at the beginning of this work.

I truly want to thank to Dr. Gabriel Montoro from UPC —*Universidad Politécnica de Cataluña*— for the collaboration to develop the BPS external amplifier; for his strong and close commitment, and lots of fruitful conversations, even those about far-west movies and conspiracy theories, during the test stays at CERN labs. And, to Dr. Benito Gimeno from the *Universidad de Valencia*, for his strong support in helping to understand waveguides and in the high frequency test bench, we had a lot of fun in making “El Embudo”.

From CERN, my sincere thanks to Dr. Steffen Döbert, the project-leader of the TBL, for having trust in our work, for his invaluable advices and the crucial help during the beam tests at the TBL controls. Thanks also to Lars Søby and Franck Guillot for their support and guiding advices at the BPS prototyping phase, helping us at every moment in the lab and for their hospitality (thanks for the good coffees).

I must acknowledge the participation of our industry partners, *Trinos Vacuum Projects* and *Talleres Lemar* for their great job in the BPS prototypes and series manufacturing.

Many thanks to the people directly involved in the BPS project at IFIC, specially to my friend César Blanch Gutiérrez for his outstanding professional work in the mechanical drawings of the BPS monitor series and the test stands, and for his willingness in our close work supporting each other. Also many thanks to my colleagues, José Vicente Civera, for the BPS prototype mechanical design and for the many answered questions, and Jorge Nácher, for making such cool PCBs as many times as I needed. Without their experience and help this work would have not been possible, thanks you guys for your dedication. I would also like to extend my gratitude to a long list of colleagues at the Group of Accelerator Physics (GAP) and IFIC for such a kind fellowship which makes me feel lucky for having shared many moments with them, thank you all.

There will never be enough gratitude for my parents, Josefina Garrigós Planells, Fina, the best mother one could ever have, and my father Juan García Segura, Juanín. He is now in our minds, hearts and all those places he gave the best of himself, always with passion, the same way taught my brother and me.

More than ever, special, warm and very well-deserved thanks to my wife, María José Bueso Recatalá, and to my kids Juan and Mateo, you cannot imagine how much I love you. MaryJo, this can better show what I mean —
she is everything I need that I never knew I wanted;
she is everything I want that I never knew I needed
(The Fray, How to Save a Life)—.

Abstract

The work for this thesis is in line with the field of Instrumentation for Particle Accelerators, so called *Beam Diagnostics*. It is presented the development of a series of electro-mechanical devices called *Inductive Pick-Ups* (IPU) for *Beam Position Monitoring* (BPM). A full set of 17 BPM units (16 + 1 spare), named BPS, were built and installed into the *Test Beam Line* (TBL), an electron beam decelerator, of the *3rd CLIC Test Facility* (CTF3) at CERN —*European Organization for the Nuclear Research*—. The CTF3, built at CERN by an international collaboration, was meant to demonstrate the technical feasibility of the key concepts for CLIC —*Compact Linear Collider*— as a future linear collider based on the novel two-beam acceleration scheme, and in order to achieve the next energy frontier for a lepton collider in the Multi-TeV scale. Here the BPS device is first described mechanically to after focus on the electronic design, electromagnetic features and operational parameters according to the TBL specifications. Moreover, it will be described the two main test carried out on the BPS units at low and high frequencies needed for their parametric characterization, as well as their respective specifically designed test stands. The low frequency test, in the beam pulse time scale (until 10ns/100MHz), was built to determine the BPS parameters related to the beam position monitoring, which is based on the precise motion of a stretched wire emulating the beam current. On the other hand, the high frequency test, beyond the microwave X band and around the beam bunching time scale (83ps/12GHz), is for measuring the longitudinal impedance of the BPS device in the frequency range of interest which is based on the S-parameters measurements of the propagating TEM mode in a matched coaxial waveguide able to emulate an ultra-relativistic electron beam. Finally, the beam test performance of the BPS units installed in the TBL line is also shown.

Contents

Resumen

Esta tesis se enmarca dentro del campo de Instrumentación Electrónica para Aceleradores de Partículas, también denominado Diagnóstico de Haz —*Beam Diagnostics*—. En este trabajo se presenta el desarrollo de unos dispositivos electro-mecánicos para monitorizar la posición del haz de partículas —*Beam Position Monitor*, BPM—, concretamente del tipo inductivo —*Inductive Pick-Up*, IPU—. Una serie de 17 unidades (16 + 1 de repuesto) de estos monitores de posición de haz o BPMs, bautizados como BPS, fueron construidos e posteriormente instalados en la línea de deceleración de electrones TBL —*Test Beam Line*—, perteneciente al complejo de aceleradores CTF3 —*CLIC Test Facility 3rd phase*— en el CERN —*European Organization for the Nuclear Research*—. La finalidad de CTF3 es la demostración de la viabilidad de la nueva tecnología de aceleración de doble-haz en la que se basaría el futuro colisionador lineal de leptones CLIC —*Compact Linear Collider*— para alcanzar la frontera de energía en la escala de varios Tera-electron-Voltios o Multi-TeV. Las nuevas generaciones de aceleradores de partículas, y en particular CLIC, requieren de BPMs de precisión y alta resolución debido a la necesidad de realizar procedimientos de alineación de sus múltiples elementos cada vez más exigentes para mejorar la calidad del haz, y en los que los monitores de posición como el BPS-IPU juegan un importante papel. Sobretodo en la técnicas de alineamiento basadas en el propio haz de partículas proporcionando la monitorización de la posición, además de la corriente del haz en el caso del BPS, en diferentes puntos a lo largo del acelerador.

El proyecto BPS, llevado a cabo en el IFIC, se realizó fundamentalmente en dos fases: la de prototipado y la de producción y test de la serie para TBL.

En la primera fase se construyeron dos prototipos totalmente funcionales, de la que esta tesis se centra en los aspectos de diseño electrónico de las tarjetas de circuito impreso PCB embarcadas en los monitores BPS, que están basadas en transformadores y son responsables del sensado de la corriente y posición del haz. Asimismo, se describe el diseño mecánico del monitor con énfasis en las partes involucradas directamente en su funcionamiento electromagnético, gracias al acoplamiento de los campos generados por el haz con dichas partes. Para ello se estudiaron sus parámetros operacionales, acorde a las especificaciones de la línea TBL, y también se realizaron simulaciones con un nuevo modelo circuital válido para frecuencias en su ancho de banda de operación (1kHz-100MHz). Dichos prototipos fueron testeados inicialmente en los laboratorios de la sección BI-PI —*Beam Instrumentation - Position and Intensity*— del CERN.

En la segunda fase de producción de la serie de monitores BPS, construidos según los estudios y la experiencia de los prototipos, el trabajo se focalizó en la realización de los tests de caracterización de los parámetros principales de la serie de monitores, para lo que se diseñaron y construyeron dos bancos de pruebas con diferente propósitos y regiones de frecuencia. El primero está destinado a trabajar en la región de baja frecuencia, entre 1kHz-100MHz, en la escala temporal del pulso de haz de electrones con periodo

de repetición de 1s y duración aproximada de 140ns. Este es un sistema de test denominado *Wire Test-bench* que habitualmente se usa en instrumentación de aceleradores para obtener los parámetros característicos de cada monitor de medida de la posición y corriente del haz, como son la linealidad, precisión y respuesta en frecuencia (ancho de banda). Gracias a que permite la emulación de un haz de partículas de baja intensidad con un cable de corriente tensado y posicionado con precisión respecto al dispositivo bajo ensayo. Este sistema se construyó específicamente adaptado para el monitor BPS y pensado para realizar una adquisición de datos de la forma más automatizada posible, con el equipamiento de medida y control de motores de posicionamiento del monitor respecto al cable, todo gestionado desde un PC. Con este sistema se caracterizaron todos los monitores BPS en los laboratorios del IFIC y cuyos análisis de resultados se presentan en este trabajo.

Por otro lado, los tests de alta frecuencia, por encima de la banda X de microondas y en la escala temporal correspondiente a los micro-pulsos de cada pulso de haz con periodo de 83ps (12GHz), se realizaron para determinar la impedancia longitudinal del monitor BPS. La cuál debe ser lo suficientemente pequeña para minimizar as las perturbaciones del haz al atravesar cada monitor, y que afectan a su estabilidad durante la propagación a lo largo de la línea. Para ello, se construyó el banco de pruebas de alta frecuencia que consiste en una estructura de guía de ondas coaxial de 24mm de diámetro adaptada a 50Ω y con ancho de banda de 18MHz a 30GHz, préviamente simulada, con espacio para la inserción del BPS como dispositivo bajo ensayo. De este modo, esta estructura es capaz de reproducir los modos propagativos TEM (Transvesales Electro-Magnéticos) del haz de electrones ultra-relativista con 12GHz de frecuencia de micro-pulsos, y así poder medir los parámetros de *Scattering* de los que se obtuvo la impedancia longitudinal del BPS en el rango de frecuencias de interés.

Finalmente, también se presentan los resultados de los tests con haz realizados en la línea TBL, con corrientes de haz de 3.5A hasta 13A (máx. disponible en el momento del test). Para la determinación de la mínima resolución alcanzada por los monitores BPS en la medida de la posición del haz, siendo la figura de mérito del dispositivo, con un objetivo de resolución de 5μm a máxima corriente de haz de 28A según las especificaciones de TBL.

Resum

Aquesta tesi s'emmarca dins del camp de la Instrumentació Electrònica per Acceleradors de Partícules, també denominat Diagnstic de Feix —*Beam Diagnostics*—. En aquest treball es presenta el desenvolupament d'uns dispositius electro-mecànics per monitoritzar la posició del feix de partícules —*Beam Position Monitor*, BPM—, concretament del tipus inductiu —*Inductive Pick-Up*, IPU—. Una serie de 17 unitats (16 + 1 restant) d'aquests monitors de posició de feix o BPMs, batejats com BPS, varen ser construïts i posteriorment instal·lats en la línia d'acceleració d'electrons TBL —*Test Beam Line*—, que pertany al complex d'acceleradors CTF3 —*CLIC Test Facility 3rd phase*— al CERN —*European Organization for the Nuclear Research*—. La finalitat de CTF3 és la demostració de la viabilitat de la nova tecnologia d'acceleració de doble-feix en la que es basaria el futur col·lisionador lineal de leptons CLIC —*Compact Linear Collider*— per aconseguir la frontera d'energia en l'escala dels Tera-electron-Volts o Multi-TeV. Les noves generacions d'acceleradors de partícules, i en particular CLIC, requereixen de BPMs de precisió i elevada resolució a causa de la necessitat de realitzar procediments d'alineament dels seus múltiples elements cada vegada més exigents per a millorar la qualitat del feix, i en els quals els monitors de posició com el BPS-IPU juguen un paper important. Sobretot en les tècniques d'alineament basades en el mateix feix de partícules proporcionant la monitorització de la posició, a banda del corrent del feix, en el cas del BPS, en diferents punts al llarg de l'accelerador.

El projecte BPS, dut a terme al IFIC, es va realitzar fonamentalment en dues fases: la de prototipat i la de producció i test de la serie al TBL.

En la primera fase es varen construir dos prototips totalment funcionals, de la que aquesta tesi es centra en els aspectes de disseny electrònic de les targetes de circuit imprès PCB embarcades en els monitors BPS, que estan basades en transformadors responsables de la mesura del corrent i la posició del feix. Així mateix, es descriu el disseny mecànic del monitor amb èmfasi en les parts involucrades directament en el seu funcionament electromagnètic, gràcies al acoblament dels camps generats pel feix amb les dites parts. Per això s'estudiaren els seus paràmetres operacionals, d'acord amb les especificacions de la línia TBL, i també es realitzaren simulacions amb un nou model circuital vàlid per freqüències en la seva amplada de banda d'operació (1kHz-100MHz). Aquests prototips varen ser testejats inicialment als laboratoris de la secció BI-PI —*Beam Instrumentation - Position and Intensity*— del CERN.

En la segona fase de producció de la serie de monitors BPS, construïts segons els estudis i l'experiència dels prototips, el treball es va focalitzar en la realització de els tests de caracterització dels paràmetres principals de la serie de monitors, pels quals es dissenyaren i construïren dos bancs de proves amb diferents propòsits i regions de freqüències. El primer està destinat a treballar en la regió de baixa freqüència, entre 1kHz-100MHz, en l'escala temporal del pols de feix d'electrons amb un període de repetició

d'1s i duració aproximada de 140ns. Aquest és un sistema de test denominat *Wire Test-bench* que habitualment es fa servir en instrumentació d'acceleradors per obtenir els paràmetres característics de cada monitor de mesura de la posició i el corrent del feix, com són la linealitat, precisió i resposta en freqüència (amplada de banda). Gràcies a què permet l'emulació d'un feix de partícules de baixa intensitat amb un cable de corrent tensat i posicionat amb precisió respecte al dispositiu sota assaig. Aquest sistema es va construir específicament adaptat pel monitor BPS i pensat per fer una adquisició de dades de la forma més automatitzada possible, amb l'equipament de mesura i control de motors de posicionament del monitor respecte al cable, tot gestionat des d'un PC. Amb aquest sistema es caracteritzaren tots els monitors BPS en els laboratoris de l'IFIC i es realitzaren els anàlisis de resultats, els quals es presenten en aquest treball.

Per altra banda, els tests d'alta freqüència, per damunt de la banda X de microones i en l'escala temporal corresponent als micro-polsos de cada pols de feix amb període de 83ps (12GHz), es varen fer per determinar la impedància longitudinal del monitor BPS. La qual deu ser prou petita per minimitzar aix les pertorbacions del feix al travessar cadascun dels monitors, i que afecten la seva estabilitat durant la propagació al llarg de la línia. Per això, es va construir el banc de proves d'alta freqüència que consisteix en una estructura de guia d'ones coaxial de 24mm de diàmetre adaptada a 50Ω i d'amplada de banda de 18MHz-30GHz, prèviament simulada, amb espaï per la inserció del BPS com a dispositiu sota assaig. D'aquesta manera, l'estructura és capaç de reproduir els modes propagatius TEM (Transversals Electro-Magnètics) del feix d'electrons ultra-relativista amb 12GHz de freqüència de micro-polsos, i així poder mesurar els paràmetres de *Scattering* dels quals es va obtenir la impedància longitudinal del BPS en el rang de freqüències d'interès.

Finalment, també es presenten els resultats de els tests amb feix fets en la línia TBL, amb corrents de feix des de 3.5A fins a 13A (màx. disponible en el moment del test). I la determinació de la mínima resolució aconseguida pels monitors BPS en la mesura de la posició del feix, sent la figura de mèrit del dispositiu, amb un objectiu de resolució de 5μm a màxim corrent de feix de 28A segons les especificacions de TBL.

Summary

The work for this thesis is in line with the field of Instrumentation for Particle Accelerators, so called *Beam Diagnostics*. It is presented the development of a series of electro-mechanical devices called *Inductive Pick-Ups* (IPU) for *Beam Position Monitoring* (BPM). A full set of 17 BPM units (16 + 1 spare), named BPS units, were built and installed into the *Test Beam Line* (TBL), an electron beam decelerator, of the *3rd CLIC Test Facility* (CTF3) at CERN —*European Organization for the Nuclear Research*—. The CTF3, built at CERN by an international collaboration, was meant to demonstrate the technical feasibility of the key concepts for CLIC —*Compact Linear Collider*— as a future linear collider based on the novel two-beam acceleration scheme, and in order to achieve the next energy frontier for a lepton collider in the Multi-TeV scale. Modern particle accelerators and in particular future colliders like CLIC requires an extreme alignment and stabilization of the beam in order to enhance its quality, which rely heavily on a beam based alignment techniques. Here the BPMs, like the BPS-IPU, play an important role providing the beam position with precision and high resolution, besides a beam current measurement in the case of the BPS, along the beam lines.

The BPS project carried out at IFIC was mainly developed in two phases: prototyping and series production and test for the TBL.

In the first project phase two fully functional BPS prototypes were constructed, focusing in this thesis work on the electronic design of the BPS on-board PCBs (Printed Circuit Boards) which are based on transformers for the current sensing and beam position measurement. Furthermore, it is described the monitor mechanical design with emphasis on all the parts directly involved in its electromagnetic functioning, as a result of the coupling of the EM fields generated by the beam with those parts. For that, it was studied its operational parameters, according the TBL specifications, and it was also simulated a new circuital model reproducing the BPS monitor frequency response for its operational bandwidth (1kHz-100MHz). These prototypes were initially tested in the laboratories of the BI-PI section —*Beam Instrumentation - Position and Intensity*— at CERN.

In the second project phase the BPS monitor series, which were built based on the experience acquired during the prototyping phase, the work was focused on the realization of the characterization tests to measure the main operational parameters of each series monitor, for which it was designed and constructed two test benches with different purposes and frequency regions. The first one is designed to work in the low frequency region, between 1kHz-100MHz, in the time scale of the electron beam pulse with a repetition period of 1s and an approximate duration of 140ns. This kind of test setups called *Wire Test-bench* are commonly used in the accelerators instrumentation field in order to determine the characteristic parameters of a BPM (or *pick-up*) like its linearity and precision in the position measurement, and also its frequency response (bandwidth). This is done by emulating a low current intensity beam with a stretched wire carrying a current signals

which can be precisely positioned with respect the device under test. This test bench was specifically made for the BPS monitor and conceived to perform the measurement data acquisition in an automated way, managing the measurement equipment and the wire positioning motors controller from a PC workstation. Each one of the BPS monitors series were characterized by using this system at the IFIC labs, and the test results and analysis are presented in this work.

On the other hand, the high frequency tests, above the X band in the microwave spectrum and at the time scale of the micro-bunch pulses with a bunching period of 83ps (12GHz) inside a long 140ns pulse, were performed in order to measure the longitudinal impedance of the BPS monitor. This must be low enough in order to minimize the perturbations on the beam produced at crossing the monitor, which affects to its stability during the propagation along the line. For that, it was built the high frequency test bench as a coaxial waveguide structure of 24mm diameter matched at 50Ω and with a bandwidth from 18MHz to 30GHz, which was previously simulated, and having room in the middle to place the BPS as the device under test. This high frequency test bench is able to reproduce the TEM (Transversal Electro-Magnetic) propagative modes corresponding to an ultra-relativistic electron beam of 12GHz bunching frequency, so that the Scattering parameters can be measured to obtain the longitudinal impedance of the BPS in the frequency range of interest.

Finally, it is also presented the results of the beam test made in the TBL line, with beam currents from 3.5A to 13A (max. available at the moment of the test). In order to determine the minimum resolution attainable by a BPS monitor in the measurement of the beam position, being the device figure of merit, with a resolution goal of 5μm at maximum beam current of 28A according to the TBL specifications.

List of Figures

List of Tables

Chapter 1

Introduction

1.1 Next generation of linear colliders

The *Large Hadron Collider* (LHC) is the latest and foremost accelerator at CERN (*European Organization for Nuclear Research*), and it was set to provide a rich program of physics at the high-energy frontier, exploring the new Multi-TeV (Tera-electron-Volt) energy region for hadrons, over the coming years. The LHC entered in operation after the first official run with the circulation of two proton beams in September 2008. From 30th March 2010 it became the most powerful collider in the world with the first collisions at an energy of 3.5 TeV per beam (7 TeV center-of-mass). The physics experiments in the LHC should confirm or refute the existence of the Higgs boson to complete the Standard Model (see Fig. 1.1), explaining how some particles get its mass through the so called Higgs mechanism. The LHC experiments will also explore the possibilities for physics beyond the Standard Model, such as supersymmetry, extra dimensions and new gauge bosons. The discovery potential is huge and will set the direction for possible future high-energy colliders. Nevertheless, particle physics community worldwide have reached a consensus that the results from the LHC will need to be complemented by experiments at a linear electron-positron (e^-e^+) collider operating in the TeV and also extended to Multi-TeV energy ranges. During the last decade, dedicated and successful work by several research groups has demonstrated that a future linear collider can be built and reliably operated.

The highest center-of-mass energy in e^-e^+ collisions so far of 209 GeV (Giga-electron-Volt) was reached at the *Large Electron-Positron collider* (LEP) at CERN. In a circular collider, such as LEP, the circulating particles emit synchrotron radiation, and the energy lost in this way needs to be replaced by a powerful Radio-Frequency (RF) acceleration system. More precisely, the energy lost by synchrotron radiation increases dramatically with the fourth power of the energy of the circulating beam, and it is also inversely proportional to the square of the ring curvature radius. In LEP, for example, in spite of its 27 km circumference intended to have as large as possible curvature radius, each beam lost about 3% of its energy on each turn. The biggest superconducting RF system built so far, which provided a total of 3640 MV per revolution, was just enough to keep the beam in LEP at its nominal energy. As the amount of RF power required to keep the beam circulating became prohibitive, it was clear that a synchrotron or storage ring is not an option for a future lepton collider operating at energies significantly above that of LEP for exploring new high energy regions.

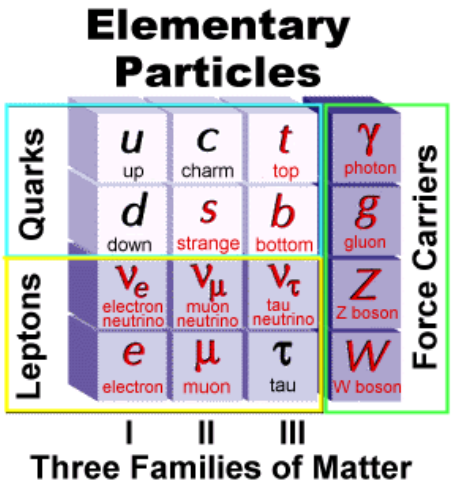

Figure 1.1: Elementary particle families of the Standard Model which describes all the fundamental forces of the nature, the electromagnetic, nuclear and weak forces; except the gravitation force, with the predicted graviton as its carrier.

Linear colliders came out naturally as the only option for realizing e^-e^+collisions around TeV energies, avoiding synchrotron radiation losses. The basic principle here is simple: two linear accelerators face each other, one accelerating electrons (e^-), the other positrons (e^+), so that the two beams of particles can collide head on. This scheme has certain inherent features that strongly influence the design. First, the linear accelerators, commonly known as linacs, have to accelerate the particles in one single pass. This requires high electric fields for acceleration, so as to keep the length of the collider within reasonable limits; such high fields can be achieved only in pulsed operation. Secondly, after acceleration, the two beams collide only once. In a circular machine the counter-rotating beams collide with a high repetition frequency, in the case of LEP at 44 kHz. A linear collider by contrast would have a repetition frequency of typically 5 to 100 Hz. This means that the rate of collisions events, or luminosity, necessary for the particle physics experiments can be reached only with very small beam dimensions at the interaction point and with the highest possible number of charged particles in a single bunch. As luminosity is proportional to beam power, the overall wall-plug to acceleration efficiency is of paramount importance.

The *International Linear Collider* (ILC) is a 200-500 GeV center-of-mass high-luminosity e^-e^+linear collider and a possible future upgrade to 1 TeV. It has an overall length of 31 Km and its technology key elements are the 1.3 GHz Superconducting Radio Frequency (SCRF) accelerating cavities fed by L-band klystrons that can generate a nominal accelerating field gradient of 31.5 MV/m (see Fig. 1.2). The use of SCRF cavities is a well-known and proven technology representing the state-of-the-art in acceleration technology. It was recommended by the International Technology Recommendation Panel (ITRP) in August 2004, and shortly thereafter endorsed by the International Committee for Future Accelerators (ICFA).

In an unprecedented milestone in high-energy physics, many institutes around the world got involved in linear collider R&D making a common effort to produce a global design for the ILC. As a result the ILC Global Design Effort (GDE) was formed. The GDE membership reflects the global nature of the collaboration, with accelerator experts from

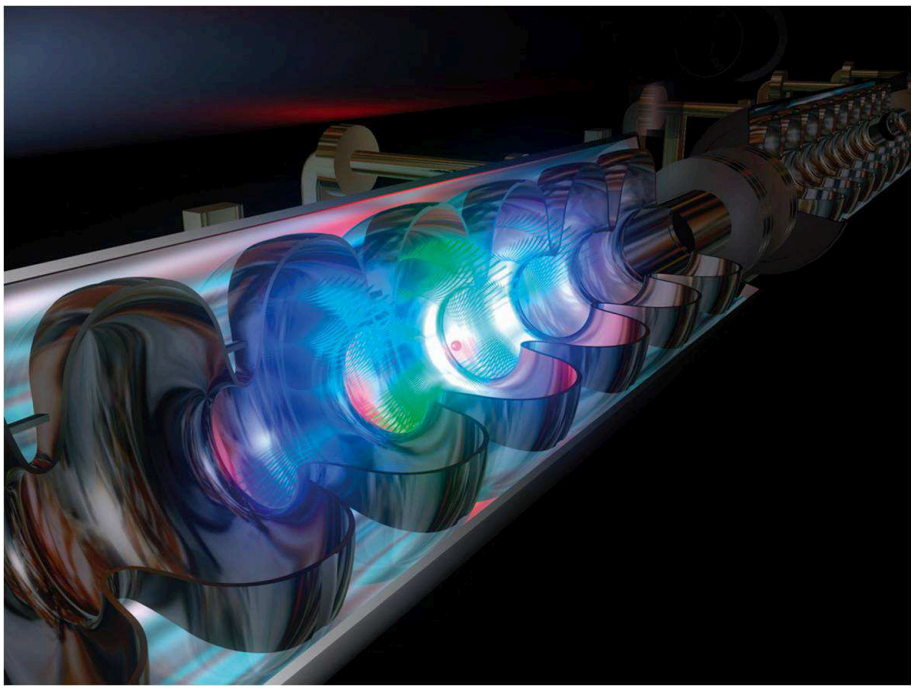

(a)

(b)

Figure 1.2: Super-Conducting Radio Frequency (SCRF) cavity: (a) Illustration of a beam bunch passing through a SCRF cavity; (b) A super-conducting TESLA cavity made of Niobium.

all three regions (Americas, Asia and Europe). The first major goal of the GDE was to define the basic parameters and layout of the machine (see Fig. 1.4). During nearly a year the Baseline Configuration Document (BCD) was used as the basis for the detailed design work and cost estimate culminating in the completion of the second major milestone, the publication of the ILC Reference Design Report (RDR) [1]. With the completion of the RDR, the GDE begun an engineering design study, closely coupled with a prioritized R&D program. The goal is to produce an Engineering Design Report (EDR) by 2012, presenting the matured technology design and construction plan for the ILC [2].

In general, beam test facilities are required for critical technical demonstrations including accelerating gradient, precision beam handling and beam dynamics. In each case, the critical R&D test facility is used to mitigate critical technical risks as assessed during the development of the RDR. Test facilities also serve to train scientific and engineering staff and regional industry. In each case, design and construction of the test facility has been done by a collaboration of several institutes. To demonstrate the industrialization of the superconducting RF technology and its application in linacs, the *European X-Ray Laser Project* (XFEL) is under construction in DESY, *Deutsches Elektronen-Synchrotron*,

Hamburg, since 2007. In this complex the TTF/FLASH linac, is the only operating electron linac where it is possible to run close to reference design gradients with nominal ILC beams. The primary goals of the 9 mA beam loading experiment are: the demonstration of the bunch-to-bunch energy uniformity and stability, characterization of the limits at high-gradient, quantification of the klystron power overhead required for control and measurement of the cryogenics loads. This facility will provide important information on several goals of the *Cryomodule-string test* and will be the only source of data before 2012.

An important technical challenge of ILC is the collision of extremely small beams of a few nanometers in size. The latter challenge has three distinct issues: creating small size and emittance beams, preserving the emittance during acceleration and transport, focusing the beams to nanometers and colliding them. The *Accelerator Test Facility* (ATF) at KEK, the *High Energy Accelerator Research Organization* in Japan, was built to create small emittance beams, and succeeded in obtaining an emittance that almost satisfies the ILC requirements. The ATF2 facility, which uses the beam extracted from ATF damping ring, was constructed to address two major challenges of ILC: focusing the beams to nanometer scale using an ILC-like final focus and providing nanometer stability. The two ATF2 goals, first one being the achievement of 35 nm beam size, and second being the achievement of nanometer scale beam stability at the interaction point (IP), have been addressed sequentially, during 2010, near end of Technical Design Phase I (TDP), and in 2012, near the end of TDP-II phase, correspondingly.

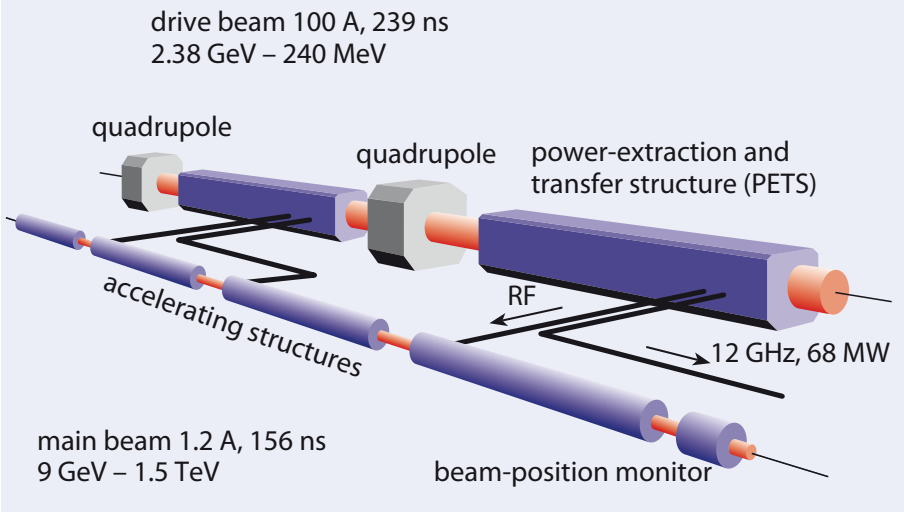

Figure 1.3: The CLIC two-beam acceleration scheme for reaching the Multi-TeV energy scale, with the main beam accelerated by the RF power provided from the lower-energy but higher-current drive beam.

At the same time, within the framework of collaboration on Linear Colliders, the *Compact Linear Collider* (CLIC) study [3] aims at Multi-TeV linear collider with a center-of-mass energy range for e^-e^+ collisions of 0.5 to 3 TeV, and foresees building CLIC in stages, starting at the lowest energy required by the physics, with successive energy upgrades that can potentially reach about six times the energy of the ILC. The CLIC scheme is based on normal conducting travelling-wave accelerating structures operating at a frequency of 12 GHz, and a very high accelerating gradient field of 100 MV/m, in order to reach this

energy in a realistic and cost efficient scenario keeping the total length to about 48 km for the baseline design optimized for a colliding-beam energy of 3 TeV. Such high fields require high peak power and hence a novel power source. An innovative two-beam system, in which another beam, the drive beam, supplies energy to the main accelerating beam.

The RF peak power required to reach the electric fields of 100 MV/m amounts to about 275 MW per active meter of accelerating structure. With an active accelerator length for both linacs of 42 km out of the 48 km total length of CLIC, the use of individual RF power sources, such as conventional X-band klystrons, to provide such a high peak power is not really possible. Instead, the key technology underlying CLIC is the *two-beam acceleration scheme* a novel linear collider concept based on the production and distribution of high peak RF power. In this system, two beams run parallel to each other: the main beam, a low current beam to be accelerated from low to high energies, and the drive beam, a low energy but high current beam to feed the main beam accelerating structures with enough RF power. In some sense this power generation and transfer principle could be thought as an analogy for a "big scale" electric transformer.

To generate the RF power, the drive beam (a pulsed beam of 12 GHz bunching frequency) passes through special Power Extraction and Transfer Structures (PETS), and excites strong electromagnetic oscillations, so that the beam loses its kinetic energy in almost a 90% and it is converted into electromagnetic pulsed RF power. Thus, as the beam is decelerated, the RF power is extracted from the PETS and sent via waveguides to the accelerating structures in the parallel main beam. The PETS are travelling wave structures like the accelerating structures for the main beam, but with different parameters. In Fig. 1.3 is illustrated the *CLIC two-beam acceleration scheme* based on this power generation principle.

The proposed CLIC layout is presented in the Fig. 1.5, where we can differentiate the main sections. In the center region are the two main beam linacs facing each other to boost electrons, from the left side, and positrons, from the right side, toward collision. The particle detectors will be installed in the interaction point (IP), where the collisions take place, but just before two sophisticated beam delivery systems (BDS), one for each beam line, will focus the beam down to dimensions of 1 nm rms size in the vertical plane and 40 nm horizontally, in order to achieve the luminosity that the experiments demand. Running in parallel to each main linac, there are the two decelerator lines, to extract the RF power from the drive beams through the PETS, and then transfer it to the main beams for accelerating them. In the top of the layout it can be seen the two-folded drive beam generation system which consists in two drive beam linacs fed by klystrons, followed by a sequence of three rings for each linac: a delay loop and two combiner rings (CR); leading to the required drive beam features of average beam current (101 A), energy (2.4 GeV) and bunches spaced by 83.3 ps (12 GHz) in pulse bursts of 240 ns long. On the other hand, the main beams will also attain the suited features due to the main beam injection system where the electron and positron beams will come from their respective injectors, at 2.4 GeV, and finally accelerated to 9 GeV by the booster linac before entering in the main linacs.

The *CLIC Test Facility* (CTF3) [4], built at CERN by an international collaboration, was meant to demonstrate the technical feasibility of the key concepts for the CLIC drive beam generation and the two-beam acceleration scheme, as required from the International Linear Collider Technical Review Committee. The results of CTF3 studies are going to be presented in the CLIC Conceptual Design Report (CDR) [5] which is expected to come out this year 2012 as a very important milestone of the road to CLIC.

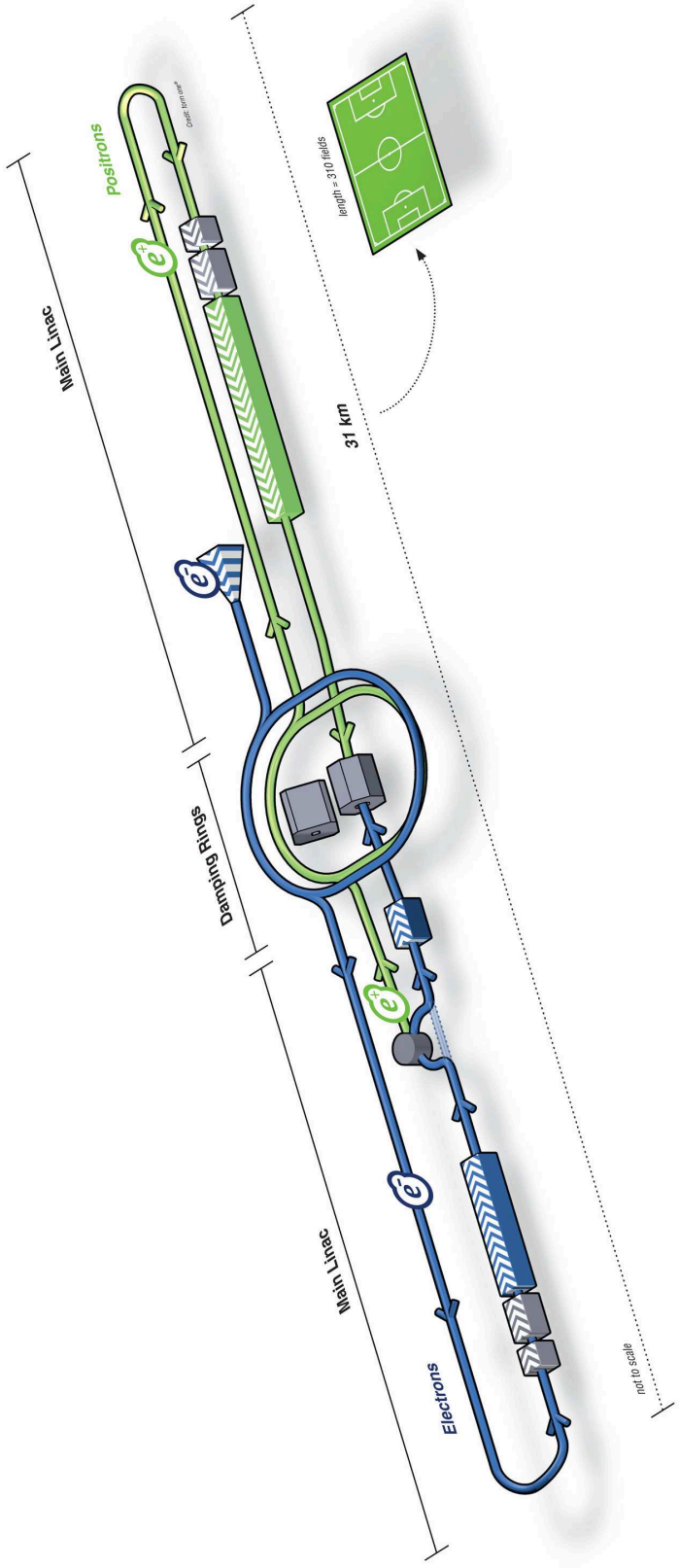

Figure 1.4: A schematic layout of the International Linear Collider, ILC.

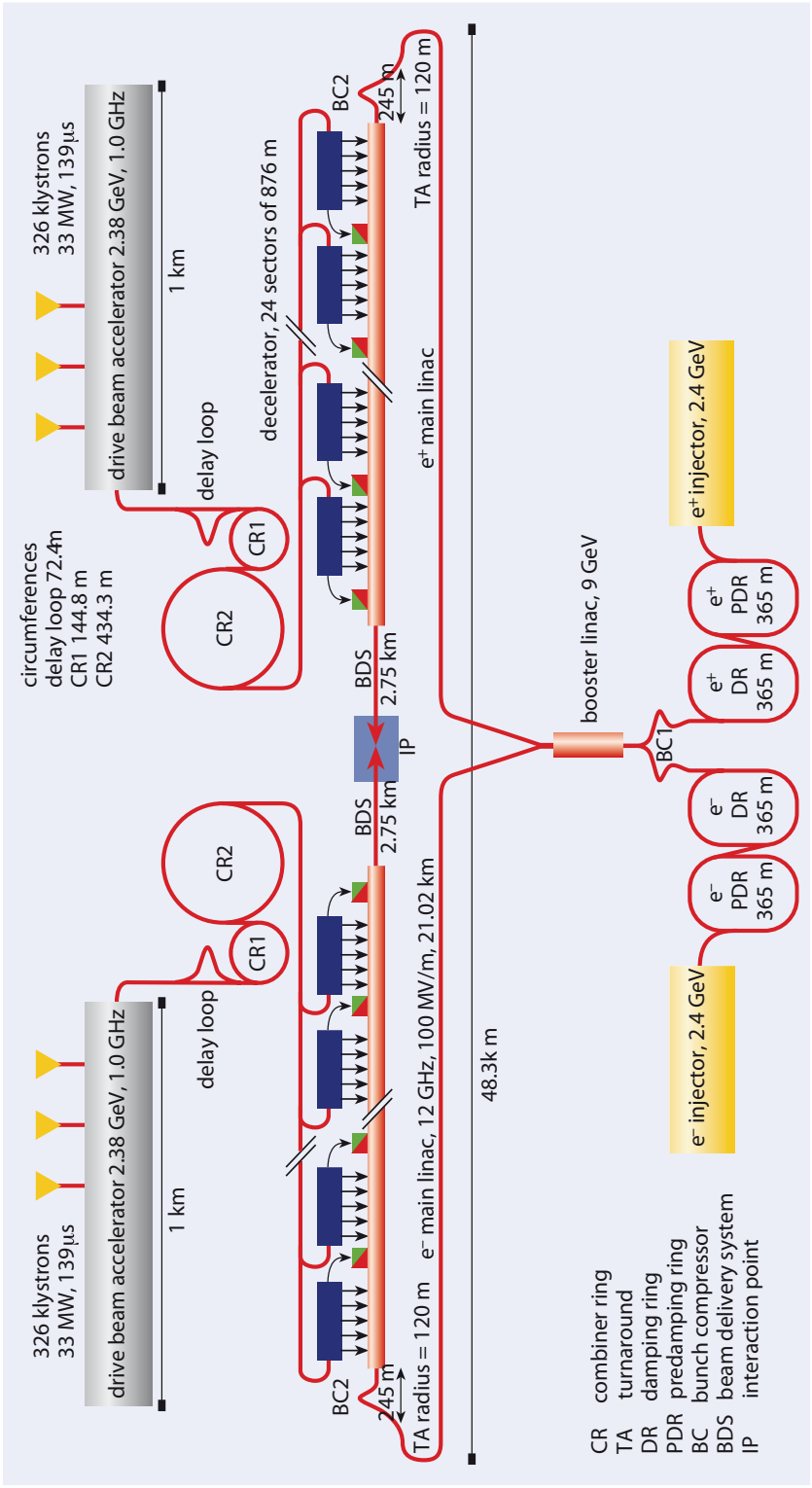

Figure 1.5: The CLIC layout, showing two-beam acceleration scheme and its dimensions (central part), the various components of the main beam injection system (lower side) and the drive beam generation system (upper side).

The two collaborations agree that the ILC technology is presently more mature and less risky than that of CLIC. Nevertheless, the CLIC CDR which collects the CLIC technology feasibility studies carried out during past years will help in reducing the associated risk in the future. The ILC collaboration will focus on consolidation of the technology for global mass production. Both collaborations consider it essential to continue the development of both technologies for the foreseeable future.

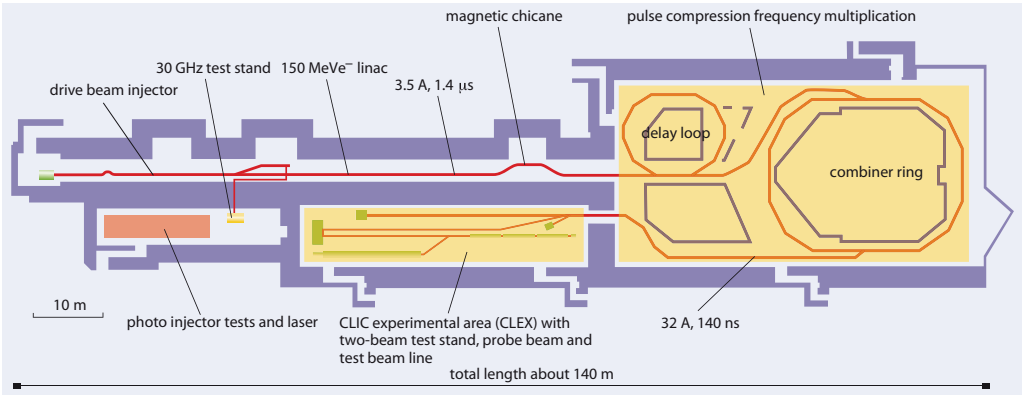

(a)

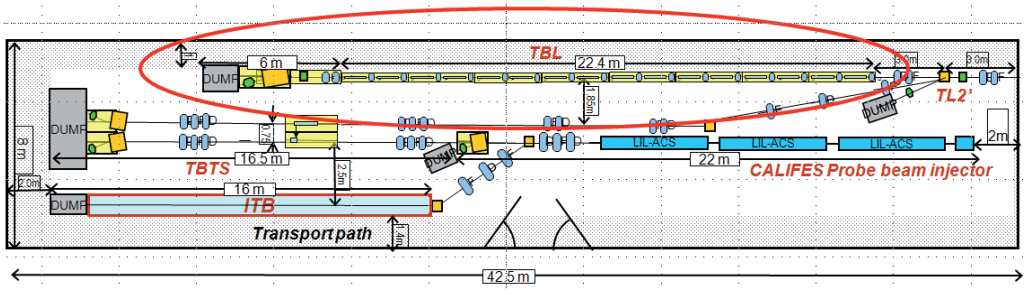

(b)

Figure 1.6: (a) Diagram of the CLIC test facility (CTF3), with 150 MeV linac, delay loop and combiner ring, together with the experimental area, CLEX. (b) Layout of the CLEX hall in building 2010 where the TBL (red circle) is located at CERN.

1.2 The CLIC Test Facility 3

The layout of the CTF3 is depicted in Fig. 1.6a. It consists of a 150 MeV electron linac followed by a magnetic chicane to provide for bunch lengthening before a series of two rings, a delay loop and the combiner ring, in order to minimize coherent synchrotron radiation effects. After the chicane, the beam may be combined by a factor two in the 42 m circumference delay loop, and up to a factor five in the 84 m circumference combiner ring; alternatively, uncombined beams of 3.5 A can be delivered to the *CLIC Experimental area* (CLEX) bypassing the delay loop and performing only half-turn in the combiner ring. Up to this point, the CTF3 is a scaled-down version of the CLIC drive beam complex required to generate the drive beam as a combined beam of high-current and high-frequency electron bunch trains as delivered by the combiner ring. It is intended to demonstrate the principle of the novel bunch-interleaving technique using RF deflec-

tors to produce the compressed drive beam pulses. In CTF3 the compressed beam, with an energy of 150 MeV, 28 A of nominal beam current, a microbunch spacing of 83 ps (12 GHz) and a pulse length of 140 ns, is then sent into CLEX. In Fig. 1.6b is shown the layout of CLEX, housing the *Test Beam Line* (TBL) and the *Two Beam Test stand* (TBTS) where the CLIC acceleration scheme is tested, including the extraction of RF power from the drive beam and the transfer of this RF power to the accelerating structure, which will accelerate a *probe beam* in a full demonstration of the CLIC acceleration principle.

Main differences between the CTF3 beam and the CLIC drive beam are the energy and the current, being, respectively, 16 times and 3.5 times lower in CTF3 than in the CLIC drive beam parameters. The CLIC drive beam has a beam current of 101 A and is decelerated from 2.4 GeV to 0.24 GeV giving up 90% of its energy, whereas the CTF3 drive beam has a beam current of 28 A and is decelerated from 150 MeV to 0.15 MeV giving up also 90% of its energy extracted but at lower absolute scale.

Construction of CTF3 started after the closure of LEP in 2001, taking advantage of equipment from LEP pre-injector complex. Its installation ran on schedule with the electron linac, delay loop and combiner ring which were operated with beam and started commissioning first. The CLEX building with most of the equipment installed in TBL and TBTS saw the first beam on August 2008. A rush of activities followed from then, with further commissioning and CTF3 beam operation improvements, remaining equipment installation, mainly at CLEX, and performance of planned test which lead to the demonstration of an important number of CLIC concepts and the release of the CDR.

The main aims of the TBL sub-project of CTF3 are [6]:

- to study and demonstrate the technical feasibility and the operation of a drive beam decelerator (including beam losses), with the extraction of as much beam energy as possible. Producing the technology of power generation needed for the two-beam acceleration scheme,
- to demonstrate the stability of the decelerated beam and the produced RF power in the X band by the Power Extracting and Transfer Structure (PETS), a well as
- to benchmark the simulation tools and computer codes in order to validate the corresponding systems for the CLIC decelerator design in the CLIC nominal scheme.

Therefore, here is studied in detail the transport of a beam with a very high energy spread, with no significant beam loss and suppression of the wake fields from the PETS. Additional goals for TBL are the test of alignment procedures and the study of the mechanical layout of a CLIC drive beam module with some involvement of industry to build the PETS and RF components, like waveguides. Finally, TBL is intended to produce RF power in the GW range which could be used to test several accelerating structures in parallel.

The TBL layout can be seen, inside CLEX hall, in Fig. 1.6b, and it consists of a series of FODO lattice cells and two diagnostic sections at the beginning and at the end of the line for completing the measurement of all relevant beam parameters. Each FODO cell is comprised of a quadrupole, a Beam Position Monitor (BPM) and a PETS, a view of a TBL cell design is shown in Fig. 1.7a. The quadrupoles, which performs the alternate focusing of the beam every two cells and also the necessary beam steering for proper beam transport along the line, are also equipped with remotely controlled movers for beam based alignment. The FODO lattice was chosen because of its energy acceptance.

Due to transient effects during the filling time of the PETS the first 10 ns of the bunch train will have a huge energy spread from the initial energy down to the final energy of the decelerated beam. The lattice is optimized for the decelerated part of the beam, higher energy particles will see less focusing. The betatron phase advance per cell is close to the theoretical value of 90 degrees per cell for a round beam.

The available space in CLEX allowed the construction of up to 16 cells with a length of 1.4 m per cell. As depicted in Fig. 1.6b, the TBL is placed after the first bending magnet of the chicane toward the TBTS line. The diagnostic section in front of the bending magnet will be used for TBL experiments to determine the beam properties at the entrance of TBL, but is formally (schedule and budget) a part of Transfer Line 2 (TL2). Therefore, TBL starts with a matching section consisting of a quadrupole doublet, a BPM and a pair of correctors to allow for parallel displacement of the beam to excite wake fields in a controlled way. The matching section is followed by sixteen identical cells as described above. At the end of the beam line another diagnostic section is installed allowing a characterization of all relevant beam parameters. This section consists of a quadrupole doublet and an Optical Transition Radiation (OTR) screen dedicated to transverse beam profile and emittance measurements. A spectrometer with an angle of 10 degrees and a second screen will provide a measurement of the energy and energy spread. It is also installed a segmented beam dump enabling time resolved energy measurements. The section is completed by another BPM and a Beam Profile Radio-Frequency monitor (BPR, button pick-up type) which will provide a signal proportional to bunch length. The total length of TBL is about 28.4 m including the decelerator line of 22.4 m with the 16 cells being a single vacuum sector, and the diagnostic section of 6 m.

Within the framework of a MoU signed in 2006 with CERN, the Spanish participation in CTF3 has been funded from national special actions, with the following significant contributions to TBL: the PETS structures and the quadrupole movers, with a 5 mm precision [7], [8], were developed by Centro de Investigaciones Energéticas Medioambientales y Tecnológicas, CIEMAT, Madrid; the BPM development, object of this thesis, along with its alignment supports was made by Instituto de Física Corpuscular, IFIC, Valencia, in direct collaboration with Universitat Politénica de Catalunya, UPC, Barcelona, responsible for BPM analog front-end amplifiers. In Fig. 1.7b is also shown a section of the TBL line with the BPS at first term in the photo, followed by a quadrupole and the the first PETS installed in TBL. The BPM design is a scaled and adapted version to the TBL specifications of an Inductive Pick-Up (IPU) installed in the Drive Beam Linac (DBL) of CTF3 [9]. The BPMs developed for TBL were labeled as BPS standing for *Beam Position Small or Spanish*.

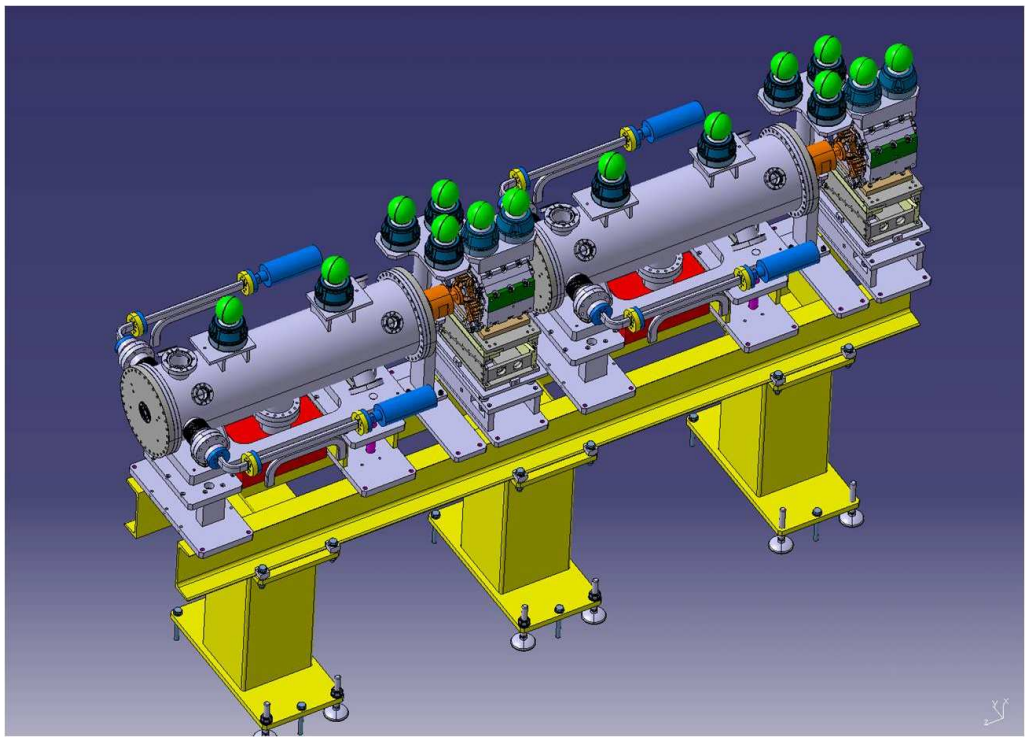

(a)

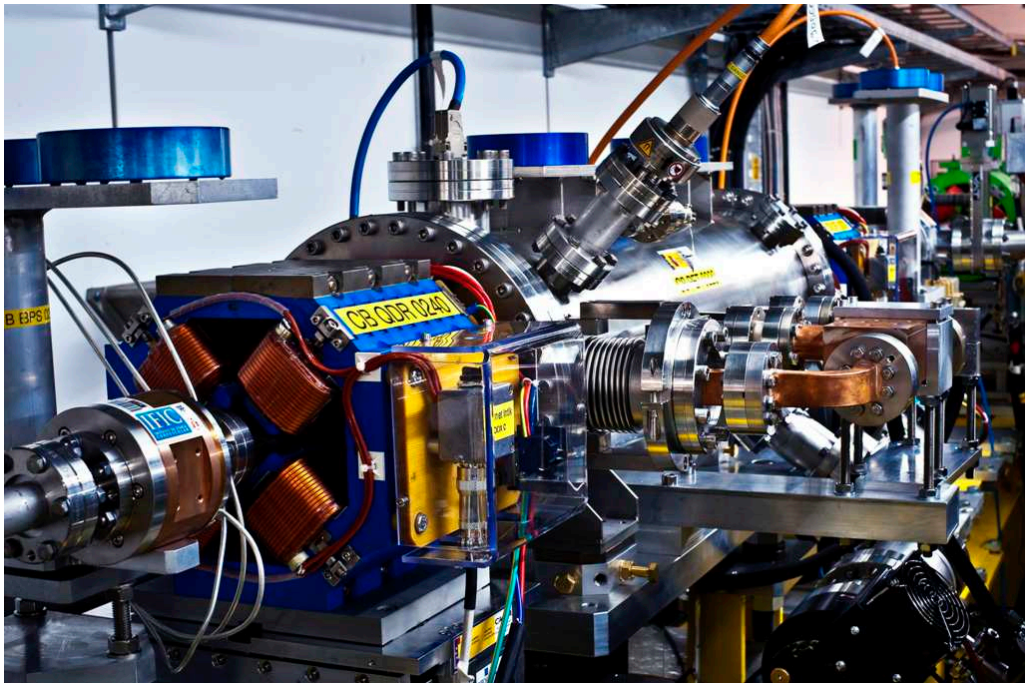

(b)

Figure 1.7: (a) 3D view of two consecutive FODO lattice cells in TBL with a PETS tank, the BPS monitor, and a quadrupole per cell (the beam direction is from right to left).(b) Section of TBL at the beginning of the line after installation in October 2009, in the photo are shown (from right to left) a PETS, a quadrupole, and a BPM labeled as BPS.

Chapter 2

Beam Diagnostics in Particle Accelerators

2.1 Introduction

The *beam instrumentation* or *beam diagnostics* deals with the design and development of the great diversity of instrumentation devices and technology needed for monitoring the beam properties in *particle accelerators*. As part of any accelerator the beam diagnostics devices are all along the machine to sense the various beam parameters converting them into directly measurable signals for further processing. These signals, carrying the beam parameter information, can then be acquired and driven through a device readout chain, usually integrated in a control architecture, to the control room main servers which finally yield all the necessary information displaying the behavior and characteristics of the beam in the accelerator.

Particle accelerator performance depends critically on the measurement and control of the beam properties, so beam diagnostics becomes an essential constituent of any accelerator. Generally the beam is very sensitive to imperfections or deviations from the ideal accelerator design produced in any real machine, and without adequate diagnostics one would "blindly grope around in the dark" for optimum accelerator operation. In numbers, about 3 % to 10 % of the total cost of an accelerator facility must be dedicated to diagnostic instrumentation. But due to the complex physics and techniques involved, the amount of man-power for the design, operation and further development exceeds 10 % in most cases [11].

2.2 Overview of beam parameters and diagnostics devices

Some decades ago, particle accelerators were controlled and optimized mainly by looking at phosphorescent screens, mostly based on zinc sulphide (ZnS), and simple beam current meters. Developments in the field of beam diagnostics have been benefiting by the development of computers, sophisticated electronic circuits, and digital acquisition modular systems based respectively on standard buses like VME (Versa Module Eurocard), PCI (Peripheral Component Interconnect) or Ethernet LAN (Local Area Network), with their respective standard bus extensions specific for instrumentation VXI, PXI and LXI (VME, PCI and LAN eXtensions for Instrumenation). This development together with powerful simulation programs to describe beam particle dynamics and computer-aided software

for the accelerator design and control, has lead to more complex accelerators machines. Nowadays, the operation and on-line control of modern accelerators, operated also in several modes, require the availability of many beam parameters. Due to the manifold machines, such as linear accelerators (linacs), cyclotrons, synchrotrons, storage rings, and transfer lines, the demands on a beam diagnostic system can differ from one to another.

Taking into account additionally the broad spectrum of particles such as electrons, protons and heavy ions, and the more demanding trends on the beam features like higher beam currents, smaller beam emittances and tighter tolerances on the beam parameters, it became essential in recent years the development of multiple and versatile measurement techniques as well as specific machine designed diagnostics devices.

Hence there is a large variety of beam parameters to be measured in an accelerator, and furthermore all relevant parameters should be controllable for a good performance and stability of the beam. In the following it is given an overview of the main beam parameters used for the characterization of the particle beams in an accelerator [11–14].

2.2.1 Beam intensity

One of the first questions in the operation of a new accelerator is how many particles are in the machine, or equivalently the flux of particles, thus for a charged particles beam it is defined the beam *current intensity* I, usually given in Ampere units, as the flow of a total beam charge Q per unit of time t

$$I = \frac{Q}{t} \tag{2.1}$$

with the total beam charge being $Q = qeN$, where N is the number of particles, $e = 1.602 \times 10^{-19}$C is the electron charge, and q is the charge state of the accelerated particle, which is an integer to represent a more general ion particle with some positive or negative charge multiple of the electron charge. With knowledge of the beam current intensity, or just the beam current, it is possible to determine the beam lifetime as the decay of its current intensity, and the coasting beam phenomenon of debunched beam particles forming a continuous current in storage rings, as well as transfer efficiencies in linacs and transfer lines.

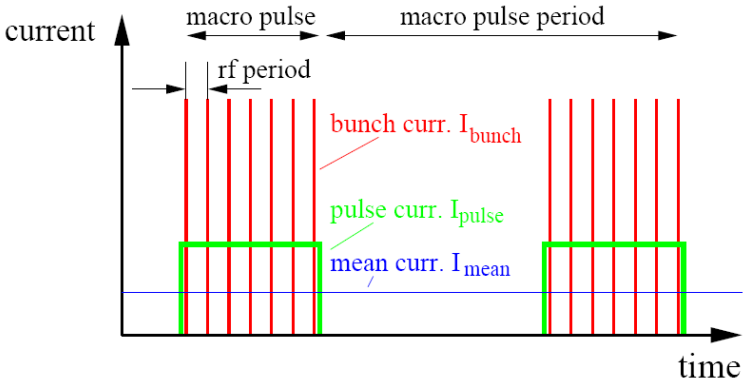

Figure 2.1: Typical beam time structure representation of an RF pulsed accelerator.

Depending on the time structure of the beam in the accelerator three main types of

beam currents can be defined, as it is depicted in Fig. 2.1 for a general case of a pulsed beam linac,

- **Bunch Current** I_b is the current within a bunch, sometime called micro-pulse current, so it is given by the charge per bunch Q_b over the bunch time length Δt_b as

$$I_b = \frac{Q_b}{\Delta t_b} \tag{2.2}$$

  The bunches can be separated at least by the RF period, as the inverse of the RF frequency. In most of the cases this is given in number of particles or charge per bunch, instead of Amperes units.

- **Macro-pulse Current**, or just pulse current, I_p is the current average over the duration of the beam pulse Δt_p which corresponds to the beam delivery time in a pulsed machine. Since the pulse is composed of a train of many bunches separated by the RF period T_{RF}, its current can be related to the bunch current through Eq. (2.3) assuming ideal conditions of constant bunch charge and length for all the bunches within the macro-pulse; or using Eq. (2.4) for a more general case of non-constant bunch current $I_b(t)$

$$I_p = I_b \cdot \frac{\Delta t_b}{T_{RF}} \tag{2.3}$$

$$I_p = \frac{1}{\Delta t_p} \int_0^{\Delta t_p} I_b(t)\,\mathrm{d}t \tag{2.4}$$

  where the pulse duration can be expressed in function of the number of bunches n_b as $\Delta t_p = n_b T_{RF}$, and the ideal case in Eq. (2.3) can be easily recovered from Eq. (2.4) provided that the bunch current I_b is constant, and non-zero, only for the bunches time length $n_b \Delta t_b$.

- **Average Current** I_{av} is the beam current averaged over several beam pulses or a given long time interval Δt_{av}. In pulsed machines the beam pulse shots are generated with a repetition frequency corresponding to the inverse of the pulse period T_p, thus the average current can be likewise related the pulse current through Eq. (2.5) assuming ideal square current pulses of constant macro-pulse current; or using Eq. (2.6) for a more general case of non-constant pulse current $I_p(t)$

$$I_{av} = I_p \cdot \frac{\Delta t_p}{T_p} \tag{2.5}$$

$$I_{av} = \frac{1}{\Delta t_{av}} \int_0^{\Delta t_{av}} I_p(t)\,\mathrm{d}t \tag{2.6}$$

  where the average time interval can be expressed in function of the number of pulse periods N_p as $\Delta t_{av} = N_p T_p$, and the ideal case in Eq. (2.5) can be easily recovered from Eq. (2.6) provided that the pulse current I_p is constant, and non-zero, only for the pulses time length $N_p \Delta t_p$.

These three beam current levels are all different for a pulsed beam like in pulsed linacs or pulsed cyclotrons. These can be used as injectors of synchrotrons, typically long pulse lengths are produced around 100 μs to perform the injection of the pulse bunches in the synchrotron in several beam turns (multi-turn injection), needing shorter pulses for single-turn injection in the order of 10 μs. Pulse lengths in the nanosecond or even down to picosecond scale can also be produced in some accelerator facilities with combined machine structures. In continuous wave accelerators, such as cyclotrons used in atomic or nuclear physics applications, likewise the pulsed accelerators the beam has a bunched time structure due to the resonant acceleration, but in contrast the bunches are delivered continuously over a long period of time. In that case the macro- or pulse current I_p and the average current I_{av} both match up.

For accelerators producing unbunched and continuous beam a DC-current level is produced and only I_{av} measurement will make sense. Examples of these accelerators, which were historically the first types of accelerating structures, are the *Van-de-Graaff* and *Cockcroft-Walton* generators using electrostatic acceleration with a constant high voltage instead of the RF acceleration power; and the Betatron that accelerates electrons in a toroidal geometry with acceleration achieved by magnetic flux increase.

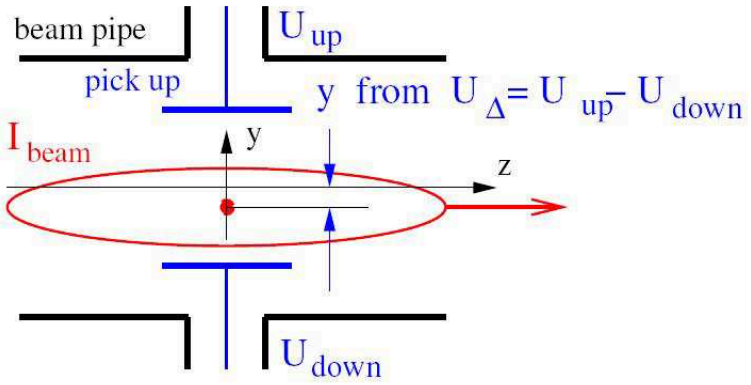

Figure 2.2: Illustration of the beam position between monitor electrodes in the *y*-vertical plane which is obtained as the difference signal between opposite pick-up electrodes (U_Δ).

2.2.2 Beam position

The next fundamental property of the beam to be determined in an accelerator would be the beam position in the transversal plane perpendicular to the beam propagation direction like shown in the Fig. 2.2. More specifically the beam position refers to the center of gravity within the transverse density distribution of the beam particles, or beam centroid. This can be determined only with a two-dimensional reference system, being *x* (horizontal) and *y* (vertical) the two coordinates contained in the transverse plane. The devices designed specifically to measure the beam position as the beam centroid are called Beam Position Monitors (BPM) which are also commonly known as Pick-Ups (PU). The beam position measurements are usually made by BPMs placed regularly along the machine executing their main task in the operation of any machine which is the determination of the beam orbit, in circular machines, and the beam trajectory, in the linear ones. In many feedback systems to correct the beam orbit or to control other beam parameters BPM measurements are necessary. More indirectly, they also give access to determine a wide number

of important accelerator parameters such as the deviation of the lattice parameters, the chromaticity or the tune.

2.2.3 Beam profile and beam size

A closer look into the shape and size of the beam bunches can be done by measuring the density distribution of beam particles projected on every 3D coordinate, as it is shown in Fig. 2.3, so each projection will define the *beam profile* for the two transversal (x, y) axes and the longitudinal coordinates with regard to the beam propagation (z) axis. The beam spot size is directly observed in the transverse beam profile measurements defining the beam size in both transverse coordinates, as well as the beam bunch length which is determined from the longitudinal profile measurements. In accelerator physics, it is usual to distinguish between longitudinal and transverse planes having different description of the beam dynamics, so the determination of the longitudinal and transverse beam profiles will also require different measuring techniques [15, 16].

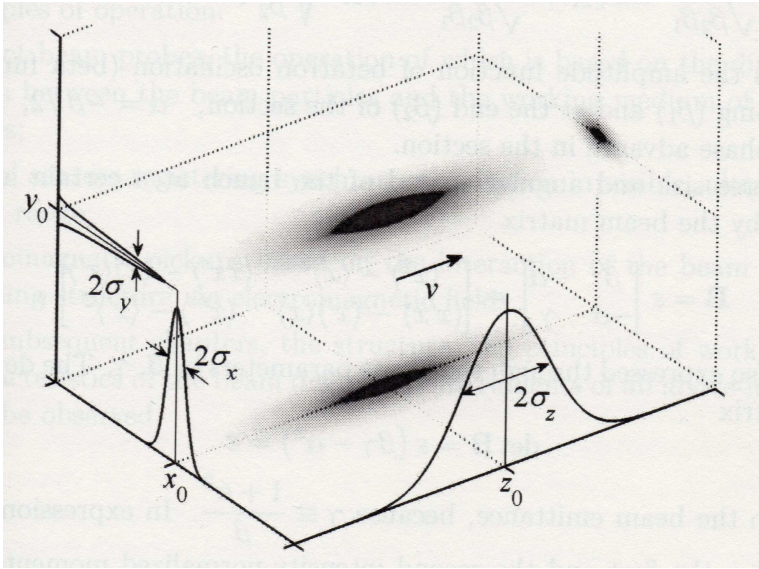

Figure 2.3: Representation of a beam bunch in the three spatial dimensions.

The transverse beam profile, and so the beam size, change along the machine mainly due to the action of the quadrupole magnets that focus and defocus the beam, apart from other magnets in the the accelerator lattice like bending dipoles and correction multipoles which, in general, can also affect the beam size. This gives rise to the need for many profile measurement stations, and depending on the type of beam particles, current and energy, a very large variety of transverse profile monitors exist. Then the beam spot size can be controlled through the beam profile measurements which are fundamental for the transverse matching between different parts of an accelerating facility as well as for the determination of such an important parameter as the *transverse emittances*, ϵ_x and ϵ_y.

The beam size measured at some accelerator location s is mainly determined by the settings of the focusing magnets and the transverse beam emittances, and they are related through the betatron function $\beta(s)$, as the envelope of the beam particles oscillations around the design trajectory, and the dispersion $D(s)$ function, taking into account for the off-momentum beam particles motion, as

$$\sigma_{x,y}(s) = \sqrt{\epsilon_{x,y}\beta_{x,y}(s) + \left(D_{x,y}(s)\sigma_\epsilon\right)^2}. \tag{2.7}$$

In a synchrotron, the emittance in both coordinate planes (x, y) can be determined from the profile measurements at some given location s according to Eq. (2.7), where $\sigma_{x,y}$ represent the beam size for their respective coordinate plane, σ_ϵ the momentum spread, and provided that the $\beta(s)_{x,y}$ and $D_{x,y}(s)$ functions at location s are a priori known or can be measured separately. Normally, the profile monitors are located at dispersion-free sections, avoiding the dispersion term contribution to the emittance ϵ, so the beam size can be obtained simply from the β function. In a transfer line or linac at least three independent profile measurements are taken to solve for the transverse emittance. Then, two common schemes are used to determine the transverse emittances, either the beam size is measured at three different locations with different profile monitors for the same beam optics settings, or with only one profile monitor producing independent beam size measurements by changing the beam optics settings through the strength of one or more quadrupoles [14]. Besides the profile monitors, more direct measurements of transverse emittance are also made with the slit-grid method sweeping in the phase space coordinates [12].

In Fig. 2.4 is shown the image from an OTR (Optical Transition Radiation) monitor of a beam spot and the beam size measurement obtained after fitting gaussians in both coordinates to the beam profile. This OTR belongs to a multi-OTR system of four devices installed in the extraction line of the ATF2 (Accelerator Test Facility) at KEK in Japan, which is able to perform bunch-by-bunch beam spot captures allowing also to obtain fast emittance measurements ($\sim$ 1 min) [17,18]. In addition, the beam position centroid can be also obtained from the transverse profile measurements just identifying the beam intensity peak value as can be seen in Fig. 2.4. More specific examples like the study of beam blow-up of individual bunches under collision in a particle collider, and beam halo diagnostics rely mainly on measurements of the transverse beam profile.

The measurements of the longitudinal beam profile in z-axis can be performed at bunch level being able to determine the bunch center of gravity giving a bunch phase position relative to the accelerating RF sine-wave, the RMS bunch length, and also the bunch head, tail and core distributions. The beam time structure of the bunches can also be inspected and depending on the time resolution of the profile measurement compared to the bunch length (usually measured in time units) a more or less detailed image of the bunch shape could be recorded. The observation and control of the longitudinal behavior at injection and during acceleration is basic for the correct performance of the machine, but also allows beam manipulations like interleaving, combining or splitting bunches. As well as for the transverse planes, the longitudinal bunch shape can be taken from capacitive, strip-line or wall current pick-ups of the same or shorter length than the bunch, and then used to get the *longitudinal emittance* ϵ_z of the beam by several methods.

Other devices for observing the bunch longitudinal shape are used, more specifically for proton/heavy-ions accelerators the secondary emission of electrons by an intercepted wire, and a streak camera capturing the synchrotron radiation generated in a bending magnet. In Fig. 2.5 an image capture of several bunches from an streak camera at the Duke storage ring [19]. Moreover, to obtain the longitudinal phase space ellipse the momentum spread can also be determined by means of Time-Of-Flight (TOF) measurements between pick-ups [11, 12].

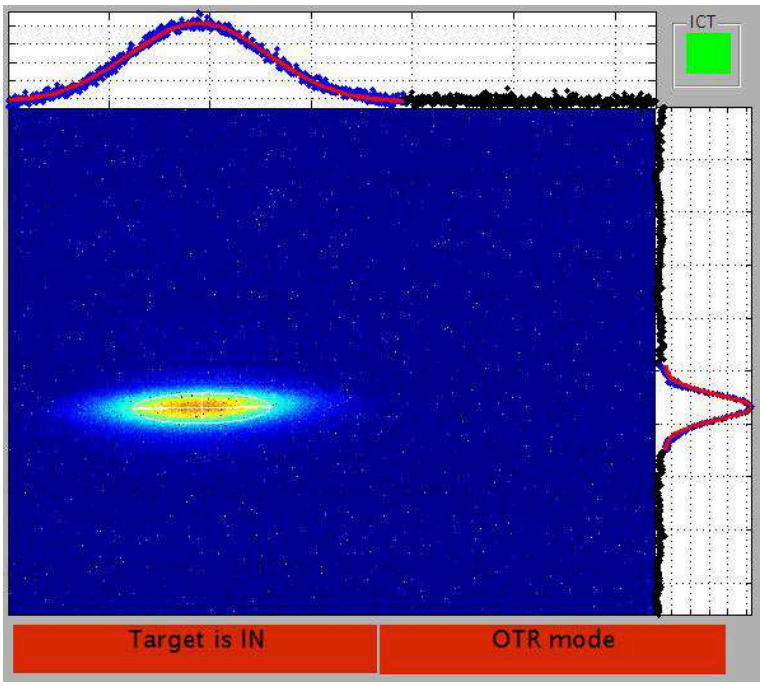

Figure 2.4: Image of the transverse beam profile and beam spot size measurement, where the beam centroid is also identified, from one of the four OTR monitors composing a multi-OTR system installed in the extraction line of ATF2 at KEK.

2.2.4 Other relevant beam parameters: tune, chromaticity and luminosity

In synchrotron machines the trajectory of the beam as a result of the action of the guiding and focusing elements describes periodic oscillation displacements around the ideal circular design orbit, or central orbit, in both transverse directions. The number of these so-called *betatron oscillations* made by the beam in one accelerator ring turn is the *tune* parameter Q. The tune is usually defined as $Q = \Delta\mu/2\pi$ in terms of the phase advance of the betatron oscillation. Then the tune can be split in an integer part Q_n and a fractional part q as $Q = Q_n + q$ where $0 < q < 1$. The tune requires precise control in order to avoid resonances driving self-amplified instabilities that eventually after several turns will lead to an increase in beam size, chaotic particle motion, and therefore, particle losses. Most measurement methods can only determine fractional part q and the total integer number of oscillations Q_n can not be seen, but this is normally of no interest as it is already known from calculations.

Moreover, the focusing properties of a quadrupole are dependent of the particle momentum, resulting in a change of the tune parameter for different momenta in synchrotron machines. This is described by the *chromaticity* defined as the proportional factor between the relative spread of tune with respect the relative spread of momentum, i.e. $\xi = (\Delta Q/Q)/(\Delta p/p)$. In the case of linear accelerators the chromaticity parameter can not be related to the tune since it has no meaning for a linear machine, but it also exists for describing the effect of quadrupoles focusing errors due to beam particles momentum spread.

In contrast to other beam parameters, such as beam positions or trajectory, beam current, and beam profiles; tune and chromaticity are the first non-trivial beam parameters

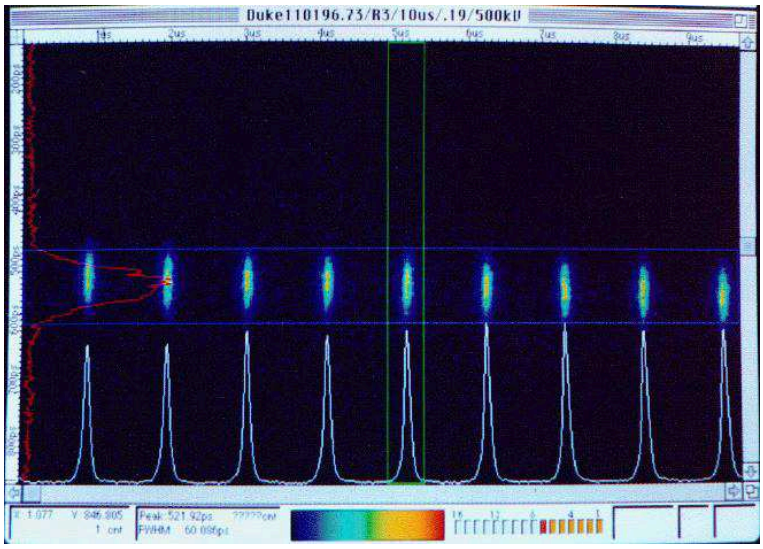

Figure 2.5: Image of the longitudinal profile of a train of beam bunches and bunch length measurement with a Streak Camera at Duke storage ring. The horizontal axis scaling is 10 μs for the bunch repetition and the vertical axis is 800 ps full scale for the bunch structure, the bunch length is 60 ps (FWHM).

that can not be derived from a direct measurements on the beam [20]. They typically rely on a coherent beam excitation, followed by measurement of the driven oscillation, and some post-processing. For example, in Fig. 2.6 it is illustrated the kick method for tune measurements. This method is based on the action of a kicker magnet which is able to generate a fast perturbation on the beam, or kick, at a given lattice location leading to the excitation of coherent betatron oscillations. The kick has to be shorter than the revolution frequency and with moderated strength to prevent the complete beam loss. Then the beam position is monitored with a pick-up turn by turn and it is stored as a function of time. Usually, to get a good resolution the pick-up is placed at a lattice point where the betatron amplitude is large. Once the excited displacement oscillations are acquired a Fourier transformation is applied to them to yield the fractional part of the tune q and the tune spread ΔQ which correspond to the excited harmonic line and its width, respectively, of the Fourier spectrum plot in Fig. 2.6. The tune measurements are used to determine the chromaticity parameter in circular machines, but also different momentum spreads has to be observed shifting the RF frequency in the acceleration cavities for that. The proportional chromaticity factor can then be obtained representing the tune spread versus the momentum spread by a linear fit, which is only valid for small relative momentum deviations.

Depending on the type of accelerator and its diagnostics needs, there will be many other relevant parameters that can be measured with specific instrumentation or combination of usual monitors. For instance, it is also important to detect the *beam losses* experienced along the accelerator for what beam loss monitors are employed to prevent damage to the accelerator, and to the other facility components, as well as for the optimization of daily accelerator operation. Moreover, in heavy-ion machines special diagnostics are used to measure the particle charge states and mass numbers.

Finally, it is mentioned here the *Luminosity L* which is one of the key parameters for particle colliders. This parameter quantifies the collider performance relating the cross

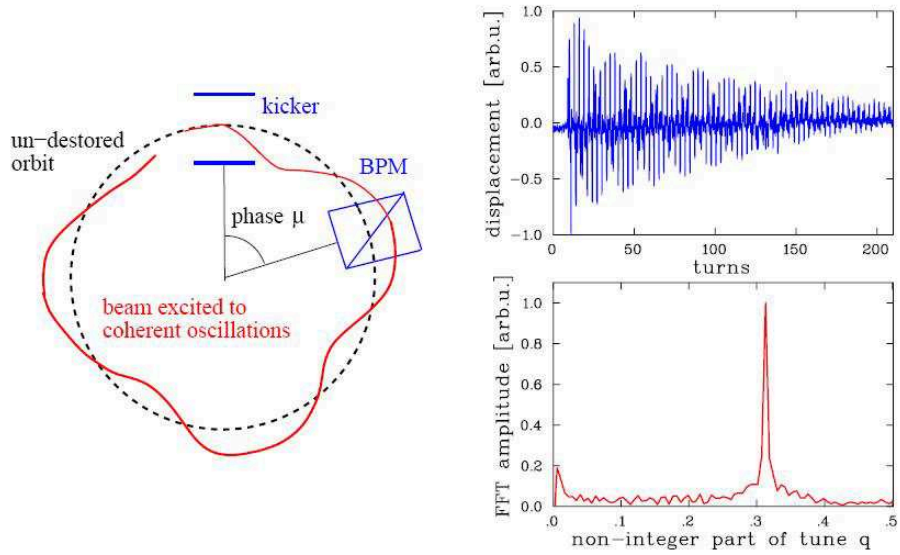

Figure 2.6: Example of tune measurement method by recording beam oscillations after a kick excitation in the time domain for 200 turns (right-top) and its Fourier transformation for q determination (right-bottom).

section σ (a property of the particle reaction itself) with the rate of collision events, which is the primary concern for experiments, being $\dot{N} = L\sigma$. While an absolute on-line luminosity determination is sometimes difficult to provide, the determination of a relative luminosity or simply a count rate which is proportional to it, is a very important tool for the optimization of the collision (angle and position) of both beams via beam steering. Then the luminosity tends to be maximized to achieve the best collider performance, for that, besides colliding beam offsets and crossing angles, the beams current should be as high as possible, and the transverse beam size in the IP as small as possible since the luminosity scales as $L \propto N^2/\sigma_x\sigma_y$ [21].

Another parameter of interest would be the beam energy, but mainly for users, and a description of the several methods to measure it based on spectrometry and mostly on particle detectors techniques can be found on [22]. In a lepton collider, for example, it defines the reaction energy which is available in order to produce new particles, while in synchrotron light sources (third-generation as well as free-electron-lasers (FELs) it defines the spectral characteristics of the emitted radiation.

Generally, depending on the operational mode of an accelerator there exist different requirements for beam diagnostics. Sometimes they cannot be fulfilled with only one device, in consequence, two or more instruments are needed in order to measure the same beam parameter under different operational conditions because the dynamical range of a single device may not be sufficient. Nevertheless, as showed in this section, one kind of diagnostic device could also serve to measure several beam properties. In Tab. 2.1 are summarized the most important beam properties and the common diagnostics devices and methods addressed to measure them [11, 23].

Beam quantity	**Use**	**LINAC, Transfer line**	**Synchrotron**
Current I	general	transformer (dc, pulsed) Faraday cup	transformer (dc)
	special	particle detector (scintillator, IC, SEM)	normalized pick-up signal
Position (x, y)	general	pick-up	pick-up
	special	profile monitor (centroid)	cavity excitation (e^-)
Profile, beam size $\sigma_{x,y}$	general	SEM-grid, wire scanner viewing screen, OTR screen	residual gas monitor synch. radiation (e^-) wire scanner
	special	grid with amplifier (MWPC)	
Trans. emittance $\epsilon_{x,y}$	general	slit grid, quadrupole scan	residual gas monitor wire scanner
	special	pepper pot	transverse Schottky pick-up wire scanner
Momentum, –spread p, σ_ϵ	general	pick-ups (TOF) magn. spectrometer	pick-up
	special		Schottky noise pick-up
Bunch length σ_z (l, Δt or $\Delta\varphi$)	general	pick-up	residual gas monitor wall current monitor
	special	particle detector secondary electrons	streak camera (e^-)
Long. emittance ϵ_z	general	magn. spectrometer buncher scan	pick-ups + tomography
	special	TOF application	
Tune, Chromaticity Q, ξ	general	—	exciter + pick-up (BTF)
	special	—	transverse Schottky pick-up
Beam losses	general	particle detector	
Polarization P	general	particle detector	
	special	Compton scattering with laser	
Luminosity L	general	particle detector	

Table 2.1: Beam parameters and most commonly used beam diagnostics devices.

2.3 Beam diagnostics requirements for different machines and operation modes

One can roughly distinguish between two different modes of operation and summarize their impact on beam instrumentation [14]:

A. diagnostics for accelerator (section) commissioning:

- applied in order to adjust the beam transport through different accelerator sections,
- required for the characterization of the beam behind each accelerator section,
- simple or more complex but robust devices with high sensitivity, allowing to operate with several beam patterns (single or few bunches) of low intensity,
- low or modest demands on accuracy,
- application of beam disturbing methods are possible and if necessary devices might be destructive for the beam, the importance is on the creation of reliable

information about the beam behavior;

B. diagnostics for standard operation:

- applied for precise beam characterization in order to control and improve the accelerator operation,
- required for daily check of performance and stability and for the diagnosis of unwanted errors and to trigger interlocks in case of machine malfunctions,
- devices are typically based on more or less sophisticated schemes,
- high demands on accuracy,
- application of minimum beam disturbing schemes and devices should be non-destructive for on-line monitoring although allowing destructive but removable devices with feed-throughs.

In general for measuring a particular beam property one has to choose or design the most suitable diagnostic device, always attending to the operational requirements but also to the type of accelerator and its particular beam features. For some beam properties, the main differences in the type of instrumentation arise between linear and circular accelerators due to their different accelerating principles.

In a linear accelerator the beam passes only once so it has many accelerating cavities pushing the beam to higher energies as the beam travels through the machine. The beam in a linac is generated as a sequence of pulses which may vary from shot to shot, and an equilibrium state can not be settled like the beam orbit in circular machines. In a linac, because beam emittance and energy are both function of the location in the accelerator, and also the beam charge can be lost everywhere in the machine, many devices are required for proper beam transport.

In contrast to a linac, the beam particles in a circular accelerator or synchrotron perform many passages around it so only a relatively small number of accelerating cavities are needed. A synchrotron is a continuous wave (cw) system, in the sense that the signals from the beam are repetitive and stable for many turns. It is also possible that the beam reaches a kind of equilibrium state as well as the beam generated signals, and feedback orbit corrections can also be performed. Therefore high precision can be achieved by averaging, and the signals are typically treated in the frequency domain. Emittance and beam current are non- or slowly varying parameters.

Furthermore, jointly with accelerator type it has to be considered the species of beam particles in the choice or development of the diagnostic devices. Electron beams have a quite different behavior as compared to protons or heavy ions. A simple example is the fact that electrons become relativistic ($\beta \simeq 1$) very soon, just after the first linac accelerating modules; while for much heavier particles like protons, several hundred meters long linacs or even a synchrotron is needed to reach significant relativistic conditions having usually non-relativistic energies ($\beta << 1$).

Since most of the beam instrumentation like pick-ups rely on measurements of the EM fields produced by the charged particles of the beam, an important consequence is that the beam EM fields behavior depends on the velocity of beam particles. In case of relativistic beams, where β is close to one, the electric and magnetic fields of the beam are both purely transversal to the direction of propagation what is equivalent to the only EM signal transmission in a coaxial waveguide and all the measurement techniques and knowledge

on this issue can be directly applied to the device design and signal treatment. In the non-relativistic case, for a low β beam its EM fields can not be approximated as being pure transversal field components, and axial or longitudinal components appear modifying the usual device signals measurements of the relativistic case, and dealing with these signals is, in general, more complicated. In particular, for pick-ups the signal spectrum and time signal shape are dependent on the beam position, and signal non-linearities and cross couplings between coordinate planes become more significant.

Another difference between the type of beam particles arise concerning the emission of synchrotron radiation. In circular colliders these radiated fields are generated due to the beam trajectory bending and represent a loss of beam energy. In the case of electron beams this effect comes out at lower energies compared to proton beams.

2.4 Underlying physical processes

The instrumentation device concepts applied to particle beam diagnostics rely typically on the following physical processes [11, 14]:

- **Electromagnetic fields**. The beam moving charges generate electromagnetic fields, as described by classical electro-dynamics and special relativity, that can be used in two ways for beam diagnostics purposes. One is the influence of the EM field bounded to the beam particles on its surroundings. This EM field generated by the beam and traveling with it, normally, is coupled to the metallic walls of the vacuum pipe inducing so voltages and currents that carry information of the beam properties. These electrical quantities can then be measured by a monitor on a low or high frequency scale. Examples of such monitors are the beam current transformers and pick-ups. The other one is the EM field radiated by accelerated charges also called synchrotron radiation which propagates away from the beam particles as emitted photons. In this case the beam information is encoded in the photon beam intensity and spectral components, and the measurement techniques are based on optical methods and photon detectors covering the visible range up to the X-ray regions. This radiation is produced significantly in circular accelerators at relativistic beam energies, so this type of diagnostics will be mainly used in electron synchrotrons like the synchrotron radiation monitors for beam profile and time measurements.
- **Coulomb interaction of charged particles penetrating matter**. Charged particles lose energy as going through matter transferring it to the medium, either directly or indirectly, via the ionization or excitation processes of the constituent atoms, as described by atomic and solid state physics. The outcome of these energy release to the medium, in case of direct ionization, are currents of charged ions or electrons which can be measured, for example, in gas ionization chambers, silicon particle detectors, residual gas monitors and secondary electron emission (SEM) grids. In case of atoms excitation and deexcitation processes, photons are emitted usually in the visible and near infrared range and can be measured by photodetectors and optical methods, for example, in scintillators, viewing screens and OTR monitors.
- **Nuclear or elementary particle physics interactions**. Nuclear or elementary particle physics interactions can arise between beam particles and a fixed target or between two counter-propagating colliding beams, with beam energies above Coulomb barrier. The signal of interest is a flux of different particles coming out

the interacting particles which can be measured with particle detectors techniques. From the beam diagnostics perspective the goal is mainly to obtain beam information as the luminosity with knowledge of the relevant cross sections, in contrast to more complex particle detectors intended to investigate the particle species of the matter constituents and its fundamentals interaction forces in high energy physics.

- **Interactions of particles with photon beams**. For the interaction of particles with photons a high power laser beam is usually scanned across the particle beam profile. For electron beams the Compton scattering is the dominant interaction and monitors based on it are laser scanners or Compton polarimeters which can get the beam profile by measuring the electron scattered photons with their associated optics and detectors. For heavier particle beams like hadrons, H^- ions or protons the Compton scattering is strongly suppressed and other methods are used. As an example of this case, for H^- beams it is produced a laser photo-neutralization mechanism where the incident laser photons can knock off electrons from H^- ions and then the liberated electrons are collected to provide a direct measurement of the beam profile.

2.5 Electronic readout chain

Once the diagnostic device senses the desired beam quantity, it produces an output usually in form of electrical signals, or if device output is not electrical (e.g. optical output) at some point it will be converted to electrical, so that can be transmitted and processed by electronic means. For that the electronic readout chain is essential for any beam diagnostic system and it comprises several stages, from the specific monitor analog output up to the servers where the acquired digital data is stored being then available to display the information in the control room monitors or to use it in a feedback control loop of other accelerator elements [24].

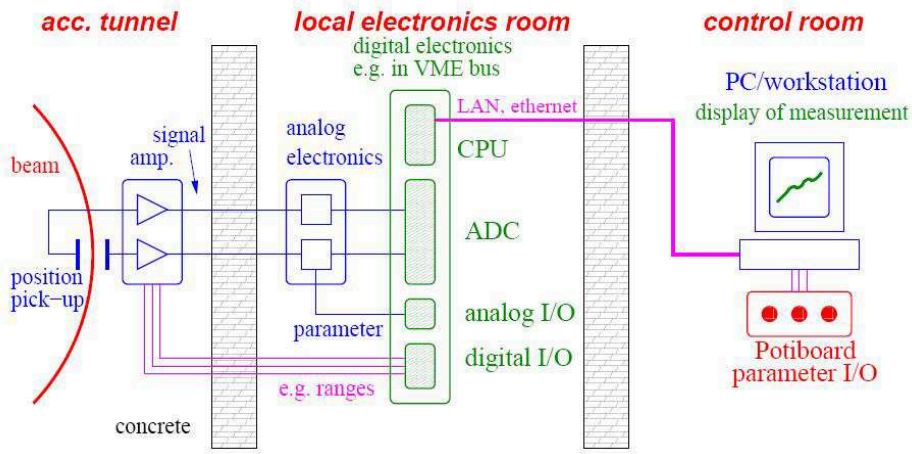

Figure 2.7: Schematics of typical beam diagnostics readout chain (here a position pick-up). The beam signal is modified by analogue electronics and digitized in a local electronics room. On the accelerator control room the measurement parameters are displayed and also the measurement settings can be modified.

In Fig. 2.7 is shown the electronic readout scheme normally implemented for electromagnetic beam position monitors, although it could be applied to many types of monitors

as a generic and common scheme. Here it will be used only for description purposes, but always bearing in mind that some diagnostic devices can have significant differences in the readout chain elements like, for instance, the OTR monitors where the device output is directly a digital image of the beam profile obtained by a CCD camera detecting the light coming out from the beam when passing through a thin target foil.

In this general scheme the yield of information from the diagnostic device follows three successive steps from the measurement up to the display of the quantity of interest which are described next and can be summarized as:

- the Analog Front-End (AFE) electronics with its particular analog signal processing scheme,
- the Analog-to-Digital Conversion (ADC) or digitalization,
- the storage of the acquired data and display in the control room.

Furthermore, besides the technical demands there is always the cost of the electronics which becomes a strong design criterion with regard to the amount of monitors installed in the accelerator looking for the best trade-off between cost and performance.

Analog front-end and analog processing schemes

There is first the interaction of the beam with the detector based on any physics phenomenon described before generates a measurable signal. This output signal has to be amplified and shaped, usually by applying several frequency filters, and here the different signals from the monitors can also be mixed using only analog electronics. Low noise processing is also important at this step which in most cases this is done close to the beam pipe. The analog front-end electronics is mostly designed ad-hoc due to the special requirements of the beam monitor where is difficult to find standard electronics. Moreover, all the electronics used in the accelerator area should be protected from the radiation generated close to the beam pipe and must have some radiation hardness qualification.

The choice of the analog bandwidth is a fundamental issue since it determines the time steps for meaningful data presentation and this has to be matched to the foreseen measurements and applications. For instance, the BPM systems covers a wide range of operational bandwidths depending on the detail level of the beam time structure that wants to be observed. The highest bandwidth is required whether the structure of the individual bunches has to be observed; for this case the upper limit of the bandwidth has to be above the acceleration or bunching frequency by typically a factor 10. For a bunch-by-bunch observation the signal from individual bunches has to be distinguishable, i.e., the bandwidth has to be at least comparable to the bunching frequency. For such a mode, each bunch delivers a position value and they are used to monitor the dynamic behavior during acceleration or to determine lattice parameters. For the turn-by-turn mode at a synchrotron, the position information of a dedicated bunch on each turn is stored and lattice parameters like the tune are calculated. The required analog bandwidth is chosen to separate one dedicated bunch from the successive bunches. A much lower bandwidth is required for monitoring slow beam variations with high resolution, like the closed orbit within a synchrotron, where the averaged behavior during thousands of turns is determined. In the case of linacs the beam use to be pulsed being the pulse repetition frequency of few Hz but every pulse can be made out of a train of bunches with bunching frequencies reaching several GHz in some cases. Here one has to chose to measure at pulse level with a

bandwidth wide enough to capture the beam pulse shape with negligible deformation, or to observe the bunch train structure for which is required a broader bandwidth including much higher frequency components, that sometimes can not be achieved for the several GHz range. Furthermore, the analog processing bandwidth significantly influences the position resolution, jointly with the digital acquisition bandwidth, directly related to the sampling rate and quantization step of the analog signal at the ADC which has to be well adapted to the analog bandwidth not limiting the desired resolution.

The more specific analog signal processing schemes, that are implemented in a more global readout scheme like the one in Fig. 2.7, can be divided in two categories, namely the broad-band and narrow-band processing. Belonging to them the most popular schemes are mentioned here but a complete description and comparison of the various analog processing schemes can be found on [12, 15, 25–27]. In the broad-band case, the behavior of individual bunches can be monitored. Here is mentioned two commonly used processing methods that belong to this category: one is based on linear amplifiers which implement the difference-over-sum method by mixing the monitor output signals; the other one is implemented with logarithmic-ratio amplifiers which leads to an improved linear position readings and a large input dynamic range without switching gains, but lacks of the sum signal proportional to the beam current and the bandwidth is reduced for the lower frequencies as compared to linear amplifiers.

For the narrow-band processing, the individual bunch properties are lost because of the specific selection of a narrow bandwidth for the output signals, but in turn it can be performed a significant noise reduction, which usually is spread out over wider frequency range, as well as resolution enhancement by the selection of the bunching frequency harmonic where the signal amplitude is higher. This processing scheme is based on the principle of heterodyne signal mixing which is widely used in telecommunication equipments like spectrum analyzers and AM radio. Here the beam signal is treated as a waveform where the position information is encoded in the modulation of the amplitude of the beam bunches with carrier being the bunching frequency so this demodulation scheme is needed to extract the amplitude envelope representing the position averaged over many bunches.

Another scheme used which also belongs to this category is the Amplitude-to-Phase (AM/PM) conversion. Here for a selected frequency it is generated a phase shift proportional to the amplitude ratio of opposite electrodes outputs of the monitor, and the phase shift is then encoded into logical pulse widths (duty factors) so that the digitization of logical pulses is straightforward and more cost-efficient compared to digitization of voltages. Such analog electronics can be placed close to the monitor and the resulting logical pulses are less sensitive to any electromagnetic interference so they can be transmitted via long cables out of the accelerator tunnel. The disadvantage is the relatively complex analog electronics dedicated to only one frequency and the fact that a beam current proportional signal is not available.

Digitalization

The amplified signal is then transferred out of the accelerator area to a local electronics room. The distance between these two locations can be around hundred meters so base-band transmission would be enough with cables of low attenuation and proper noise immunization and shielding. Further shaping can proceed here and the signal might be combined with other parameters as given by the accelerator settings. This is done in most cases with analogue electronics. The modified signal is then digitized by an Analog-to-

Digital Converter (ADC) which use to be embedded in a digitizer card with other elements as a memory buffer for storing temporarily the acquired data, digital and analog I/O interfaces for controlling the analog front-end electronics and passing other needed parameters respectively, as well as a CPU for the management of the digitizer and performance of the data transmission protocol link with the control room servers.

The options for implementing the digitizer are diverse and it can be done using a simple oscilloscope, a commercial instrumentation mainframe crates like CAMAC, VME, PXI or CompactPCI, or a custom developed digitizer, depending on the accelerator diagnostics requirements. For the data transmission to control room servers long-medium distance buses use to be implemented. For instance, Ethernet protocol over LAN is the most widely used since it is easily integrated in the accelerator system architecture. For that other field buses could also be used like like CAN or PROFI-bus, even though they are usually addressed for control of the analogue electronics.

It must be noted that there exist many techniques of digitalization and data transmission protocols not mentioned here which are are of great importance and occupies a significant effort in the implementation of a complete beam diagnostics systems, but that are not a pure diagnostics subject. A review of common digitalization methods can be found in [28], in general their realization is comparable to a great variety of other digital electronics applications for many other systems out of the accelerators development from which the diagnostic field is profited, without forgetting that many digital electronics advances came out from the technology developed for nuclear and high energy physics experiments most of them at accelerator facilities.

Storage and display

The data, or in most cases a reduced subset of the data, are passed and stored more permanently to the system computer servers, PCs or workstations usually located in the operators control room. These are generally the same ones responsible for the control and management of the full accelerator machine operation running the associated software and algorithms for this purpose. In the control room monitors the visualization is done providing to the operators only the necessary information and controls of the diagnostic device and readout chain. Nevertheless for accelerator commissioning where special diagnostics are requested raw data are shown to visualize a more detailed monitor functionality.

In order to achieve the desired performance of the accelerator and thus a good beam specifications, the machine control is performed from the control room servers correcting essentially the parameters of the magnetic elements and accelerating cavities which influence the beam and drive it to the right settings. The resulting effect on the beam is then observed with a new set of measured data, which can also serve as input of the feedback control loop for automatic beam parameter correction. Depending on the time response restrictions demanded for the beam correction, a real-time feedback control system is implemented or, simply, the control room operator close the loop changing the machine settings for those parameters that do not need fast and periodic control. An example is the reading of the beam positions and the correction of the orbit to its nominal value changing properly current intensities of the steering magnets.

Chapter 3

Fundamentals of the Inductive Pick-Up for Beam Position Monitoring

3.1 The Inductive Pick-Up (IPU) concept

Beam diagnostics is mostly based on the electromagnetic (EM) fields created by charged particles, as introduced in the previous chapter. We distinguished between the *near field* which is attached or bounded to the charges and the *far field* or radiation field which propagates away from the charged particles that generates them, like synchrotron radiation. Particularly, under the denomination of Beam Position Monitors (BPM) there are all the types of diagnostics devices that can measure, as its primary purpose, the transverse beam position inside the accelerator vacuum pipe. The beam position is one of the beam properties that can be measured for a great diversity of diagnostics devices, but the most popular and widely used in the case of bunched beams are the *electromagnetic pick-ups*. These pick-ups are mainly conceived to detect the effects of the near EM field induced by the beam, in order to get a local measurement being not-sensitive to other propagating fields through the conducting vacuum pipe that could interfere [29]. Eventually, the measurable quantities are voltages and electric currents produced by the beam-induced EM fields in the pick-up electrodes, that can be coupled in many different ways to the beam fields to yield their output signals feeding the first stage of the readout chain, usually, an analog amplifier.

In general the pick-up concept offers relatively simple device designs, small and adaptable sizes (some types of pick-ups can be introduced inside quadrupole magnets) and high reliable measurements, besides its very important feature of being a non-intercepting method of beam detection which is preferred whenever possible to not degrade the beam itself. Many specific pick-up realizations have been implemented depending on the target accelerator needs, but they could be grouped into the following types according to the way of coupling to the beam fields: *electrostatic pick-ups*, including here the *capacitive pick-up* and the *button pick-up* types with plates as electrodes which both accumulate beam induced charge but having different electrode housing and plate geometries for each type, as well as the *shoe-box pick-up* with the electrodes being the sections made by diagonal cuts on its case-like geometry; *strip-line pick-ups* with its electrodes designed as transmission lines; *cavity BPMs* with waveguide couplers to measure the standing wave modes

into its resonant cavity; and, finally, the *Magnetic Pick-Ups* (MPU) and the *Inductive Pick-Ups* (IPU), at which the BPS belongs, both based on same principle of sensing the beam magnetic field by means of transformer coils but with different electro-mechanical designs. A more detailed description of the above mentioned EM pick-ups can be found on general readings on beam instrumentation like [11–13], [15] and [23], besides the many publications of their particular realizations for specific accelerator machines.

Moreover, the, generally called, Beam Current Monitors (BCM) use to be also included within the family of the electromagnetic pick-up devices. This is because, in spite of being designed mainly to measure the beam current intensity instead of the beam position, most of them may have similar design concepts since they are also based on a EM sensing principles like the pick-ups, by either measuring directly the EM fields generated by the beam or through the *wall image current* which is induced by the beam fields on the vacuum pipe conducting walls, as it will be described in the next section.

Some aspects of the BCM devices are next highlighted due their similarities and common design features as compared to the IPU devices. These are essentially of two types: the Beam Current Transformers (BCT), and the Wall Current Monitors (WCM) which in addition to beam current is also able to measure the beam position. The first type can have many different designs but basically all are based on the same principle that is using one or various transformers surrounding the vacuum pipe, with the beam acting as the primary winding, to measure the magnetic flux generated by the beam current itself which is, in general, proportional to the beam current AC components. A particular device design is the DC Current Transformer (DCCT) which is also able to measure the DC components of the beam current. A key feature in the design of these devices is the ceramic or plastic insulator gap that would break the natural flow path of the wall current on the vacuum pipe inner surface. This is done, in the case of BCT designs, to let flow only the beam current inside the transformer, being able to measure it, and bypassing the wall current overhead the transformer through some metallic housing what will prevent the beam current fields to be canceled out by the wall current flowing inside the transformer. On the other hand, the WCM monitors type are based on sensing the beam-induced wall current which is also proportional to the beam current. In this case an insulator gap is also inserted in the vacuum pipe so the wall current is forced to follow a path through the monitor wall surrounding the vacuum pipe gap, where several resistors are placed regularly around it and connected in parallel, being able to measure the voltage drop across them which is just the parallel equivalent resistance multiplied by the wall current.

The IPU is able to measure the beam position and the beam current simultaneously for a pulsed beam modulation, as well as some WCM devices which can also detect the beam position because the monitor wall around the insulator gap has been divided into several independent strip electrodes. Particularly, these WCMs have a similar design and function principles to the IPU, both sensing the wall current directly on their monitor wall electrodes around the vacuum pipe insulator gap.

The main difference arise in the way the output voltage signals are picked up from the wall current flowing through their strip electrodes. For the IPU, like a BCT device would do for the beam itself, a few toroidal transformers are coupled at the end of its electrodes for measuring the wall current inductively, as it is shown further on in the IPU conceptual scheme in Fig. 3.7, instead of using a bridge of parallel resistors as in the WCM designs. In consequence, in some cases the IPU devices are included in the WCM category, and

both are referred respectively as *Inductive WCM* and *Resistive WCM*. In fact, first design trials of MPUs differed from any WCM design, but it evolved towards a design solution which eventually resembled to a WCM design.

In the following sections it will be presented the fundamental principles in which the IPU devices base their operation, the performance issues common to generic IPU design, while in Chap. 4 we will focus in the particular design features of the BPS device.

3.2 Characteristics parameters for beam position measurements

The definitions included here are mainly taken from [26,27] with the purpose of introducing the main parameters often considered, like for the BPS-IPU monitor, in the development and design of a beam position measuring system:

- **Sensitivity** is the proportional constant specific for every pick-up giving its signal strength from the beam position or displacement. It is defined as the slope for the linear approximation in the two orthogonal horizontal and vertical coordinate planes, being more accurate for small displacements around the pipe center. It use to be expressed in units of mm^{-1} (since typical beam pipe diameters are of few cm) and the signal strength is given as a dimensionless ratio of the pick-up measured signals. Also the offsets of the both coordinate linear relations are determined in order to get the absolute beam position, although sometimes are not needed if only relative beam displacements are wanted.
- **Accuracy** is the ability to determine the position of the beam relative to the device being used for measuring the beam position. This is limited by some combination of pick-up nonlinear response to displaced beams, mechanical alignment errors, mechanical tolerances in the beam detection device, calibration errors in the electronics, attenuation and reflections in the cables connecting the pick-up to the electronics, electromagnetic interference, and circuit noise. Signal processing introduces additional inaccuracies such as the granularity of the Analog-to-digital Converters (ADC) given by its number of resolution bits determining the quantization step through the Least-Significant-Bit (LSB). All these effects are reflected in the position measurement errors usually having a random gaussian distribution.
- **Resolution** differs from accuracy in that it refers to the ability to measure small displacements of the beam, as opposed to its absolute position (see Fig. 3.1). In consequence, it will represent the minimum displacement or beam position variation the pick-up could detect. Typically, the resolution of a system, specifically in a pick-up, is much better (lower) than the accuracy, being the accuracy as low as the resolution for the best performance case which will be eventually limited by the noise background present in whole system, the pick-up and the readout and acquisition electronics.
- **Bandwidth**. Some types of bandwidth are usually defined: the frequency response of the monitor and the analog front-end electronics have to be matched to the frequency spectrum delivered by the bunched beam time structure, defining so the analog bandwidth between the lower and upper cutoff frequencies. For noise reduction, the bandwidth can be limited by analog filters. The acquisition bandwidth

refers to the frequency range over which the beam position is recorded and should be matched to the analog bandwidth. For monitoring fast changes of beam parameters (like beam jitter), or within short beam delivery times, a much larger bandwidth is required, resulting in a lower position resolution. The bandwidth can be restricted to achieve a high resolution in case of slow varying beam parameters, like is done in the analog narrowband processing. Finally, real-time bandwidth is the data rate of producing an analog or digital position signal with predictable latency to be used as the readout in a closed-loop or feedback beam control.

- **Dynamic range** refers to the range of beam current levels over which the diagnostic system must respond. Often large dynamic range response is achieved by gain switching at different levels. Alternatively, special signal processing methods can provide a large dynamic range response and eliminate the need for gain switching. Also it is defined the input dynamic range of an ADC that should be matched to the output signal level of the analog front-end feeding it.
- **Signal-to-Noise Ratio (SNR)** refers to the power ratio of wanted signal to unwanted noise. An unavoidable contribution is given by thermal noise, where cooling of the first stage amplifier reduces this thermal noise. Other noise sources along the system come from electro-magnetic or RF interferences (EMI) from another devices, ground-loops in our system (behaving like an antenna) can contribute significantly to be more sensitive to the unwanted signals. Careful shielding and grounding is required to suppress these disturbances. The SNR will place limits on the ultimate resolution of the system.

3.3 Beam-induced electromagnetic fields and wall image current

A static point-like charge q in free space generates an electric field $\vec{E}$ with typical radial distribution of field lines given by Coulomb's Law. Nevertheless, the electric field of this charge inside the beam vacuum chamber has to fulfill the boundary conditions of $\vec{E}_{\parallel} = 0$ imposed at the wall of the conducting beam pipe for the field components parallel to it. In Fig. 3.2 [32] are shown the resulting field lines for $\vec{E}$ coupled to a long conducting pipe with circular cross section of radius a, where the field has only transversal components $\vec{E}_{\perp}$ due to the boundary conditions at the pipe metallic surface with the field lines ending perpendicularly to the pipe wall. In consequence, a surface charge density is induced on the pipe wall depending only on the field transversal components as

$$\sigma_q^w = -\epsilon_0 E_{\perp}, \tag{3.1}$$

with the induced charge distribution per unit length along the longitudinal direction s being

$$\Lambda_q^w(s) = \mathrm{d}q_w/\mathrm{d}s = 2\pi a \sigma_q^w. \tag{3.2}$$

This line-charge density, also depicted in Fig. 3.2, is obtained after integrating the surface charge density σ_w^q over the azimuthal direction, following the notation of the w superindex representing the field induced quantity on the pipe wall, and the subindex for indicating the source charge q. Thus, the total induced charge in the beam pipe wall, as being

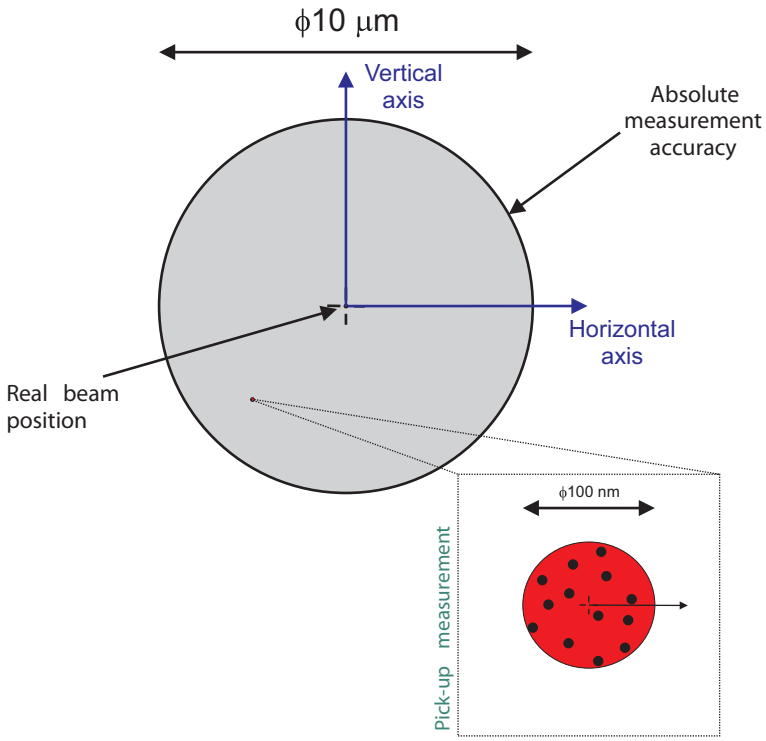

Figure 3.1: Illustration of the difference between the resolution and the overall precision/accuracy parameters considered for the performance characterization of an IPU [37]. For both coordinate planes, the gray circle represents the accuracy (10 μm) and the red one the resolution (0.1 μm) of a given device. Readouts of the same beam position are depicted as black dots.

integrated over the longitudinal direction, would be equal to the original charge but of opposite sign $q_w = -q$.

For a charge moving longitudinally with constant velocity, $v_s = \beta c$, besides the electric field, a magnetic field appears as a consequence of the charge motion representing a current intensity. The change in the electric and magnetic fields due to the change of charge motion from static to moving is described by the Lorentz transformations of special relativity between two inertial reference frames as applied to the fields. One is the rest reference frame which is chosen to be always at rest with respect the charged particle q with its origin seated at the position of q and moving along with it. The other one is the laboratory reference frame that will observe a change in the fields due to motion of q with respect to it, but for the static case seeing the same fields as in the rest frame. Then, the fields, separated in the parallel and perpendicular components to the direction of charge motion given by $\vec{v}$, are transformed from the rest frame $(\vec{r}', t')$ denoted with prime to the lab frame $(\vec{r}, t)$ according to the Lorentz transformation as follows

$$\begin{aligned} \vec{E}_{\parallel} &= \vec{E}'_{\parallel} & \vec{H}_{\parallel} &= \vec{H}'_{\parallel} \\ \vec{E}_{\perp} &= \gamma\left(\vec{E}'_{\perp} - \vec{v}\times\vec{H}'\right) & \vec{H}_{\perp} &= \gamma\left(\vec{H}'_{\perp} + \tfrac{1}{c^2}\vec{v}\times\vec{E}'\right). \end{aligned} \tag{3.3}$$

where the Lorentz factor $\gamma = 1/\sqrt{1-\beta^2}$ depends on the charge velocity. It must be remarked that the Lorentz transformation of the fields holds for any arbitrary fields and it is

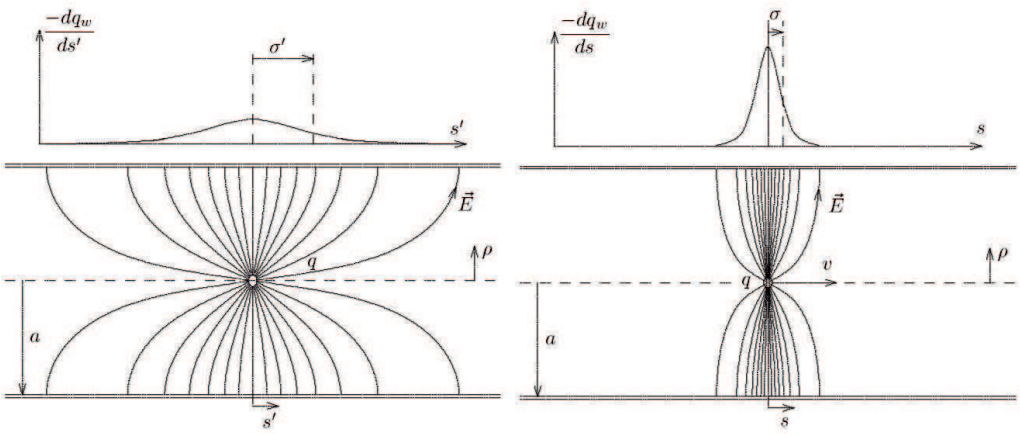

(a) (b)

Figure 3.2: Electric field of a static (a) and a relativistic moving charge ($\gamma = 4$) at 97% of the speed of light (b) in a cylindrical metallic chamber.

left implicit the dependence of the fields with the spatial position $\vec{r}$ and time t in each reference frame. For our particular case, there is only electric field in the rest frame because q is static having $\vec{H}' = 0$, nevertheless in the lab frame a purely azimuthal magnetic field is produced due to the charged particle velocity and the electric field which is now time varying. Both fields are related in the lab frame by

$$\vec{H} = 1/c^2(\vec{v} \times \vec{E}) \tag{3.4}$$

which is easily derived from Eqs. (3.3) [33].

Furthermore, from the equations can be seen that the perpendicular components of the fields grow with the Lorentz factor γ while the longitudinal components remain constant so getting a more transversal fields as charge velocity increases. In Fig. 3.2 are represented the electric field lines for a charge moving at $\gamma = 4$ corresponding to the 97% of the speed of light ($\beta = 0.968$) as seen fom the lab frame at certain time instant. Accordingly, at relativistic velocities the electric and magnetic field lines tend to be concentrated within smaller angle around the transverse direction, and subsequently the longitudinal distribution of the wall induced charge $\Lambda_q^w(s)$ narrows with an average length given by its RMS value σ_Λ (not to be confused with the surface charge density σ_w^q) as

$$\sigma_\Lambda = \frac{a}{\gamma\sqrt{2}} \tag{3.5}$$

decreasing proportionally to the inverse of γ factor, where a is the radius of the vacuum beam pipe, as it is shown in top of Fig. 3.2 for the particular case of $\gamma = 4$ [29]. This quantity indicates that eventually for this point-like charged particle q at the ultra-relativistic velocity limit, $\beta \approx 1$ and $\gamma >> 1$, all the induced charge q_w tends to be concentrated in a point since $\sigma_\Lambda \to 0$. At the same time, the electric field lines become purely transversal and confined to a thin disc moving along with the particle q like is depicted in Fig. 3.3. This effect can also be seen as the Lorentz contraction of the space in the direction of motion observed in the laboratory reference frame.

The same situation described for a point-like charge can be used to understand the

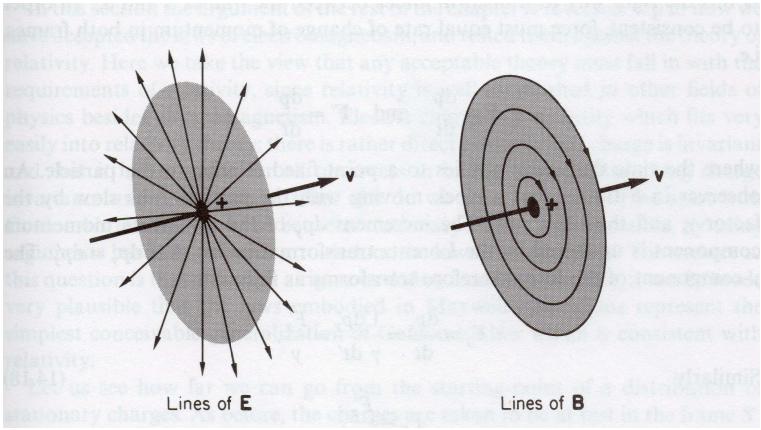

Figure 3.3: Representation of the pure transversal electric and magnetic fields for a charge moving at ultra-relativistic velocity.

behavior of a highly relativistic beam bunch containing many charged particles. The extent of the line-charge density of the induced charge for every particle within a bunch, given by σ_Λ, is reduced to much less of the bunch length, $\sigma_{bunch} >> \sigma_\Lambda$. Therefore the longitudinal distribution of the wall image charge induced by a bunch $\Lambda^w_{bunch}(s)$ will reproduce the line-charge density of the bunch but with opposite charge polarity being $\Lambda_{bunch}(s) \approx -\Lambda^w_{bunch}(s)$ and provided that $\beta \approx 1$ and $\gamma >> 1$ with the bunch associated EM fields considered as purely transversal as illustrated in Fig. 3.4.

Thus, a single bunch with N particles of charge e traveling at velocity $v_s = \beta c$ in the longitudinal direction s along the vacuum pipe, will represent an instantaneous current of

$$I_w(t) = \Lambda^w_{bunch}(s)\beta c \tag{3.6}$$

which has a longitudinal profile given by the bunch shape line-charge density, as it is also plotted in Fig. 3.4).

In general, a beam is composed of a train of bunches with a given bunch spacing T, and either for a Continuous-Wave (CW) or a pulse modulated beam respectively in circular accelerators or linacs, the beam current $I_b(t)$ can always be expressed as a Fourier cosine series expansion of the RF acceleration or bunching frequency $\omega_0 = 2\pi/T$ being the fundamental frequency of the carrier signal:

$$I_b(t) = \overline{I_b} + 2\overline{I_b}\sum_{m=1}^{\infty} A_m \cos(m\omega_0 t) \tag{3.7}$$

where $\overline{I_b} = eN/T$ is the average beam current, so called DC current component, being the total bunch charge over the bunching period. The factor A_m is the intensity amplitude of the *mth* Fourier harmonic. This factor will depend on particular bunch shape that, among others, can be gaussian, parabolic or even for very short bunches, the bunch profile can be approached by a Dirac δ. In this last limiting case all harmonics become equal to one since A_m is normalized to one as the bunch length σ_{bunch} goes to zero. Regardless of the specific bunch shape, for the low harmonics of the fundamental bunching frequency, A_m will be close to one and with a peak amplitude about twice the DC current amplitude [27].

Since the EM fields accompanying a beam bunch traveling at ultra-relativistic veloci-

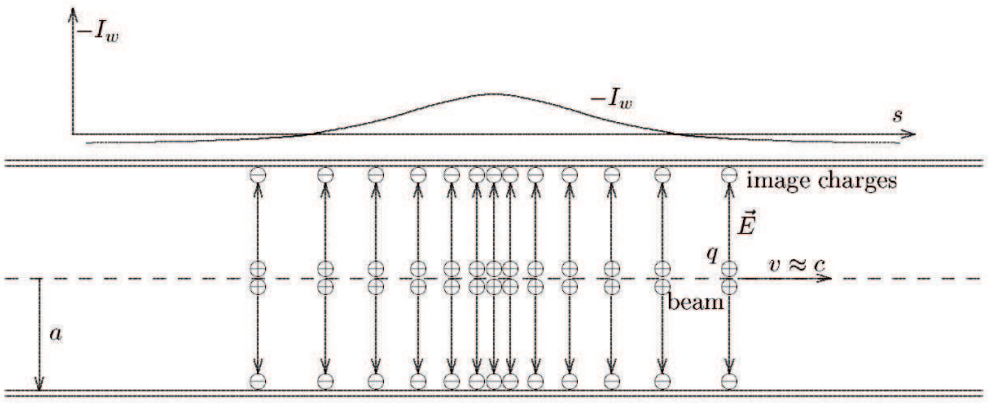

Figure 3.4: Charges and current induced by a beam bunch in the vacuum pipe walls.

ties become purely transversal, even though this is only exact for $\beta = 1$, a bunched beam will generate a nearly Transverse Electric-Magnetic (TEM) wave propagating down with the beam at velocity $\beta \approx 1$. The beam-induced TEM waves propagate inside a vacuum pipe of uniform cross section in a similar way as it does a signal (only the fields) propagating in a coaxial transmission line or a waveguide with vacuum or air as a dielectric filling, since both dielectric constants are almost equal being $\epsilon_r = 1.00059$ the relative permittivity of air at 1 atm pressure. The ratio between the modules of the orthogonal electric and magnetic fields gives the characteristic impedance of free space (or vacuum) for a TEM wave

$$\eta_0 = \frac{\vec{E}}{\vec{H}} = \sqrt{\frac{\mu_0}{\epsilon_0}} = \mu_0 c = \frac{1}{\epsilon_0 c} \tag{3.8}$$

which, from Eq. (3.4), can be expressed in terms of the vacuum permeability $\mu_0 = 4\pi \times 10^{-7} Hm^{-1}$ and vacuum permittivity $\epsilon_0 = 8.854 \times 10^{-12} Fm^{-1}$, and also related to the speed of light in free space through its definition $c = 1/\sqrt{\epsilon_0 \mu_0} = 2.998 \times 10^8 ms^{-1}$, yielding a value of $\eta_0 \approx 377\Omega$.

The beam TEM fields, consequently, will induce a wall image current flowing on the vacuum pipe which is proportional to the induced charge density and hence to the electric field falling on its inner surface as related in Eqs. (3.1, 3.2, 3.6). For a beam centered in a circular pipe of radius a with infinite length and conductivity, the wall current is uniformly distributed on the inner surface of the pipe with the wall current density being

$$i_w(t) = \frac{I_w(t)}{2\pi a} \tag{3.9}$$

where $I_w(t) = -(I_b(t) - \overline{I_b})$ is the total wall image current integrated over the beam pipe circumference and measured at time t, which reflects the beam current $I_b(t)$ but with opposite charge and without containing its average or DC component $\overline{I_b}$. Only a longitudinal variation of the induced charge density along the pipe, and not a constant charge density, will produce a wall current including only AC components of the beam current [29]. An average or a constant uniform beam current induce a constant charge density along the pipe walls but it does not have to move jointly with the beam to satisfy the EM fields

boundary conditions since $E_\perp$ and $E_\parallel = 0$ are also constant through the pipe longitudinal direction s, and no net flow of charge is produced.

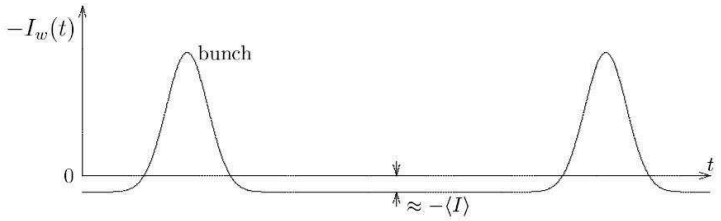

Figure 3.5: Beam profile of two widely spaced bunches and the average or DC current signal baseline.

The wall current will then reproduce the time structure or waveform of the bunched beam current, so the longitudinal intensity profile of the beam could be directly obtained by measuring it. Although it must be considered the wall current different aspects of opposite charge sign and its lack of the average beam current $\overline{I_b}$ DC component that represents an offset with respect the beam current baseline, as it is shown in Fig. 3.5 for two widely spaced bunches.

For a pulsed beams like in linacs, the repetition frequency of the pulses use to be low in the order of several Hz getting small duty cycles, with long pulse periods as compared to the pulse lengths, and hence a low beam average current. For low enough levels, below the system noise, the wall current baseline offset could be neglected, yielding a correct measurement of the beam current amplitude. In contrast, for a CW beam like in synchrotrons, the average current use to be the half of the peak amplitude at the bunching frequency, so the wall current measurements would have a non-negligible offset not matching the beam current amplitude. In that case if the true beam current want to be measured a DC current level measurement must be implemented. This can be done provided that the azimuthal and constant magnetic field of the beam DC component is the only one not shielded by the metallic vacuum pipe so it exists outside the walls and could be measured by for instance a DCCT current transformer.

Due to the change of sign of the wall current with respect to the beam current, two equivalent views can be used to describe the flow of the wall current. It can be seen either as the wall current flowing in the same direction of the beam but with opposite charge or, alternatively, as having the same charge but flowing in the opposite direction of the beam.

Regardless of the view chosen to describe the beam, the induced wall currents and EM fields associated with periodically spaced beam bunches may be considered as the pick-ups excitation signal which will be treated either in the time domain or frequency domain, and processed in many convenient ways for instance, working only with certain harmonics of the full frequency range or performing some gating techniques for time signals.

In general, pick-ups are able to sense the position of the beam with respect the vacuum pipe because the wall currents, or equivalently the EM fields, induced by the beam on the conducting pipe are position dependent and the wall current intensity is redistributed in function of the beam proximity to the walls. Then, the position measurement rely on the relative amplitudes of the induced signals in the pick-up electrodes, which usually

are distributed at uniform azimuthal steps around the vacuum pipe, in order to set the horizontal and vertical position coordinate planes. This operation principles, particularly focused on the BPS-IPU, are discussed below.

3.4 Electrode wall currents for beam position and current measurements

As mentioned before, the wall current induced by a centered beam is uniformly spread over the vacuum pipe surface, but when the beam is displaced from the center, the wall current is redistributed according to the beam proximity increasing its magnitude in the closer pipe sections and, therefore, diminishing in the further ones. Taking the cross section of a longitudinally uniform circular beam pipe of radius a, a time-varying pencil beam current $I_b(t)$ at transverse position (r, θ) inside the beam pipe, and running parallel to it, will produce a wall current $I_w(t)$ over the pipe inner circumference at radius $r_w = a$. This wall current will not contain the DC or average beam current component as stated in Eq. (3.9), and its density $i_w(t)$, in A/m units, can be obtained at the angular coordinate ϕ_w of the wall current element as

$$i_w(\phi_w, t) = \frac{I_w(t)}{2\pi a}\left[1 + 2\sum_{n=1}^{\infty}\left(\frac{r}{a}\right)^n \cos\left[n(\phi_w - \theta)\right]\right] \tag{3.10}$$

the wall current density is expressed in an infinite series with terms of the form $r^n \cos(n\theta)$ indicating solutions of cylindrical geometry which is often preferred when it must be integrated. Alternatively, there exists also an equivalent closed form expression that sometimes is easier to deal with,

$$i_w(\phi_w, t) = \frac{I_w(t)}{2\pi a}\left[\frac{a^2 - r^2}{a^2 + r^2 - 2ar\cos(\phi_w - \theta)}\right]. \tag{3.11}$$

The derivation of Eqs. (3.10) and (3.11) are based in, the solutions of Laplace's equation in two dimensions with cylindrical geometry for the first [35], and, for the second, applying the method of images considering that the potential at the pipe circumference (without the pipe itself) is zero and then solving for the differential form of Gauss's Law [36]. Most recent derivations of these expressions of the wall current density can be also found in [15].

Then for dual plane beam position monitoring, the beam displacement from the vacuum pipe center can be detected by dividing up the pipe circumference in, at least, four independent sections (without electrical contact) extended longitudinally as strip electrodes. The wall current is thus running independently on the inner surface of each electrode and parallel to the beam, so to eventually yield a measure of the beam proximity to them. The four electrode sections are centered at azimuthal steps of 90°to set the dual transverse position coordinate planes, being the Right (R) and Left (L) electrodes for the horizontal plane and, the Up (U) and Down (D) electrodes for the vertical plane. Every electrode section is chosen to have the same angular width up to a maximum of $\pi/2$ where the four electrode sections will cover the full pipe circumference.

Now, as illustrated in Fig. 3.6, for a beam at position in polar coordinates (r, θ), the induced wall current can be calculated by integrating the wall current density in Eq. (3.10)

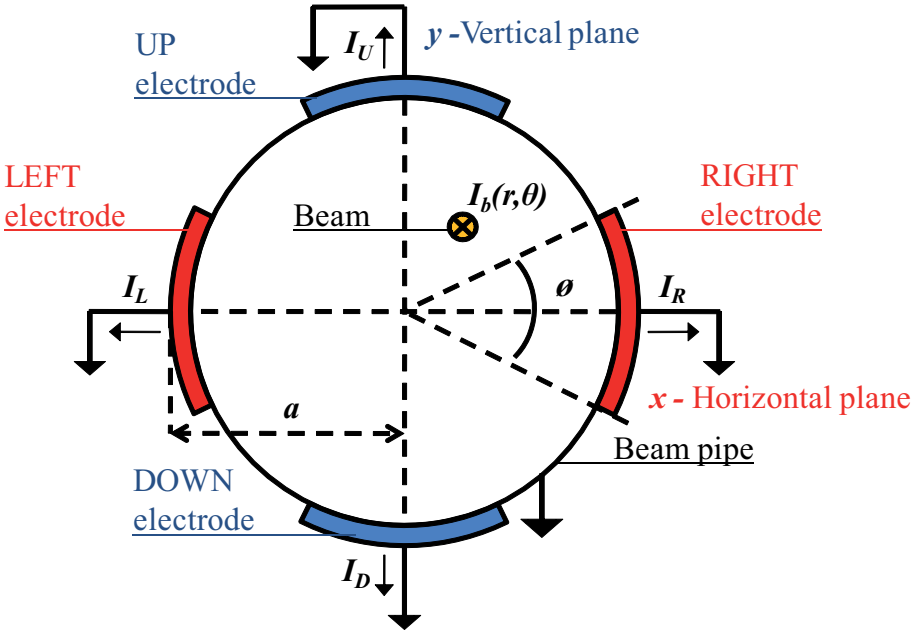

Figure 3.6: Cross section of the strip electrodes geometry used for the calculation of beam induced wall currents.

over each of the four electrode sections of angular width ϕ, at radius a and angular coordinate ϕ_w covering the angles $\phi_w = [-\phi/2 + j\pi/2, \phi/2 + j\pi/2]$ with the index for each electrode $j = 0, 1, 2, 3, 4$ corresponding respectively to the electrode (R, U, L, D). Then, for the horizontal plane the resultant wall currents at the (R, L) electrodes are

$$I_R(t) = \frac{I_w(t)\phi}{2\pi}\left[1 + \frac{4}{\phi}\sum_{n=1}^{\infty}\frac{1}{n}\left(\frac{r}{a}\right)^n \cos(n\theta)\sin\left(\frac{n\phi}{2}\right)\right] \tag{3.12}$$

$$I_L(t) = \frac{I_w(t)\phi}{2\pi}\left[1 + \frac{4}{\phi}\sum_{n=1}^{\infty}\frac{1}{n}\left(\frac{r}{a}\right)^n \cos(n\theta)\sin\left[n\left(\frac{\phi}{2} + \pi\right)\right]\right] \tag{3.13}$$

and for the vertical plane the wall currents at the (U, D) electrodes are

$$I_U(t) = \frac{I_w(t)\phi}{2\pi}\left[1 + \frac{4}{\phi}\sum_{n=1}^{\infty}\frac{1}{n}\left(\frac{r}{a}\right)^n \cos\left[n\left(\theta - \frac{\pi}{2}\right)\right]\sin\left(\frac{n\phi}{2}\right)\right] \tag{3.14}$$

$$I_D(t) = \frac{I_w(t)\phi}{2\pi}\left[1 + \frac{4}{\phi}\sum_{n=1}^{\infty}\frac{1}{n}\left(\frac{r}{a}\right)^n \cos\left[n\left(\theta - \frac{\pi}{2}\right)\right]\sin\left[n\left(\frac{\phi}{2} + \pi\right)\right]\right] \tag{3.15}$$

here one can realize that once it is set the wall current expressions for the electrodes of the horizontal plane, the ones for the vertical plane are equivalent but with a $\pi/2$ rotation performed to the electrodes plane what only affects to the factor containing the beam angular coordinate θ since the vertical electrodes see the beam with different angle relative to them.

From Eq. (3.10) integrating the wall current density over the full pipe circumference, $\phi_w = [0, 2\pi]$, it is recovered the total wall current induced by the beam. In the case of the four separate electrodes the induced wall current will be totally collected only if the

electrodes cover the full pipe circumference, for an electrode angular width of $\phi = \pi/2$. In consequence, the idea when designing the electrodes is to cover the pipe circumference with the four electrodes to collect with their sum the induced wall current as much as possible yielding so a "mirror" measurement of the beam current, but keeping them independent or unconnected being able to measure beam position as well.

Therefore, for any given angular width of the electrodes, the general expressions of the sum of the four electrode currents $I_\Sigma = I_R + I_L + I_U + I_D$, and the difference of the electrode currents for the horizontal and vertical planes respectively, $I_{\Delta H} = I_R - I_L$ and $I_{\Delta V} = I_U - I_D$, can be obtained straightforward from Eqs. (3.12) to (3.15) as

$$I_\Sigma(t) = \frac{I_w(t)2\phi}{\pi}\left[1 + \frac{4}{\phi}\sum_{n=1}^{\infty}\frac{1}{4n}\left(\frac{r}{a}\right)^{4n}\cos(4n\theta)\sin\left(\frac{4n\phi}{2}\right)\right] \tag{3.16}$$

$$I_{\Delta H}(t) = \frac{I_w(t)4}{\pi}\left[\sum_{n=1}^{\infty}\frac{1}{(2n-1)}\left(\frac{r}{a}\right)^{(2n-1)}\cos[(2n-1)\theta]\sin\left[\frac{(2n-1)\phi}{2}\right]\right] \tag{3.17}$$

$$I_{\Delta V}(t) = \frac{I_w(t)4}{\pi}\left[\sum_{n=1}^{\infty}\frac{1}{(2n-1)}\left(\frac{r}{a}\right)^{(2n-1)}\cos\left[(2n-1)\left(\theta - \frac{\pi}{2}\right)\right]\sin\left(\frac{(2n-1)\phi}{2}\right)\right] \tag{3.18}$$

where for the sum current of the four electrodes all the terms cancel out except the four multiple terms $4n$ besides the zero order term or constant term representing most of the wall current. For the difference currents of each coordinate plane, only the odd terms $(2n-1)$ have survived, having been canceled the constant term, and with the first term $n = 1$ being linear with the beam radial position r.

In order to get the beam position related to the electrode currents in the linear approximation, the Eqs. from (3.16) to (3.18) of the sum and difference currents are written at first order in n as

$$I_\Sigma(t) = \frac{I_w(t)2\phi}{\pi} \; + \; h.o.[4n, n \geq 1] \tag{3.19}$$

$$I_{\Delta H}(t) = \frac{I_w(t)4}{\pi}\left(\frac{r}{a}\right)\cos(\theta)\sin\left(\frac{\phi}{2}\right) \; + \; h.o.[(2n-1), n \geq 3] \tag{3.20}$$

$$I_{\Delta V}(t) = \frac{I_w(t)4}{\pi}\left(\frac{r}{a}\right)\sin(\theta)sin\left(\frac{\phi}{2}\right) \; + \; h.o.[(2n-1), n \geq 3]. \tag{3.21}$$

where the high order (h.o.) terms are neglected at fourth power of the beam radial position normalized to the beam pipe radius $(r/a)^4$ for the sum current, and at the third power $(r/a)^3$ for the difference currents.

At this point, the difference currents for each coordinate plane are normalized by the sum current in order to remove the dependence of the beam current through the wall current $I_w(t)$, from the beam position coordinates, where the horizontal and vertical beam position are given by $x = r\cos(\theta)$ and $y = r\sin(\theta)$, respectively. Thus, from Eqs. (3.19) to (3.21), the so called difference-over-sigma (Δ/Σ) processing method will provide a good

linear relation, up to $(r/a)^3$, between the beam position in the central region of the pipe aperture and the wall currents measurements as

$$\frac{I_{\Delta H}}{I_\Sigma} = \frac{2sin(\phi/2)}{\phi}\left(\frac{x}{a}\right) \tag{3.22}$$

$$\frac{I_{\Delta V}}{I_\Sigma} = \frac{2sin(\phi/2)}{\phi}\left(\frac{y}{a}\right) \tag{3.23}$$

where the time dependence of the difference and sum currents is left implicit. It can be easily seen that for a centered beam at the mechanical center of the electrodes, and assuming an ideal geometry of equally sized and uniformly placed electrodes at the same radius around the vacuum pipe, the wall current is uniformly distributed among the four electrodes. In that case the difference currents are just canceled out $I_{\Delta H} = I_{\Delta V} = 0$, with the electrode currents having the same magnitude simply given by the sum current divided by four as $I_{elec} = I_\Sigma/4 = I_w\phi/2\pi$, according to Eq. (3.19). This also holds not only for the linear approximation but for the general case as can be checked in Eq. (3.16) taking $r = 0$ for a centered beam. Moreover, only in the particular case of $\phi = \pi/2$, corresponding to the electrodes angular width covering the whole vacuum pipe surface, the total wall current is once again recovered $I_\Sigma = I_w$ with each electrode carrying a fourth of it, $I_{elec} = I_w/4$.

The proportional factor between the beam position and the currents ratio I_Δ/I_Σ is called *Sensitivity* having with units of mm^{-1}. In general the sensitivities for each coordinate plane $S_{x,y}$ will be different being only equal $S_x = S_y$ for an ideal electrodes geometry so it is theoretically defined from Eqs. (3.22),(3.23) as

$$S \equiv S_{x,y} = \frac{2sin(\phi/2)}{\phi}\left(\frac{1}{a}\right) \cong \frac{1}{a}. \tag{3.24}$$

The electrodes angular width ϕ is usually chosen to give the maximum coverage, typically around the 90%, of the vacuum pipe circumference. This is usually preferred in order to have a better beam current measurement by means of a higher proportion of the wall current collected in the strip electrodes as follows from the sum current in Eq. (3.19). But in turn the sensitivity is reduced with wider ϕ, although only less than a 10%, according to its definifition above that ranges between $[1, 0.9]$ for $\phi = [0, \pi/2]$. Hence for a wide angular coverage the sensitivity is just approximated as the inverse of the beam pipe radius a.

Also it must be noted that, usually for other BPMs, the sum current is taken only for the two electrodes corresponding to each coordinate plane, while in the case of BPS-IPU is taken the sum of the four electrode currents, so, in general, the sensitivity would be two times greater with a two electrodes sum current. This is done in order to have only one channel for the sum signal yielding the beam current measurement, and also provided that the foreseen output signal levels are high enough to accept a factor two reduction of the BPS-IPU sensitivity.

The horizontal and vertical beam position coordinates will be finally obtained for the linear approximation from

$$x = \frac{1}{S_x}\left(\frac{I_{\Delta H}}{I_\Sigma}\right) + \delta_x \tag{3.25}$$

$$y = \frac{1}{S_y}\left(\frac{I_{\Delta V}}{I_{\Sigma}}\right) + \delta_y \tag{3.26}$$

where the beam position is inversely proportional to the sensitivity meaning that a smaller beam displacement can be determined from a given currents ratio measurement as the sensitivity increases. The *position offsets*, also called *electrical offsets*, for both planes $\delta_{x,y}$ represent the difference between the true electrodes mechanical center and the electrical center, which are defined as the position reading when the electrode currents cancel out $I_{\Delta H} = I_{\Delta V} = 0$. Ideally both centers should coincide but they use to differ due to non-ideal electrodes geometry and also to an unbalanced measurements of the electrodes.

3.5 Operation principles of the BPS-IPU

3.5.1 Basic sensing mechanism

In Fig. 3.7 it is shown a sketch drawing of an IPU longitudinal section which will help to explain more in detail several particular aspects in the sensing mechanism of this pick-up. Briefly, the IPU wall is divided longitudinally into four independent strip electrodes which are placed outside and surrounding a ceramic gap tube of the same electrodes length replacing a vacuum pipe section inside the device. Therefore the wall current is forced to follow the electrodes path instead of the non-conducting inner path corresponding to the ceramic gap pipeline section. As stated before, the four strip electrodes are orthogonally spread over the pipe circular cross section so that the beam position horizontal and vertical coordinates is determined just by measuring the wall current intensity flowing through them according to Eqs. (3.25) and (3.26), as well as the beam current is also obtained by summing up all the wall electrode currents according to Eq. (3.19).

The electrode currents are then sensed by converting them into voltage signals and sent to the monitor outputs. Basically in an IPU device this is done at the end of each of four strip electrodes by connecting a narrow conductor that can go through a small toroidal transformer being the responsible for the inductive sensing of electrode wall currents, as it is depicted in Fig. 3.7. A Printed Circuit Board (PCB) located inside the IPU monitor will hold the four transformers for each electrode which acts as one turn primary winding so its wall current component is converted to a voltage signal in the secondary winding turns. The voltage signals are thus connected to their respective pick-up outputs by a small conditioning circuit in the transformer secondary side over the PCB. Therefore, the voltage amplitude at every output port will be related to its respective electrode current by the characteristic *transfer impedance* $Z_t(\omega)$ of the transformer plus the secondary circuit and stray elements, that, in general, depend on the signal frequency content $\omega = 2\pi f$ as it will be described in the following sections.

For a complete characterization of the IPU performance one has to consider its behavior in function of the frequency content of the wall image current which is that of the beam excitation signal (except for the DC level). This will mostly depend on the combined frequency response of the transformers circuits jointly with some of its constituent mechanical parts with a functional role interacting with the beam fields. In that sense a big magnetic loop is formed by a cylindric ferrite core of high permeability filling the space between the electrodes and the metallic external body, with the main purpose of inserting

a high inductance in parallel to the electrodes current path in order to improve the device frequency response at the bandwidth lower region.

In general the IPU is designed to have an operational bandwidth according to the beam time structure specifications and, typically, it is able to measure the longitudinal, or time, profile of a pulsed beam from low frequency components in the order of kHz and up to hundreds of MHz, being considered, like the WCM as its resistive counterpart, a broad-band device. In the following sections it is introduced the basic function of the BPS-IPU according the analysis of a single electrode channel which has a typical pass-band frequency response profile, going into a complete description of the BPS design and its behavior, through a more specific and accurate electric model, along the Chap. 4.

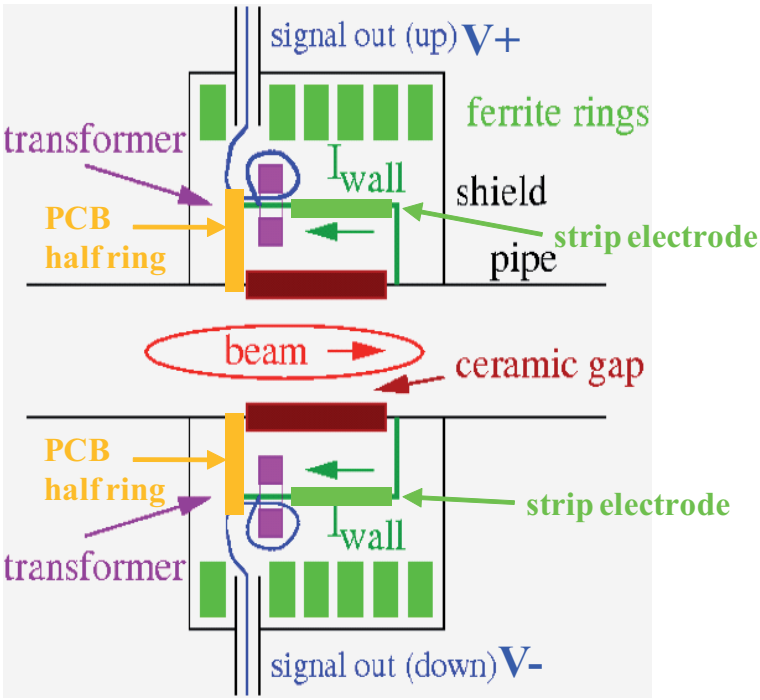

Figure 3.7: IPU conceptual scheme where are depicted the main functional parts. This scheme shows a longitudinal cut view of the monitor vertical plane with their corresponding output signal channels V_+ (Up) and V_- (Down) (being the same for the horizontal plane).

3.5.2 Output voltage signals

Assuming that in principle the four electrode channels are independent, the BPS-IPU output voltages are here obtained through the transfer impedance of one electrode channel and are also related to the beam position coordinates. The expression of the single channel transfer impedance in function of the frequency is obtained and analyzed in order to set the basis of the device frequency response, which essentially has a characteristic pass-band profile determining the device pulse signal transmission. The overall BPS-IPU performance will generally depend on the combined response of the four electrode channels, which are indeed coupled at low frequencies, jointly with other mechanical parts actively involved in its function and leading to a more complex behavior as it will described with the help of the BPS-IPU electrical model in Chap. 4.

Each strip electrode ends in a smaller cross section cylindrical screw in order to pass through the center of its respective toroidal transformer core, thus acting as a one-turn primary winding, as shown in Fig. 3.8b. Consequently, as the wall image current is spread over the four strip electrodes, every electrode current component will induce a current in the transformer secondary winding due to the magnetic flux variation produced by this time-varying current according to the Faraday-Lenz's Law

$$\varepsilon = -\frac{d\Phi_B}{dt} \tag{3.27}$$

where ε is the electromotive force (in Volts) that would induce a time-varying current in a closed circuit, and Φ_B is the magnetic flux (in Webers, Wb). This law states that the transformer will also not be able to detect DC-current component because it only produces a constant magnetic field magnitude, and so a constant magnetic flux, which can not induce a stationary current into the secondary winding. In that sense, it is of no importance since the beam-induced wall current does not contain already the beam DC current component. Nevertheless, for the time-varying wall current the strip electrodes can carry higher frequency components than the toroidal transformer along with its secondary circuit and stray elements will filter, so imposing a high cut-off frequency to the device output signals and limiting its operational bandwidth, as it will be described in next section.

The generated magnetic field from a cylindrical current source represented in Fig. 3.8a, as a good approximation of the electrode current going through the toroidal transformer, is obtained from the Biot-Savart's Law

$$\vec{B}(t) = \mu_0 \frac{I_{elec}(t)}{2\pi r} \vec{e_\varphi}, \tag{3.28}$$

where $\vec{B}(t)$ is the magnetic field generated by the time-varying electrode current source $I_{elec}(t)$, r is the distance from the source current to the field point, $\vec{e_\varphi}$ is the azimuthal unitary field vector, and μ_0 is the magnetic permeability of the vacuum. Instead, for the field in a given material μ_0 may be just replaced by the material magnetic permeability $\mu = \mu_r \mu_0$ usually referenced to the vacuum permeability through its relative permeability. The longitudinal current distribution in the electrode will fundamentally generate an azimuthal magnetic field component, so the toroidal core shape is best suited for guiding the magnetic field lines and measuring the primary electrode current.

The inductance of a winding in a toroidal transformer core can be obtained from

$$L = \frac{\mu_0 \mu_r}{2\pi} l N^2 \ln \frac{r_o}{r_i} \tag{3.29}$$

with a length l, inner radius r_i and outer radius r_o, for a magnetic material of μ_r relative permeability and directly proportional to the squared number of winding turns N.

Generally for an ideal transformer, assuming it is working in its pass-band with no frequency dependence, the ratio of currents and voltages between the primary I_1 and the secondary I_2 windings are given by

$$\frac{I_2}{I_1} = -\frac{1}{N} \tag{3.30}$$

$$\frac{V_2}{V_1} = N \tag{3.31}$$

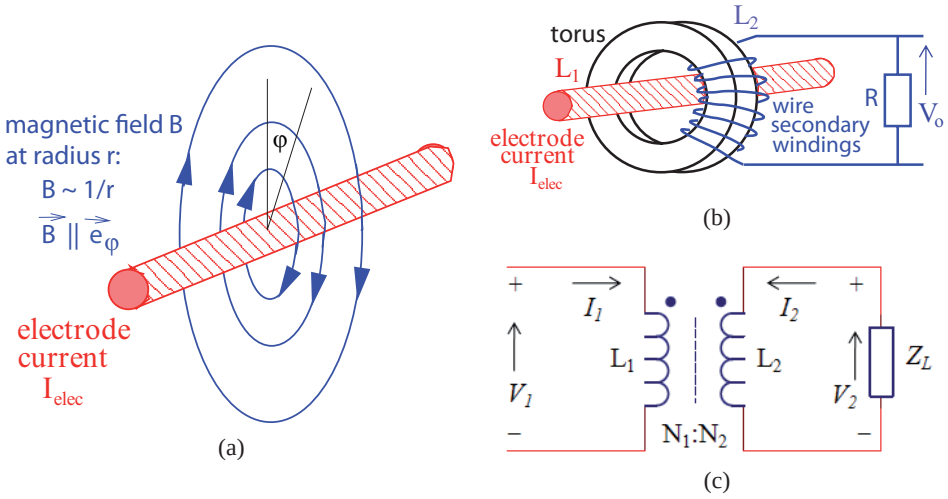

Figure 3.8: (a) Magnetic field generated by the electrode current, (b) basic scheme of an electrode with its toroidal transformer and, (c) its ideal transformer circuit representation.

where N is a real positive number for the ratio of turns of the primary N_1 and secondary winding N_2, being represented as $N1{:}N2$ or $1{:}N$ in the circuit notation, which from Eq. (3.29) are also related to the ratio of their respective inductances as

$$N \equiv \frac{N_2}{N_1} = \sqrt{\frac{L_2}{L_1}}. \tag{3.32}$$

For an ideal transformer it is considered a perfect coupling between the primary and secondary windings having then no magnetic flux leakage, and also without ohmic losses in their windings, so the power $P = IV$ is fully transferred from the primary to the secondary since, multiplying Eqs. (3.30), (3.31), the sum of powers of each transformer sides is $P_1 + P_2 = 0$.

In the current ratios the negative sign just indicates the current flow direction in the windings according to the convention usually taken with the current going inwards from the terminals to the winding, and also for the same relative windings orientation, as indicated by the the dots symbol convention for the circuit representation in Fig. 3.8c. Each winding orientation is given by the right-hand rule between the winding current and the magnetic flux, so accordingly, a positive sign in the currents ratio will correspond to the opposite relative orientation of the windings with the dots at opposite position ends.

The output voltage at the transformer secondary with the impedance load Z_L is simply obtained as

$$V_2 = -Z_L I_2 \tag{3.33}$$

then, dividing both Eqs. (3.30), (3.31) and substituting in the above relation, it can be obtained the *input impedance*, as seen from the input terminals,

$$Z_i \equiv \frac{V_1}{I_1} = -N^2 \frac{V_2}{I_2} = N^2 Z_L \tag{3.34}$$

which is a very useful relation for analyzing a more complex transformer circuit,

allowing to refer the impedances behavior of the secondary to the primary side of the transformer, or viceversa, after after multiplying by the impedance scaling factor N^2.

Besides the inductances, or self-inductances, of each of the transformer windings, it exist a mutual inductance M between them reflecting the coupling of their respectively generated magnetic fluxes, which is defined from the windings inductances as

$$M = K\sqrt{L_1 L_2} \tag{3.35}$$

where $K \leq 1$ is the coupling coefficient with $K = 1$ for a perfectly coupled transformer as the ideal transformer case above, and with the sign of the windings orientation also included. In the more realistic case of not perfectly coupled transformer, the secondary current and voltages of the ideal transformer are proportionally reduced by $K < 1$. This is only for the pass-band of the transformer, but it will also have different effects on the full transformer frequency response depending specifically on the configuration of the primary and secondary circuits connected to it.

Particularly for every electrode-transformer channel of the BPS-IPU, as depicted in its circuit scheme of Fig. 3.8b, the primary winding is $N_1 = 1$ due to the single pass of the electrode through the torus, so the turns ratio is given only by the the secondary winding turns $N \equiv N_2$, which will be an important design parameter. Thus, for a transformer secondary winding loaded with a shunt or parallel resistor R, the output voltage level V_o is written in function of the electrode primary current $I_{elec} \equiv I_1$, just using Eq. (3.33) and substituting the secondary current $I_{sec} \equiv I_2$ through Eq. (3.30),

$$V_o = -RI_{sec} = \left(\frac{R}{N}\right) I_{elec} \equiv Z_t I_{elec} \tag{3.36}$$

where V_o is used for denoting any of the four electrode channels outputs, as well as I_{elec} is used for any of the electrode current excitation inputs, with the *transfer impedance* Z_t, expressed in Ω or V/A, relating both for each electrode channel.

This relation stands only for the frequency components of the electrode current signal in the pass-band of the transformer circuit. Further on it is discussed the general case where the transfer impedance $Z_t(\omega)$ depends on the frequency defining so the bandwidth of every electrode channel.

Every electrode channel output V_o in Eq. (3.36) will implicitly depend on the beam position through its beam induced wall current component I_{elec}, as expressed in Eqs. from (3.12) to (3.15), and thereby changing its voltage magnitude with the beam proximity to the corresponding strip electrode in the same way as the electrode current does, since they are linearly related by its channel transfer impedance Z_t.

In consequence, the delta-over-sigma (Δ/Σ) processing method can be applied to the voltage output signals of the device, so the beam position coordinates can be determined from the electrode channel outputs of the BPS-IPU, where a more compact notation is followed further on to label them as $(H_\pm, V_\pm)$ corresponding to the (L, R) and (U, D) electrodes for horizontal and vertical plane respectively. The beam position is then obtained from, the difference between the output pairs $V_{\Delta H} = V_{H+} - V_{H-}$ and $V_{\Delta V} = V_{V+} - V_{V-}$, for the horizontal and vertical coordinate planes respectively, and both normalized to the voltage sum signal $V_\Sigma = V_{H+} + V_{H-} + V_{V+} + V_{V-}$. This method is commonly implemented by mixing the four electrode signals in an external amplifier, as it is done in for the BPS and described for its readout chain in next chapter.

Assuming the ideal case where Z_t is equal for all the electrode channels, these mixed voltage signals can be easily obtained from the four voltage outputs, using Eq. (3.36), as well as they are also related to the position using the electrode currents relations from Eqs. (3.22) to (3.24), as

$$V_{\Delta H} = Z_t I_{\Delta H} = Z_t S_x I_\Sigma x \tag{3.37}$$

$$V_{\Delta V} = Z_t I_{\Delta V} = Z_t S_y I_\Sigma y \tag{3.38}$$

$$V_\Sigma = Z_t I_\Sigma = Z_t I_\Sigma \tag{3.39}$$

where V_Σ is a measurement of the total wall current proportional to the beam current since the sum of the four electrode current components I_Σ, is is proportional to the beam current, and approximately independent of the beam position, as stated in Eq. (3.19). The difference voltage signals V_Δ of Eqs. (3.37) and (3.38) depend on the beam position like for the difference currents in the linear approximation, but being also proportional to the transfer impedance Z_t.

The difference voltage signals can be explicitly written in function of the wall current I_w, by substituting the sum current I_Σ of Eq. (3.19) in Eqs. (3.37) and (3.38), yielding

$$V_\Delta = Z_t S_x (2\phi/\pi) I_w x, \tag{3.40}$$

where x stands also for y coordinate. Therefore, it is defined the *transverse transfer impedance* as

$$Z_\perp = Z_t S_x (2\phi/\pi), \tag{3.41}$$

which will carry the electrodes geometric dependence through their angular coverage ϕ, leaving

$$V_\Delta = Z_\perp I_w x, \tag{3.42}$$

which is written in terms of the dipole moment of the beam that could be corrected with higher order moments, as another view of the linear approximation [11].

Finally, equivalently as for the electrode currents in Eqs. (3.43) and (3.44), the vertical and horizontal beam position coordinates in function of the voltage signals are directly obtained from Eqs. (3.37) to (3.39) as

$$x = \frac{1}{S_x}\left(\frac{V_{\Delta H}}{V_\Sigma}\right) + \delta_x \tag{3.43}$$

$$y = \frac{1}{S_y}\left(\frac{V_{\Delta V}}{V_\Sigma}\right) + \delta_y \tag{3.44}$$

where in order to make the beam position measurement independent of the beam current, both V_Δ signals are normalized to the sum of all the electrode output signals V_Σ. Often the inverse of the sensitivity so-called *position sensitivity* $k_{x,y} = 1/S_{x,y}$ given in mm units is used instead.

The above relations for the beam position coordinate represent an ideal case where Z_t is the same for all the electrode channels, so it is ruled out from them leaving only the sensitivity factors S_x and S_y as they were defined in Eq. (3.24) depending only on the electrodes geometry as defined in Eq. (3.24). In a real case Z_t is not canceled out and contributes to the sensitivities because of the differences between the electrode channels, which may include not only the transformer circuits unbalance but also the electrodes geometry imperfections due to fabrication tolerances. The position measurement offsets with respect the device mechanical center, or electrical offsets, $\delta_{x,y}$ will appear reflecting also both circuit and geometry differences of the electrode channels.

In order to know the sensitivity factors and the offsets, a characterization test procedure must be performed to measure these parameters which will be specific to each monitor. Moreover, in order to establish the goodness of a pick-up performance are used two main characterization parameters which were previously defined in Sec. 3.2. The *accuracy*, or *overall Precision*, in the absolute position determination, where besides the uncertainties due to system noise, in the case of using a linear approximation the non-linear deviations within the position measurement range of interest are also included. As well as the *resolution* that will represent the minimum displacement or beam position variation the pick-up could detect which is eventually limited by the noise background present in whole system, the pick-up and the readout and acquisition electronics. These issues will be discussed in the further on in Chap. 5 describing the characterization and beam tests carried out to determine the performance in measuring the beam position of the BPS units delivered to the TBL line.

3.5.3 Frequency response and signal transmission

The BPS-IPU transmission behavior of any arbitrary time-varying excitation signal, like is the beam current, can be analyzed in the frequency domain, without loss of generality, by means of the Fourier superposition principle, which states that any signal are a composition of multiple frequency harmonics. Then, a beam current harmonic will be of the form, $I_{beam} = I_0(\varphi)e^{i\omega t}$, with angular frequency, ω=2πf, containing the signal frequency, f and φ the signal relative phase.

A pick-up, like any other electromagnetic device, will have a determined output response, in magnitude and phase, for every frequency harmonic of the signal spectrum. Hence, the BPS-IPU can be ideally characterized in the frequency domain by its transfer function, defined as the ratio of the output over the input signal, for a given frequency harmonic; and, then, obtaining its typical frequency response pattern by the evaluation of the transfer function magnitude and phase in the frequency band of interest.

Each electrode-transformer channel of the BPS-IPU represented in Fig. 3.8b, can be individually modeled using the equivalent circuit of Fig. 3.9. This is a first approximation of the BPS-IPU frequency response basic pass-band profile which does not take into account the combined behavior of the four electrode-transformer channels and the surrounding ferrite as it will be described in Chap. 4 and particularly in the BPS full electrical model in Sec. 4.7.

In the equivalent circuit of Fig. 3.9, the electrode current of the primary side, as the input excitation signal, is modeled as a current source of I_{sec} in the secondary side, according to the currents ratio of an ideal transformer (Eq. 3.30). This is in parallel to the

inductance L of the transformer secondary winding, a capacitance C_s for taking into account the stray capacitances present mainly between the transformer secondary windings, and the load resistance R. In this circuit model is also assumed an ideal primary electrodes with low ohmic losses and inductance, so the frequency response would be determined by the elements of the transformer secondary circuit. Thus the equivalent impedance of the secondary circuit Z_S can be directly calculated from the parallel association of these three element impedances $j\omega L$, $1/j\omega C_S$ and R, yielding

$$Z_S(\omega) = \frac{i\omega L}{1 + i\omega L/R + (i\omega L/R)(i\omega RC_S)} \tag{3.45}$$

which relates in the frequency domain the output voltage signal of each secondary channel V_o to the transformer secondary current I_{sec} as

$$V_o(\omega) = Z_S(\omega) I_{sec}(\omega). \tag{3.46}$$

The output voltage V_o in function of the primary electrode current I_{elec} is simply obtained by substituting the ideal transformer relation for the currents Eq. (3.30) into Eq. (3.46) as

$$V_o(\omega) = \frac{Z_S(\omega)}{N} I_{elec}(\omega) \equiv Z_t(\omega) I_{elec}(\omega) \tag{3.47}$$

where the transfer impedance of one-electrode channel is just the secondary equivalent impedance Z_S divided by the number of winding turns of transformer secondary N. This frequency dependent relation is equivalent to the one corresponding to the output voltage V_o in Eq. (3.36) for the pass-band region.

Then, the transfer impedance is defined as the ratio of the usable output signal voltage V_o and the input electrode current I_{elec} which can be written explicitly in function of the one-electrode channel equivalent circuit as

$$Z_t(\omega) = \left(\frac{1}{N}\right) \frac{i\omega L}{1 + i\omega L/R + (i\omega L/R)(i\omega RC_S)} \tag{3.48}$$

From the analysis of the transfer impedance Z_t in Eq. (3.48), it can be obtained the typical frequency response pattern, and its characteristic frequencies, of the BPS-IPU device for one-electrode channel. Therefore the transfer impedance asymptotic response is obtained for the following frequency ranges of interest:

- **Low frequency range**, assuming $\omega << \frac{R}{L}$:
  In this case, the second and third term in the denominator of Eq. (3.48) can be neglected. The resulting transfer impedance is then,

  $$Z_t \rightarrow \frac{i\omega L}{N}. \tag{3.49}$$

  The meaning of this equation is, that the usable output signal at the resistor R decreases proportional to the excitation frequency because the inductance acts as a short-circuit for the considered low frequencies. In particular, at $\omega = 0$ no signal is recorded. This reflects the well known fact, that a transformer can not handle dc-currents.

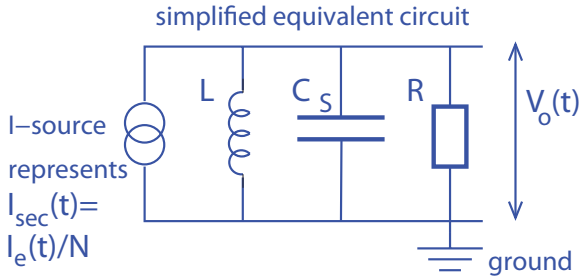

Figure 3.9: Equivalent circuit of the transformer secondary winding.

- **High frequency range**, assuming $\omega >> \frac{1}{RC_S}$:
  In this case, the third term in the denominator of Eq. (3.48), scaling with the frequency square, gets much bigger than the first and second term, so the last can be neglected. The transfer impedance is then,

$$Z_t \rightarrow \frac{1}{i\omega C_S N}. \tag{3.50}$$

  Due to the complementary behavior of the inductance and the capacitance, for high frequencies the current is mainly flowing through the capacitor, acting almost like a short-circuit, and therefore the voltage drop at the resistor R will be very low.

- **Pass-band frequency range**, assuming $\frac{R}{L} << \omega << \frac{1}{RC_S}$:
  For this frequency range the second term in the denominator of Eq. (3.48) dominates and the first and third term can be neglected. Then, the transfer impedance tend to its maximum magnitude *R*, in the middle of the pass-band, and in the whole region is,

$$Z_t \approx \frac{R}{N}. \tag{3.51}$$

  This is the usable working region, since the voltage drop at the output resistor, *R*, is significant and proportional to its value. Therefore, in the pass-band frequency region or working region will stand the relation (3.36) of the output voltage level for each BPS-IPU electrode, presented previously.

From the previous asymptotic analysis of the transfer impedance, it can be distinguished two characteristic frequencies which are the low cut-off frequency, ω_{low}, and the high cut-off frequency, ω_{high}, corresponding to the lower and the upper boundary of the pass-band, respectively. In a general case, the criterion to determine both cut-off frequencies is at $1/\sqrt{2}$ (in linear scale), or -3 dB, drop from the maximum magnitude of the transfer function, delimiting exactly the bandwidth of the pass-band region. In the case of our transfer impedance, the cut-off frequencies, that agree the last criterion, are defined in terms of the circuit elements as

$$\omega_{low} = \frac{R}{L} \qquad \omega_{high} = \frac{1}{RC_S}, \tag{3.52}$$

and, thus, the bandwidth of the pass-band, or working region, can be very broad $\omega_{low} << \omega_{high}$ by selecting the appropriate values of the electronic elements.

As the transfer impedance represents a 2^{nd} order passive circuit, there is another characteristic frequency called the resonance frequency, which corresponds exactly to the point of the maximum transfer impedance magnitude R, and is defined as

$$\omega_{res} \equiv \sqrt{\omega_{low}\,\omega_{high}} = \frac{1}{\sqrt{LC_S}}, \tag{3.53}$$

where the first is a general definition for a 2^{nd} order RLC passive circuit, which states that the resonance frequency is the geometric average of the bandwidth interval (placed in the middle for a logarithmic frequency scale); and, in second place is written in terms of the circuit elements. The resonance frequency can be identified in the third term of the denominator of the transfer impedance expression in Eq. (3.48), using the cut-off frequencies relations in Eq. (3.52).

In the Figs. 3.10 and 3.11, it is represented the ideal BPS-IPU frequency response pattern, in magnitude and phase, respectively. These plots are obtained by the evaluation of the modulus and phase of the transfer impedance in a given frequency range. Then, in order to get its magnitude and phase expressions, the transfer impedance can be written, operating from its expression in Eq. (3.48), in a more convenient form with separated terms of R_t, as the real or resistive part and, X_t, as the imaginary or reactive part,

$$Z_t(\omega) \equiv R_t(\omega) + iX_t(\omega) = \frac{R}{N(1+F^2(\omega))}\left(1 + iF(\omega)\right), \tag{3.54}$$

where the $F(\omega)$ term contains the frequency dependence of the transfer impedance, and it is written in terms of the cut-off frequencies as

$$F(\omega) \equiv \left(1 - \frac{\omega^2}{\omega_{low}\,\omega_{high}}\right)\frac{\omega_{low}}{\omega}, \tag{3.55}$$

or, likewise, in terms of the circuit elements, just by substituting the cut-off frequency relations (3.52) into the previous expression,

$$F(\omega) \equiv R\left(\frac{1}{L\omega} - C_S\,\omega\right). \tag{3.56}$$

Thereby, taking the modulus of the new transfer impedance form (3.54), the magnitude of transfer impedance (Fig. 3.10) can be written as

$$|Z_t(\omega)| = \frac{R}{N\sqrt{1+F^2(\omega)}}, \tag{3.57}$$

which has Ω units, but it is usually represented in dB units just by making $20\log(|Z_t(\omega)|)$. And, the phase of the transfer impedance (Fig. 3.11), is simply written as

$$\phi_t(\omega) = \arctan(F(\omega)); \tag{3.58}$$

taking into account that ω=$2\pi f$, for eqs. from (3.54) to (3.58), the same expressions can also be written for the frequency variable, f, making the change, $\omega \rightarrow f$.

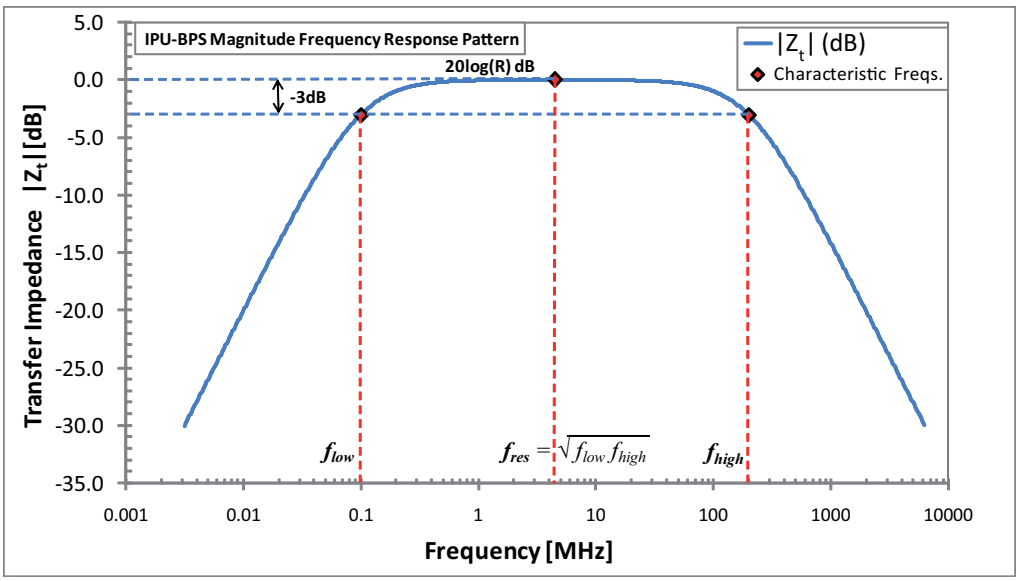

Figure 3.10: Frequency response pattern (typical) of the BPS-IPU transfer impedance magnitude. There is also marked with red dots the magnitude of the three characteristic frequencies: the low and high cut-off frequencies, f_{low} and f_{high} respectively, which delimit the BPS-IPU bandwidth and are defined at -3 dB drop from the maximum magnitude; and, the resonance frequency, f_{res}, in the middle of the bandwidth as the geometric average of the cut-off frequencies.

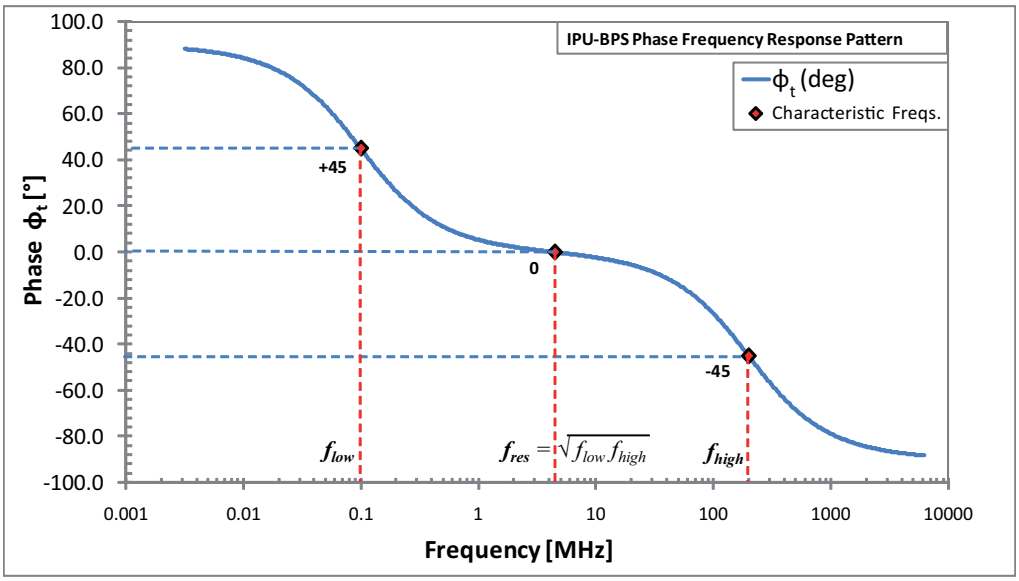

Figure 3.11: Frequency response pattern (typical) of the BPS-IPU transfer impedance phase. There is also marked with red dots the middle point in the phase transitions which occur at the low and high cut-off frequencies, and the resonance frequency.

Now, using the set of Eqs. (3.57), (3.55), (3.58), it can be calculated the values of magnitude (depicted in dB units in Fig. 3.10) and phase (depicted in degrees in Fig. 3.11) for the characteristic frequencies:

- **Low cut-off frequency**, $\omega = \omega_{low}$:

  if $\omega_{low} << \omega_{high}$, then $F(\omega_{low}) = 1 - (\omega_{low}/\omega_{high}) \approx 1$
  $\Rightarrow |Z_t| = R/(N\sqrt{2})$, and $\phi_t = \pi/2$;

- **Resonance frequency**, $\omega = \omega_{res} \equiv \sqrt{\omega_{low}\,\omega_{high}}$:

  $F(\omega_{res}) = 0 \Rightarrow |Z_t| = R/N$, and $\phi_t = 0$;

- **High cut-off frequency**, $\omega = \omega_{high}$:

  if $\omega_{low} << \omega_{high}$, then $F(\omega_{high}) = (\omega_{low}/\omega_{high}) - 1 \approx -1$
  $\Rightarrow |Z_t| = R/(N\sqrt{2})$, and $\phi_t = -\pi/2$.

Finally, in the frequency response analysis, the secondary equivalent circuit of a BPS-IPU electrode, represented by the transfer impedance, could lead to undesirable oscillations for a frequency components close to the resonance frequency, because, as it was mentioned before, this circuit is a 2^{nd} order RLC that could have a resonant behavior. To avoid this, one must be sure that the circuit element values, through the transfer impedance, are far away from giving a resonant frequency response behavior. Therefore, the secondary circuit design must fulfill the following condition to have a non-resonant behavior,

$$\omega_{high} > 2\omega_{low} \quad \Leftrightarrow \quad R^2 < \frac{L}{2C_S}, \tag{3.59}$$

where the second equivalent condition in terms of the circuit values is easily obtained substituting the cut-off frequencies definitions of Eqs. (3.52) in the first condition. This particular non-resonance condition can be derived from the more general form for a 2^{nd} order RLC circuit in the Laplace domain,

$$\left\| \frac{\mathrm{Re}(p_0)}{|p_0|} \right\| > \frac{1}{\sqrt{2}}, \tag{3.60}$$

where p_0 can be either of the two complex poles of the transfer impedance expression in Eq. (3.48) evaluated in the Laplace domain, $Z_t(p)$ (just by making the variable change, $i\omega \rightarrow p$), which is a more general complex plane using the Laplace variable, $p \in \mathbb{C}$; $|p_0|$ and $\mathrm{Re}(p_0)$ are the modulus and the real part of the poles, respectively.

A more relaxed condition would be, if the poles of the transfer impedance were purely real, then, $|p_0| = \mathrm{Re}(p_0)$, and there would be no resonance since the general condition (3.60) is fulfilled. As a result, turning to the particular non-resonance condition (3.59), the resonant behavior would be avoided by selecting a low value for the output resistor, R, and a high secondary transformer inductance, L, resulting in an over-damping of possible oscillations may appear, and, also, increasing the bandwidth of the device; as it is the case represented in Figs. 3.10 and 3.11.

On the other hand, turning to time domain, the limited bandwidth of the BPS-IPU frequency response will affect to the transmitted beam signal shape, as it is shown in the Fig. 3.12 for a beam pulse, and a beam bunch. Since the beam position measure will be

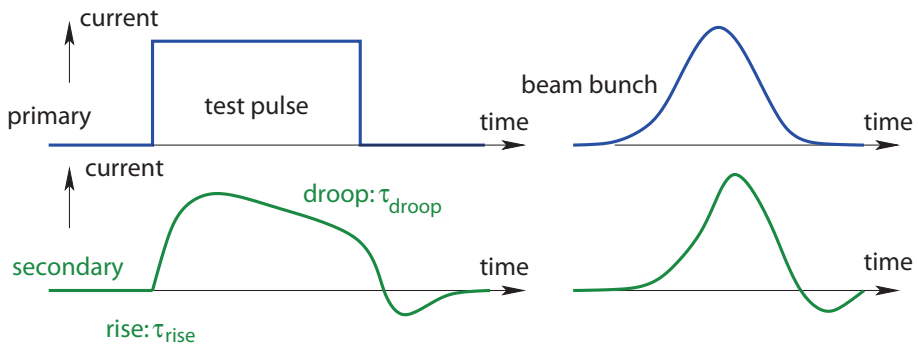

Figure 3.12: Beam pulse and bunch time signal shaping for a band-pass frequency profile.

proportional to the amplitude of the transmitted signal, the device must let pass the signal shape without too much deformation. As a consequence two time parameters are defined from the characteristic cut-off frequencies

$$\tau_{droop} = \frac{1}{\omega_{low}} \qquad \tau_{rise} = \frac{1}{\omega_{high}}; \tag{3.61}$$

and, substituting the cut-off frequencies depending on the secondary components,

$$\tau_{droop} = \frac{L}{R} \qquad \tau_{rise} = RC_S\,. \tag{3.62}$$

These characteristic time parameters, τ_{rise} and τ_{droop}, corresponds, respectively, to the exponential setup and decay characteristic times of a pass-band type circuit response, when it is excited with a step-wise function like a beam pulse signal.

Usually for a square-pulsed beam, the droop time parameter, τ_{droop}, is the most important since the beam position measure will be sampled from the transmitted pulse signal, and it must have a pulse top as flat as possible, in a predetermined time interval, to do not have different signal measurement in the same pulse. Hence the criterion used to consider a good flat-top pulse response is that the droop time constant might be hundred times larger than the beam pulse duration, $\tau_{droop} \sim 10^2 t_{pulse}$.

Chapter 4

Design of the BPS Monitor for the Test Beam Line

4.1 Design background of the BPS-IPU

First *Magnetic Pick-Ups* (MPU) [31] were developed at CERN for beam position monitoring at the *LEP Pre-Injector* (LPI) of the *Large Electron Positron Collider* (LEP), and installed particularly in the LEP Injector Linac (LIL) and the Electron-Positron Accumulator (EPA) ring of the LPI complex.

The first IPU device was developed for the Drive Beam Linac (DBL) of the CTF3 at CERN, with a 168 mm overall length and 40 mm beam pipe aperture. It was based on previous MPU design, having essentially the same functional principles but with a different geometry and improvements as required for the DBL, eventually becoming the precursor of later IPU designs [9]. Like the *Precision Beam Position Monitor* (PBPM), with a length of 95 mm and for two beam pipe apertures of 4/6 mm, which was also made at CERN for the future linear colliders in the framework of the EUROTeV design study [37].

The development of the BPS monitors for TBL was carried out at IFIC labs within the framework of the CTF3 collaboration and with the help of the knowledge acquired in both mentioned IPU developments. The BPS is based in those designs basically as a scaled and adapted mechanical realization to the TBL dimensions with a length of 126 mm and for a 24 mm beam pipe aperture, but also being specifically designed and tested to fulfill the performance requirements of the TBL beam. Sometimes these TBL BPMs are hence referred as BPS-IPU for recalling its pick-up base technology.

4.2 Main features of the BPS-IPU and TBL line specifications

Generally, an IPU or any other pick-up which are based on EM measurements principles, can be used and adapted to a wide range of accelerators, from linacs to synchrotrons and also to different particles, but of course a particular pick-up choice will rely on the accelerator requirements and beam specifications that makes a given pick-up technology more convenient.

The IPU devices have been regularly used in many accelerators but not as often as their pick-up counterparts based on electrostatic or RF measurement principles. This may be due to its main drawback of having a complex mechanics with an assembly of many

parts and with different materials. In turn, an IPU device offers many beneficial features listed below

- simultaneous beam position and current measurements for pulse modulated bunched beams;
- the difference-over-sum method is used to measure the horizontal and vertical beam position (x, y) by mixing the four BPS output signals $(H_{\pm}, V_{\pm})$ into $(\Delta H/\Sigma, \Delta H/\Sigma)$ signals being proportional at first order approximation to the beam position. The difference signals are obtained as $\Delta H = [H_+ - H_-]$ and $\Delta V = [V_+ - V_-]$, which are highly sensitive to the beam position. While the sum signal Σ apart from being used to normalize the difference signals, it also gives a proportional measurement of the beam current;
- broad bandwidth device operation with a typical flat bandpass response in order to work at beam pulse time scale. Starting around 1 kHz it covers 7 or 6 decades getting easily above 100 MHz. Due to its low frequency cutoff the device is able to measure the position and current within relatively long beam pulses up to 1 μs. In turn, its high cutoff determines the time resolution, being able to detect fast changes down to 1 ns (typically surpassing 100 MHz);
- the BPS output channels drive an external analog amplifier to yield the three signals $(\Delta H, \Delta V, \Sigma)$, which finally are converted to digital signals by a digitizer, as the main elements of the BPS readout chain, and are eventually sent to the control room where the beam position coordinates and beam current are displayed;
- two calibration input circuits $Cal_{\pm}$ are used to compensate the readout chain influence as well as to get a good accuracy in the beam current pulse measurement with a typical error less than 1%;
- high dynamic range for beam current levels from few mA and up to 4 or 5 orders of magnitude until around 100 A, mainly due to the relatively high output voltages given by the high permeability step-up transformers of the device and limited by the saturation of these magnetic cores;
- expected overall precision typically under 50 μm, which can be achieved just with linear approximation for beam position within the half aperture radius;
- expected resolution below 5 μm at beam current levels of around 30 A, particularly to the BPS in TBL with a 12 mm aperture radius. The attainable resolution will be smaller for larger sensitivity going basically as the inverse of the aperture radius, and eventually limited by the system noise. Resolutions of 100 nm has been reported for the PBPM with 3 mm aperture radius [37];
- less perturbed by high beam losses experienced in linacs like TBL, and expected good immunity to the external magnetic fields that may come from the close quadrupoles;
- all the position and current sensitive parts are placed outside the vacuum chamber, so the outer assembly parts could be replaced at some moment without breaking the vacuum in the line sector, and also, from the design perspective, this ease the components material selection that is often much more restrictive for vacuum components.

TBL beam parameters	
Beam current range, I_b	1–28 A
Bunch train duration, t_{pulse}	20–140 ns
Injection beam energy	150 MeV
Microbunch spacing, f_{bunch}	83 ps(12 GHz)
Microbunch duration, t_{bunch}	4–20 ps
Microbunch charge, Q_b	0.6–2.7 nC
Repetition frequency, f_r	0.83–50 Hz
Radiation level	≤1 kGray/year
Emittance, $\epsilon_{x,y}$	150 μm

BPM/BPS parameters	
Analog bandwidth	10 kHz–100 MHz
Beam position range	±5 mm (H/V)
Beam aperture diameter	24 mm
Overall mechanical length	126 mm
Number of BPMs in TBL	16
Resolution at maximum current	≤5 μm
Overall precision (accuracy), $\sigma_{V,H}$	≤50 μm

Table 4.1: Specifications of TBL beam parameters and BPM/BPS parameters.

Essentially, for the reasons above the IPU pick-up technology was considered the most suitable to develop the TBL line BPMs, which could eventually match up to all the TBL requirements after careful design of BPS-IPU devices. In Tab. 4.1 are summarized the main beam characteristics of the TBL, taking into account also the BPM parameter specifications that the BPS monitor must fulfill.

Fig. 4.1 shows a scheme and a 3D view of one TBL cell of 1.4 m length, out of the sixteen identical FODO cells composing the TBL of 22.4 m plus ending 6 m of diagnostics section. The beam in the TBL flows (from right to left in the figure) from a quadrupole magnet, steering and focusing the beam, downstream to the PETS tank, where RF power is extracted from the beam to an RF load being thus decelerated. The BPS is placed between them and has its own line alignment support for the beam position and intensity monitoring. A set of close-up pictures of the BPS are shown in Fig. 4.2, with side and top views of the first BPS prototype and other one of a BPS installed in TBL.

The electron beam arriving at the TBL line are injected with an energy of 150 MeV meaning that the electrons, with 0.51 MeV/c^2 rest mass, are already in the ultra-relativistic regime at practically the speed of light with $\beta \cong 1$ and $\gamma = 295$. According to Sec. 3.3, for the beam coupling to the BPS monitor it is assumed that the beam fields propagate as TEM modes along the line.

The beam time structure in the TBL is made of pulses of length t_{pulse} between 20–140 ns, typically with pulse shots repeated at few Hertz, which are composed of micro-bunches spaced by 83ps, hence with a bunching frequency f_{bunch}=12 GHz, and a bunch width t_{bunch} between 4–20 ps, as it is depicted in Fig. 4.3. This pulse modulated beam,

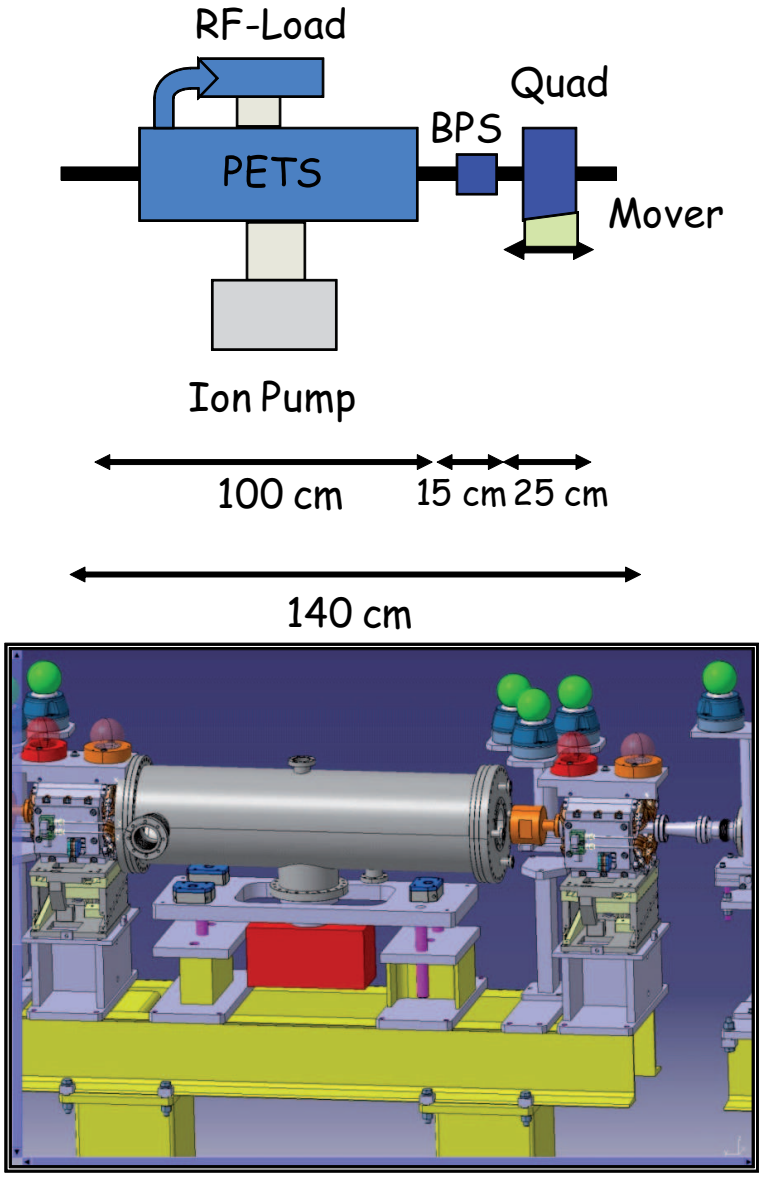

Figure 4.1: Scheme (top) and 3D view (bottom) of a TBL cell which comprises (from right to left) a quadrupole, a BPS-IPU monitor and a PETS tank.

hence its induced wall image current, has a frequency content spread over a very wide spectrum that reaches the X-band microwave region because of the 12 GHz main bunching frequency, and far beyond continues extending over 250 GHz, estimated as the inverse of the shorter bunch width 4 ps. This means a signal wavelength of around 1 mm within the upper side of the microwaves region, that may go even into the infrared region with harmonics produced by the particular pulse shape of the beam micro-bunches.

The BPS monitor is intended to work in the low frequency region around the beam pulse time scale with a band-pass response profile of bandwidth determined by the low and high cutoff frequencies, from f_{low}=10 kHz to at least f_{high}=100 MHz, according to the TBL specifications. This operation bandwidth was set in order to measure the beam position and intensity from the square pulse signals induced by the beam, which was consid-

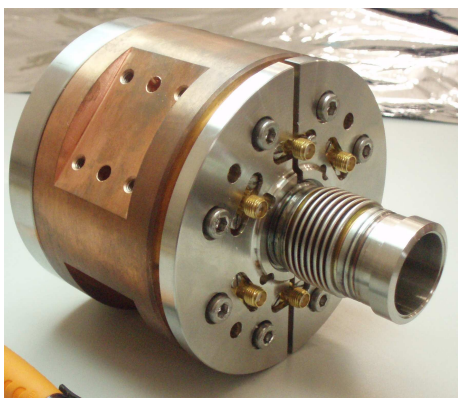

(a)

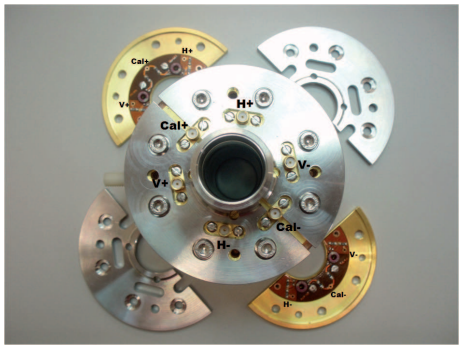

(b)

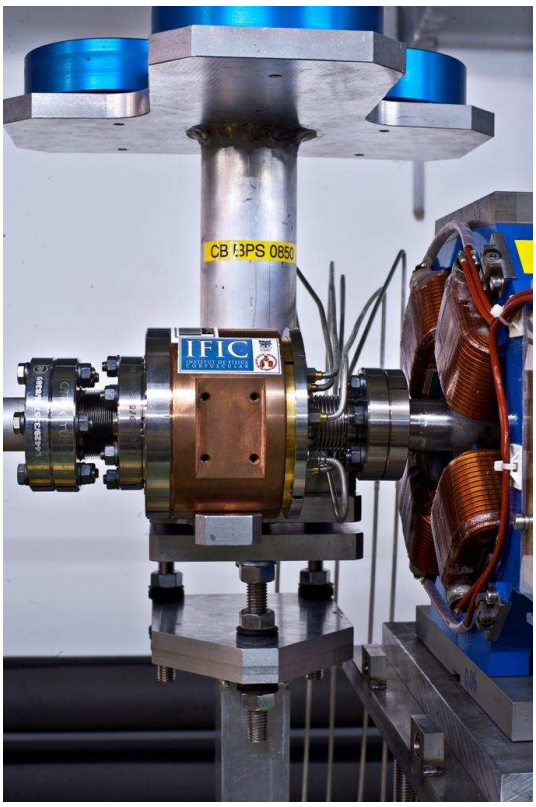

(c)

Figure 4.2: (a) Side view of the BPS monitor (BPS1, first prototype), and (b) top view, SMA ports: 4 position outputs ($H_{\pm}, V_{\pm}$) and 2 calibration inputs $Cal_{\pm}$, PCBs and closing clamp plates. (c) BPS installed in the TBL with its alignment support, six SMA semi-rigid coaxial cables connect to the external amplifier placed just below in the girder.

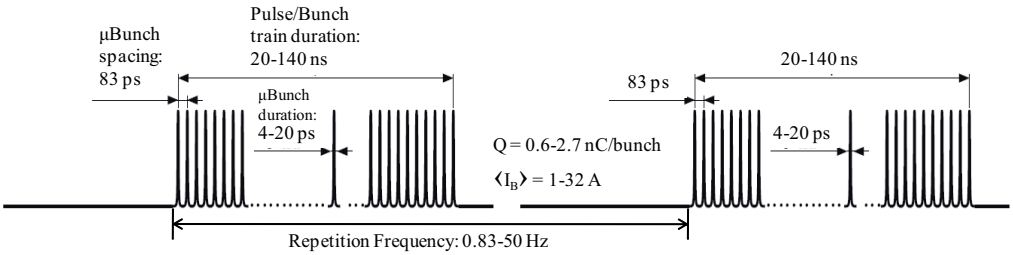

Figure 4.3: Time structure of the TBL pulsed beam.

ered wide enough to get an acceptable low distortion for the pulse signal transmission to the device outputs, following the criterion established in Chap. 3 for their pulse time constants corresponding to the low and high cutoffs, $\tau_{droop} = 16$ µs and $\tau_{rise} = 1.6$ ns, being respectively around hundred times larger or smaller than the longer pulse $t_{pulse} = 140$ ns. In the case of shorter pulse length $t_{pulse} = 20\ ns$, τ_{rise} is now only 12 times smaller, but the original criterion can be relaxed here since it still provides fast enough pulse edges and accepting a small shortening of the flat top pulse length. While τ_{droop} is even longer having better pulse top flatness from where the position and current measurements are

sampled.

In consequence, with this operation bandwidth the beam micro-bunch structure is not observed at the monitor outputs, due to its high frequency components that are filtered out. Instead the beam is detected as a continuous pulse with the fastest amplitude changes permitted by the high cutoff frequency f_{high}=100 MHz, in the order of τ_{rise}=1.6 ns.

Nevertheless, the beam high frequency content must be still considered in order to know the influence of the monitor on the beam itself. This is done by measuring the longitudinal coupling impedance inserted by the monitor and seen by the beam in his passage. Basically it represents the longitudinal voltage drop divided by the beam current, which is related to the generation of wakefields and resonances at some frequencies that may disturb the beam. Since the longitudinal coupling impedance depends on the frequency, it is measured according the beam frequency content considering that the beam signal energy is spread until the very high harmonics mentioned before, but it will be mostly concentrated around the bunching frequency at 12 GHz (X band) with decreasing amplitudes at higher frequency harmonics.

4.3 Outline of the BPS project development phases

The BPS project was carried out essentially in two phases:

- **Phase I**: consisted in the design, construction and characterization test of two BPS-IPU prototypes [10], in Fig. 4.2 are shown two views of the BPS1 prototype, from 2007 to end of 2008. The first prototype (labeled as BPS1) was tested with two different design options of the on-board PCB's, leading to BPS1–v1 and BPS1–v2 prototype versions. Afterwards, the BPS1-v2 was validated and installed in TBL in July 2008.
- **Phase II**: this phase was for the BPS series production in order to build 15 more units, jointly with its respective mechanical alignment supports, completing the 16 cells of the TBL line. It started with the series construction just after the first prototype installation at the beginning of 2009. In March 2009 a pre-series of two BPS units, labeled as BPS2 and BPS3, were requested in advance due to TBL beam test needs. After their corresponding characterization tests these units were delivered and installed in May 2009, having thus 3 fully operational units in the TBL. The BPS parts construction, and follow-up of processes, continued until the final assemblies when there were ready for the characterization test of the full BPS series at IFIC labs made during September 2009. Two specific test benches were also designed and constructed for these BPS tests, at low and high frequencies. The 15 BPS units were finally delivered at the end of September 2009. The installation of all BPS monitors in the TBL finished by mid October 2009.

In total 17 BPS units were constructed which were labeled as BPS1, BPS2, BPS3 for prototype and pre-series; and BPS-1s to BPS-14s for the series. BPS-5s unit remained at IFIC as spare to perform the test for evaluating the BPS response at high frequencies and measuring its longitudinal coupling impedance beyond the bunching frequency (12 GHz) in the X-band microwave region.

The project historic is shown in Fig. 4.4 where are outlined the main milestones represented until the final BPS beam tests in the TBL which were performed in order to measure the BPS resolution tendency with an increasing beam current and with the main goal of achieving the desired resolution below 5 μm for the maximum beam current of 28 A, as the BPS monitor figure of merit.

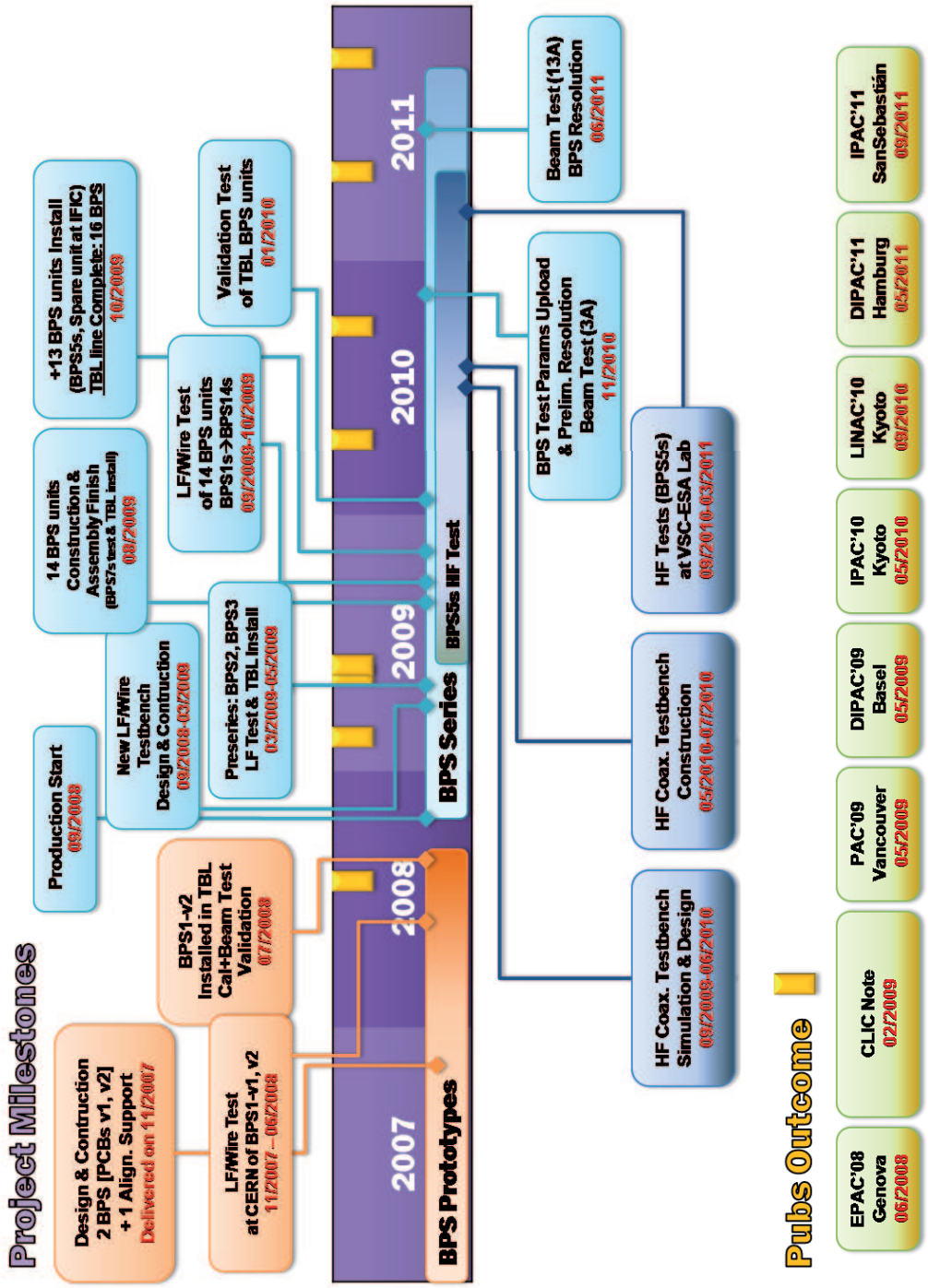

Figure 4.4: Milestones of the BPS project for the BPM's development of TBL line.

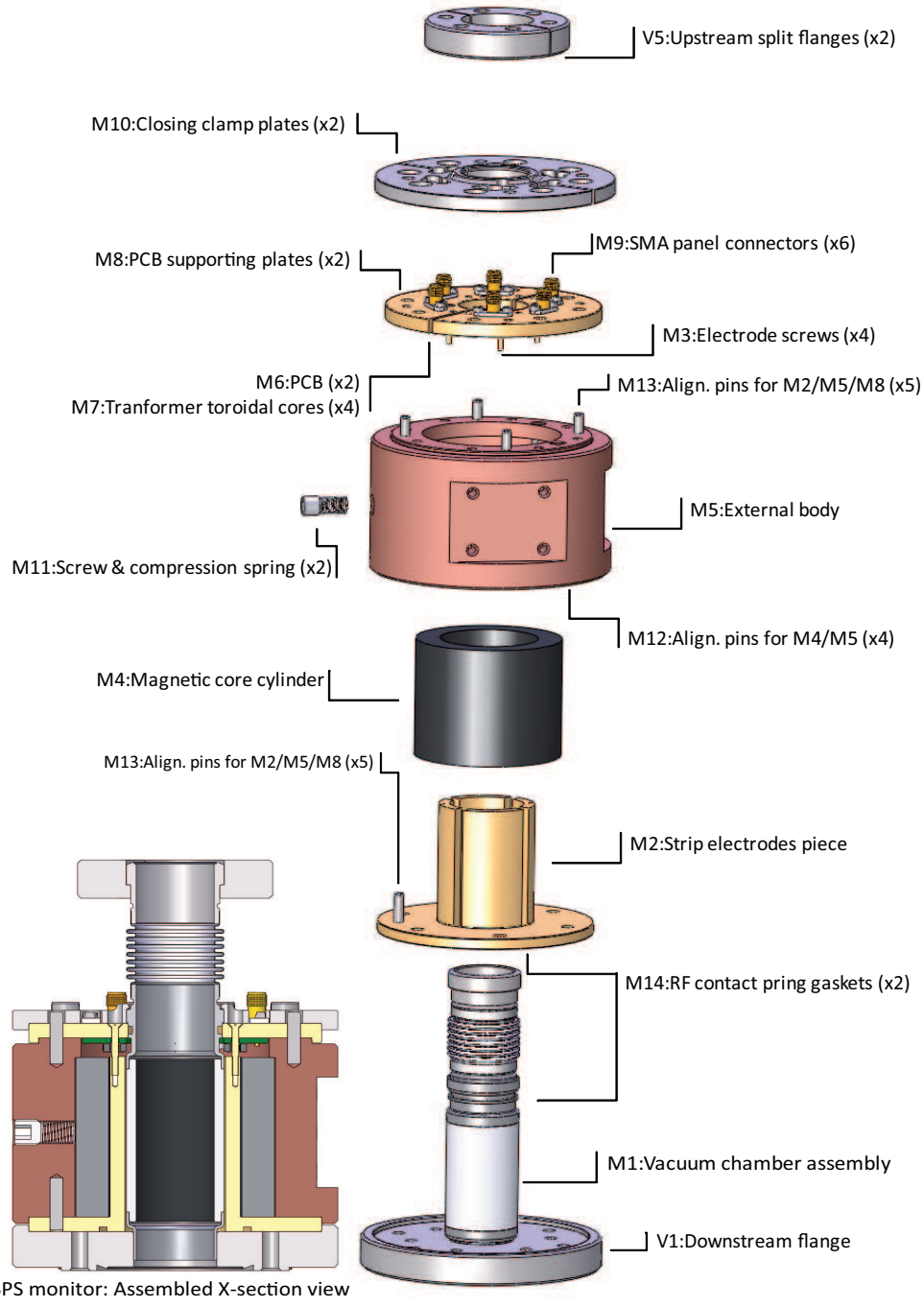

Figure 4.5: Exploded view of the BPS monitor showing its main labeled parts (fastening screws, RF contact springs and RF finger are not depicted).

BPS monitor main parts

Label	Name/Description	Material	Observations
M1	Vacuum chamber assembly	—	Subparts specified in Tab. 4.4
M2	Strip electrodes piece	Cu-OFE, gold plated	Detailed view in Figs. 4.7b, 4.9
M3	Electrode screws (×4)	Cu-Be alloy 25, gold plated	M2×16 (mm)
M4	Magnetic core cylinder	Ni-Zn ferrite	C2050, Ceramic Magnetics [38]
M5	External body	Cu-OFE	—
M6	PCB (×2)	—	Ring-shaped and half split, transformers circuits, see Sec. 4.6
M7	Transformers toroidal cores (×4)	Vitrovac	W650, Vacuumschmelze [39]
M8	PCB supporting plates (×2)	Cu-OFE, gold plated	Half split plates
M9	SMA panel connectors (×6)	—	23_SMA-50-0-13/111_N, Huber+Suhner [40]
M10	Closing clamp plates (×2)	s. steel, AISI 304L	Half split plates
M11	Screw & compression spring	s. steel	Ferrite fixing, screw DIN913, M8×8 (mm)
M12	Align. pins for M4/M5 (×4)	s. steel	ISO 8734 - ⌀ 6h6 ×14 (mm)
M13	Align. pins for M2/M5/M8 (×5)	s. steel	ISO 8734 - ⌀ 4h6 ×16 (mm)
M14	RF contact spring gaskets (×2)	Cu-Be alloy 25, gold plated	BalShield BG 15H5, Bal Seal Engineering [41]

Table 4.2: Summary of the BPS monitor main structural parts and materials (fastening screws of the BPS assembly are not specified).

4.4 Layout of the BPS monitor: mechanical and functional design aspects

The main parts that made up the BPS monitor can be identified in the exploded design views shown in Fig. 4.5. In the figure the device is disassembled in the different parts that are joined together only by fastening screws and alignment pins. The main parts shown, labeled as M{1...N}, are involved in the final assembly of the device, as well as it is illustrated the way these elements can be assembled. It must be noted that fastening screws are not depicted in these design views for illustration clearness. In addition, the name, or a short description, of these labeled M-parts are summarized in Tab. 4.2, including also the materials of which are made and particular remarks on their specifications. A picture of these main parts belonging to a disassembled BPS monitor can be seen in Fig. 4.6.

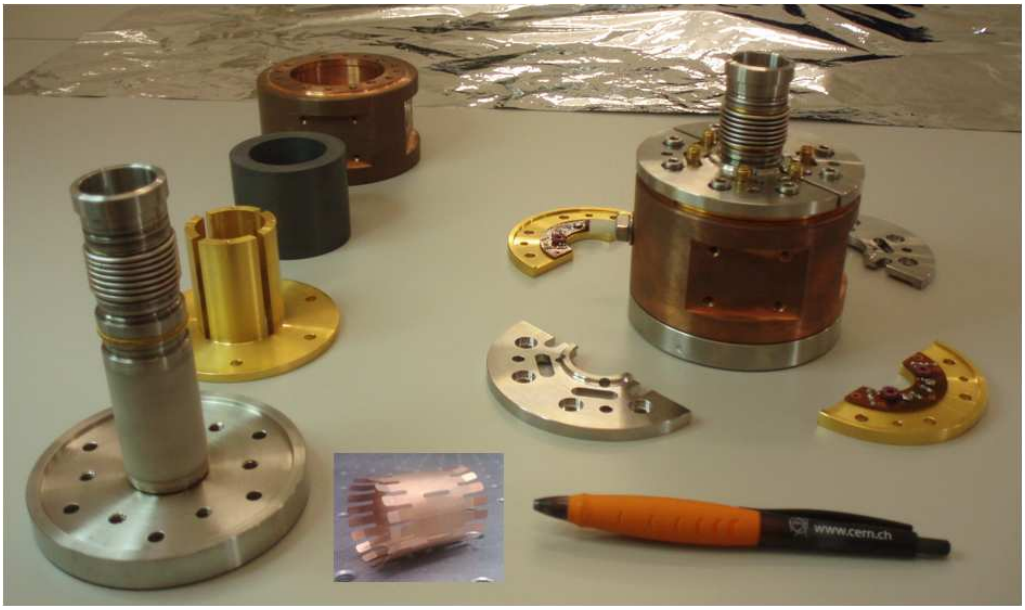

Figure 4.6: Picture of a disassembled BPS monitor showing its main parts, an assembled one is also shown (overimposed on the photo is included the RF finger). These units correspond to the two first constructed BPS prototypes, the BPS1 assembled (right) and the different parts of the BPS2 spread around.

The mechanical design of the BPS monitor is conceived in two fundamental structures; the vacuum chamber assembly (M1), and the outer non-vacuum parts around its vacuum pipe section. The vacuum chamber has more demanding requirements for the its manufacturing procedures and a very specific materials selection in order to be compatible with an Ultra High Vacuum (UHV) environment. Below are described in detail the structure and mechanical design aspects of both the vacuum chamber and the outer parts of the BPS monitor with an emphasis also on the functional roles of those elements involved directly in the beam position monitoring and based on EM considerations.

The overall shape of the BPS monitor and also of its main elements around the vacuum pipe of circular cross section is essentially cylindrical, as can be seen in Fig. 4.5, with a resulting revolution or axial symmetry except for some mechanical details. The fundamental dimensions, only the ones relevant for the device description are indicated in Fig. 4.7 which shows the monitor longitudinal section and a detail of the strip electrodes piece cross section. In Tab. 4.3 are summarized these basic dimensions referred to their corresponding device parts. The dimensions constraints directly imposed from the TBL line requirements was on the length of the monitor which was set to 126.18 mm, with its bellow in a relaxed state and giving a longitudinal stroke of ± 1 mm; and the vacuum chamber inner diameter of 24 mm following the minimum aperture of TBL beam line. The total weight of the fully assembled device is around 5 kg.

4.4.1 Vacuum chamber assembly

Since the device is inserted in the TBL line its innermost part is a vacuum chamber section giving continuity to the TBL line vacuum pipe where the beam flows in the direction right to left in Fig. 4.8. The vacuum chamber assembly consists of a ceramic tube (V2) brazed

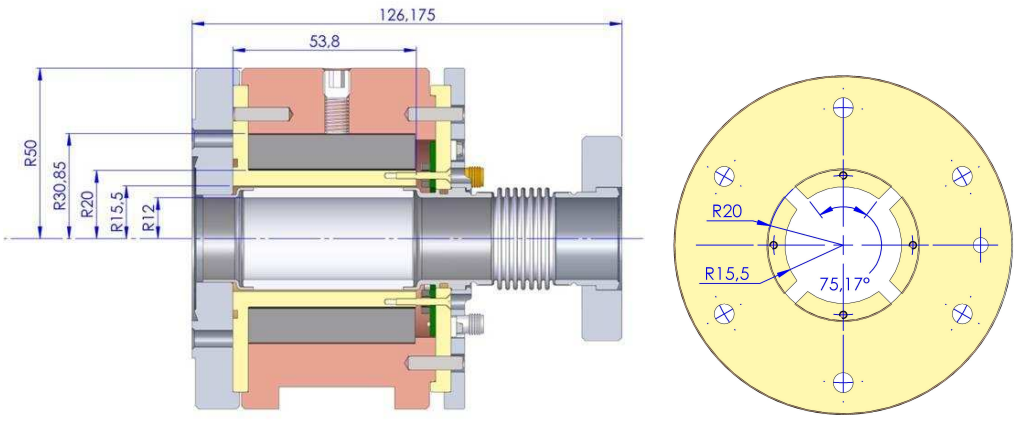

(a) (b)

Figure 4.7: (a) View of the longitudinal section of the assembled BPS monitor with main dimensions in mm units. (b) Detail of the strip electrodes piece cross section where is depicted the inner and outer radius as well as the angular width of the electrodes.

Main dimensions of the BPS monitor

Monitor total length (bellow stroke)	126.18 (±1) mm
Vacuum chamber (M1) inner radius	12 mm
Electrodes (M2) length	53.8 mm
Electrodes inner radius	15.5 mm
Electrodes outer radius	20 mm
Inter-electrodes spacing	4 mm
Electrodes angular width (inner radius)	75.17°
Ferrite cylinder (M4) length	49 mm
Ferrite cylinder inner radius	20.5 mm
Ferrite cylinder outer radius	30.5 mm
External Cu body (M5) length	57 mm
External Cu body outer radius	50 mm
PCB plates (M8) thickness	4.5 mm
Closing flanges (M10) thickness	4 mm

Table 4.3: Summary of the main dimensions of the BPS monitor depicted in its cross section views (Fig. 4.7), where it is also indicated the label of the main parts to which the dimension corresponds.

to two Kovar collars at both ends, with one collar (V6) TIG (Tugsten Inert Gas) welded directly to the downstream flange (V1), and the other one, the connection collar (V7), being part of a longer duct section which is connected to the bellow (V4) by Electron Beam Welding (EBW), and it is also grooved to insert the PCB supporting and closing-clamp plates (M8, M10). The other side of the bellow is also welded by EBW to a short pipe section (V8) machined in order to fit in the upstream split flanges (V5).

For the steel parts of the BPS vacuum pipe it was used the type 316L stainless steel (according to SAE steel grades designation). This type is a variant of the 316 stainless

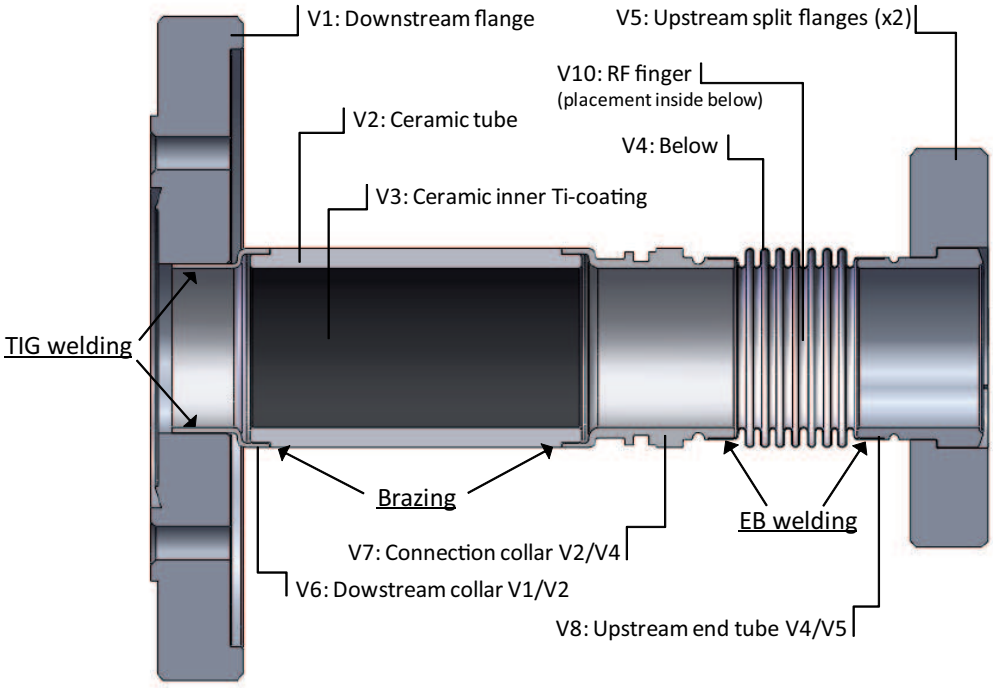

Figure 4.8: Detailed view of the BPS monitor vacuum chamber assembly indicating its main parts and the welding techniques employed.

steel, and it differs by having a lower Carbon content with slightly lower yield and tensile strengths but, otherwise, with improved weldability and also reduces the possibility of lower the corrosion resistance around welded areas, what makes more suitable for pipeline applications. In general, this alloy type offers outstanding properties, preserving standard procedures and tools for proper machinability, in ductility, corrosion resistance, non-magnetic intrinsic behavior (usually required a magnetic permeability $\mu_r < 1.01$), and UHV performance mainly given by its low outgassing rate required for CTF3 vacuum specifications.

In general, standard welding techniques, TIG and EBW, were employed in the vacuum chamber assembly to make UHV connections of all metal parts. As it is recommended these welding techniques use no filler material avoiding to add extra material non compatible with UHV, and also in order to prevent contamination, weldings are done in an inert gas atmosphere like Argon. For welding thin materials usually is necessary a precise EBW technique so, as mentioned before, it was used to weld the bellow (V4) made of stainless steel, at its respective ends with the connection collar (V7) of Kovar, and the upstream end tube (V8) of stainless steel.

Vacuum flanges

The monitor vacuum flanges at both ends was custom-made due to the special dimensions required for the installation in the TBL vacuum pipe. The downstream flange (V1) is a custom-made fixed flange of 24 mm inner diameter but machined to be compatible with a CF40 standard flange (Conflat^{TM} of 40 mm inner diameter) using a copper gasket (V9) placed between coupling flanges with knife edges, at 40 mm diameter, to achieve an

BPS monitor vacuum chamber assembly parts

Label	Name/Description	Material	Observations / Dimensions
V1	Downstream flange	s. steel, AISI 316L	Special fixed flange, compatible with a fixed CF40, ⌀ int./ext. 25.6/100 mm
V2	Ceramic tube	Alumina 99.7% (Al_2O_3)	A-480S, Kyocera [42], ⌀ int./ext. 24/30 mm, length 50 mm
V3	Ceramic inner Ti-coating	Titanium Nitride (TiN)	Thin conducting film deposited by sputtering, thickness [20-100] nm
V4	Bellow	s. steel, AISI 316L	Special bellow, Heitz [43], length (stroke) 26.55 (± 1) mm, ⌀ int. 24 mm
V5	Upstream split flanges (×2)	s. steel, AISI 316L	Special rotating flange, fitted to V8, ⌀ ext. 60 mm
V6	Downstream collar V1/V2	Kovar (Fe54% Ni29% Co17%)	TIG welded to V1 with ⌀ int. 24/ mm, brazed to V2
V7	Connection collar V2/V4	Kovar (Fe54% Ni29% Co17%)	Brazed to V2, EBW welded to V4 with ⌀ int. 24/ mm
V8	Upstream end tube V4/V5	s. steel, AISI 316L	EB welded to V4, machined to fit V5, ⌀ int. 24/ mm
V9	Vacuum seal gaskets (×2)	Copper	for V1 and V5
V10	RF finger	Cu-Be alloy 25	Placed inside V4 before installation, see Fig. 4.6

Table 4.4: Summary of the parts and materials of the BPS monitor vacuum chamber assembly, corresponding to the monitor main part labeled previously as M1 and depicted in Fig. 4.8.

ultra-high vacuum seal. On the other hand, the upstream flange (V5) is a smaller rotating and split flange with special screw holes placement, having the same inner diameter and vacuum sealing type as the downstream flange, but with the knife edge machined in the upstream end tube and the copper gasket at 24 mm instead. This kind of flange is chosen to ease the installation of the monitor, with two flange halves to close the monitor once it is settled down on its alignment support, which can also be rotated to face the screw holes of the fixed flange in the beam pipe side.

Ceramic gap tube

The ceramic tube (V2) has a key role in the BPS functionality that is to insert an insulating gap in the vacuum chamber for bridging the wall image current through the four strip electrodes (M2) surrounding this gap, being also transparent to the beam induced electromagnetic fields, while keeping high vacuum conditions.

A high purity Alumina ceramics (Aluminium Oxide, Al_2O_3, purity of 99.7%) is used for the gap tube which after vitrification feature the same crystal structure as sapphire and ruby. This is a widely used and cost effective oxide ceramic material for many in-

dustrial and accelerators applications because it exhibits desirable characteristics of high electrical insulation and mechanical strength, as well as high wear and chemical resistance [42]. Then the both ends of the ceramic tube are connected to metal collars made of a Kovar (Iron-Nickel-Cobalt alloy, Fe54% Ni29% Co17%) by brazing technique, usually preferred for ceramic to metal joints in high vacuum applications, where their overlapped surfaces, with a filler metal (AgCu alloy) in between, are sealed by melting it in a furnace at high temperatures around 1000°Cand below the Kovar melting point of 1450°C. For the Alumina-Kovar brazing process, the chosen high purity Alumina is best recommended, besides the other mentioned properties; Kovar is also a suitable metal to braze the ceramic because of their similar coefficients of thermal expansion. The last is required to keep the integrity of a good high vacuum sealing thanks to a matched thermal expansion of both materials during temperature cycles that undergo, not only in the brazing process, but also when baking the vacuum chamber at high temperatures, often needed to reach pressures in the UHV range [44, 45].

Additionally, the inner surface of the ceramic gap is coated with a thin layer of Titanium Nitride (TiN) which is deposited using the cathode sputtering technique performed at CERN. Although this ceramic coating is also useful to improve the ceramics vacuum performance and to suppress secondary electron emission, its main purpose considered for the monitor design is to reduce and limit the beam coupling impedance at high frequencies. This is done, basically, because this thin conducting layer enables a lower impedance path for the high frequency components of wall image current as an alternative to the strip electrodes path. This will be treated further on, since the Ti-coated ceramic gap is a fundamental part for the functionality of the monitor jointly with the strip electrodes and other parts actively involved in its EM behavior.

Bellow and RF finger

In order to relieve mechanical stress or to absorb vibrations transmitted by the line that might damage some fragile components of the device, like the ceramics tube (V2) or the ferrite cylinder (M4), the bellow (V4) is a necessary element permitting typical deformations with axial and transversal strokes within ± 1 mm. On the other hand, the bellow must be electrically shielded to prevent major disturbances in the beam that often may be produced by some non-gradual and sharp variations along vacuum pipe cross section, like are the ripples of the bellow. An effective shielding can be done by the RF finger (V10), which is shown in Fig. 4.6, by offering a smooth surface to the wall image current path and the induced EM fields. The RF fingers are made of a Cu-Be alloy, and just before installation, all of them are placed inside the bellows of every monitor by pushing up the tabs at both finger ends, but being able to slide off the vacuum pipe so as not to restrict the bellow function.

Finally, as one of the most critical steps of the BPS construction all the pieces must be perfectly welded, with the techniques mentioned above, to ensure the UHV level required for the CTF3 and TBL vacuum sector, with a residual gas pressures of the order of 10^{-10} mbar and leakage levels of 10^{-10} mbar l/s [6]. After their construction the vacuum chamber of all the delivered BPS units were exposed to CERN standard cleaning procedures, CERN/PS.TR01, and passed the vacuum tests according to technical reference, CERN/PS.TR05, giving the leakage levels specifications.

4.4.2 Non-vacuum outer assembly

Strip electrodes and transformers PCB assembly

Fig. 4.9 shows a detailed design view of the strip electrodes channels assembly which, surrounding the vacuum chamber over the ceramic gap, is directly involved in the wall current sensing to measure the beam position.

The monitor strip electrodes (M2) are formed basically by a cylinder split off into four longitudinal strips and joined by a base plate which are machined in one piece to achieve good mechanical precision as well as, to avoid resistive surface contacts with poor conductivity, both issues affecting in last term the beam position measurement.

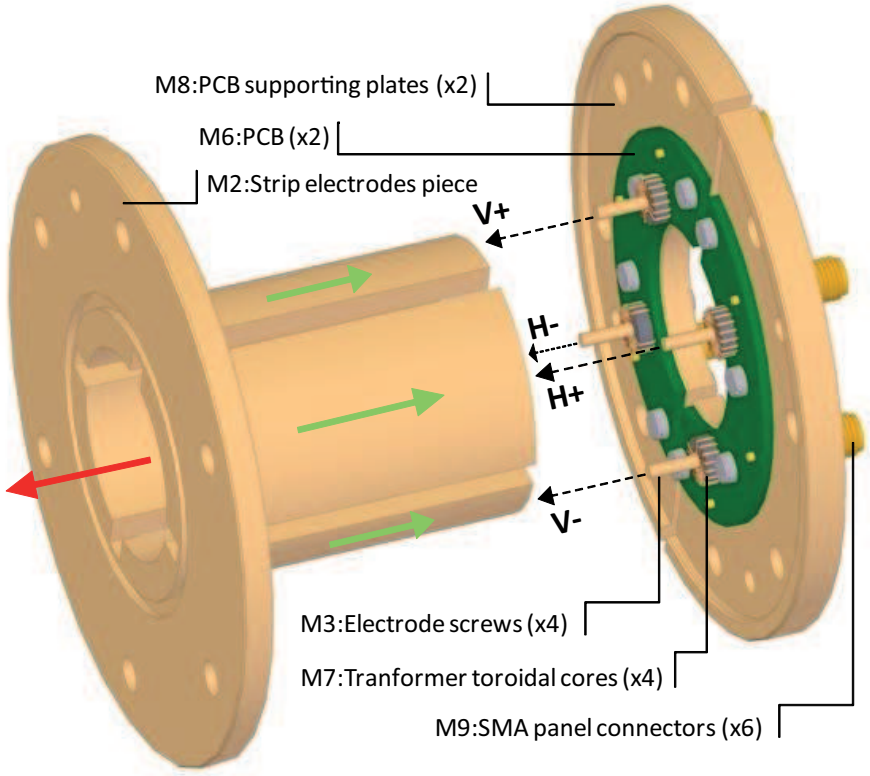

Figure 4.9: Detailed view of the strip electrodes channels and transformers PCB assembly where dashed arrows points the screwing direction of end electrode screws into the four strip electrodes (part labels are from Tab. 4.2). The wall current (green arrows) flow in the opposite direction of beam (red arrow), and the electrode channels ($H_{\pm}, V_{\pm}$) are labeled according to TBL line specifications.

These strip electrodes are extended by four thin screws (M3) in order to pass through the center of the four small toroidal transformers (M7) which are the key components of the PCB's sensing circuit (M6) and are mounted on top of them. The screws allow a tight connection of each strip electrode to the PCB's supporting plates (M8), with tips screwed on the electrodes and heads resting on the supporting plates receptacles. Then the wall current, flowing in the beam opposite direction, follows the path set by the strip electrodes, bypassing the ceramic gap, where it is split into four current branches running in parallel. These current components will converge again into the plates after being

channeled through the transformers by the connection screws. Altogether the strip electrodes, the connection screws and the PCB's supporting plates behave as the one-turn loop primary circuit for each transformer channel, with their secondary circuits implemented on the PCBs. Furthermore, both ends of this electrodes assembly are in contact with the monitor vacuum chamber in order to give electrical continuity to the beam pipe carrying the wall current. Thus to ensure good RF surface contacts for the beam high frequency components, two spring gaskets (M14) are inserted in their respective slots (see Fig. 4.7a), one between the downstream flange and the electrodes base plate, and the other between vacuum connection collar and the inner sides of the PCB plates.

Due to monitor assembly needs, the transformer's sensing circuit is divided in two equal and circular PCB halves which are fastened by screws to their respective supporting plates halves. The on-board PCBs are hence responsible for an inductive current-to-voltage conversion, from the electrodes current signals to the voltage signals at the monitor output ports. The beam position is obtained through the four output signal ports of the BPS monitor with signal amplitude depending on the beam proximity to their corresponding strip electrodes channels, which are labeled as $(V_{\pm}, H_{\pm})$ for the vertical and horizontal coordinate planes respectively, as it is shown in Fig. 4.9, and in the BPS monitor top view (Fig. 4.2b) showing its four output ports, including the $Cal_{\pm}$ input ports going into the PCB circuits that are used for signal calibration. The electrodes channels labeling is done according to the orientation convention given in the TBL line for an electron beam for which the beam position coordinate sign +/- is assigned respectively to the Up/Down and Right/Left electrodes.

All of the device ports (M9) are implemented with SMA coaxial connectors of flange mount type placed over the PCB plates. Since the six connectors are at the other side of the PCBs, a SMA type of straight connectors with an extended center conductor and dielectric jacket are used [40], in order to go through the holes in the plates and being soldered on the PCB's top circuits. The connectors coaxial shields are also connected to the plates that hence will act as a ground or potential reference plane for the BPS signals.

The strip electrodes piece and the PCB's supporting plates are made out of Oxygen-Free Electronic grade copper, or Cu-OFE, as a pure copper with only a maximum of 0.0005 % oxygen content that achieves a high electrical conductivity of 101.0 % IACS (International Annealed Copper Standard), as usually expressed in reference to 100 % IACS conductivity of 5.8001×10^7 S/m at 20°C. The Cu-OFE grade copper provides a low resistivity rating needed to keep the overall resistance of these parts as low as possible.

For the connection screws, as part of the electrodes primary channels, it was used a Cu-Be alloy 25 (Copper Beryllium CDA-17200 alloy). These screws has a typical resistivity of 10 $\mu\Omega/cm$ (conductivity $\sim$ 17 % IACS), higher than the Cu-OFE parts but still keeping low enough resistance due to their short length. In turn the screws made of Be-Cu offer well suited properties for their function like: better strength and elastic properties commonly required for electric contacts, high thermal conductivity favouring heat dissipation and current carrying capacity. The last is a well suited material property taking into account the high current level ($\sim$ 7 A) coming from the strip electrodes and concentrated in the screws smaller cross section.

The overall resistance of each electrode primary channel assembly is kept typically below 1 $m\Omega$, what is important to offer a low resistance path to the wall current, as required to have a good response at low frequencies for square pulse transmission in the monitor.

In addition, the strip electrodes piece, the connection screws and the PCB supporting plates, as the set of parts composing the BPS transformers primary channels, are gold-plated as can be seen in Fig. 4.6. This is done for preventing corrosion and oxidation of these parts that may degrade conductivity performance. The deposited gold layer is around 0.5–1 μm and it has a the next good conductivity of 70.7 % IACS from copper. At frequencies below 100 MHz in the operation bandwidth, the lower conductivity of the thin gold layer will not affect the overall resistance of the primary channels assembly since the current conduction is mainly done by the Cu-OFE. But at higher frequencies above the operation bandwidth, the skin effect produces a current concentration near the conductor surface which decreases inward exponentially, so at the 63 % fall of the current intensity is defined the *skin depth* which can be calculated from

$$\delta = \sqrt{\frac{2\rho}{\mu\omega}}, \tag{4.1}$$

where the material resistivity is given by ρ as the inverse of conductivity $\sigma = 1/\rho$, and depending also on the signal frequency is $\omega = 2\pi f$ and μ the magnetic permeability of the material. For gold being a diamagnetic metal is essentially equal to the magnetic permeability of vacuum μ_0.

According to Eq. (4.1), the skin depth for gold goes below 1 μm for frequencies beyond 6 GHz, so only then the current conduction will be mainly concentrated in the thin gold layer. As a result, the gold plating will produce a resistivity increase of at much 30 % in the Cu-OFE parts, and compensated a bit by a 10 % resistivity decrease in the the Cu-Be screws. Although still leaving an overall resistance of the electrodes primary channels below 1 $m\Omega$, even at these high frequencies far above the operation bandwidth.

As can be seen in Fig. 4.7b the four strip electrodes are separated only by 4 mm with a coverage angle $\phi = 75.17°$ having then the most beam pipe circumference 84% covered by the electrodes. This is convenient to have a higher level of beam current measurement, while keeping the electrodes spacing for better sensitivity to the beam position, because from Eq. (3.19) on page 40, the ratio of the beam current collected by the sum of the wall current in the electrodes is proportional to the percentage of circumference covering. Although, it must be noted that a measurement of the beam current with enough precision is always done after performing a current calibration available in the BPS monitor through its $Cal_{\pm}$ circuits.

External body and ferrite cylinder

Fig. 4.7 shows the BPS longitudinal section where can be seen the next outer layers of the device: the magnetic core cylinder (M4) surrounding the four strip electrodes which is made of a Ni-Zn ferrite (C2050 of Ceramic Magnetics) and having a high permeability of $\mu_r \geq 100$ (at 25°and increasing approx. linearly with temperature); and the external cylindrical body (M5) also made out of Cu-OFE for best conductivity performance, enclosing the center assembly of the device. A big magnetic loop for the wall current is then formed by the external body jointly with the electrodes primary channels closing a cylindrical loop at both ends and with the ferrite load filling the space between them.

Then, these parts have mainly a three-fold purpose. First, and being the main design objective, is that this magnetic loop introduces a big inductance in the electrodes wall

current path in order to extend the device operation bandwidth toward DC and hence to improve the monitor response to the square pulse signal induced by the beam.

Second is to provide a good shielding to the inner sensitive parts of the device against the influence of external stray fields. Generally, they could come from a high EM radiation environment, and more particularly, from near magnets where slow varying magnetic fields are canceled out due to the closed geometry of the ferrite loop. Nevertheless, it must be considered the presence of strong magnetic fields that could lead to saturation of the ferrite due to its high permeability, reducing its effectiveness [23, 30]. According to ferrite specifications [38], before going into saturation it can stand a magnetic flux density of $B_{sat} = 370$ mT.

Finally, using a high-μ ferrite helps to damp resonances at not so high frequencies that occur easily in an otherwise empty metallic body [25, 31].

It must be noted that these design features and derived effects are common to the WCMs and the different IPU types, but having different geometries and arrangements for the the metallic body and the filling ferrite depending on the device specifications.

Other mechanical design issues

Finally, here are mentioned the rest of BPS monitor elements playing a relevant role in the mechanical stability of the assembly.

Four alignment pins (M13) are uniformly distributed over the top of the assembly, passing through the PCB's plates and inserted into the external body, with one extra pin to fix the electrodes base plate also to the external body. This is to guarantee a correct alignment of these assembled parts, and thus avoiding large linearity errors in the beam position measures, or changes in the monitor working parameters once it has been set by the characterization tests. The ferrite cylinder is also aligned with the rest of the assembly by four additional alignment pins (M12) inserted in the inner side of the external body. In order to prevent fractures of the fragile ferrite due to clearances in its placement, it is well fixed by a screw that compresses a spring (M11) at one side of the ferrite surface.

The BPS monitor set is closed by a pair of Aluminium split plates (M10) which are clamped to the PCB's plates and fitted to the connection collar of the vacuum chamber. They have slotted holes for the six SMA connectors and round holes for the top alignment pins as well as for the electrodes connection screws which are placed after completion of the monitor assembly.

4.5 Outline of the BPS monitor function: the wall image current paths

The monitor excitation produced by the coupling to the beam EM fields and all its frequency content is reflected in the wall image current induced on the metallic surfaces around the beam, except for the DC level, as stated in Chap. 3. The detectable or measurable frequency components will rely on the specific dimensions and geometry of the device, like an antenna, being more sensitive to some set of frequencies and determining its frequency response profile. Then a global picture of the BPS monitor performance can be given in terms of the wall image current flowing through the device which is split in different paths depending on its frequency range [25].

According to the beam time structure of the TBL described before, two frequency

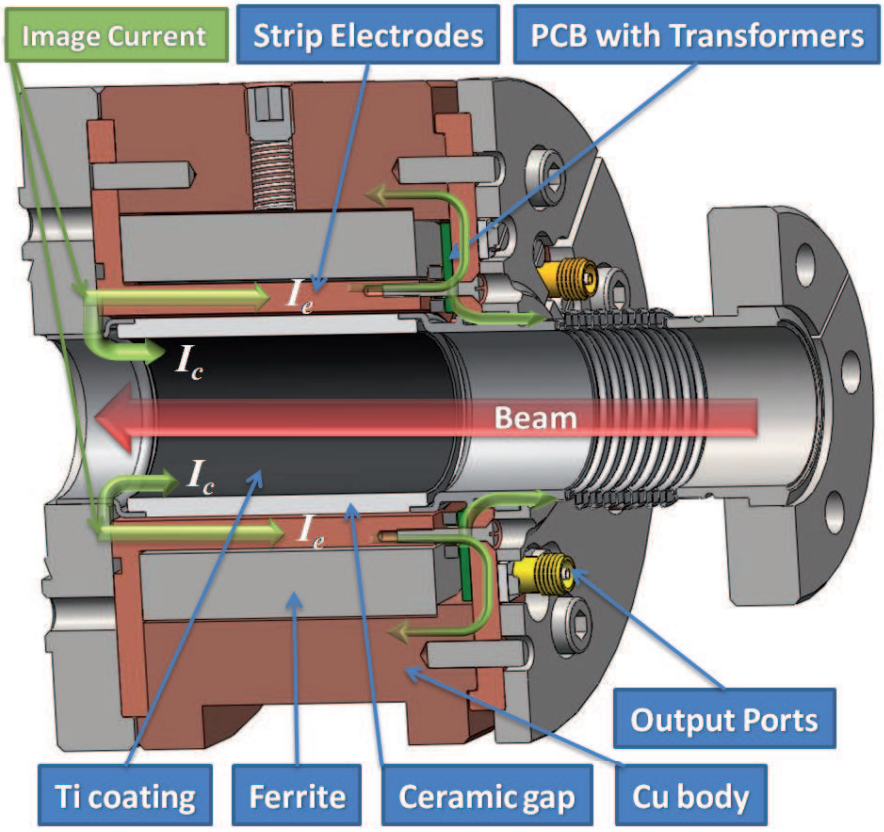

Figure 4.10: View of the BPS monitor longitudinal section showing the two main alternative paths for the wall image current induced by the beam (indicated by the green arrows): I_e, the inductive path (low resistance) by the strip electrodes and the Cu body–ferrite loop, and I_c, the resistive path by the inner Ti coating of the ceramic tube.

regions can be distinguished for a pulse modulated beam. One at low frequencies around the monitor operation bandwidth working in the beam pulse time scale, and the other for the high frequency harmonics generated by the train of micro-bunches composing every beam pulse. Basically, two main competitive paths are established respectively for these low and high frequency components of the wall current.

Taking into account the wall current azimuthal distribution over the cylindrical geometry of the device, these wall current paths are depicted in the BPS longitudinal section of Fig. 4.10 being: I_e, the strip electrodes providing a path that goes through the toroidal transformers and forms a one turn loop with the external body and the ferrite; and I_c going through the ceramic inner coating. The I_e path has the smallest resistance but also having an inductive behavior determined by the intrinsic inductances of the strip electrodes, the bigger inductance is introduced by the ferrite loop, as well as the transformers secondary circuits in the PCBs. The I_c path is fundamentally resistive with negligible inductance and larger resistance of around 10 Ω set by the thin layer of the Ti coating.

In consequence, the the dominant path for the low frequency components of the wall current is the I_e path offering the lowest impedance with their inductive reactances still kept down at these frequencies, as compared to a higher resistive coating path. The wall current behavior through the electrodes path will be then responsible for the function of

the monitor determining its frequency response and operation bandwidth as seen from the device outputs.

Above the bandwidth low cutoff frequency (from ~ 1–10 kHz), the wall current that goes through the strip electrodes primary channels is also circulating by the body-ferrite loop, what inserts a big inductance in parallel to the strip electrodes, done precisely to increase the monitor sensitivity at these low frequencies and to extend its operation bandwidth setting the low cutoff frequency. At mid to high frequencies within the operation bandwidth(up to ~ 100 MHz), the loop reactance increases so that, the wall current stops circulating by the loop with increasing frequency and eventually it is only driven by the strip electrodes passing through the toroidal transformers of the PCBs. At this point, the monitor frequency response is determined basically by the intrinsic inductances of the strip electrodes path as well as the transformers secondary circuits, where the bandwidth high cutoff frequency is set by stray capacitances in the PCBs. This will leave basically a band-pass profile for the monitor frequency response, but only with a centered beam having a different profile for an off-center beam, as it will be discussed further on.

From the perspective of the beam the monitor inserts a longitudinal coupling impedance $Z_{\|}$ that, in principle, is determined by the strip electrodes as passing the wall current over them. At frequencies far above the monitor operation bandwidth, a stronger inductive behavior is exhibited roughly due to the intrinsic inductances set by the strip electrodes length and diameter step. Therefore, if the electrodes inductive path were the only way for the wall current, $Z_{\|}$ would increase linearly with the frequency and it would become too large for the high frequency components of the beam, going beyond the 12 GHz bunching frequency. For that reason, the ceramic Ti-coating enables then a bypass for driving the high frequency components of the wall current offering a lower impedance path, that will not grow up with increasing frequency, because it is mainly resistive. In consequence, the Ti-coating path is intended for setting an upper limit to the monitor $Z_{\|}$ as seen by the beam at these high frequencies.

The transition of the wall current between both paths will be produced at a given frequency region depending on their specific path impedances. Particularly, a compromise has to be taken for the resistance of the Ti-coating path. In principle, a small value would keep down the monitor $Z_{\|}$ at high frequencies what is directly related to the reduction of the beam wakefields generated at each monitor, so minimizing the beam instabilities and improving the beam transport along the line with a small $Z_{\|}/n$ for the n number of monitors. On the other hand, the Ti-coating resistance must be large enough so as not to limit the operation bandwidth at the upper end, as seen from the monitor outputs. This is because a much smaller value would make the wall current to be significantly driven by the Ti-coating at much lower frequencies, and hence being reduced on the strip electrodes what might lower the high cutoff frequency, usually set by the stray capacitances within the transformers PCBs.

The BPS monitor has a quite different behavior, with also different functional goals, for the wall image current induced by the beam EM fields along its broad frequency content. Therefore, its analysis and design will be treated separately within the following two frequency regions:

- **Low Frequencies (LF)**, in the beam pulse time scale determining the BPS operation bandwidth (10 kHz – 100 MHz) for its main function as a BPM with also current intensity measurement. This is discussed first, in the following sections,

from the point of view of the design of the BPS on-board PCBs and the electrical lumped elements model for analyzing the frequency response of the BPS-IPU monitor at low frequencies. Later on in Sec. 5.3, we present the LF test bench design for the characterization tests of the BPS series, jointly with the test results and analysis.

- **High Frequencies (HF)**, in the beam micro-bunch time scale extending from above the BPS operation bandwidth (≥100 MHz) up to the beam bunching frequency and upper harmonics (≥12 GHz). In order to measure at these frequencies the longitudinal coupling impedance $Z_{\|}(\omega)$ of the BPS, and for which a specific HF coaxial test bench was designed and built. This is presented in Sec. 5.4.

4.6 Electronic design of the on-board BPS PCB

The Fig. 4.11 shows the schematic circuit design for the two PCB halves of the BPS prototype. It can be seen that both halves are completely equivalent. We can identify the calibration primary circuit with one winding turn at the left side of the toroidal transformers coming from the calibration inputs, Cal+ and Cal−; and the transformer secondary circuits, with N turns, connected to the BPS outputs at the right side through a resistors divider. The BPS electrodes end screws are not represented since they cross the PCB and the toroidal transformers, as it is depicted in Fig. 4.9, but of course, each electrode acts also as a primary circuit for the wall image current when sensing the beam position.

The calibration circuits have 50 Ω input resistance (two branches of 100 Ω in parallel) at each input port to match the connected cable. They are used to excite the BPS with pulsed calibration signals of known amplitude which will be equivalent to the electrode wall current signals but of 0.1% amplitude level. Then, from the control room, the operators will be able to calibrate and check the performance of the BPS and the amplifier Δ and Σ channels without beam. This is important, since the external amplifier are only one meter away from the beam line and it is exposed to some radiation. The calibration signals, Cal_+ and Cal_-, will excite each half PCB corresponding, respectively, to a pair of outputs, the positive, V_+ and H_+, and the negative ones, V_- and H_-. Hence, when exciting only one calibration input this will be equivalent to a have the beam in a equidistant position from the V_+ and H_+ electrodes. Similarly, when exciting both calibration inputs with identical signals, it will be equivalent to have a centered beam. This situation is also useful to check the common mode rejection ratio (CMRR) of the amplifier Δ channels, because they should get a zero output and only noise will be present.

In order to get the basic BPS output voltage relations in the pass-band, we consider each transformer electrode current, I_{elec}, exciting its respective secondary circuits, shown in the schematics (Fig. 4.11), and inducing a secondary current, $I_{sec} = I_{elec}/N$, using the ideal transformer relation with N turns in Eq. (3.30). From the secondary circuit of the schematics with the resistors R_{S1} and R_{S2}, and taking into account the resistor loads $R_{Load} = 50\ \Omega$ when the outputs are connected, we can obtain the output voltage relation for the BPS

$$V_o = \left(\frac{R_{S1}R_{Load}}{R_{S1}+R_{S2}+R_{Load}}\right) I_{sec} = \left(\frac{R_{S1}R_{Load}}{(R_{S1}+R_{S2}+R_{Load})N}\right) I_{elec} \equiv Z_t I_{elec} \tag{4.2}$$

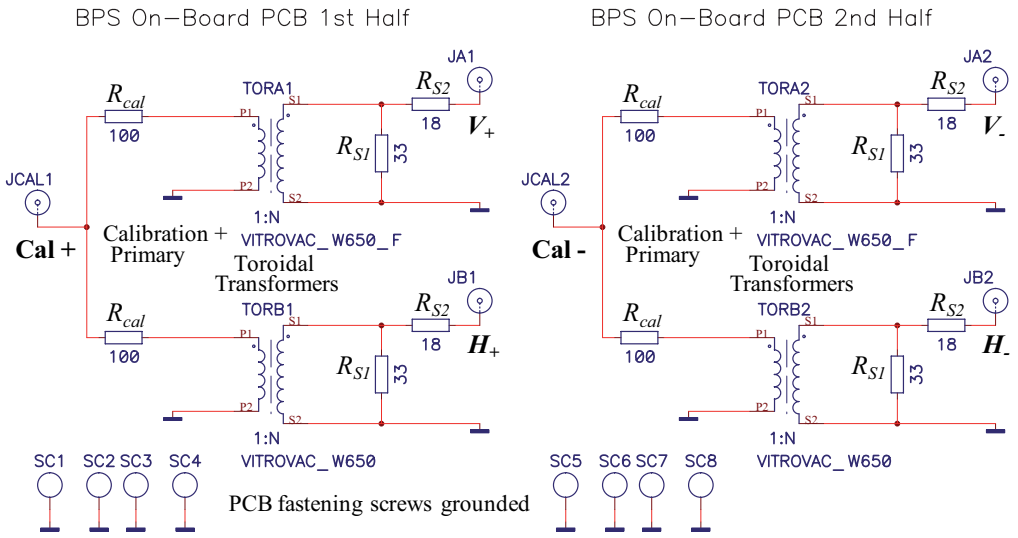

Figure 4.11: Schematic circuit design of the BPS on-board PCB halves.

which is equivalent to previous relation in Eq. (3.36) for a generic IPU, and where the transfer impedance Z_t relate the input electrode current I_{elec} to the output voltage V_o standing for each of the BPS output channels, V_+, H_+, V_- or H_-. In order to match the output resistance to the load, avoiding possible signal reflections at high frequencies, and at the same time to be able to select freely the output voltage level with the resistor value, R_{S1}, the resistor divider of the secondary circuit must fulfill the condition, $R_{S1} + R_{S2} = R_{Load} = 50\ \Omega$. In this case, the general output relation in Eq. (4.2) is simplified, and can be written as

$$V_o = \left(\frac{R_{S1}}{2N}\right) I_{elec}. \tag{4.3}$$

Therefore, the output signals will depend on the varying electrode current, as the beam changes its position, and from the more general output relation in Eq. (4.2) we can also get the sum of the output signals, Σ, as

$$V_\Sigma = \left(\frac{R_{S1} R_{Load}}{(R_{S1} + R_{S2} + R_{Load})N}\right) I_\Sigma, \tag{4.4}$$

where I_Σ is the sum of the four electrode currents. The sum signal is then proportional to the wall image current I_w flowing through the electrodes as it was related by Eq. (3.19). Hence being a measure of the total beam image current magnitude I_{beam} within the pass-band frequencies of the BPS.

As for the particular output relation of Eq. (4.3), the sum voltage signal V_Σ is simplified by matching the output resistor divider to the load, and it is likewise written as

$$V_\Sigma = \left(\frac{R_{S1}}{2N}\right) I_\Sigma. \tag{4.5}$$

In these relations for the PCB design it is assumed that the electrodes are independent with no electrode crosstalk or coupling effects between them, so the transfer impedance Z_t is the same for each electrode channel outputs and their sum. Hence for the selected

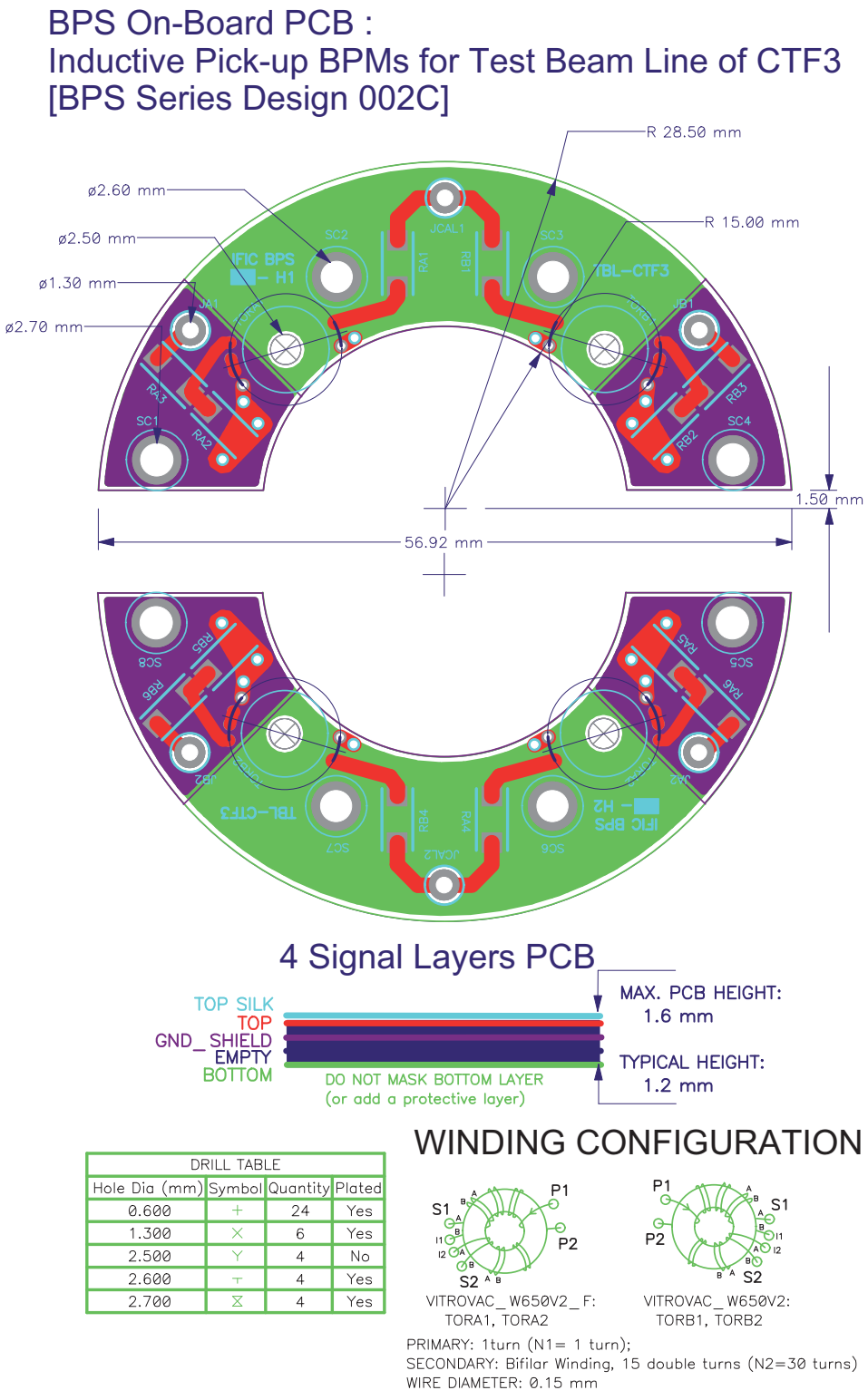

DRILL TABLE			
Hole Dia (mm)	Symbol	Quantity	Plated
0.600	+	24	Yes
1.300	X	6	Yes
2.500	Y	4	No
2.600	T	4	Yes
2.700	⧖	4	Yes

Figure 4.12: Layout of the BPS on-board PCB halves depicting their main dimensions, layers structure with drill table and specifications detail of the two transformers winding configurations (with bifilar type coil).

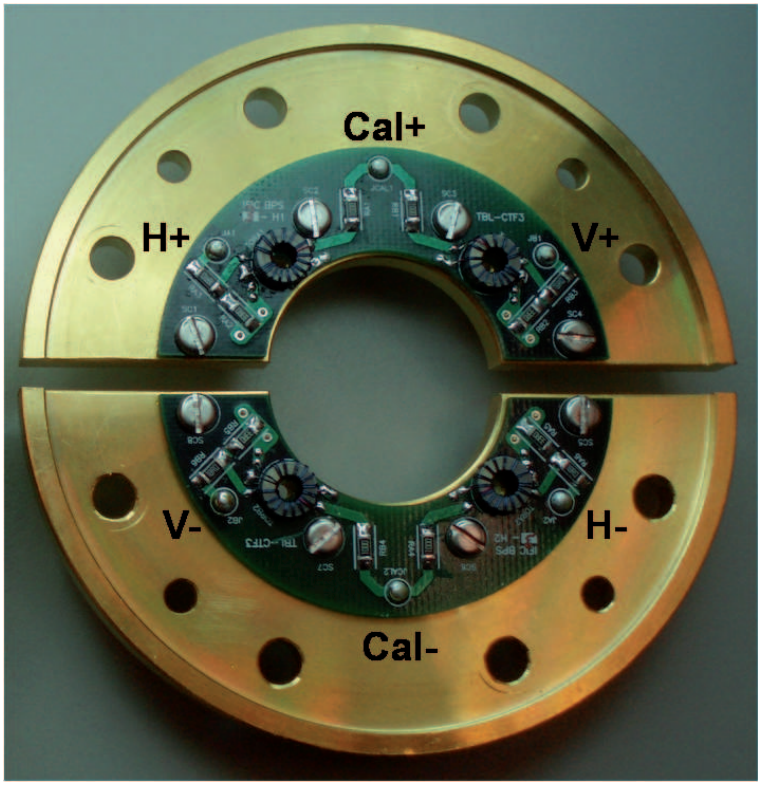

Figure 4.13: Picture of the BPS PCBs mounted on top of gold-plated supporting plates. Each PCB has two toroidal transformers corresponding to two BPS channels. For each transformer a calibration track (at PCB center) ends in a one-turn calibration primary winding (purple wire), and having 30 turns in the secondary winding (blue wire) going to the output channel circuit (at PCB sides).

design values of $N = 30$ secondary winding turns and $R_{S1} = 33\ \Omega$ and from Eqs. (4.2) and (4.4), we get the magnitude of the transfer impedance within the BPS bandwidth

$$|Z_t| \equiv \frac{V_o}{I_{elec}} \equiv \frac{V_\Sigma}{I_\Sigma} = 0.55\Omega \tag{4.6}$$

as a characteristic design parameter representing the output voltage sensitivity to the electrode current variation. In the next Sec. 4.7 is obtained the frequency dependence of the transfer impedance from the analysis of the BPS-IPU general electric model.

Once this parameter is fixed, we can get the maximum output voltage levels for the given nominal beam current for TBL and assuming that is a maximum value for the wall current sum $I_\Sigma \leq I_{beam} = 28$ A.In Tab. 4.5 are summarized these BPS nominal output voltage levels calculated for $I_{beam} = 28$ A corresponding to: the sum signal V_Σ, each of the four BPS electrode signals with a centered beam the electrodes $V_o = V_\Sigma/4$, and the maximum difference signals for the maximum off-center beam displacement for each coordinate plane $\left|V_{\Delta(H,V)}\right|_{max} = V_\Sigma/2$, which can be obtained taking differences in Eq. (4.6). These voltage levels are used as the maximum inputs feeding the external amplifier in order to properly select the gains that match the signals to the ADC input span, as it is described in Sec. 4.8.

Also in Tab. 4.5 are shown the relative increment of the difference signals $\delta V_{\Delta(H,V)}$ per beam position step of 1 mm and 5 μm has been estimated directly from $\left|V_{\Delta(H,V)}\right|_{max}$ over the BPS beam pipe aperture (24 mm dia.). The PCB design values were selected in order to get a high enough $V_{\Delta(H,V)}$ signal variation above 3 mV (typically measurable and far above thermal noise levels) for the smallest wanted beam position step of 5 μm, which would represent the BPS resolution goal.

BPS nominal output voltage levels

Σ signal, V_Σ	15.4 V
Δ signals (at max. displacement), $\left\|V_{\Delta(H,V)}\right\|_{max}$	7.7 V
Electrode signal (at center position), V_o	3.85 V
Δ signal increment per 1 mm position step, $\delta V_{\Delta H}\|_{1\text{mm}}$	642 mV
Δ signal increment per 5 μm position step, $\delta V_{\Delta H}\|_{5\mu\text{m}}$	3.2 mV

Table 4.5: BPS nominal output voltage levels for the sum Σ, difference $\Delta(H,V)$ and electrode signals $H_\pm, V_\pm$. Below, the relative voltage increment of the Δ signals corresponding to a 1 mm and 5 μm beam position steps (resolution goal). The voltage values would correspond to I_{beam}=28 A the maximum nominal beam current.

The layout design of the two PCB halves of the BPS is shown in Fig. 4.12. The PCB tracks were chosen to have at least 30 mils (≈ 0.8 mm) in order to reduce as possible the track resistance for typical flowing currents in the order of 1 A. The PCB layered structure is composed of the components layer or top layer (in red), the bottom layer used as the ground plane (in green), and an intermediate ground plane (in violet) closer to the top layer. This layer is intended to help in keeping the secondary current return paths concentrated below each transformer secondary circuit, and then reduce the ground coupling in the other secondary circuits when, as the worst case, the current is totally balanced to one electrode.

Notice the room left in the PCB layout to place the toroidal transformers, with circular footprint and holes for the screw electrodes that will act as the primary winding for sensing the beam position. It was used the Vitrovac W650 core for the transformers which, according to its specifications [39], has a high relative permeability $\mu_r = 10^5$, getting then a high inductance with few turns. This permeability value could be reduced dramatically if core magnetic flux hits its saturation level, also departing from linear operation. In consequence, it was checked to be far from saturation according to the selected core specifications and for the TBL beam structure. Considering the low value of the average current per electrode (as the one-turn primary of the transformer) of 0.05 mA (0.2 mA for ×4 electrode current) for the maximum ratings of TBL beam, with 28 A peak current, 140 ns pulse length and 50 Hz repetition frequency.

This is important in order to decrease the low cutoff frequency of each transformer as much as possible by increasing their inductance, according to Eq. (3.52). From Eq. (3.29) the relation of a toroid-shaped transformer, and knowing the core specifications, it was obtained the maximum estimated values of the inductance per square turn, and thus the primary and secondary winding inductances with 1 and 30 turns respectively,

$$L/N^2 = 35.35\ \mu\text{H};$$

$$L_1(N = 1) = 35.35\ \mu\text{H};$$
$$L_2(N = 30) = 31.8\ \text{mH}.$$

At the bottom of the PCB layout design in Fig. 4.12 there are also detailed the two orientation arrangements of toroidal transformer windings. The secondary windings of 30 turns are implemented as a bifilar coil with 15 double turns which is better for having a lower inter-winding stray capacitance C_S, and thus a higher cutoff frequency at the transformer outputs. The transformers were made with two different winding orientations for placing one by each side of half PCB, having then the same relative orientation with respect the single turn primary, the screw electrode or the calibration turn. It was selected an inverting winding orientation to yield a negative output pulse polarity for an electron beam pulse flowing downstream, i.e. an electrode positive current pulse flowing upstream through the transformers, in agreement with the electron accelerators convention.

Finally, in Fig. 4.13 it is shown a manufactured on-board PCB halves with mounted components and responsible of the BPS inductive current sensing described before. There were performed the validation test on all the on-board PCBs of the BPS series before installing them into the units in order to check their correct function. As it can be seen in Fig. 4.12, an identification number to ensure traceability of validation test data was assigned and printed to each PCB half ring, which is of the form X-H1 and X-H2 indicating its BPS unit number and corresponding PCB half ring respectively.

4.7 BPS electrical model and frequency response simulations

In Fig. 4.14 is presented the electrical lumped element model of the BPS-IPU for the low frequencies around its operational bandwidth. This new model was developed during the BPS series production and testing in order to reproduce, and to better understand, some cases of the measured frequency response of the device, generalizing the previous IPU model in which the BPS electrical model is based [9].

In the BPS electrical model of Fig. 4.14 can be identified the four strip electrodes modeled by four circuit branches at the primary side of the toroidal transformers with a 1:N turns relation. Their respective secondary sides represent the PCB secondary circuits in which are also mounted the transformers, as it was shown in previous Sec. 4.6.

The beam image current flowing through the four strip electrodes, i.e. the wall current I_w, is then modeled by four independent current sources $I_{elec(1..4)}$ which build up the sum current I_Σ proportional (at zero-order) to I_w, as they were geometrically related by Eqs. (3.16, 3.19).

Each current source feeds its corresponding strip electrode circuit branch going into the transformers, and also the inductance of the single-turn magnetic loop L_Σ in parallel to all of them. This magnetic loop is made up from the strip electrodes and the Cu-body walls enclosing the outer ferrite cylinder as it can be seen in the BPS physical layout of Fig. 4.10.

For each strip electrode in the model there are considered the following lumped circuit elements: the electrode intrinsic inductance L_{elec} and the parasitic resistance R_{elec}, the last mainly due to the assembly connections of the electrodes at both ends. In addition, since the strip electrodes are physically arranged circularly to form the electrodes piece

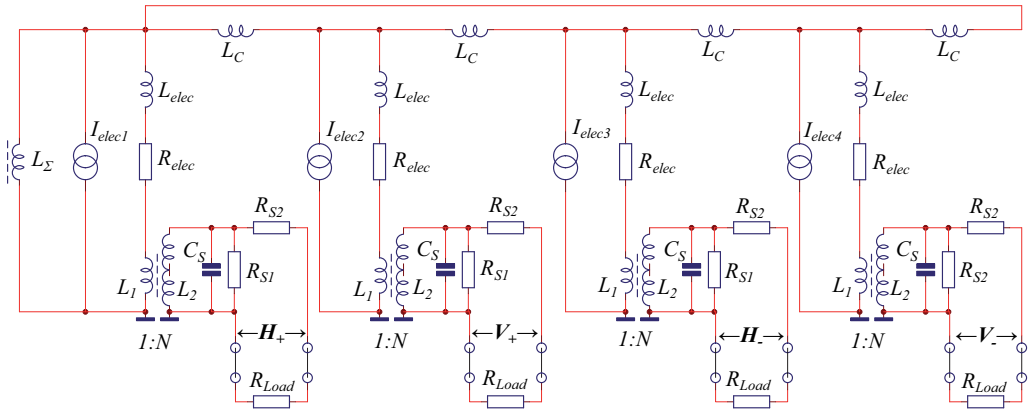

Figure 4.14: Electrical lumped element model of the BPS-IPU for reproducing the frequency response behavior within its operational bandwidth.

cylinder, and connected at both ends, there exists an inductive coupling between the strip electrodes which is modeled by the inductances L_C connected between them in the circuit model. Both electrode inductances L_{elec} and L_C play an important role in the frequency response of the Δ signals particularly determining their low cutoff frequencies for both coordinate planes.

The toroidal transformers and the secondary circuit resistors R_{S1} and R_{S2} of every electrode branch are included in the model as real elements of the PCB circuits (see schematic circuit in Fig. 4.11), as well as the external load resistor R_{Load}. In contrast, the stray capacitances C_S are added to the transformers secondary side as lumped elements and in parallel to the transformer, which are originated mainly between the secondary winding turns and are responsible for setting the high cutoff frequency of the BPS bandwidth.

In Fig. 4.15 is shown the schematic used for the PSPICE simulation of the BPS-IPU frequency response which corresponds to the BPS electrical model of Fig. 4.14 with the specific model components values. Notice that the coupling resistors R_C in the simulation schematic are not considered in the model but just added with negligible values due to PSPICE circuit simulation requirements to avoid pure inductor loop with the current sources. Those coupling resistors R_C could have been also considered for taking into account possible losses though they are expected to be very small.

The wall image current distribution between the four electrode primary branches, which depend on the beam position, is controlled by four independent current sources. Then it is possible to simulate the two main different behaviors of the BPS-IPU frequency response which are: for the centered beam case, the wall current is equally distributed or balanced between the four strip electrodes at equal distance from the beam; for the off-center beam case, the wall current intensity increases in the closest electrodes to the beam and decreases in the distant ones, thus producing a current unbalance between them.

The resulting frequency response simulations corresponding to the center and off-center beam cases are presented respectively in Figs. 4.16 and 4.17. For the center beam case, the wall current is uniformly balanced among the strip electrodes, so the inter-electrodes coupling inductances L_C in the model do not take part because of no net current flow through them. In that case the circuit model can be simplified just by removing

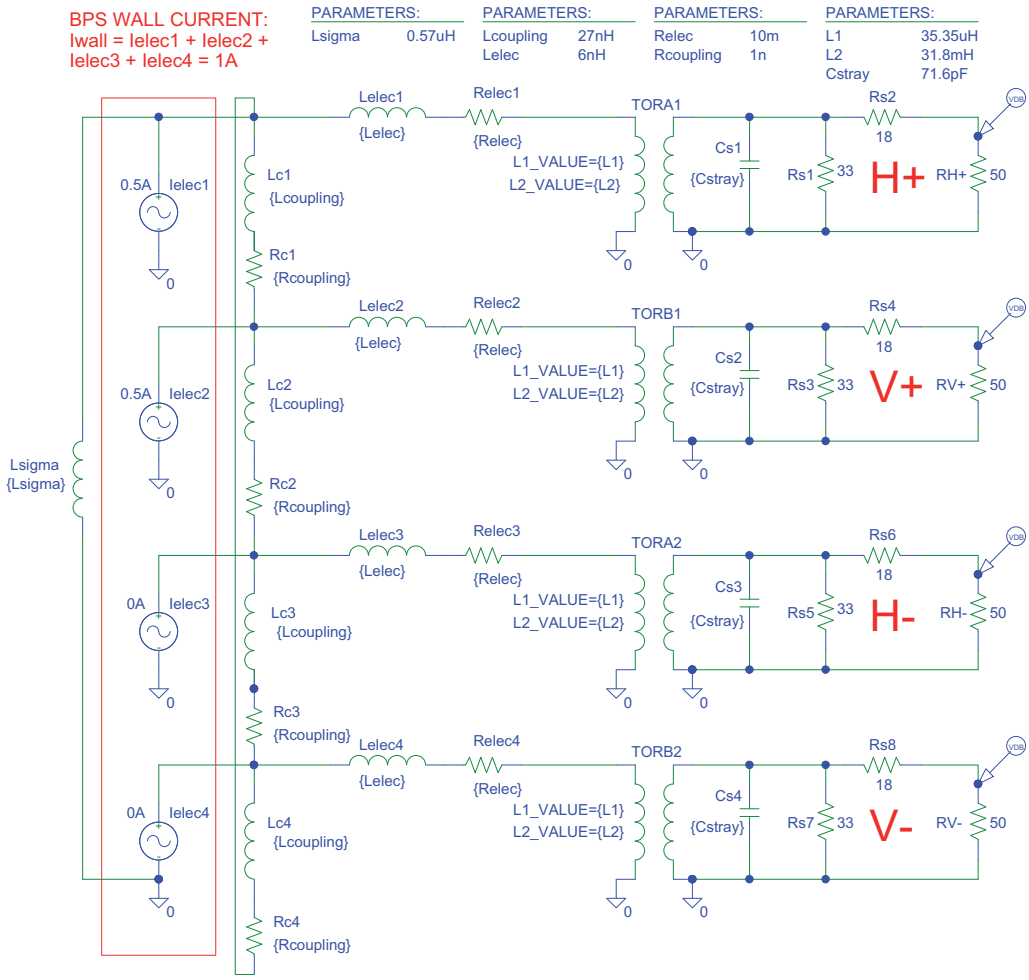

Figure 4.15: Schematic of the BPS lumped circuit model simulated in PSPICE, from which are obtained the BPS-IPU frequency response for the center and off-center beam cases, respectively shown in Figs. 4.16 and 4.17.

them. This is the BPS simplest frequency response case (as it was discussed previously in Sec. 3.5.3) which corresponds to the typical bandpass profile of each electrode signal channel ($H_{\pm}, V_{\pm}$) and their sum signal (Σ), shown in the simulation output frequency response of Fig. 4.16. The low cutoff frequency $f_{low\Sigma}$ is then set by the ferrite single-turn loop inductance L_{Σ} for the electrodes and the Σ signals, where the Δ signals are canceled out in the centered beam case. Concerning the high cutoff frequency it is set by the stray capacitance of the toroidal transformers windings modeled by C_S of each output electrode channel.

In the case of an off-center beam, the current is unbalanced between electrodes, more wall current flowing through the electrodes closer to the beam than through the other ones. Thus, in the circuit model there is reproduced by a net current flow through the inter-electrode coupling inductances L_C. This will modify the typical bandpass profile of the BPS electrode channels for the beam centered case, as shown in Fig. 4.17. The individual electrode responses show how they start to be sensitive to the beam position variation only at higher frequencies from the low cutoff determined by the bigger inductance of the ferrite magnetic loop L_{Σ}, that is for the centered beam case. Hence when making the

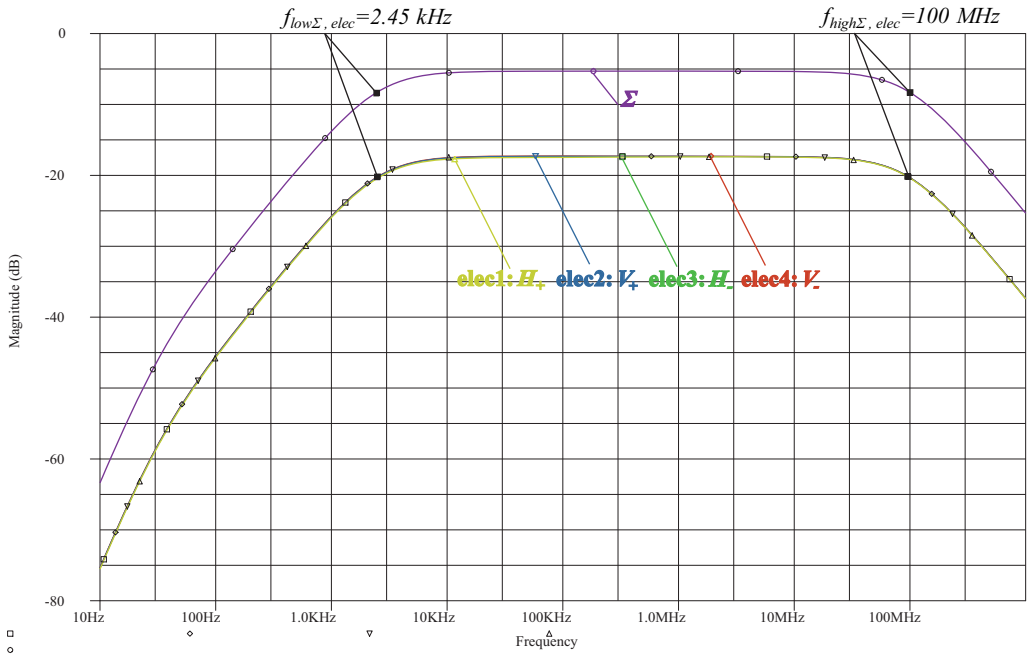

Figure 4.16: Simulation plots of the BPS circuit model frequency response corresponding to a center beam case, where the wall current is evenly distributed between the four strip electrodes and fully balanced among them. [Measurements at Fig. 5.11].

difference of the opposite electrode responses they are canceled out at lower frequencies yielding a higher low cutoff $f_{low\Delta}$ that explains the effect of the low cutoffs increase for the Δ signals.

The BPS electrical model simulations were compared to the measurements performed with the low wire test bench (presented in next Chap. 5). Thus, the circuit elements in the model were tuned in order to reproduce the measured BPS frequency response. The particular values of the lumped elements in the model were obtained after fitting the model frequency response to the measured low cutoff frequencies $f_{low\Sigma}$ and $f_{low\Delta}$, and also to the high cutoff frequency f_{high}, which are shown in Tab. 5.2 and correspond to their average values of all the tested BPS units. In consequence, the PSPICE model of Fig. 4.15 was used to estimate the lumped circuit elements of the BPS-IPU consisting of: the inductances, L_Σ related to the low cutoff of the electrodes and Σ signals, and L_C and L_{elec} related to the low cutoffs of Δ signals; the electrode resistance R_{elec} related to both cutoffs; and finally, the secondary stray capacitance C_S directly related to the high cutoff frequency limiting the monitor operational bandwidth at the upper side.

In Tab. 4.6 are presented the estimated values of the lumped elements as determined by the BPS model simulations for the average of the measured frequency cutoffs (see Tab. 5.2). Beside are included the frequency cutoffs obtained from the relations derived in the equivalent circuit analysis of the model, as described in detail further on. Applying the lumped element values estimated with the PSPICE simulations, the Σ and Δ low cutoffs are calculated respectively from Eqs. (4.22, 4.24), and the common high cutoff from Eq. (4.10), which coincide with the simulated ones.

The simulated BPS frequency response for the center and off-center beam cases repec-

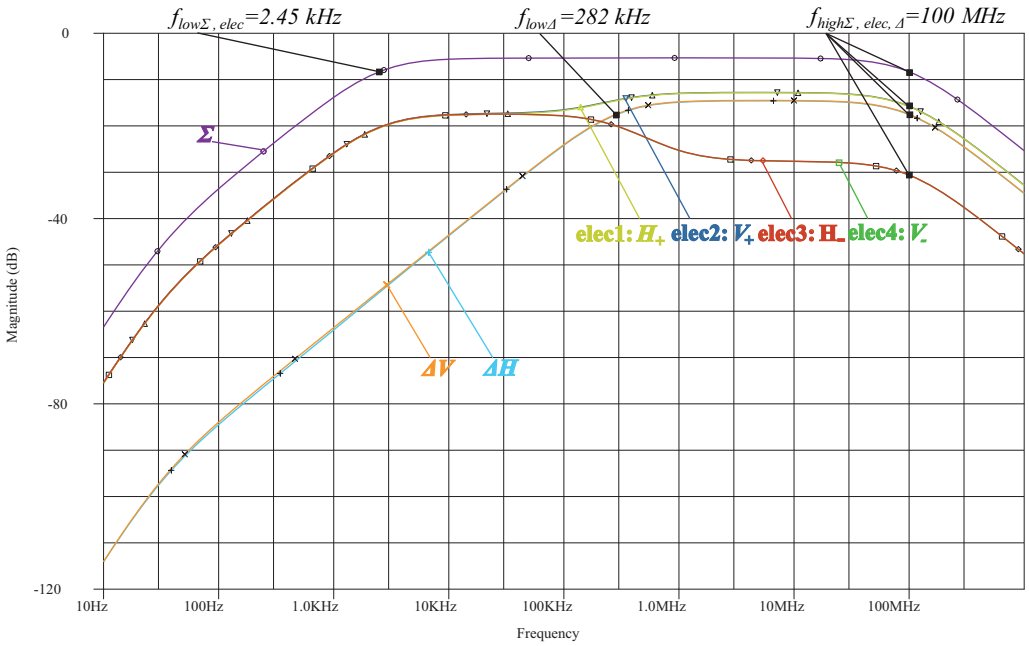

Figure 4.17: Simulation plots of the BPS circuit model frequency response corresponding to an off-center beam case, where the wall current is unevenly distributed between the strip electrodes and unbalanced to the ones closer to the beam, H_+, V_+. [Measurements at: Fig. 5.12 of independent electrodes; Figs. 5.15, 5.17 of Σ, Δ mixed signals].

tively in Figs. 4.16 and 4.17 show a good agreement as compared to their measurement counterparts which can be looked up in Chap. 5 of the characterization test. Respectively for both center and off-center beam cases: in Figs. 5.11, 5.12 the measured frequency response of the independent electrode channels; and, in Figs. 5.15, 5.17 the measured frequency response of the Σ and Δ mixed signals.

As some final considerations to the simulated BPS-IPU model, it must be mentioned that a lower bound to the BPS high cutoff could only be measured, due to limited frequency range of test equipment, subsequently setting an upper bound to the stray capacitance C_S value estimation.

Also remark that, for the obtained simulation results the toroidal transformers in the BPS model are assumed to be lossless and fully coupled transformers with a coupling coefficient $K = 1$ (from Eq. (3.35) of mutual coupling between electrode primary and secondary winding). Though this factor can be changed at anytime which would affect only to the bandpass magnitude level and not the cutoffs which were the main simulation target.

Finally, it must be mentioned that the Σ and Δ low cutoffs will remain constant with the simulated beam position, i.e. the current redistribution among the electrodes, as long as they are fixed by their respective lumped inductances in the model. Therefore, in this circuit model are not reproduced the shifts of the low frequency cutoffs with the beam position that otherwise exist in a real BPS monitor, as they were measured and shown in next chapter.

Lumped elements values of the BPS circuit model		Cutoff freqs.	
Inductance of the ferrite/Cu-body single-turn loop, L_Σ	570 nH	$f_{low\Sigma}$	2.4 kHz
Inter-electrodes coupling inductance, L_Δ	27 nH		
Intrinsic inductance of the strip electrodes, L_{elec}	6 nH	$f_{low\Delta}$	282 kHz
Parasitic resistance of the strip electrodes, R_{elec}	10 mΩ		
Capacitance of the toroidal transformer windings, C_S	$\leq$ 71.6 pF	f_{high}	$\geq$ 100 MHz

Table 4.6: Simulation values of the model lumped elements which determine the cutoff frequencies of the BPS frequency response associated to them.

4.7.1 Analysis of the circuit model and derived formulas

The full circuit model of Fig. 4.14 must be analyzed by parts. First from the transformers secondary side on the PCBs, with the aim of getting the high frequency response of the pass-band profile which is common to all the BPS-IPU output signals, the electrode channels and the Σ and Δ mixed output signals. And after from the transformers primary side in order to analyze BPS-IPU model in the low frequency region which has a more complex and different frequency response for the mixed output signals, as it is for the real BPS device.

High frequency region of the bandwidth

It is recalled here the circuit analysis of one-electrode channel made for a generic IPU at the end of Chap.3 (in Sec. 3.5.3). This previous analysis is now applied to the particular design elements of a BPS device from which the high frequency response of its bandwidth is determined.

From the equivalent circuit of one-electrode channel in Fig. 3.9, the secondary winding is modeled as its inductance L_2 with the secondary equivalent current source as $I_{sec} = I_{elec}/N$, which is the electrode primary current I_{elec} that is ideally transformed to the secondary side dividing by the number of secondary winding turns N. The output voltage of each BPS channel V_o was obtained in Eqs. (3.46, 3.47) either from the equivalent impedance of the secondary side circuits Z_S with the input current being the secondary current I_{sec}, or from the transfer impedance Z_t with the electrode current I_{elec} as the input current and hence containing the transformer N turns ratio, which is rewritten here as

$$V_o(\omega) = Z_S(\omega)\frac{I_{elec}(\omega)}{N} \equiv Z_t(\omega)I_{elec}(\omega). \tag{4.7}$$

Therefore, the secondary equivalent impedance of a generic IPU in Eq. (3.45) is now particularized to the BPS-IPU model elements, which in the frequency domain using the Laplace variable $s \equiv j\omega$ is written as

$$Z_S(s) = \left(\frac{R_{Load}}{R_{S2} + R_{Load}}\right)\frac{sL_2}{1 + sL_2/R_e + (sL_2/R_e)(sR_eC_S)} \tag{4.8}$$

where L_2 is the inductance of the N turns secondary winding, C_S is the stray capacitance mainly present between the windings of the transformer secondary, and R_e stands for the

equivalent resistance of the PCB secondary circuit resistors including the load resistor, which are in parallel with the stray capacitance, being

$$R_e = R_{S1} \parallel (R_{S2} + R_{Load}). \tag{4.9}$$

Notice that the equivalent impedance of the BPS secondary circuits above in Eq. (4.8) is essentially the same as the one of a generic IPU in Eq. (3.45). They only differ in the resistive factor multiplying the same impedance rational form, and that the BPS particular circuit elements, L_{sec}, R_e and C_S has been used.

In consequence, the pass-band frequency profile of the BPS secondary circuits will be the same as for the generic IPU, as well as the low and high cutoff frequencies relations in Eq. (3.52), but now expressed in terms of the BPS secondary circuit elements,

$$\omega_{low} = \frac{R_e}{2\pi L_2} \qquad \omega_{high} = \frac{1}{2\pi R_e C_S}, \tag{4.10}$$

where the angular frequency is related to the measurable frequency by well-known relation $\omega = 2\pi f$.

In principle, these cutoff frequencies will delimit the bandwidth of the BPS output signals, and the transfer impedance $Z_t(\omega)$ will be ideally flat in the pass-band frequency range. The secondary equivalent impedance in Eq. (4.8) can be approximated in the pass-band region by its equivalent resistance as

$$Z_S \approx R_S \equiv \frac{R_{Load} R_e}{R_{S2} + R_{Load}} = \frac{R_{Load} R_{S1}}{R_{S1} + R_{S2} + R_{Load}} = \frac{R_{S1}}{2} \tag{4.11}$$

where first, the equivalent resistance R_e of the PCB output circuit resistors has been replaced by Eq. (4.9) to get the secondary impedance Z_S only in terms of the secondary circuit elements. And after the matching condition of PCB secondary circuits $R_{S1} + R_{S2} = R_{Load} = 50\ \Omega$ has been also applied to Eq. (4.11). Thus, from the simplified Z_S, the transfer impedance in the pass-band frequency region is obtained just as

$$Z_t \equiv \frac{Z_S}{N} \approx \frac{R_{S1}}{2N}. \tag{4.12}$$

From this frequency domain analysis, the last expressions recover the ones used in the design of the BPS PCBs, in the previous section, which correspond respectively to the BPS output voltage relations in Eqs. (4.2, 4.3).

In addition, as it was discussed in Chap. 3, the design values of the secondary circuit in the PCB must be chosen in order to avoid a resonant behavior. Hence, the non-resonance condition of Eq. (3.59), which is expressed below in terms of the BPS PCB circuit elements and using the cutoff frequencies in Eqs. (4.10), shall be fulfilled

$$\omega_{high} > 2\omega_{low} \quad \Leftrightarrow \quad {R_e}^2 < \frac{L_2}{2C_S}. \tag{4.13}$$

Based on this, the design values for the secondary circuit elements were determined in order to have a broad bandwidth, with a relatively high secondary inductance L_2 and a low equivalent resistance R_e, favouring the non-resonance condition though the stray capacitance C_S was not known a priori. In specific elements values we have: $L_2 = 31.8$ mH

as it was calculated in the previous section for the secondary coil of toroidal transformers with $N = 30$ turns, and $R_e = 22.2\ \Omega$ from Eq. (4.9) with $R_{S1} = 33\ \Omega$, $R_{S2} = 18\ \Omega$ and $R_{Load} = 50\ \Omega$. Then, applying them to Eq. (4.13) is set an upper limit to the stray capacitance of $C_S < 32.2\ \mu$F in order to meet the non-resonance condition, what is far above the typical values for inter-windings stray capacitances. The last was confirmed when the BPS high frequency cutoff was determined to be above 100 MHz, as it is presented in the next chapter of BPS test results. Since the non-resonance condition is fulfilled by far getting a much lower stray capacitance limit of $C_S < 72$ pF, as obtained from Eq. (4.10) for high frequency cutoffs being $f_{high} > 100$ MHz.

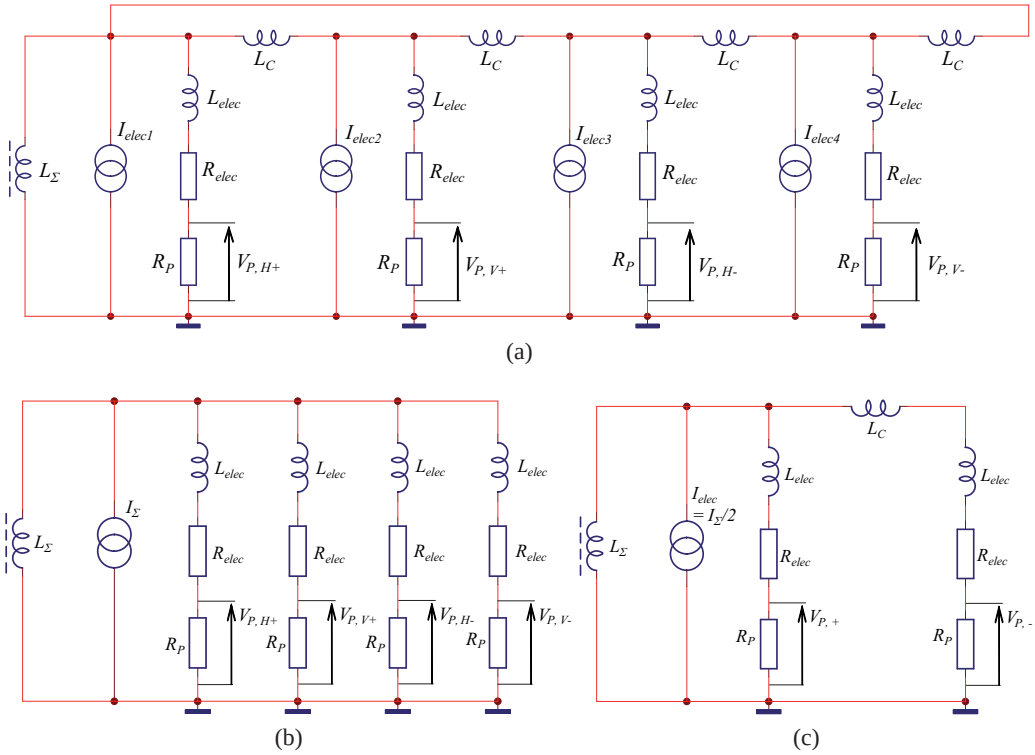

Figure 4.18: Equivalent circuits of BPS-IPU electrical lumped element model used for circuit analysis in the lower bandwidth frequencies. (a) Full equivalent circuit model with transformer secondary circuits moved to primary sides and approximated by equivalent resistance R_P where the BPS output voltages are $V_o = NV_P$. (b), (c) Simplified equivalent circuits to obtain the transfer impedances and low cutoffs of the mixed BPS-IPU outputs signals Σ and Δ.

Low frequency region of the bandwidth

The analysis of the BPS-IPU model at the low bandwidth frequencies is done now from the primary transformers side for which is used the equivalent circuit of Fig. 4.18a. Basically, each of the secondary circuits in the model has been approximated by an equivalent resistor R_P sent into their respective primary electrodes side. This is an important approximation in the model, which is justified below, and that will allow to get the final transfer impedances reproducing the lower frequency response and cutoffs of all the BPS signals.

In this equivalent model moved to the primary side, the four BPS output voltages V_o are simply obtained from V_P as the voltage seen between the transformer primary terminals, as

$$V_o(\omega) = NV_P(\omega). \tag{4.14}$$

which are related by the N turns ratio through the ideal transformer voltage relation in Eq. (3.31).

In a general way, the secondary circuits frequency dependence is included into the electrodes primary side by transforming back the secondary equivalent impedance Z_S of Eq. (4.8), as seen from the transformer secondary terminals, into the primary equivalent impedance Z_P in series with the strip electrode branch of the circuit model. The impedances transformation is performed by

$$Z_P(\omega) = \frac{Z_S(\omega)}{N^2} \tag{4.15}$$

which is derived considering the toroidal transformer again as an ideal transformer that transmits all the power from the primary to the secondary side, $P_1 = P_2$, and applying the ideal transformer relations for the currents and voltages in Eqs. (3.30, 3.31).

The secondary equivalent impedance Z_S of Eq. (4.8) is written in the more appropriate form of resistive and reactive parts, being analog to Eq. (3.54) as it was derived for a generic IPU in Sec. 3.5.3,

$$Z_S(\omega) = \frac{R_S}{1 + F^2(\omega)} \left(1 + iF(\omega)\right) \tag{4.16}$$

where R_S is the secondary equivalent resistance according to Eq. (4.11), and $F(\omega)$ is the factor containing all the frequency dependence of Z_S explicitly written as

$$F(\omega) \equiv \left(1 - \frac{\omega^2}{\omega_{low}\, \omega_{high}}\right) \frac{\omega_{low}}{\omega} \tag{4.17}$$

with the low and high cutoff frequencies specified in function of circuit model elements in Eq. (4.10).

Thereby, the primary equivalent impedance Z_P is obtained in the form of resistive R_P and reactive parts X_P, simply by substituting the last form of Z_S into the impedances transformation of Eq. (4.15),

$$Z_P(\omega) \equiv R_P(\omega) + iX_P(\omega) = \frac{R_S}{(1 + F^2(\omega))N^2} + i\left(\frac{R_S F(\omega)}{(1 + F^2(\omega))N^2}\right). \tag{4.18}$$

The last is a general expression which captures all the frequency dependence through factor $F(\omega)$, but for the analysis at the low frequency region of the bandwidth it can be approximated just to the resistive part R_P being the only term contributing significantly to the primary equivalent impedance Z_P at that low frequencies. This is because the low frequency cutoff ω_{low} in Eq. (4.10) is in principle set very low by the secondary transformer inductance L_2, but the low cutoffs that dominate and limit the bandwidth are instead much higher as set inversely by the lower inductances L_Σ and L_Δ of the electrodes primary side, which are derived below. Thus, at that frequencies around the dominating

low cutoffs, the secondary circuits frequency dependence can be neglected since they are still in their pass-band region with $F(\omega) \approx 0$, as it was discussed in Sec. 3.5.3.

In consequence, for the low frequency analysis based on the equivalent circuit of the full BPS model in Fig. 4.18a, only the resistive term of the primary impedance in Eq. (4.18) is considered, where its frequency dependence factor is also canceled, yielding

$$R_P = \frac{R_S}{N^2} = \frac{R_{S1}}{2N^2} \tag{4.19}$$

where it is used the simplified secondary equivalent resistance R_S of Eq. (4.11). From the PCB design values of the secondary output circuit with $N = 30$ turns for the transformer and the shunt resistor $R_{S1} = 33\ \Omega$, the primary equivalent resistance is set to $R_P = 24.7\ \text{m}\Omega$.

The BPS-IPU frequency response at low frequencies has different behaviors for the two main cases of a center and off-center beam, as it was shown in the simulations before and now after the low frequency analysis based on the equivalent circuit models of Fig. 4.18.

For the center beam case, only the individual electrode and the Σ signal are considered since for the Δ signals the response is canceled out. In that case the equivalent circuit model of Fig. 4.18a can be simplified to get the one in Fig. 4.18b where the coupling inductances L_C can be neglected because there is no net flow between the electrode primary branches and hence not having any effect on the frequency response.

In the case of an off-center beam the equivalent circuit model can be reduced to the one in Fig. 4.18c by applying the same concept of net current flow among the electrode primary branches. This is that only between the opposite electrodes would exist a net current flow across the coupling inductance and for the extreme situation of fully unbalanced wall current to the positive electrodes, which is the simulated off-center beam case.

The BPS transfer impedances are thus obtained for the Σ and Δ signals respectively from the circuit analysis of the equivalent circuits in Figs. 4.18b, 4.18c. As being defined by the ratio of the BPS mixed output signals V_Σ and V_Δ (meaning for each one of the horizontal and vertical coordinate planes) over the total wall current of the electrodes I_Σ. Then, both transfer impedances can be written in the same functional form, again in the Laplace domain with $s \equiv j\omega$, as

$$Z_{\Sigma,\Delta}(s) \equiv \frac{V_{\Sigma,\Delta}}{I_\Sigma} = G_{\Sigma,\Delta}\left(\frac{s}{s + \omega_{low\Sigma,\Delta}}\right) \tag{4.20}$$

what means that for both signals the BPS behave as a common high-pass frequency response profile at low frequencies with one pole determining the corresponding low cutoff frequencies $\omega_{low\Sigma,\Delta}$, and the pass-band gains $G_{\Sigma,\Delta}$, which are explicitly written below

$$G_\Sigma = N\frac{4R_P L_\Sigma}{4L_\Sigma + L_{elec}} \approx NR_P \qquad (L_{elec} << 4L_\Sigma) \tag{4.21}$$

$$\omega_{low\Sigma} = \frac{R_P + R_{elec}}{4L_\Sigma + L_{elec}} \approx \frac{R_P + R_{elec}}{4L_\Sigma} \qquad (L_{elec} << 4L_\Sigma) \tag{4.22}$$

$$G_\Delta = N\frac{R_P L_C}{L_C/2 + L_{elec}} \tag{4.23}$$

$$\omega_{low\Delta} = \frac{R_P + R_{elec}}{L_C/2 + L_{elec}}. \tag{4.24}$$

In the model equivalent circuits, the sum and difference signals are determined through the transformer primary voltages V_P of each independent electrode which are proportional to the BPS output signals V_o by the number of transformer turns N according to Eq. (4.14). Hence, with N appearing as a multiplicative factor in the gain relations of Eqs. (4.21, 4.23).

Concerning the low cutoff relations in Eqs. (4.22, 4.24) is observed that both depend on the series of the primary equivalent resistance R_P and the electrode parasitic resistance R_{elec}. Particularly for the Σ signal, the gain can be approximated just to R_P and the inductance determining the low cutoff being only L_Σ, provided that this inductance of the magnetic ferrite loop with the BPS electrodes and the Cu-body, is much bigger than the intrinsic electrode inductance L_{elec}. While for the Δ signal L_{elec} is in the order of the electrodes coupling inductance L_C, and both are combined to determine its corresponding gain and low cutoff.

Pulse time constants

Finally, turning to the time domain, as it was discussed at the end of Sec. 3.5.3, the transmitted pulse will suffer from a exponential droop from the flat top level due to the defined low cutoff frequencies for the Σ and Δ signals, and also it will have a rise or setup time constant caused by the high cutoff frequency (common to all signals). Then, summarizing for the characteristic cutoff frequencies obtained before, and using the relations in Eq. (3.61), we define

$$\tau_{droop_\Sigma} = \frac{1}{\omega_{L_\Sigma}}, \tag{4.25}$$

as the characteristic droop time from the low cutoff frequency, $\omega_{L_\Sigma} = 2\pi f_{L_\Sigma}$, for the Σ signal, and also for the output electrodes with a centered beam;

$$\tau_{droop_\Delta} = \frac{1}{\omega_{L_\Delta}}, \tag{4.26}$$

as the characteristic droop time from the low cutoff frequency, $\omega_{L_\Delta} = 2\pi f_{L_\Delta}$, for the Δ signals, and also for the output electrodes when the beam is out of the center; and, finally,

$$\tau_{rise} = \frac{1}{\omega_{high}}, \tag{4.27}$$

as the characteristic rise time from the high cutoff frequency, $\omega_{high} = 2\pi f_{high}$, for the output electrodes, the Δ and Σ signals.

All the defined low and high cutoff frequencies, and its associated characteristic time constants, can be measured for a beam (or current wire) input excitation, and also for the calibration input excitation, as it will be shown in Chap. 5 of the characterization test results. In both cases, the output signals are generated through the transformer secondary circuits but induced from different primary circuits: the electrodes for beam (or current wire) excitation; and, the calibration turn for the calibration inputs excitation (see Fig. 4.11).

4.8 The BPS readout chain

Here is given an overview of the two main readout stages for the operation of every BPS monitor in the TBL line, following essentially the same configuration as the other BPMs in CTF3 [46]. The scheme of the specific implementation for the BPS with its main involved elements, signals flow and connections are shown in Fig. 4.19.

The *Analog Front End (AFE)* stage is a tandem composed by, the BPS sensing PCBs doing the very first electrode signals conditioning, and after, directly connected to the BPS monitor, the external or AFE amplifier. As the first element of the readout chain directly interfacing the BPS, it is installed very close to the BPS monitor, around 1 m apart below in the beam line girder, trying to have less noise influence. The amplifier is basically responsible of the first processing of the four BPS output voltage signals ($V_{H\pm}, V_{V\pm}$), which consists in the signals mixing and amplification of these signals to yield the horizontal and vertical difference voltage signals, $V_{\Delta H}$ and $V_{\Delta V}$ respectively, as well as the sum voltage signal V_{Σ}, at its three corresponding output ports. This analog signal treatment is implemented inside the amplifier for the corresponding signals in three channels based on operational amplifiers. Two equivalent Δ channels (ΔV, ΔH) with two operational amplifier stages, and a third Σ channel with only one stage, which will perform an overall amplification or attenuation to adapt the three amplifier output signals to the input dynamic range of the *digitizer* as the next readout chain stage.

The AFE amplifier was developed by UPC [47] in close collaboration with IFIC, so we will focus on its specific features further on mainly due to the direct performance relation between the BPS monitor and the amplifier, as well as having some strongly coupled design choices.

The digitizer board also called the *Digital Front End (DFE)* was developed by LAPP. It first performs the analog to digital conversion of the amplifier output signals (ΔH, ΔV, Σ) within their pulse widths, to later send the digital samples via ethernet links to the control room servers, where are usually stored in the system database. Eventually the beam position and the beam current of each BPS in the line are displayed in the operator's control room screens. The beam position and current are calculated from the digitizer signal samples by using the scaling factors and calibration coefficients previously uploaded into the system database and provided by the characterization tests. All the design details and specifications of the DFE board can be found in [48], so here are described the relevant features in relation to the BPS and amplifier performance.

The connections between the BPS and the corresponding amplifier inputs are made by six semi-rigid SMA coaxial cables of 1 m long which were all cut with 1 mm tolerance to the same length in order to avoid signals delays downstream in the digitizer. The four BPS signals outputs are bipolar and single-ended as well as the two calibration inputs although a monopolar current pulse signal from the current generator is used for calibration. The three amplifier output signals (ΔH, ΔV, Σ) are also bipolar but differential signals so they are sent differentially through a balanced two-wire line per channel to the digitizer inputs (also bipolar and differential) by using ethernet cable of category 6 shielded twisted-pairs with RJ-45 connectors.

The DFE boards, installed in a 19″ crate, are also located a few meters apart of the amplifier box inside the beam line area. This is mainly because the overall cost per channel is reduced by taking advantage of having a good noise rejection with differential signal-

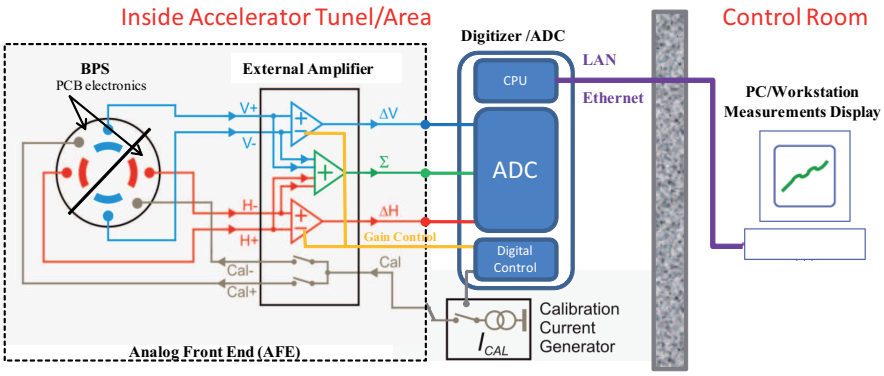

Figure 4.19: Diagram of the readout chain stages of the BPS.

ing implemented in shorter and cheaper twisted pairs cables, but always assuming that, in principle, the DFE boars could withstand the present radiation environment.

In addition, all the AFE amplifier available modes can be configured from the control room consoles and through the DFE board sending the corresponding five control signals to the amplifier, which will be specified below. These are 3.3V DC signals generated in the DFE board which are connected to the amplifier by a MIL multi-pin circular plug using six wires plus one more for digital ground. Two more connector pins are also used for the 6 V power supply and the analog ground of the amplifier, coming also from its corresponding digitizer board.

4.8.1 Characteristics of the Analog Front-End (AFE) electronics

Operation and calibration modes of the amplifier

The amplifier can operate in four modes giving different overall gains to the three mixed signals channels in order to better fit to the broad output voltage range of the BPS signals produced by the different beam measurement conditions. In the amplifier can be also selected either of the two calibration current signals going into the BPS calibration inputs. The amplifier operation modes and the calibration configuration modes are described below and summarized in Tab. 4.7 and Tab. 4.8 respectively:

- **Gain selection modes.** The two available modes of Low/High Gain only will have effect on Δ channels, and not affecting the Σ channel. The whole Δ channels amplification is implemented by two series stages, where the difference signals mix is just performed at the first stage. In the *Low Gain mode* only the first stage acts bypassing the second stage by means of relays, so the overall gains for both horizontal and vertical channels are ideally the same, $G_{L,\Delta H} = G_{L,\Delta V} \equiv G_{L,\Delta}$. While for the *High Gain mode* the two amplifier stages work together yielding higher gains, $G_{H,\Delta H} = G_{H,\Delta V} \equiv G_{H,\Delta}$. The Σ channel has a fixed gain G_Σ since it practically do not vary with the beam position, only with the beam current. The switching between both gain modes is performed by the H-GAIN control signal of two states OFF (default) or ON.

  For the beam displacement over the pipe aperture are expected a wide range variation of the Δ signals, from milivolts to tens of volts, thus the low gain will be set to

cover the full range of beam displacements (±12 mm), while the high gain will be used for measuring small beam displacements around the pipe center (±1 mm), like a zoom to the small Δ signal levels. In the Fig. 4.20 are plotted the amplification scales corresponding to the low and high gain modes relating the amplifier input voltage range of $\Delta(H,V)$ channels $V_{\Delta(H,V)MAX} = \pm 4$ V in order to match up the digitizer input voltage range $V_{DIGMAX} = \pm 0.75$ V, and in general trying to do not saturate the input stages of the amplifier and the digitizer.

- **Attenuation selection modes.** A resistive attenuator is implemented at the input stages of the three channels. This will produce the same attenuation on all the channels and for both low and high gain settings, so the attenuated overall gains are lowered in the same amount of $G_{Att}(dB) < 0$ as simply calculated in dB by: $G'_{L,\Delta} = G_{L,\Delta} + G_{Att}$ and $G'_{H,\Delta} = G_{H,\Delta} + G_{Att}$, for the ΔH and ΔV channels respectively; as well as $G'_{\Sigma} = G_{\Sigma} + G_{Att}$ for the Σ channel. Like in the gain selection modes, relays are used to select whether the attenuation is performed or not. Thus with the control signal BYPASS set to OFF or ON (default), respectively, the input amplifier signals are sent through the attenuator or are just sent directly to the input amplifier stages bypassing the attenuator.

  The attenuation is mainly wanted to reduce the high voltage levels of the BPS outputs feeding the input stages of the Δ and Σ channels which will be produced by the higher beam currents within the nominal beam current range of 1–28 A.

- **Calibration configuration modes.** The two signals $Cal\pm$ used for the BPS calibration come from the same positive pulse current signal which is produced at a common calibration current generator. Current pulses of three different intensities I_{cal} =(300 mA, 1 A, 2.5 A) and 200 ns duration are used for the calibration procedure. As can be seen in Fig. 2.7 this current pulse is simply split in two calibration signal branches inside the amplifier. Thus, one or both calibration signals with a current per signal of I_{cal} or $I_{cal}/2$ respectively, are selected to be sent to the BPS calibration inputs by switching their corresponding relays. The calibration control signals are CAL+ and CAL- which are set to ON for closing the circuit and sending respectively the $Cal_{\pm}$ signals to the BPS, or set to OFF for breaking each circuit path. According to these control signals, in Tab. 4.8 are summarized the four possible configurations, which one of them is to allow the BPS normal operation with beam switching off both calibration signals, and the others emulate the beam position at the positive and negative diagonal extremes and at the center. As the calibration configuration modes are just for selecting the way the BPS is excited, with a calibration signals or with beam, the gains of the amplifier operation modes are independently applied in the same way to both.

In Tab. 4.9 are also summarized the AFE amplifier main characteristics of the Input/Output (I/O) ports, Power Supply (PS) and control signals. In Fig. 4.21 is depicted the block diagram of the amplifier showing the basic layout of the Δ and Σ channels. The calibration circuit, the power supply regulation and the control signals circuits are not specified but showing the container block with the signals used. The Σ channel layout is in principle more generally designed in order to have: two amplification stages with a relay for gain selection; and a first stage split in two operational amplifiers to sum the BPS output signals in two parts improving so the possible crosstalk between them. Finally,

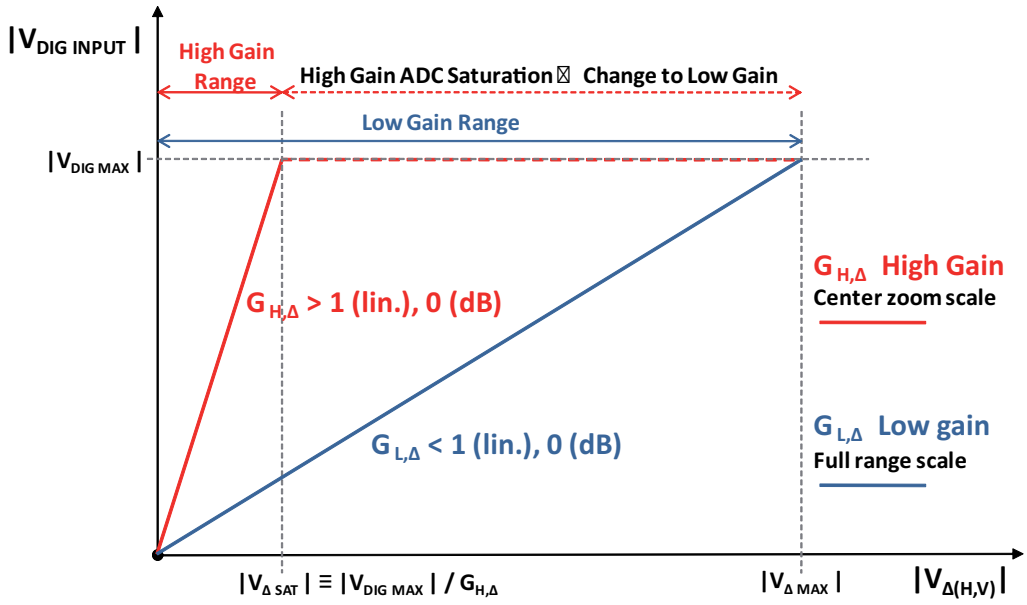

Figure 4.20: Amplifier input signal range for $\Delta(H,V)$ channels ($V_{\Delta(H,V)MAX} = \pm 4$ V) adapted to ADC input range($V_{DIGMAX} = \pm 0.75$ V) by the low ($G_{L,\Delta}$) and high gain ($G_{H,\Delta}$) scales corresponding to the amplifier operation modes (equivalent absolute voltage values are plotted).

Operation Modes	**Control signals**		**Channel Gains**		
Attenuation/Gain	**BYPASS**	**H-GAIN**	**Δ (dB)**	**Σ (dB)**	**Δ/Σ (dB)**
OFF/LOW(d)	ON(d)	OFF(d)	$G_{L,\Delta} = -1.175$	$G_\Sigma = -5.15$	$g_L = 3.975$
OFF/HIGH	ON(d)	ON	$G_{H,\Delta} = +15.055$		$g_H = 9.905$
ON/LOW	OFF	OFF(d)	$G'_{L,\Delta} = -22.955$	$G'_\Sigma = -26.930$	$g'_L \equiv g_L$
ON/HIGH	OFF	ON	$G'_{H,\Delta} = -6.725$		$g'_H \equiv g_H$

Table 4.7: Summary of the operation modes and channel overall gains of the BPS AFE amplifier, (d) indicates the default mode or control signal state. The attenuator decrease all the channel gains by $G_{Att}(dB) = -21.78dB$ to get the attenuation ON modes.

Calibration modes	**Control signals**		**BPS electrode channels excitation**		
BPS signal(s)	**CAL+**	**CAL-**	**Channels**	**I Cal./ch.**	**Beam position Emulated**
Beam (d)	OFF(d)	OFF(d)	$(H_\pm, V_\pm)$/All	—	(Beam operation)
Cal_+	ON	OFF(d)	(H_+, V_+)/(R,U)	$I_{cal}/2$	Max. + diagonal
Cal_-	OFF(d)	ON	(H_-, V_-)/(L,D)		Max. − diagonal
$Cal_\pm$	ON	ON	$(H_\pm, V_\pm)$/All	$I_{cal}/4$	Centered

Table 4.8: Summary of the calibration modes of the BPS which are configured from the AFE amplifier, (d) indicates the default mode or control signal state. Available current intensities I_{cal} = (300 mA, 1 A, 2.5 A) are applied through the amplifier to one BPS calibration input, or split into both inputs as $I_{cal}/2$.

these elements were not mounted being enough with the one amplifier stage Σ channel, although the amplifier PCB layout footprint for them was implemented, allowing for an upgrade in case of necessity.

Two fundamental characteristics of the readout chain must be considered which will affect directly the performance of the BPM system, and thus the BPS. First, the amplifier frequency response or bandwidth for the correct pulse signals transmission from the BPS; and second, the signals acquisition in the digitizer taking into account its input characteristics that must be adapted to the amplifier output side, further described in the digitizer section.

AFE amplifier I/O ports characteristics

Signal ports	**Inputs** $H_{\pm}, V_{\pm}$	**Input** Cal **/ Outputs** $Cal_{\pm}$	**I/O** Δ**,** Σ **channels**
Port & Signal types[a]	SE & BIP	SE & MOP	DIF & BIP / DIF & BIP
Max. voltage range (V)	$\pm V_S$	—	±4/±0.75[b]
Cal. currents I_{cal} (A)	—	0.3, 1, 2.5	—
I/O Impedances R_i/R_o (Ω)	49	49	49/50

AFE amplifier power supply and control

	Global PS	**Op-Amp**[c] V_S	**Relay** V_{CC}**/Control**[d]
Voltage level (V)	+6	+5	+5/+3.3

[a] Ports: Single-Ended (SE), Differential (DIF); Signals: Monopolar (MOP), Bipolar (BIP).
[b] Max. differential input $V_{\Delta(H,V)MAX}$ / Max. differential output matched to V_{DIGMAX} digitizer max. input range.
[c] THS4508 power supply.
[d] Teledyne172 power supply / control signals level for CAL ±, H-GAIN, BYPASS.

Table 4.9: Summary of the AFE amplifier I/O ports, power supply and main control signals.

One-stage amplifier: gain, analog bandwidth and pulse droop compensation

The *analog bandwidth* of the amplifier is in principle from DC up to 200 MHz, wide enough to do not limit the BPS output signal bandwidth and with its high cutoff frequency fixed by the typical gain-bandwidth constant product of the operational amplifier stages at a given gain level. According to the specifications for the correct BPS pulse signals transmission along the readout chain, the amplifier analog bandwidth for each Δ and Σ signal channels must be set at least from 10 kHz up to 100 MHz.

As explained previously in the BPS model description, for an off-center displaced beam the low cutoff frequencies of the electrode signals difference is higher than for the sum signal of each electrode, $f_{low\Delta} >> f_{low\Sigma}$, where the $f_{low\Sigma}$ is already below the 10 kHz specifications but $f_{low\Delta}$ is in the order of ten times bigger and out of specifications.

In the time domain this results in a shorter pulse time constant, and hence a faster droop for the Δ signals as compared to the Σ. Since the Δ/Σ signals normalization has to be performed to get the beam position, both pulse signals should have approximately the same pulse response according the specifications chosen before to get the desired flat pulse transmission within certain error limits.

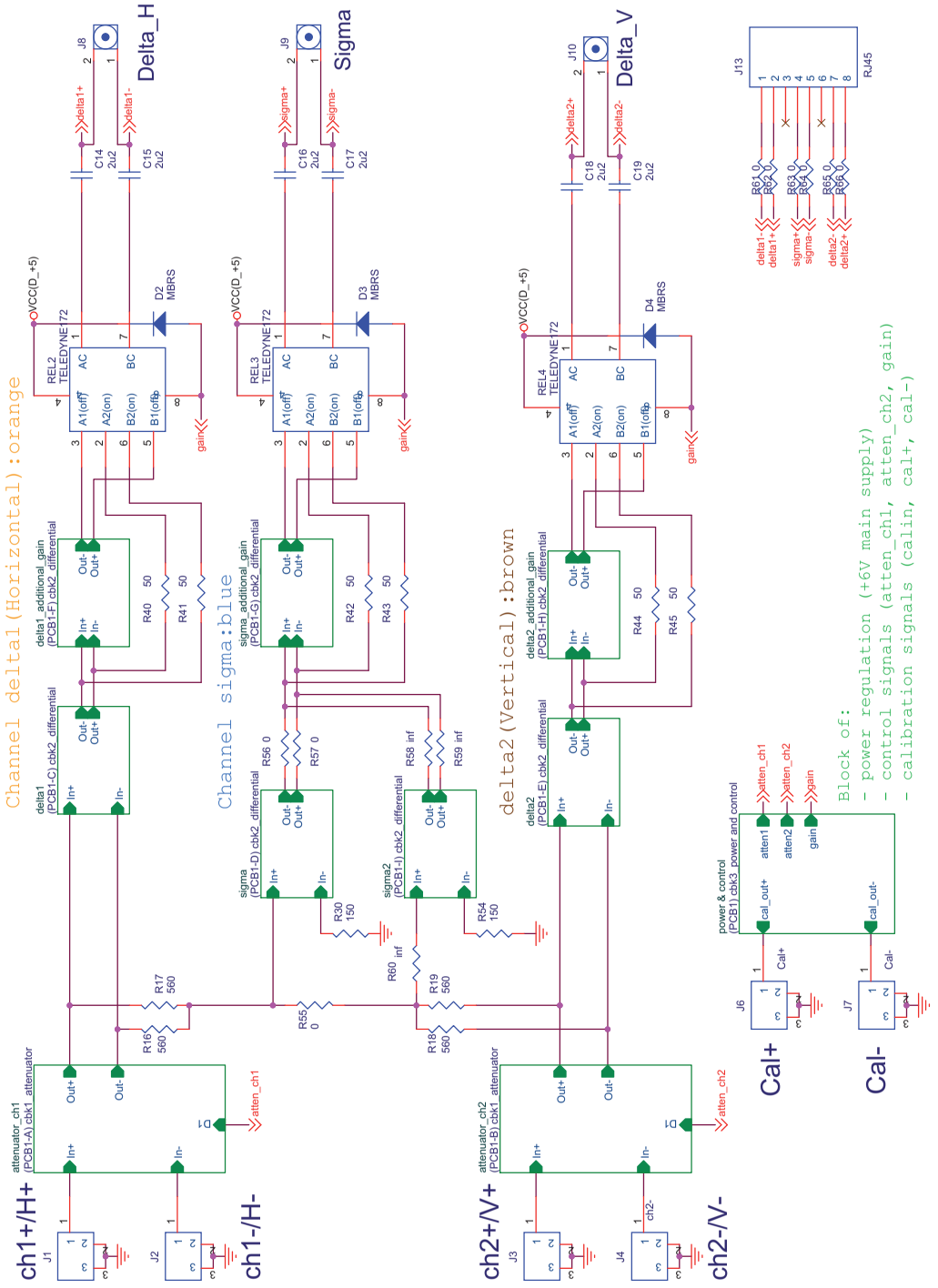

Figure 4.21: Block diagram of the BPS AFE amplifier showing the main layout of the horizontal ΔH (top), vertical ΔV (bottom) and Σ channels (middle). From the Σ channel in the scheme the final implementation only included one amplifier stage with the four input signals connected the positive operational amplifier input, and just with the output lines going through the second stage and the gain selection relay directly to the channel output.

In consequence, the *pulse droop compensation* is implemented in the amplifier Δ channels in order to lower $f_{low\Delta}$ below the specified low cutoff frequency, as explained below.

In Fig. 4.22a is detailed the scheme of one amplifier stage with an RC network added to the feedback loops of the differential operational amplifier for the pulse droop compensation. In the scheme are also shown the input and output termination networks used mainly for matching to the BPS and digitizer at both ends of the Δ and Σ channels. This scheme, and hence transfer function $H(s)$ below (Eq. 4.28), will be common to all the amplifier channels, but taking into account the following specific implementation cases: 1) the pulse droop compensation must be performed on the Δ signals, so it is only implemented in the first stage of the Δ channels by mounting the corresponding components R_3 and C_f in the feedback loops; 2) for the Σ channel to implement the sum of the four BPS signals, the four amplifier input lines are connected to the same positive terminal with each line having the corresponding input termination and a R_1 resistor, like is also shown in Fig. 4.21; 3) the input termination is simply a resistor divider to match the impedance of the BPS outputs and corresponding to the operation mode without attenuation; 4) the output termination, implemented for all the channels, is an RC network made by a resistor divider to match the digitizer input impedance, jointly with a capacitor to filter the unwanted DC level at the operational amplifiers differential outputs adapting to the input digitizer voltage range.

The differential output $V_{od} = V_{o+} - V_{o-}$ are then obtained directly through the transfer function of a fully differential amplifier and from the difference of the input terminals $V_{id} = V_{i+} - V_{i-}$ as $V_{od} = H(s)V_{id}$, where the difference signal between the BPS output signals for each coordinate plane is made by the amplifier differential input as $V_{id} = V_{\Delta(H,V)}$, and for the sum is $V_{id} = V_\Sigma$ but with all the BPS output signals feeding the positive terminal $V_{i+} = V_\Sigma$ and with the negative terminal grounded $V_{i-} = 0$.

The transfer function of the one-stage amplifier (without the input/output terminations) can be explicitly obtained from the two symmetric feedback branches in the circuit of Fig. 4.22a by applying a circuit analysis at each input terminal node and assuming an ideal operational amplifier, so that using the Laplace variable $s \equiv j\omega$,

$$H(s) = \left(\frac{R_2}{R_1}\right)\left(\frac{s+\omega_2}{s+\omega_1}\right), \tag{4.28}$$

where the theoretical gain G for the differential input and output in the amplifier pass-band is just determined by

$$G = \frac{R_2}{R_1}, \tag{4.29}$$

where considering the resistor dividers at the input and output terminations the gain will be reduced by a factor four ($\times$ 1/2 for each divider), so $G_{io} = G/4$.

The frequency response of the amplifier is then set by the two characteristic frequencies $\omega_{1,2}$ which are defined respectively by the pole (denominator) and the zero (numerator) of the transfer function as

$$\omega_1 = \frac{1}{R_3 C_f} \qquad \omega_2 = \frac{1}{(R_2 \| (R_3) C_f} \approx \frac{1}{R_2 C_f}. \tag{4.30}$$

Since the pulse droop compensation is only needed for the Δ signals, it is implemented only in the first stage of the amplifier Δ channels. Thus for the rest of the amplifier stages, the Σ channel and the second stage of the Δ channels, the droop compensation is not implemented just by making $R_3 = 0$, a short-circuit, and $C_f = \infty$, leaving an open-circuit instead of this capacitor.

Analyzing the transfer function asymptotically for the three frequency regions delimited by these characteristic frequencies, with the component values chosen as $R_3 >> R_2$ to get $\omega_1 << \omega_2$, the bode diagram of the resulting frequency response is obtained as shown in Fig. 4.22b. Basically, at high frequencies the gain in the flat frequency pass-band of the Δ channels is determined by $G = R_2/R_1$ since C_f can be considered as a short-circuit. Then starting at the zero ω_2, it ramps up with a -20 dB/decade slope in the transition toward the pole ω_1 having again now a flat response level of $(R_2 + R_3)/R_1$. Thus, setting $\omega_2 = \omega_{low\Delta}$ the slope of -20 dB/decade starts precisely at the low cutoff frequency of the BPS Δ signal to ideally compensate its falling slope of +20 dB/decade and resulting in a flat combined response. This can be extended until ω_1 setting the new low cutoff frequency for the V_Δ output signals, as it is also depicted in Fig. 4.22b.

According to the expressions above, and for the more general case of the Δ channels amplifiers with droop compensation, the steps followed for choosing the amplifier component values are: 1) select R_1 and R_2 to fix the desired gain at high frequencies $G_{io} = R_2/4R_1$ with the input/output terminations considered which will be the final gain level of the amplifier stage after compensating the Δ signal; 2) set ω_2 at the low cutoff frequency values $\omega_{low\Delta(H,V)}$ of the BPS measured in the characterization tests, calculating C_f just from R_2 according to the approximation in Eq. 4.30 for $R_3 >> R_2$; 3) set ω_1 at the new desired low cutoff calculating R_3 with known C_f from Eq. 4.30.

Considering both input and output terminations for every differential line as shown in Fig. 4.22a and also a second amplifier stage only applied for the case Δ channels, the general transfer function of the Δ and Σ amplifier channels can be obtained from the one-stage amplifier transfer function in cascade with the new added elements as

$$H_{io}(s) = \left(\frac{R_{i2}}{R_{i1} + R_{i2}}\right) H_1(s) H_2(s) \left(\frac{1}{s + \omega_{lowout}}\right) \left(\frac{R_L}{R_o + R_L}\right), \tag{4.31}$$

where H_1 and H_2 correspond respectively to a first and second amplifier stage as calculated particularly from the one-stage transfer function $H(s)$ of Eq. (4.28). Multiplying at both sides are included the input matching resistor dividers with R_{i1} and R_{i2} values, and the output resistors dividers formed by the output matching resistor R_o and the load of the digitizer input R_L. Therefore, the channel gain level will be set by

$$G_{io} = \left(\frac{R_{i2}}{R_{i1} + R_{i2}}\right) G_1 G_2 \left(\frac{R_L}{R_o + R_L}\right), \tag{4.32}$$

where G_1 and G_2 correspond respectively to a first and second amplifier stage as calculated particularly from the one-stage gain G of Eq. (4.29).

The output termination RC networks used in principle to filter the unwanted DC level for all the amplifier channels, as mentioned before, will eventually modify their low frequency response by inserting a pole in the full channel transfer function of Eq. (4.31) with ω_o the low cutoff frequency being

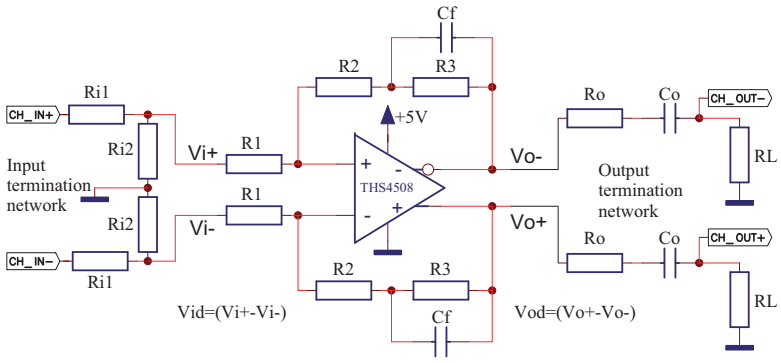

(a)

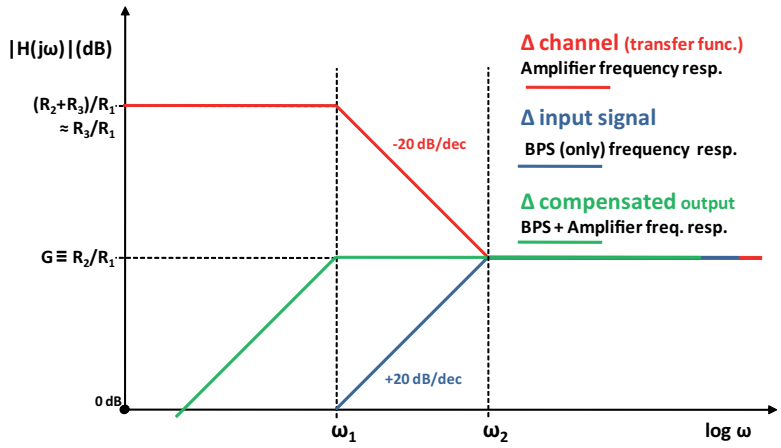

(b)

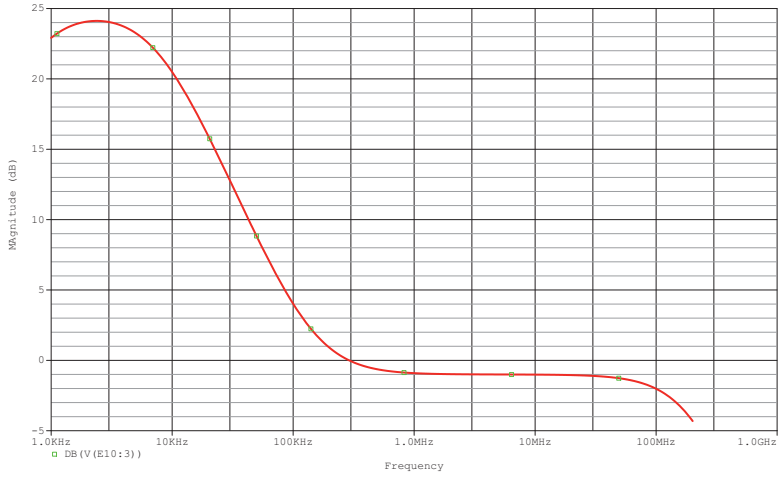

(c)

Figure 4.22: (a) Schematic of the one-stage fully differential amplifier and I/O termination networks of Δ and Σ channels. (b) Bode diagrams of: Δ channel first stage with pulse droop compensation (red), BPS Δ signal frequency response (blue) with low cutoff frequency at $\omega_{low\Delta} = \omega_2$, combined response of BPS and amplifier (green). (c) Simulation (PSPICE) of Δ channel first stage (low gain) with op-amp model THS4508.

$$\omega_o = \frac{1}{(R_o + R_L)C_o}. \tag{4.33}$$

where for every differential line as shown in Fig. 4.22a, the C_o is the output capacitor in series with the output resistor R_o and with the load R_L of the digitizer input.

The Eq. (4.31) can be applied particularly to the two amplifier stages of Δ channels and in the case of the two gain operation modes, thus resulting the specific transfer functions for the low gain $H_{L,\Delta}(s) = H_{io}(s)$ with $H_2 = 1$, where only the first stage $H_1(s)$ is activated with the droop compensation implemented and the second stage bypassed. For the high gain mode the two stages are activated but the second without droop compensation, so the full transfer is $H_{H,\Delta}(s) = H_{L,\Delta}(s)G_2$. While for the Σ channel of a single stage without droop compensation is simply $H_\Sigma(s) = H_{io}(s)$ with $H_1 = G_1$ and $H_2 = 1$.

From Eq. (4.32) the theoretical gains for the Δ and Σ channels in the case low and high gain operation modes are written explicitly as

$$G^t_{L,\Delta} = \left(\frac{R_{i2}}{R_{i1} + R_{i2}}\right) G_{1,\Delta} \left(\frac{R_L}{R_o + R_L}\right) \tag{4.34}$$

$$G^t_{H,\Delta} = \left(\frac{R_{i2}}{R_{i1} + R_{i2}}\right) G_{1,\Delta} G_{2,\Delta} \left(\frac{R_L}{R_o + R_L}\right) = G^t_{L,\Delta} G_2 \tag{4.35}$$

$$G^t_{\Sigma} = \left(\frac{R_{i2}}{R_{i1} + R_{i2}}\right) G_{1,\Sigma} \left(\frac{R_L}{R_o + R_L}\right) \tag{4.36}$$

where the specific channel resistor values are used to calculate the corresponding G_1 and G_2 from the one-stage gain relation in Eq. (4.29). The *t* superscript indicates that is a theoretical design value to be compared with the measured counterparts in Tab. 4.7.

In Tab. 4.10 are summarized the component design values for the one-stage amplifier considering the input/output termination networks and for all the stages of the Δ and Σ channels. These values correspond to the definitive ones obtained after a being measured in the lab test taking into account the real system performance, and which were applied to all the BPS amplifiers units, being different for the first prototype BPS1-v2 due to its different PCB design version.

Moreover, in Tab. 4.10 are collected the theoretical gain values in the pass-band, the characteristic frequencies of the droop compensation, the low cutoff introduced by the output termination network, and the high cutoff frequency which is set by the operational amplifier gain-bandwidth product [49]. All of them calculated according the equations above and from the final design values.

Comparing the theoretical channel gain values in Tab. 4.10, for an ideal operational amplifier, and the final measured ones in Tab. 4.7, it can be seen that are slightly different with only around 1 dB loss for all the channel gains. This can be explained just by the real operational performance so giving a good design starting point. The real gain values were first obtained by simulations in PSPICE with a more realistic model of the amplifier, and after measured for all the operation cases leaving the final gain values of Tab. 4.7.

In the case of the pulse droop compensation first it was simulated with PSPICE the frequency response of the first stage of the Δ channel as shown in Fig. 4.22c, where the gain of -1dB at high frequencies is closer to the $G_{L\Delta}$ value corresponding to the low gain

operation mode and without attenuator. But in turn for the final design values of the RC network in the amplifier feedback loop, it was needed the measurements of the real combined frequency response of the BPS Δ signals and the amplifier in the lab characterization tests, as it will explained in Chap. 5.

Finally, from the Tab. 4.10 the overall analog bandwidth of the AFE amplifier is set by the lowest cutoff frequency f_1 or f_o in the case of each Δ and Σ channel and the high cutoff f_{high} common to all the channels.

One-stage amplifier design characteristics

Op-amp stage	**Op-amp feedback components**				**Gains**	**BW freqs.**	
	$R_1(\Omega)$	$R_2(\Omega)$	$R_3(\Omega)$	C_f(nF)	G(dB)	f_1(kHz)	f_2(kHz)
$\Delta(H,V)$ 1st stage	560	2.4 k	47 k	0.470	G_1=+12.6	7.2	141
[droop comp.][a]			220 k	1		0.7	66.3
$\Delta(H,V)$ 2nd stage	100	680	(short)	(open)	G_2=+16.7	—	—
Σ single stage	560	1.6 k	(short)	(open)	G_1=+9.1	—	—

Amplifier channels with I/O termination networks

Chs. / Gain mode	**Termination networks components**				**Gains**	**BW freqs.**	
	$R_{i1}(\Omega)$	$R_{i2}(\Omega)$	$R_o(\Omega)$	C_o(nF)	G_{io}(dB)	f_o(kHz)	f_{high}(MHz)
$\Delta(H,V)$ / Low	27	22	50	2200	$G^t_{L,\Delta}$= -0.34	0.7	200
$\Delta(H,V)$ / High					$G^t_{H,\Delta}$= +16.3		
Σ / Both					G^t_{Σ}= -3.9		

[a] Pulse droop compensation values for: BPS1-v2 / PCB v2 (2nd line); rest 16 BPS / PCB v1 (1st line).

Table 4.10: Summary of the AFE amplifier $\Delta(H,V)$, Σ channels components design values for gain, bandwidth and pulse droop compensation. Each channel bandwidth is set from the highest low cutoff frequency between f_1 or f_o and the high cutoff f_{high} common to all three channels.

4.8.2 Characteristics of the Digital Front-End (DFE) electronics

In the scheme of Fig. 4.23 can be identified the basic elements and signal flow of the digitizer board architecture. The signal digitalization is performed for each analog input channel (ΔH, ΔV, Σ) by two main input stages, a previous stage of 12 bits analog memories (SAM) of 500 MHz sampling rate and the 14 bit resolution ADCs of 800 kHz as the last stage where a down-rated digitalization is effectively completed. Then the SAMs stage is used as a fast sampling rate buffers, storing one signal sample every 1.95 ns in its memory cells, from where the ADCs can read out and digitize the memory samples at lower sampling rate of 800 kHz. In addition, two analog stages are implemented with differential amplifiers for signal levels matching: a first stage at the digitizer analog input channels in order to allow the differential reception of the Δ and Σ bipolar signals in the range of ±0.75 V adapting them to the SAM positive voltage range of 0.5 – 2 V and a common mode voltage of 1.25 V; and an intermediate stage with a three gain factor for changing the SAM samples voltages to the ADC input levels again bipolar in the range ±2.5 V.

After the input signals are digitized, the 14 bit data samples are temporarily stored into the RAM memory blocks of the FPGA and finally sent to the control room servers

through the SPECS board made specifically for the ethernet network data handling. The FPGA also generates the clock signals needed for the SAM and ADC timing and samples readout synchronization. For completing the BPS readout system, a common distribution board is responsible for managing the global timing signals and power supply provided by the accelerator facility, and sending them to several DFE boards installed in the same crate. It also will spread the calibration pulses between several AFE amplifiers from the external current generators.

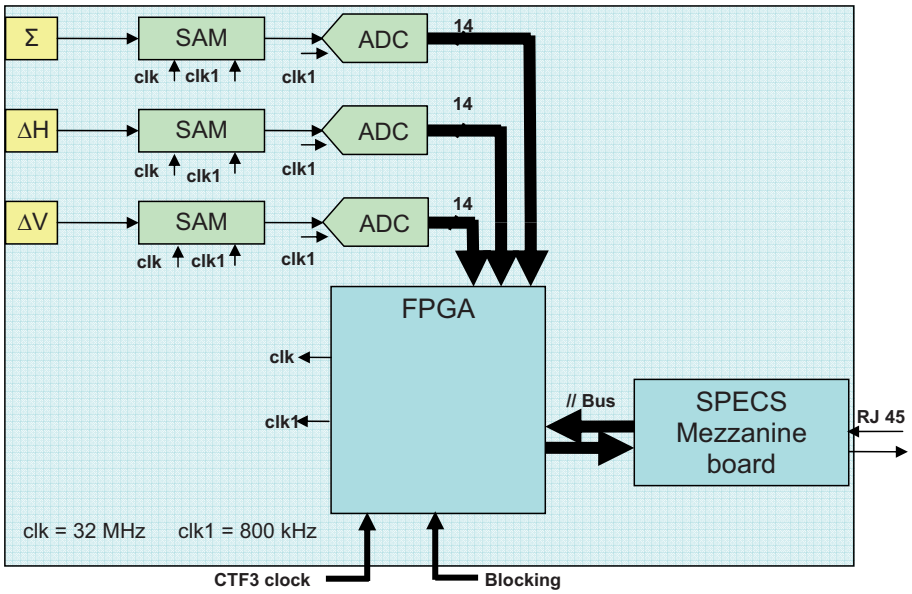

Figure 4.23: Scheme of the Digital Front-End (DFE) board or Digitizer for the BPS readout chain.

This digital conversion strategy was followed mainly to perform a fixed time window acquisition at a high rate within the beam pulse length of 20 – 140 ns, where the beam position and current information is, instead of a free running digitalization, less suitable for the low pulse repetition frequency of 1 – 50 Hz (and hence low duty cycle) which would acquire unwanted samples from the long period between beam pulses. The SAM has a 16×16 array memory cells having thus a memory depth of 256 samples, which allows to capture a fixed number of samples in a maximum time window of 500 ns with room enough for the considered beam pulse lengths.

In conclusion, from the perspective of the beam position and current calculations from the data samples, the digitizer will perform an effective digitalization of the analog voltage pulses (V_Δ, V_Σ) with the following parameters: a 12 bit resolution with an input dynamic range V_{DIGMAX} ± 0.75 V, and a sampling rate of 800 kHz with 1.25 μs data samples spacing.

Therefore, an important condition for the digitizer resolution is that it must be as good as to not limit the achievable resolution for the beam position measurement, as a fundamental parameter in the BPS system performance. More specifically this implies that the voltage quantization step given by the digitizer resolution as $V_{DIGMAX}/2^b$ with b the number of resolution bits, must be smaller than the analog voltage step given by the BPS

outputs (as theoretically determined in the PCB design) for the minimum beam displacement of 5 *muup*m, which would correspond to the desired beam position resolution. Also the quantization noise may degrade the digitizer resolution by reducing the effective number of bits, and so the bigger quantization step might be considered. The beam position resolution will be eventually restricted by the noise level present in the whole system so it must be measured, as it is presented in Sec. 5.5.

4.8.3 Rad-hard considerations and components

An important issue when designing electronics for being close to the accelerator is that will suffer from radiation losses in the beam line. In consequence the electronic components should have a radiation hardness (rad-hard) specification with a maximum radiation tolerance level, usually given by the Total Ionization Dose (TID) parameter, that guarantees their correct performance during a certain period of time. For the TBL line case the maximum radiation level present in the accelerator area is 1 kGray (100 krads) per year (Tab. 4.1). For the BPS electronics mounted on a PCB there is no problem because it has only passive components and their performance are much less affected by radiation than the integrated circuits (ICs) and the SMD thick film resistors used are rad-hard enough.

In the case of the AFE amplifier and the DFE board (digitizer) the following critical components were selected in order to withstand the expected radiation levels in the TBL, most of them having rad-hard specifications and testings from the manufacturer, but other components (difficult to find rad-hard ones or with overcost) at least having good expected rad-hard performance given by their use in similar environments. For the amplifier: the rad-hard wideband IC amplifier THS4508 from *Texas Instruments* was used for the operational amplifier channel stages; the power supply voltage regulators RHFL4913 from *ST Microelectronics*, where LM317 from *National Semiconductor* was also considered although not having rad-hard specifications; and the electromechanical switching relays *Teledyne* 172. For the digitizer: SAM analog memories with ASIC (Application Specific Integrated Circuit) rad-hard design developed by *CEA, Saclay*; the ADCs LTC419A from *Linear Technology* and the FPGA *Actel ProAsicplus* APA300 with no explicit rad-hard specifications; and the SPECS network board with a rad-hard design developed by *LAL, Palaiseau*. All the digitizer components mentioned herein are included in the digitizer development document from LAPP [48].

Chapter 5

Characterization Tests of the BPS Monitor

Two different characterization tests, at low and high frequencies, were carried out on the BPS units: the low frequency test, in the beam pulse time scale (until 10ns/100MHz), determined the BPS working parameters directly related to the beam position monitoring; and the high frequency test reaching the microwave X-Ku bands around the beam bunching time scale (83ps/12GHz) in order to obtain the longitudinal impedance in the frequency range of interest.

The BPS main working parameters, sensitivity and electrical offset of each independent horizontal and vertical plane, have to be measured for its operation as a beam position monitor by means of the linearity tests for the positions range of interest. In order to check and fulfill the performance specifications requested for the TBL BPS units, the accuracy and resolution benchmarks of the BPS position measurement are also determined from the linearity tests. The device frequency response (with frequency cutoffs and bandwidth) and derived pulse response are obtained from their respective tests in the frequency and time domains. These low frequency characterization tests were realized using a special setup commonly called the wire method test bench, as it is usually done for testing precision pick-ups. This test bench allows the emulation of the beam passing through the BPS device under test by a thin stretched conducting wire which carries a given current intensity and can be moved to a known different positions relative to the BPS vacuum pipe aperture. Essentially, the conducting wire forms a coaxial structure with the surrounding vacuum pipe of the BPS and it is able to effectively reproduce a real beam behavior provided that both have the same TEM fields propagating down the vacuum pipe and generating a purely transverse wall image current mirroring a given wire or beam current waveform. Therefore, as it was stated previously in Chap. 3, this will stand only for ultra-relativistic or high-β beams having purely transverse EM fields as it is the case of the TBL electron beam with a nominal energy of 150 MeV.

The first characterization tests for the BPS1 prototype (with v1 and v2 PCB versions) were carried out on an existing wire test bench previously used for testing and calibrating the BPMs for the DBL of the CTF3, and during several short stays at CERN. Particularly in the laboratories of Position and Intensity (PI) section, of the Beam Instrumentation group (BI) in the Beams department (BE), where this wire test bench was located and with the help of PI team.

After solving some mechanical design adjustments based on the prototyping experience during the year 2007 and part of 2008, the fabrication of the different BPS parts started in November 2008 for the production of the BPS series of 16 units (15 for the TBL and one spare) as well as their corresponding on board PCBs. At the same time a new wire test bench was specifically designed and constructed to perform the characterization tests of the full BPS series at IFIC labs. Also a validation tests was done on the PCBs to check their correct functionality prior to the BPS units final assembly which was finished around August 2009. Then the characterization tests lasted until October 2009 when finally 13 BPS series units were delivered to CERN for installation in the TBL, where there were already installed the BPS1, and the BPS2 and BPS3 units constructed and tested in advance as a pre-series delivered to CERN in March 2009.

In the first following sections are described the low frequency test benches, just briefly the one used for the BPS1 prototype at CERN, and after the ad hoc wire test bench design for the BPS series at IFIC. Further on are presented these characterization test results of all the BPS units.

Apart from the main operation parameters for beam position monitoring, it is also needed to determine the longitudinal impedance of the BPS monitor for the high frequency components generated by the beam bunching frequency in the GHz range. This is important since every BPS monitor produces a longitudinal impedance, $Z_{\|}$, in the line, and higher values of $Z_{\|}$ will produce stronger wake-fields leading to beam instabilities. For that purpose it was designed and built a special high frequency test bench. In Sec. 5.4 we describe the results and methods used to obtain the longitudinal impedance in the frequency range of interest. This test will provide us the S-parameters measurements of the propagating TEM mode in a matched coaxial waveguide, specifically designed for the BPS, which is able to emulate an ultra-relativistic electron beam. The BPS-5s remained at IFIC labs as a spare units and also to perform these high frequency tests.

Finally, in Sec. 5.5 we present the results of the beam test in the TBL (CTF3, CERN) carried out on the BPS monitor in order to fundamentally determine the position resolution parameter as the BPS figure of merit according to TBL demands which is expected to reach the 5 μm resolution at maximum beam current of 28 A. The beam test results of the BPS units are also compared with the resolution obtained from their previous characterization test at lab.

5.1 The BPS prototype wire test bench at CERN

As can be seen in Fig. 5.1, this wire test bench consists in a stage where are installed the BPS1 prototype with its adaptation support. The stage holding this setup is attached to a 3-axes manual positioning structure which has a digital display encoder reading the stage displacement with a ± 5 μm resolution [50].

On the other hand, the top of the wire is soldered to a SMA connector screwed it down to a static roof, which will be the input of the excitation signal. Because the wire has to simulate the beam, it cross the BPS longitudinally and a weight is hanging at the bottom end of the wire to keep it aligned with the BPS longitudinal axis just by gravity (depicted in Fig. 5.1 with a dotted line and a blue triangle). This weight is inside a tank floating on mercury in order to make contact with the tank walls and, then, close the circuit of the wire. Because of this, the wire current will have its return path mainly through the

BPS body, but, it is worth to remark that the current sensed in the BPS electrodes is not this return current, being actually the transient wall image current induced in the BPS conducting walls by the TEM modes of the wire current.

Also to mention that in the tank there is oil to allow a soft motion of the weight floating on the mercury when making a platform displacement. Therefore, the current wire will stand still, while moving the platform jointly with the BPS. This procedure of moving the BPS instead of the wire is preferred because, making wire displacements to a certain position would cause oscillations in the wire after reach this position, so it would be necessary to wait each time until they stop completely.

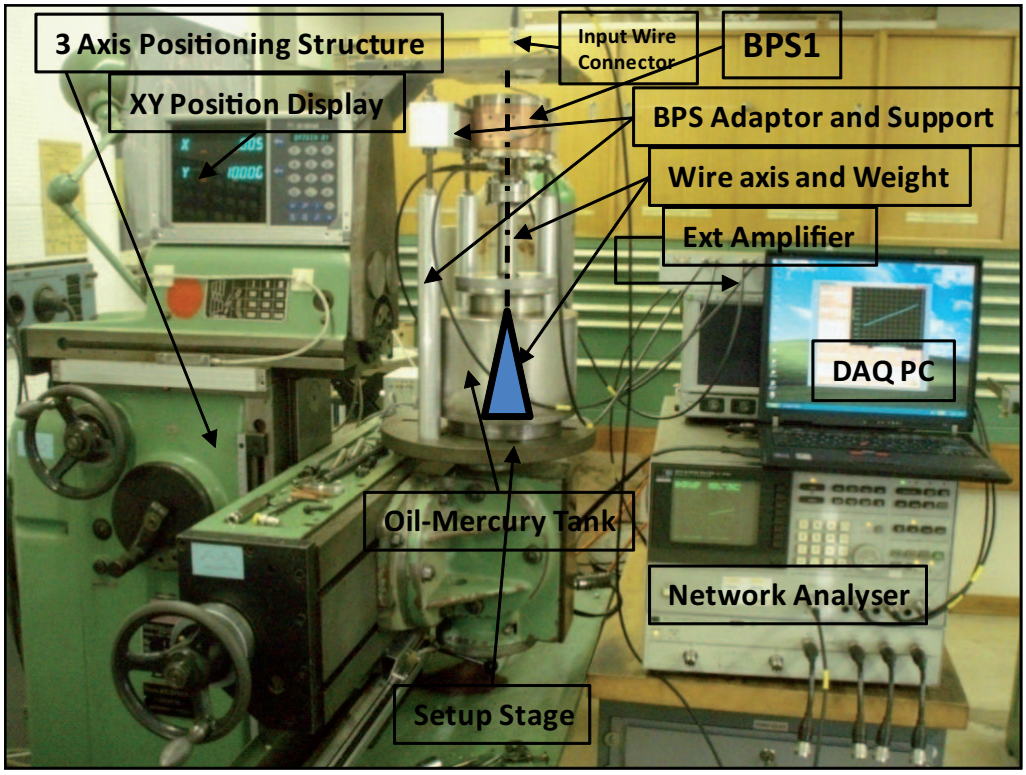

Figure 5.1: Wire method test bench with the BPS installed (left side) at CERN-BI-PI section labs; AFE amplifier connected to the four electrode signals: $H_{\pm}$, V_{pm}; Network Analyzer to generate the excitation signal and read the amplifier output signals ΔH, ΔV and Σ; and a laptop PC running the acquisition application.

5.2 The BPS series wire test bench at IFIC

In Fig. 5.2 are shown a picture and a 3D design view of the wire test bench where are depicted its main elements with a BPS unit under test. A centered axial line is also depicted in the picture to show the wire going through the BPS which can not be seen directly.

The fundamental design concept is that the BPS and the main test stand elements are in-tower mounted within an aluminium frame in order to vertically stretch the wire between two fixed points from the upper to the lower square frame rods, passing through the hollow center of the rotation stage, and thus avoiding any wire bending due to gravity. With the wire remaining at a fixed position, the BPS sitting on the reference platform is

then moved by the micro-mover stages to yield the wire relative displacement respect to the BPS through their position readout. Moving the BPS instead of the wire is preferred in order to avoid vibrations of the wire that otherwise would be produced at every motion step and would interfere in the precision measurement of the position.

Also special care was taken for choosing the way of anchoring and stretching the wire at both points in the frame. The selected wire is made of CuZn-37 alloy of 250 μm diameter and the key element is a small ceramic ring with a thin diamond inner hole of nearly the same wire diameter to thread the wire in. Then each of these two ring holes are inserted in the center of a bigger diameter teflon cylinders and finally fitted to the upper and lower round through-holes made in the square frame. Since the wire has to be taken in and out and also stretched for every BPS unit to be tested, the main concern was to guarantee the wire position repeatability as much as possible. For that reason, the wire and the two small ceramic-diamond ring was borrowed from an electro-erosion machine, with the wire being able to stand high tensile strengths and with the ceramic-diamond ring holes highly resistant to deformation and friction when pulling to stretch the wire against them.

Following the Fig. 5.2 the main elements of the BPS test bench are described below:

- **The wire elements.** The wire is stretched between the two teflon pieces with ceramic-diamond ring holes at the top and bottom of the square frame, as explained before, having a length of 38 cm between them. At the top of the frame there is an SMA connector, screwed to a small metal support, as the wire input signal port with its center conductor soldered and tightly tied to a wire end. The other wire end is fixed by an SMA connector at the bottom of the frame. A resistor divider was implemented at the wire input connector to get an input impedance of $R_{in-wire}$=50 Ω in order to match the incoming signal from the signal generator equipment. Also a load of R_{L-wire}=180 Ω was added at the wire end connector (after measuring its output impedance) for approximately matching the coaxial line formed by the wire and the BPS pipe. This was made to improve the test bench frequency response reducing the signal reflections appearing at the higher frequencies around 100 MHz.
- **Micro-mover stages.** The two linear translation stages are orthogonally mounted providing the BPS displacement relative to the wire in the (x, y) or (H, V) directions. On top of them a metallic case platform holds the rotation stage allowing to make BPS-wire relative rotations of a given angle α in the same (x, y) plane like in polar coordinates. The ILS100CCHA model was chosen for each translation stage and the URS150BCC model for the rotation stage, both models being a high performance precision micro-movers driven by DC motors from *Newport* [51, 52]. The maximum linear travel range of the translation stages is 100 mm having an on-axis accuracy of 4 μm in this range and, for the position readout, features an encoder with integrated linear scale providing a 0.1 μm resolution. The rotation stage has a 360°motion with a high-precision rotary encoder yielding an accuracy of 0.012°(209 μrad) in the bi-directional angular positioning, and a resolution of 0.0005°(8.7 μrad), which means having an arc accuracy of 2.5 μm and arc resolution of 0.1 μm at a radius of 12 mm corresponding to the maximum wire off-center displacement. The maximum normal load capacity for maintaining specifications of the stages are 250 N (25.5 kg) and 300 N (30.6 kg) for the translation and the rotation stages respectively, which was considered enough to stand a maximum weight

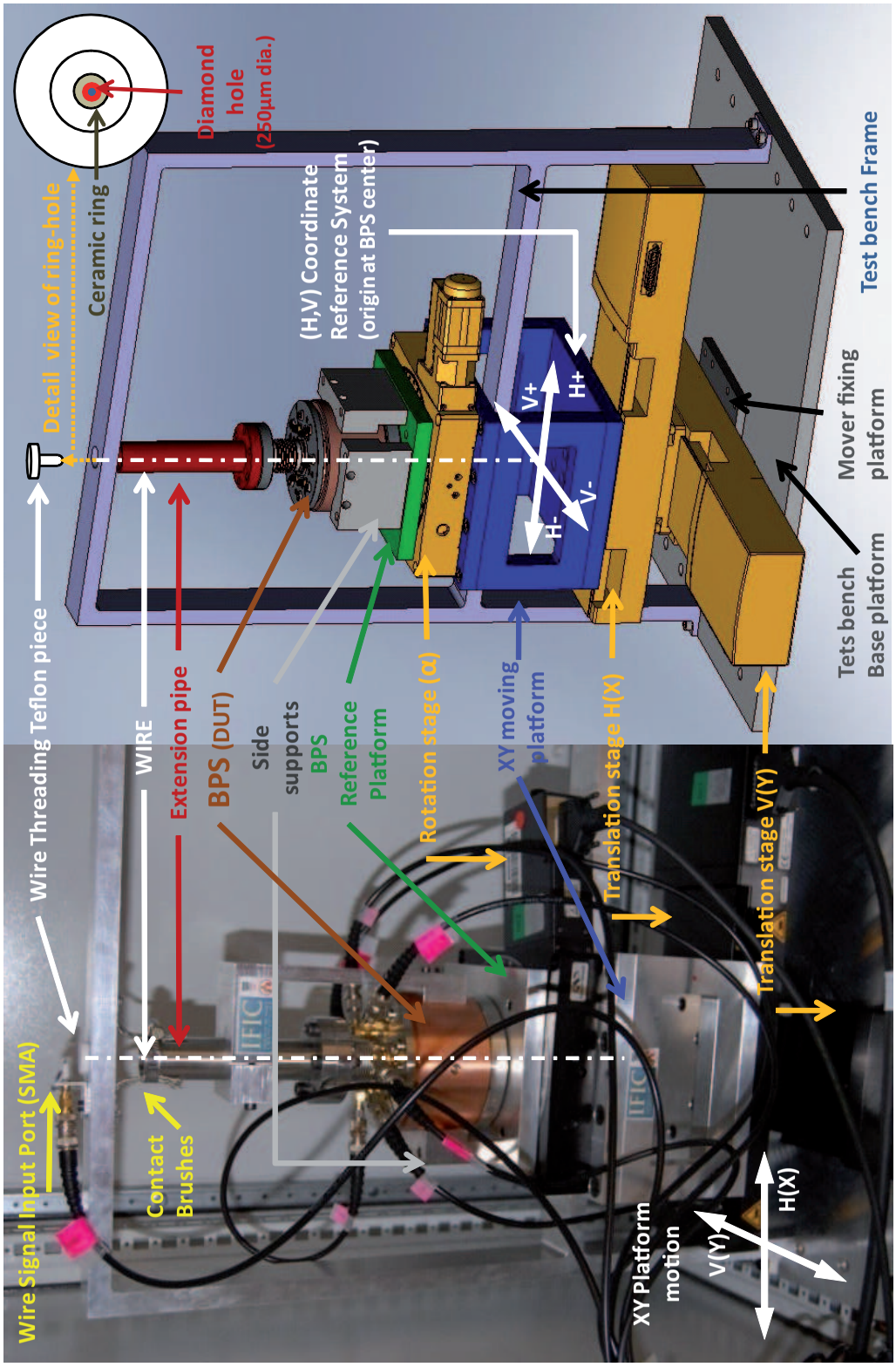

Figure 5.2: Picture (left) and 3D design view of the wire test bench for the BPS series characterization tests at the IFIC labs. The name of the main elements are depicted as well as the motion of the platform (left) and the equivalent coordinate reference system with origin at the BPS center.

of 15 kg (supported by the stage beneath) and with only a ± 12 mm off-center displacement.

- **Supporting mechanical elements.** The test bench tower is placed over a heavy iron base platform where the aluminium frame just holding the stretched wire is also tightly bolted, giving so a good stability to the whole setup. A small platform provided by the micro-movers manufacturer was also used for precisely fixing the bottom translation stage. An aluminium case platform placed on top of the translation stages in XY configuration, was made in order to rise the BPS and the rotation stage over the lower frame rod allowing the free motion in both (x, y) directions. The BPS reference platform, made also in aluminium and with a hollow center for the wire, was used to eventually fix the BPS placement with two side supports and to the rotation stage beneath. An alumnium tube of the same BPS vacuum pipe diameter and the corresponding coupling flanges was added to extend the pipe line, like in an accelerator, and cover the wire as much as possible. Due to the weight of the extension tube it is clamped by a supporting arm fixed to the one BPS free side. Finally, two contact brushes permitted the electric contact between the extension tube and the upper frame rod while moving the BPS, with the aim of closing the currents return path, back to the wire input connector, by the BPS body and the extension tube, and thus avoiding the ground current loop that otherwise would be formed by the wire and the aluminium frame acting like a big area antenna. This improved the EMI immunity to the external signals mainly coming from the FM radio broadcast band (87.5 MHZ to 108 MHz) in the upper range of the BPS bandwidth of interest.
- **Test bench accommodation.** Furthermore this test stand was placed inside a Faraday Cage for better EMI immunity by the test bench screening but mainly of the wire-antenna of 38 cm length. The pneumatic vibration-damping table (or optical table) helped to minimize the wire vibrations during measurements that might be produced by a variety of external sources, considering also the building low frequency vibrations since the lab was located in a first floor instead of a ground floor or a basement.

The wire test bench used for the BPS characterization tests will work only at low frequencies up to around 100 MHz, which barely is enough to specify the desired BPS operation bandwidth with a high cutoff frequency at least being above 100 MHz although it is not sufficient for precisely measuring the bandwidth high cutoff, as it will be shown below in the frequency response test results. This limitation will relay mainly on its particular design but, basically, this type of wire test bench will be limited by the difficulty to get a matched coaxial line with a thin and off-center wire, as a center conductor, while having an external coaxial conductor fixed by the BPS vacuum chamber diameter.

5.2.1 Metrology of the wire test bench

The accuracy of the position measurement that the BPS must achieve is set to 50 μm according to the TBL specifications. In consequence the uncertainties introduced by the test bench tower in the wire relative positioning should be minimized to be able to measure the wire position from the BPS at least with an accuracy of 50 μm, as it is mainly required for the linearity characterization tests. This was proved to be critical for such precision

measurements since the accuracy results from the prototype tests was worse than expected due to the misalignments influence of the test bench which was not well adapted for the particular BPS design. In that sense, it was carried out a metrology of the wire relative to the BPS supporting reference platform where there were considered the following typical misalignments produced in the mechanical fabrication, micro-movers positioning uncertainties and the assembly of the test bench elements indicating the method used to measure them.

Wire tilt

The inclination of the wire with respect the BPS reference platform was determined with the *Zeiss Calypso* 3D metrology machine. First by positioning the reference platform surface with a sensitive touch sensor, and after basically measuring two extreme points of the wire line with a camera vision system, in order to perform a more accurate measurement without touching the wire that would invalidate the measurement by an unknown wire displacement.

In Fig. 5.3 are shown the measurement analysis results of the wire metrology in a 3D reference system with the (x, y) coordinates for the horizontal and vertical displacement and the z coordinate for the height from the reference platform surface. The wire line (in red) was indeed obtained from the wire line projections in the XZ and YZ planes since it was measured a pair of 2D data points in the XZ and YZ planes at the top and bottom of the wire. Only a segment of the 380 mm wire corresponding to the BPS length ($\sim$ 126 mm) is plotted in Fig. 5.3, and the side lines (in green) represent the error of the wire line measurement.

The wire was measured with the translation stages at his home reference position, with a zero reading of the (x, y) coordinates and for a height from the platform surface at $z = 38.9$ mm, which corresponds to the middle point of the BPS electrodes length. Then the wire home point in the XY-plane at the specified height and with measurement errors is

$$W_H = (0, 0) \pm (0.013, 0.005) \text{ mm},$$

is taken as the wire origin for the translation axes reference system, as shown in Fig. 5.3 where are also depicted dashed circles of 0.1, 0.5, and 1 mm radius with center at the wire home point (only for illustration reference).

Wire offset and rotation center

The wire home origin is at different offset position with respect the BPS theoretical mechanical center point, and it is located in the translation axes reference system coordinates at

$$M_c = (-0.557, 1.005) \pm (0.013, 0.005) \text{ mm},$$

which is indicated in Fig. 5.3 with the wire line (dotted red) transported to this point.

The BPS sitting on its reference platform can be rotated by the rotation stage beneath, so the BPS mechanical center point M_c will be rotated around the reference platform rotation axis. Therefore, in order to calculate the new rotated coordinates of the BPS

mechanical center M_c^α for a given rotation angle α, the rotation center of the wire R_c has to be known which for a tilted wire is defined at a given height from the platform surface in the same XY-plane specified for the chosen reference system. In Fig. 5.3 are shown the platform rotation axis (dashed blue) and the measured wire rotation center, which in the XY-plane at the specified height and with measurement errors is located at

$$R_c = (-0.676, -0.947) \pm (0.0025, 0.0025) \text{ mm}.$$

Around the rotation axis are also shown in Fig. 5.3 the location of the BPS mechanical centers M_c^α (green dots) that has been rotated by the BPS platform, as well as four rotated wire lines (dotted red) corresponding to the BPS reference platform rotation angles $\alpha = 0°, 90°, 180°, 270°$.

For measuring the wire rotation center R_c, it was implemented an ad hoc method using a metrology laser device for distance measurements. The idea is to point the laser beam of 50μm spot size to the stretched wire of 250μm diameter at a wanted height from the platform, and then with the laser mounted in the platform make successively 180°rotations and XY translations corrections to point again the wire with the laser, in order to eventually find the wire rotation center being by definition the only wire point that do not change its position under rotations and which s determined by the XY reading of the translation axes when the laser distance reading remains unchanged between 180°rotations. In Fig. 5.4 is shown the laser setup, and a detail of the laser pointing the wire used for measuring the wire rotation center R_c.

Orthogonality and parallelism of wire trajectories

According to the manufacturer specifications of the translation stages mounted in XY configuration the relative orthogonality between them is ±2.9° (±50 μm). This will change the trajectories followed by the wire relative to the BPS motion in the (x, y) directions, being deviated from the ideal parallel wire positions along the corresponding horizontal and vertical coordinate lines. Nevertheless the wire trajectories deviations were measured with the camera vision method at a middle point in the wire and for a wire travel from -10 mm to +10 mm in both coordinate lines, obtaining much smaller deviations. Then the angular deviations, with the convention of positive clockwise angles in the translation axes reference system, for the horizontal wire trajectory is +0.05°and +0.005°for the vertical wire trajectory. Corresponding to deviation slopes of the horizontal and vertical coordinate wire lines of 0.9 μm/mm and 0.1 μm/mm, hence with respective vertical and horizontal deviations at both ends of the wire travel ±10 mm of 9 μm and 1 μm.

Compensation of the wire test bench alignment errors

The main concerns were first to position the wire at the BPS mechanical center M_C and then correcting for the wire offset between this point and the wire at the home position W_H determined by the zero of both translation axes. This is mainly needed to get the wire absolute position for the linearity test and particularly to determine the electrical offsets of BPS knowing that the wire is positioned precisely at its mechanical center.

A second issue was the influence of the wire tilt relative to the base of the BPS in the test results. For a wire (or similarly a beam) with a given diameter, the BPS gets a measure of the proximity of the respective wire side facing each electrode (by the wall current

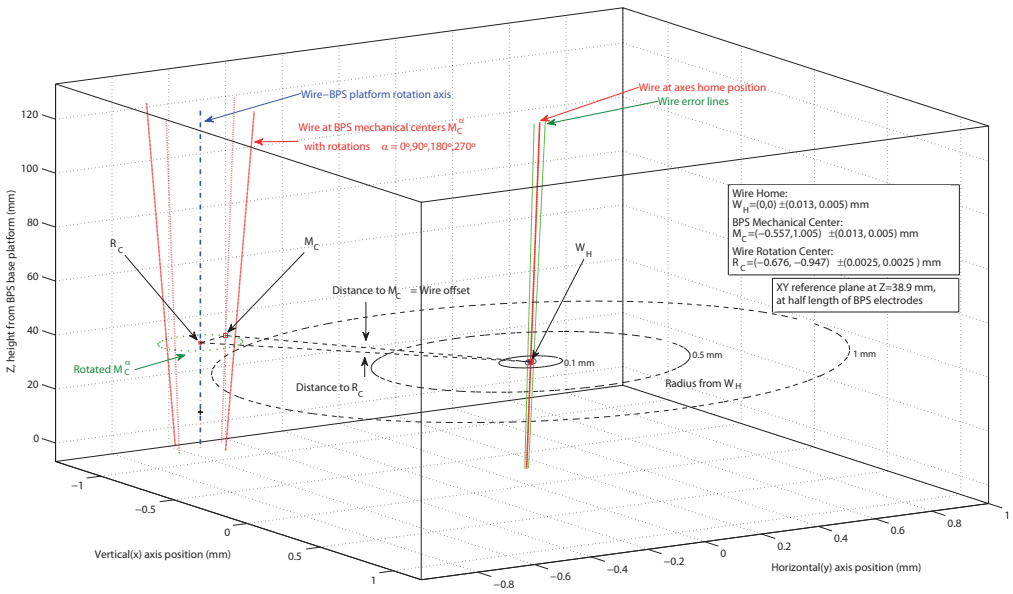

Figure 5.3: Plot 3D of the test bench metrology measurements of the wire relative to the BPS reference platform. The (x, y) coordinates represent the wire relative motion due to the XY translation stages with origin at their home position and the z coordinate is the height from the BPS reference platform until approximately the length of the BPS 126.18 mm. The BPS mechanical center points M_C^α for platform rotations of angle α and the wire home position W_H are in the XY-plane at half of the BPS electrodes length. The measured tilted wire (red) and side wire error lines are shown (blue) and it is also translated and also rotated as indicated in the plot.

induction mechanism explained before) and then determining the wire or beam centroid by making the difference between the electrode output signal level. For a perfectly perpendicular wire to the BPS base and assuming ideal strip electrodes perpendicular to the

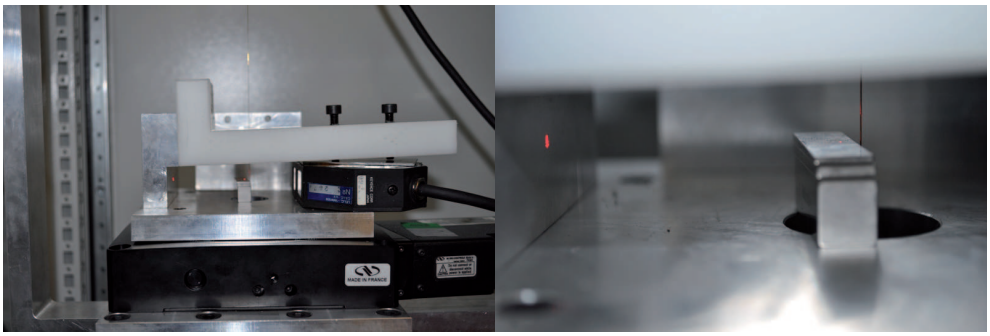

(a) (b)

Figure 5.4: (a) Picture of the laser setup used to measure the wire rotation center relative to the rotated BPS reference platform (aluminium). Laser device is fixed over the platform being rotated together by the rotation stage beneath. (b) Detail of the laser beam pointing the wire at a given height. The laser device measures the distance to the wire in order to find out the wire rotation center which is the only static point under rotations.

base and thus parallel to the wire, the position coordinates of wire centroid will be clearly determined since all the centroid points of the wire portion seen by the electrodes are projected down to the same position coordinates in the XY-plane. Considering now a tilted wire (not parallel to the strip electrodes) the centroid points of the wire are projected down to a linear range of positions in the XY-plane instead of just one position. In this case, since the electrodes are not able to detect longitudinally the change of the wire centroids because the induced wall current is integrated along their length, they yield a measure of the tilted wire position as an average of its centroids projected to each coordinate line of the XY-plane, just like measuring a wire with a thicker effective diameter but determining its averaged centroid position correctly. In principle this will not need to be compensated, just losing positioning resolution in the worst case due to the wire thickness, but the wire tilting can also change along its trajectory thus increasing the uncertainty of the wire positioning. The wire tilt variation can be caused for instance by the translation stages pitch variation as move away their supporting load from the center.

Concerning the orthogonality errors of the wire trajectories, it was measured the wire travel orthogonality with respect the motion of the XY translation stages, having negligible deviation errors. But other orthogonality error sources have to be considered like the BPS electrodes orientation with respect the wire travel and the yaw deviations of the translation stages as they move away along the XY coordinates.

These metrology measurements were performed in order to reduce or at least minimize the main test bench alignment errors that might degrade the accuracy needed for the linearity characterization tests of the BPS series, as mentioned before. But some source of errors were difficult to quantify and not all of them can be corrected directly as well as other may be self-compensated.

Therefore, besides the wire offset that can be corrected directly in the test bench, the compensation strategy were based in performing BPS platform rotations in order to change symmetrically the wire alignment errors produced in the non rotated case. For each considered alignment error were applied the following compensation (or corrections) strategies to the wire trajectories in the linearity tests:

- **Wire tilt.** For the wire position steps followed in a trajectory, an $\alpha = 180°$ rotation of the BPS will result in having just the opposite wire tilt relative to the BPS electrodes, so performing this rotation for every wire trajectory it would compensate for the possible effect of the wire tilt in the measurement of the linearity test parameters.
- **Wire offset.** The wire at the home position of translation stages W_H is moved to the horizontal and vertical coordinates of the known BPS mechanical center $M_C \equiv M_C^{0^\circ}$. The wire offset is then corrected to perform the wire trajectories in the linearity test. For the wire trajectories with an α rotation, the wire offset is gain corrected by positioning the wire on the corresponding BPS mechanical center M_C^α previously calculated.
- **Orthogonality and parallelism of wire trajectories.** For the wire position steps followed in a trajectory, an $\alpha = +90°$ rotation of the BPS will allow to measure both horizontal $H_\pm$ and vertical $V_\pm$ electrodes coordinate lines with the same translation stage, avoiding thus the orthogonality deviation between both wire travel coordinate lines.

In addition, to compensate for the parallelism deviations of each horizontal $H_{\pm}$ and vertical $V_{\pm}$ electrodes coordinate line from the respective wire travel along the coordinate lines defined by the XY translation stages, rotations of $\alpha = 180^{\circ}$ are made to the $\alpha = (0^{\circ}, +90^{\circ})$ trajectories which would also compensate the wire tilt effect on the measurements, as explained before.

5.2.2 Instrumentation equipment setup and test configurations

In Fig. 5.5 is shown the block diagram of the instrumentation equipment setup for the wire test bench with connection scheme of all involved signals which was used to perform the BPS characterization test. In Fig. 5.6 is also shown a picture of the setup and the wire test bench at the IFIC labs depicting the name of the equipment employed.

This setup was conceived with the main aim of automatizing as much as possible the measurements that had to be made on all the BPS units, thus favouring the data taking by programming measurements with many samples for each BPS unit and, on the other hand, increasing also the reliability of the test measurements with well defined and repetitive test procedures. In that sense, a key element is the PC running application *SensAT v1.0* developed in *LabVIEW* for the control and data acquisition (DAQ) of the whole test setup which is described below.

In addition, just to remark that the same setup elements were used during the BPS series characterization test campaign including the cabling for all the setup signals. For signals cabling there were used 50 Ω BNC coaxial cables, taking special care in the selection of cables with the same length in order to avoid as much as possible delays for the signals running in parallel like, for instance, the ones from the BPS to the amplifier and the amplifier to the measurement equipment.

Next, there are described the three main configurations of the instrumentation equipment setup specifically tailored for the set of BPS characterization test.

Linearity test configuration

The wire input is fed by a sinusoid signal in the pass-band of the BPS at 1 MHz which comes from a Vector Network Analyzer (VNA) MS4630B of a 10 Hz to 300 MHz bandwidth from *Anritsu*, after passing through a current amplifier ZHL-3A from *Mini-Circuits* which is DC powered with 24 V [54]. A 10 dBm output power from the VNA is sent to the current amplifier yielding 30.5 dBm of signal power to the wire input. This signal power will boost the current to $I_{in-wire} = 212$ mA over the $R_{in-wire} = 50\ \Omega$ resistor divider of the wire input to finally give a 28 % of this current to the wire leaving almost $I_{wire} = 60$ mA. As compared to the previous tests made for the BPS1 prototype at CERN which the wire current was $I_{in-wire} = 13$ mA, the current amplifier provided a wire current significant increase thus improving the signal to noise ratio of the former test.

The four BPS electrode outputs are then connected to the BPS external amplifier (or AFE amplifier) which will send the mixed and amplified signals ΔH, ΔV and Σ to the three available VNA inputs after having previously converted the differential amplifier outputs to the single ended inputs of the VNA with signal mixers (180°power combiner ZFSCJ-2-2, 10 kHz – 20 MHz, from *Mini-Circuits* [55]).

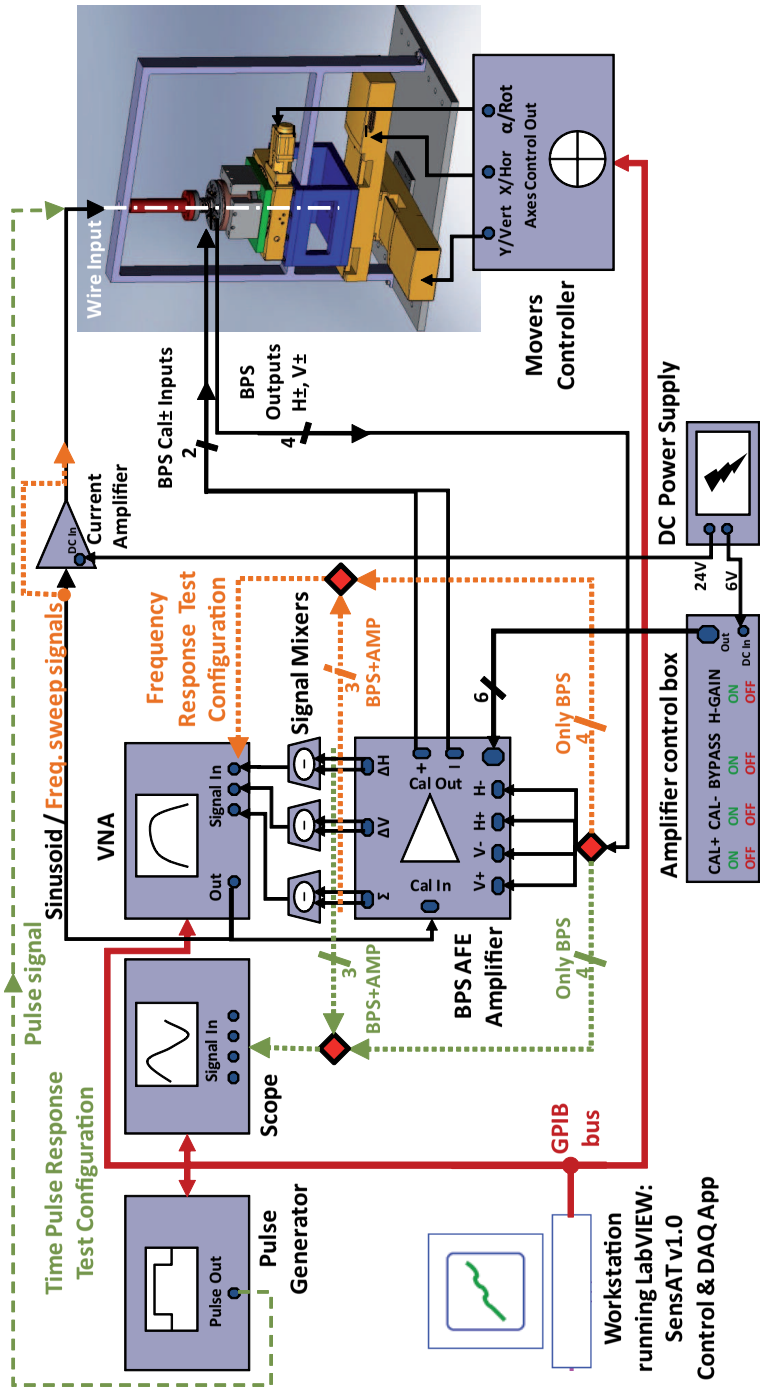

Figure 5.5: Block diagram of the instrumentation equipment setup and the wire test bench (3D view, right) showing their connection scheme for the set of BPS series characterization tests. Red diamonds depicted in the scheme indicate alternative connection points for the different test configurations: linearity test or common signals (black), frequency test (orange) and pulse test (green).

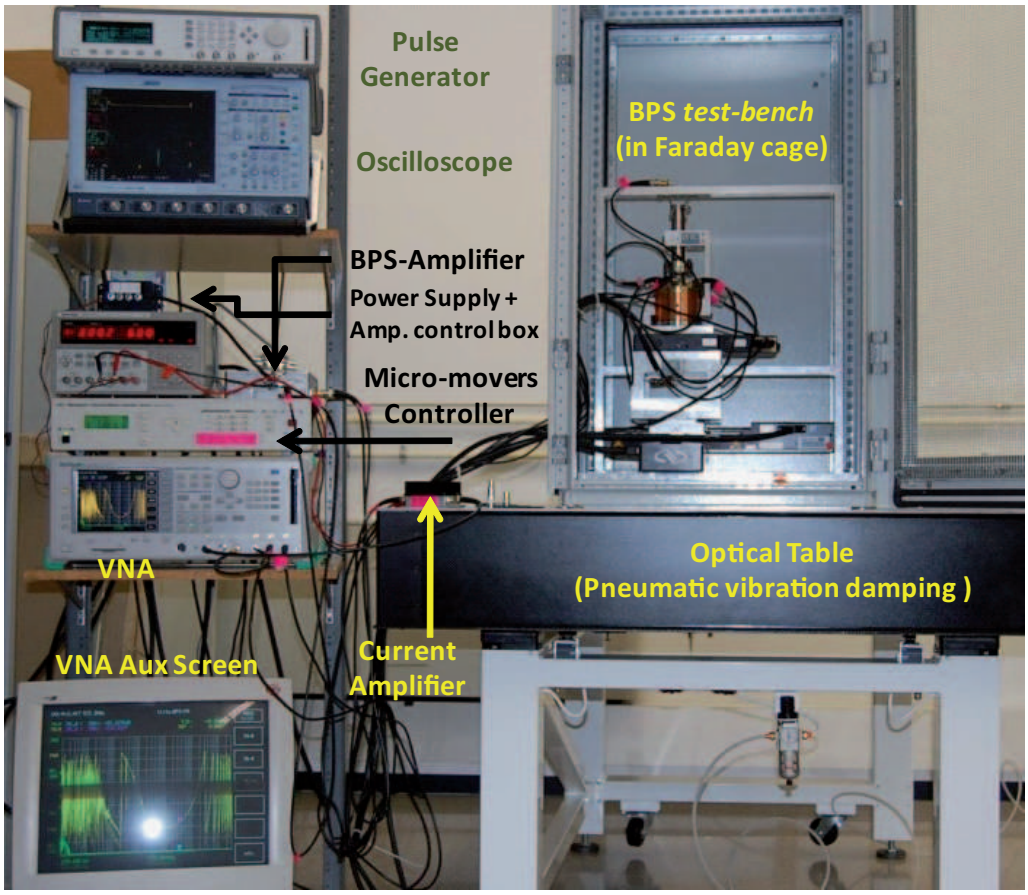

Figure 5.6: Picture of the instrumentation equipment setup and wire test bench for the BPS series characterization tests at the IFIC labs. The name of the main elements are also depicted.

Then the VNA will calculate the horizontal $\Delta H/\Sigma$ and vertical $\Delta V/\Sigma$ voltage amplitudes (averaged with 16 samples to reduce the noise influence), corresponding to each programmed wire position. Both results are eventually sent through a GPIB bus and stored in the PC by the SensAT LabVIEW application for further processing of the linearity test. This application is also responsible of the micro-mover stages control by programming the wire position step trajectories through the motion controller ESP300 also from *Newport* [53].

For the linearity test the AFE amplifier was configured in the low gain mode and no-attenuation operation mode (H-GAIN OFF; BYPASS ON), and the results of the linearity test parameter were obtained for the naked BPS after removing the amplifier gain factors of this specific operation mode, according to the AFE amplifier specifications given in Sec. 4.8.1 and in Tab. 4.7 of the amplifier gain factors.

Frequency response test configuration

The VNA outputs makes now a frequency sweep of the bandwidth of interest covering from 100 Hz to 300 MHz, and with the same output signal power of 10 dBm as for the linearity test but directly feeding the wire input and bypassing the current amplifier due

to bandwidth limitations. The calibration inputs of the BPS $Cal_{\pm}$ are also excited with the VNA and passing through the AFE amplifier only for switching them, in order to get the frequency response for these calibration signals.

The AFE amplifier was not used for this test so the VNA input ports were connected directly to the BPS outputs in order to get the characteristic frequency response profile and cutoff frequencies of the BPS outputs and of the difference $\Delta(H, V)$ and sum Σ signals which were obtained by mixing them in the VNA. For the sum of the four BPS outputs first was used two signal combiners (0°power combiner ZFRSC-2050, DC – 2 GHz, from *Mini-Circuits* [56]), but signal mixers could not be used for the BPS outputs difference signals due to their narrow bandwidth limitation.

In Fig. 5.5 the signals flow and connections are depicted in orange for this test configuration and in red the GPIB bus for controlling the equipment involved in this test configuration.

Only in the case of BPS and amplifier combined frequency response, the BPS output signals were sent through the AFE amplifier. This joint frequency response test was mainly performed to adjust the pulse droop compensation of the Δ signals.

Pulse response test configuration

The BPS input signal(s) to the wire or to the calibration inputs is now provided by a pulse generator 81104A (80 MHz) from *Agilent*. Typically a square pulse signal of 2.5 V amplitude and 2 μs width was used for this tests.

Then the four output signals from the BPS are read directly by the oscilloscope a Wavepro950 (1 GHz) from *Lecroy* in order to get the pulse response of the standalone BPS. Like for the frequency response test, no signal mixers were used for the $\Delta(H, V)$ signal which were mixed in the oscilloscope itself, as well as for the Σ signals but first using signal combiners without limiting the bandwidth of interest.

In Fig. 5.5 the signals flow and connections are depicted in green for this test configuration and in red the GPIB bus for controlling the equipment involved in this test configuration.

Only in the case of BPS and amplifier combined pulse response the BPS output signals were sent through the AFE amplifier. This joint pulse response test was mainly performed to adjust the pulse droop compensation of the Δ signals, likewise the frequency response test.

5.2.3 System control and data acquisition software application

In Fig. 5.7 is shown a snaphot of the front panel of SensAT v1.0 application which was specifically developed in LabVIEW for the control and DAQ of the characterization test setup.

The application front panel is divided in small panel areas which have a title top indicating their function. At the front panel top are displayed the basic information of the BPS under test, the AFE amplifier used and the date of the test (top left), as well as the undergoing wire step trajectory and the elapsed time of test (top right). The BPS and amplifier information has been introduced before in the panel “BPS+Amplifier Definition” (mid left). In the panel below are displayed the coordinate reference system used for the

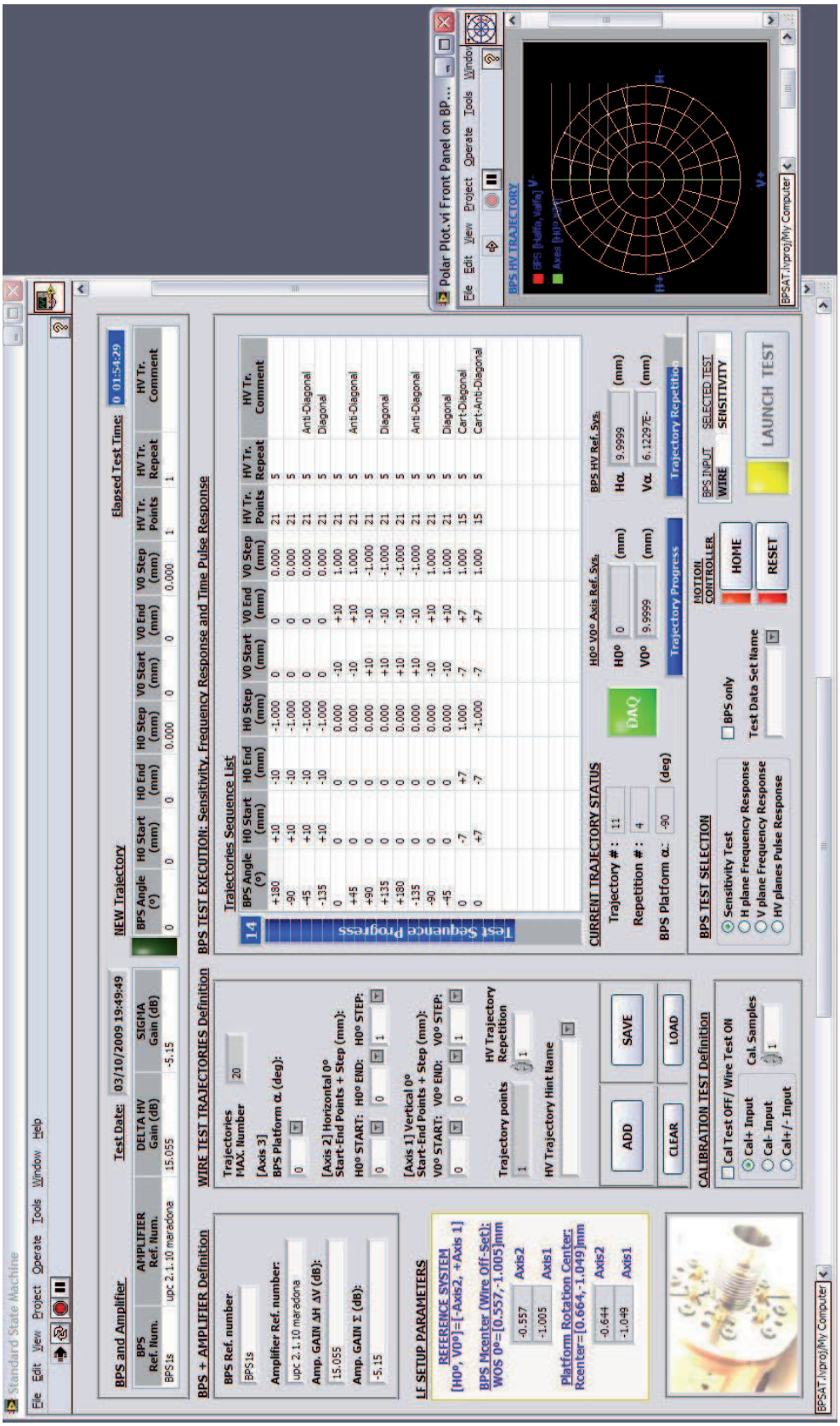

Figure 5.7: Snapshot of the front panel of SensAT v1.0 LabVIEW application for the control and DAQ of the characterization test setup. A pop-up window is displayed in the application to follow the wire position trajectories during the test (bottom right).

test, the BPS mechanical center and the wire rotation center coordinates which are corrected for every test launched by the application (for precaution this metrology info can not be edited from this panel).

Just next to these panels, a control panel with title "WIRE TEST TRAJECTORIES Definition" allows to define every wire trajectory with the wire position steps, relative rotation angle and the number of trajectory repetitions (getting then the same number of signal samples per position). Here each wire trajectory can be programmed for every test and thus added to the "Trajectories Sequence List" at the right. The list can be saved to disk with a simple formatted text in order to be loaded at any other moment. Below this list is displayed the current trajectory information and status with also progress indicators of the whole test. Also the same wire trajectory path is displayed graphically in a pop-up window to follow it within the BPS reference horizontal and vertical coordinate axes (bottom right).

At the front panel bottom are placed the following control panels: "CALIBRATION TEST Definition" for choosing the BPS excitation signal, wire input or calibration input, in this case has to be selected which BPS calibration inputs are excited and the wanted number of calibration samples; "BPS TEST SELECTION" determining which test want to be performed among the available test configurations mentioned before; and three control buttons (bottom right), the "HOME" and "RESET" for homing all the micro-movers and reseting the motion controller respectively, the last "LAUNCH TEST" is to start the programmed test. Like for the wire trajectory, particularly for the frequency and pulse response tests are also used pop-up windows showing a first plot of the acquired signals (not shown in this front panel snapshot).

Finally, the acquired data is stored in formatted text files and classified in folders with the BPS unit name and with also a formatted file name corresponding to the type of performed test in order to later on link the files and import them with MATLAB for off-line processing.

5.3 Characterization low frequency tests results. The BPS benchmarks

In this section are presented the characterization test results corresponding to: first, the linearity test in order to determine the sensitivity, electrical offset and accuracy parameters for both horizontal and vertical coordinates; and after, to the frequency response test from which were extracted the characteristic cutoff frequencies of the standalone BPS for the Δ and Σ signals and in the wire and calibration input excitation cases.

The plots for these test cases are presented with an example of, and corresponding to, the BPS1s unit. The characterization test were performed systematically on all the 16 BPS units after installed in the TBL, the main plots are also shown with the results for each BPS overlapped in the same figure. The BPS specific parameters, as well as their averages over all the units are then summarized at the end of this chapter, in Tab. 5.1 for the linearity test and in Tab. 5.2 for the characteristic cutoff frequencies and pulse time constants. These are considered the BPS parameters benchmarks that characterized the lab performance of the BPS units and in principle fulfilled the TBL specifications.

Concerning the BPS resolution parameter, an estimation at low current was done from the data collected in these characterization tests and it will be presented in Sec. 5.5 to be compared to the BPS resolution obtained from the beam test study with a higher beam current.

5.3.1 Linearity test

The purpose of this test is to obtain the vertical and horizontal sensitivity $S_{x,y}$, as the slope of the linear fit, according to the inverse of the linear approximation Eqs. (3.43, 3.44) in Sec. 3.5.2, by measuring the variation of the normalized difference signals, $V_{\Delta H}/V_{\Sigma}$ and $V_{\Delta V}/V_{\Sigma}$, with respect to the wire vertical and horizontal positions (x, y) programmed in the translation stages. With the same measurements can be calculated the horizontal and electrical offset $\delta_{x,y}$ as the intercept of the linear fit getting the position deviation from the BPS mechanical center given by the BPS signals with $V_{\Delta(H,V)}/V_{\Sigma} = 0$.

The measurements were taken for each BPS unit following the procedure described before in Sec. 5.2.2 and corresponding to the linearity test configuration where the known AFE amplifier gain factors are corrected in order to get the parameters for the standalone BPS.

The BPS signals output is measured for a typical wire trajectories following each horizontal and vertical coordinate lines (H, V), or (x, y), in a range of ±10 mm with 1 mm position steps and to 5 repetitions of the wire trajectories (5 samples/position).

In addition, as commented before in Sec. 5.2.1 of the wire test bench metrology, the wire offset of the test bench is corrected for every wire trajectory placing the wire at the BPS mechanical center, and the other considered alignment errors of wire tilt and wire coordinate lines orthogonality and parallelism are compensated by measuring the typical wire trajectory under 4 different rotations of the BPS reference platform with angles $\alpha = 0°, 90°, 180°, -90°$.

The results of the linearity test below are then obtained with 20 samples per wire position for each coordinate line corresponding to the 5 wire trajectories repetition under 4 wire trajectory rotation angles.

Therefore, in Fig. 5.8a is presented the resulting test plot for the BPS1s from which the sensitivity and electric offsets are determined by a linear fit the measured data in the position range of interest of ±5 mm, according to the TBL specifications, and for both horizontal and vertical coordinates respectively as

$$S_x = (41.56 \pm 0.11) \times 10^{-3}\ \text{mm}^{-1} \text{ and } \delta_x = (-0.003 \pm 0.008)\ \text{mm};$$
$$S_y = (41.16 \pm 0.10) \times 10^{-3}\ \text{mm}^{-1} \text{ and } \delta_y = (-0.06 \pm 0.008)\ \text{mm}.$$

In Fig. 5.8b is also shown the linearity test plot for the full measured position range of ±10 mm. Larger linear deviations are observed at the end positions, although those can be better seen after the linearity error analysis below.

The BPS performance in measuring the beam absolute position is mainly determined by the overall precision (accuracy), σ_x and σ_y, for each horizontal and vertical coordinate. The linearity error plot in Fig. 5.9a is obtained from the residuals of previous linear data fits of BPS1s for each position coordinate. Then, the accuracy are calculated as the root mean square (rms), or variance, of the linearity errors at the wire positions in the range of interest of ±5 mm, and for both horizontal and vertical coordinates respectively yielding

$$\sigma_x = 27.2\ \mu\text{m and } \sigma_y = 24.9\ \mu\text{m}.$$

In Fig. 5.9b is also shown the linearity error plot for the full measured position range of ±10 mm where much larger linear deviations can be observed at the end positions.

Finally, in Figs. 5.10a and 5.10b are plotted the linear data fit lines and the linearity errors with the specified accuracy limits ±50 μm for all the BPS units installed in the TBL. The linearity parameters for each of the BPS units are summarized in Tab. 5.1, where are also included the averages of their parameters and measurement errors. In this characteristic parameters table are also included for both horizontal and vertical coordinates: the position sensitivity corresponding to the inverse parameter of the sensitivity calculated as $k_{x,y} = S_{x,y}^{-1}$, and the maximum linearity deviations $\epsilon_{devx,devy}$ obtained as the maximum excursion percentage of the linearity error within at the wire position range of interest (±5 mm); which are sometimes required and also useful for comparison with other pick-ups.

There can be seen that the accuracy is under specifications for all the BPS, although the worse accuracy result was for the prototype BPS1-v2 which was measured with, and perhaps affected by, the first test bench not so well-adapted to the BPS test needs.

In principle the sensitivity parameter can be roughly approximated by the inverse of the beam pipe radius $a = 12$ mm for the BPS. Although the sensitivity can be better estimated from Eq. (3.24) (Sec. 3.4) for the BPS electrodes radius $r_{elec} = 20$ mm instead and also considering the electrode angular width or angular coverage of $\phi = 75.17°$ (1.312 rad) specified in Tab. 4.3 (Sec. 4.4), getting respectively theoretical sensitivity and position sensitivity of

$$S_{x,y}^{t} = 46.5 \times 10^{-3}\ \text{mm}^{-1} \text{ and } k_{x,y}^{t} = 21.5\ \text{mm},$$

as a good starting point for the electrodes design compared to the measured sensitivity. The remaining difference can be explained by the losses mainly in toroidal transformers of the PCB circuits, since a slightly lower transfer impedance Z_t of the $V_{\Delta(H,V)}$ voltage signals than of the V_Σ in Eqs. (3.37,3.38,3.39) (Sec. 3.5.2) would reduce the normalized voltage $V_{\Delta(H,V)}/V_\Sigma$ measurements, from which the sensitivity $S_{x,y}$ for both coordinates are obtained decreasing them as well.

In addition, a higher order non-linear fit can still be performed on the BPS position data in order to improve (reduce) the accuracy in the absolute position measurement, as can be seen in the well defined shape of the linear fit residuals of Figs. 5.9a and 5.10b, although was not in principle required for the TBL specifications.

Calibration procedure of the BPS units in the TBL

The sensitivity and electrical offset parameters for both (x, y) horizontal and vertical coordinates are incorporated to the TBL instruments database in order to measure the beam position along the line, after performing the calibration procedure described in [57]. Basically, in this procedure are used the BPS calibration inputs $Cal_\pm$ to get the scaling factors that will calibrate the influence of the cabling and devices of the signal paths from each BPS in the TBL/CTF3 facility. These scaling factors are directly applied as a proportional

correction factor to the Δ and Σ voltage signals in the linear relations of Eqs. (3.25, 3.26) with the BPS linearity test parameters herein determined.

Moreover, in order to measure the absolute beam position, the mechanical offsets introduced when installing the BPS units in the TBL line are corrected by adding them to the electrical offsets of each unit in the TBL instruments database, as provided by this characterization tests. Although this correction would not be needed for the relative beam position measurement according in principle to the beam positioning needs of TBL.

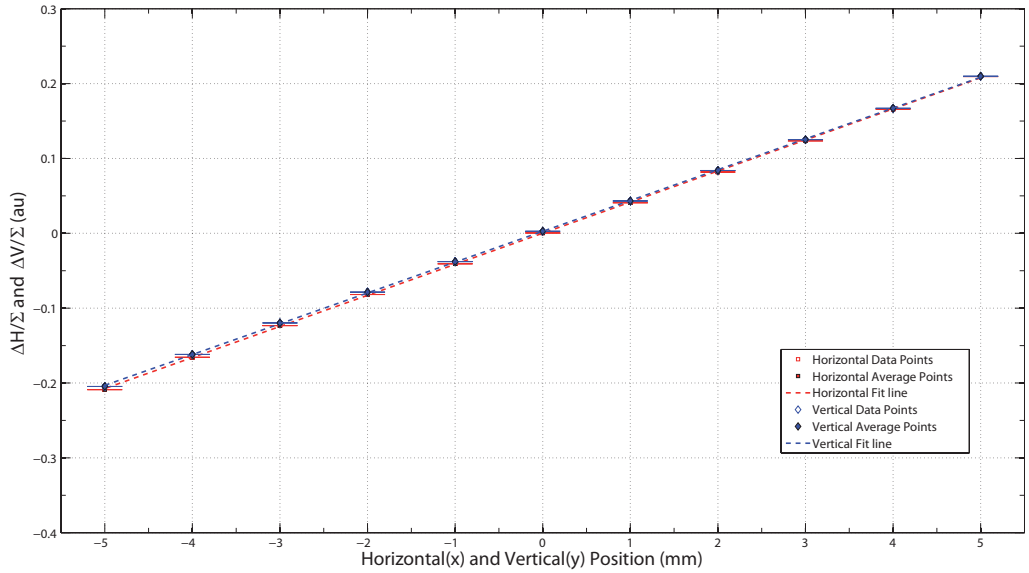

(a)

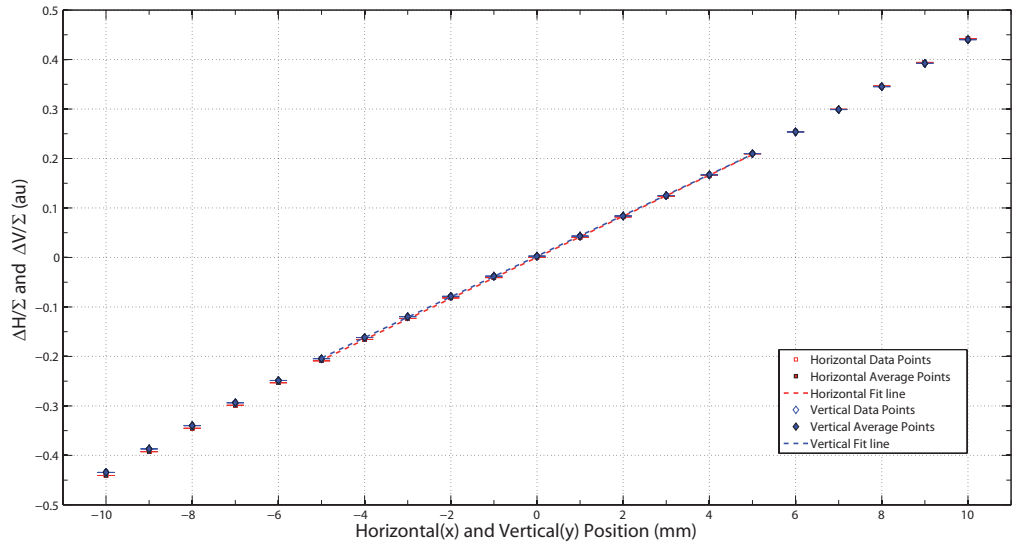

(b)

Figure 5.8: Linear fits of BPS1s unit for calculation of the (H, V) sensitivity $S_{x,y}$ and electrical offset $\delta_{x,y}$. (a) Measured data with 20 samples/position in the position range of interest ±5 mm with 1 mm position step. (b) Same data fit but for the full measured position range of ±10 mm.

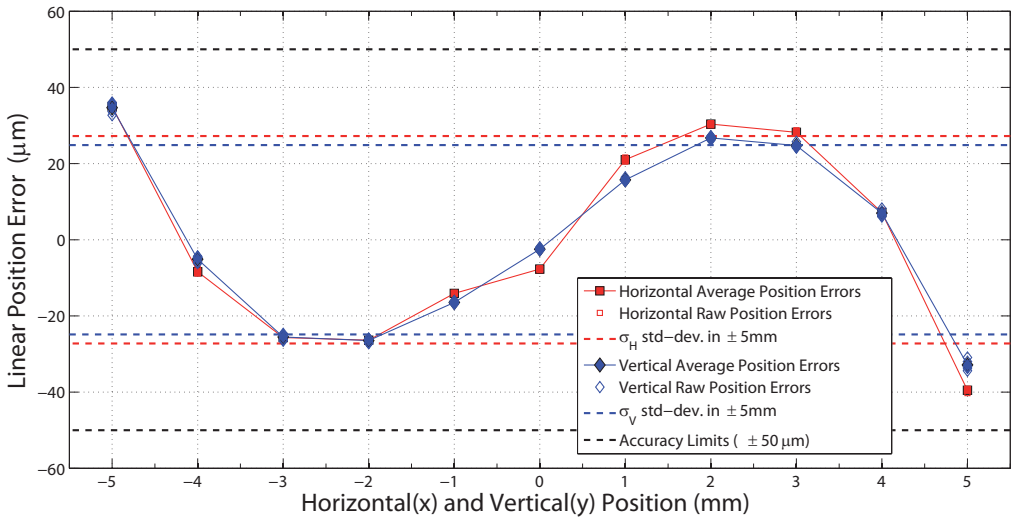

(a)

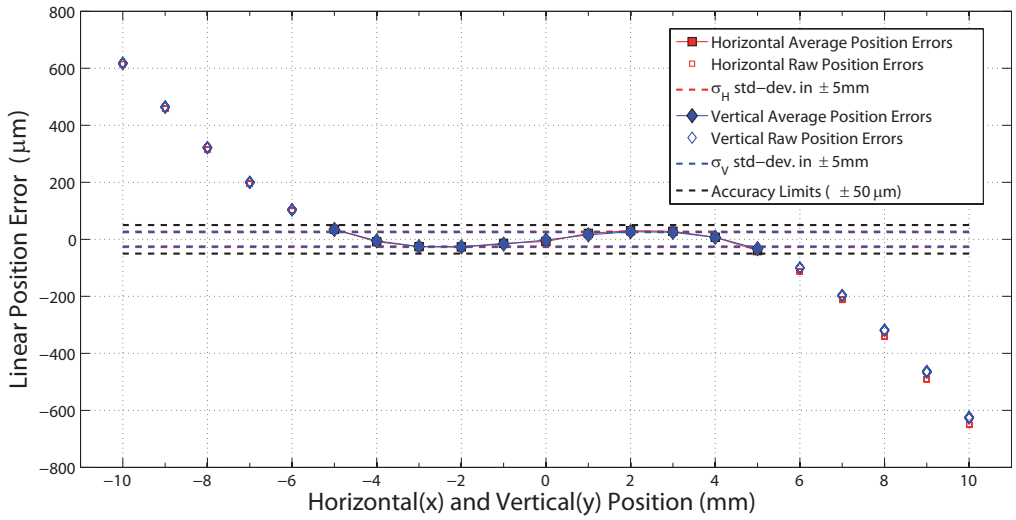

(b)

Figure 5.9: Linearity error of BPS1s for the calculation of the (H, V) accuracy $\sigma_{x,y}$ (red, blue dotted lines) as the rms of the position errors. (a) Measured data with 20 samples/position in the position range of interest of ±5 mm with 1 mm position step. (b) Same data fit but for the full measured position range of ±10 mm.

5.3.2 Frequency response test

The main aim of this test to measure the BPS frequency response profile (bandwidth) with two ways of exciting the BPS unit under test, the wire and the calibration inputs $Cal_{\pm}$, and in order to mainly determine the characteristic low and high cutoff frequencies, f_{low} and f_{high}, for the Δ and Σ signals. Then, its associated pulse droop and rise time constants, $\tau_{droop\Delta}$ and τ_{rise}, can be calculated as the inverse of the low cutoff frequencies from Eqs. (3.61) in Sec. 3.5.3.

This test was performed following the procedure described in the frequency response

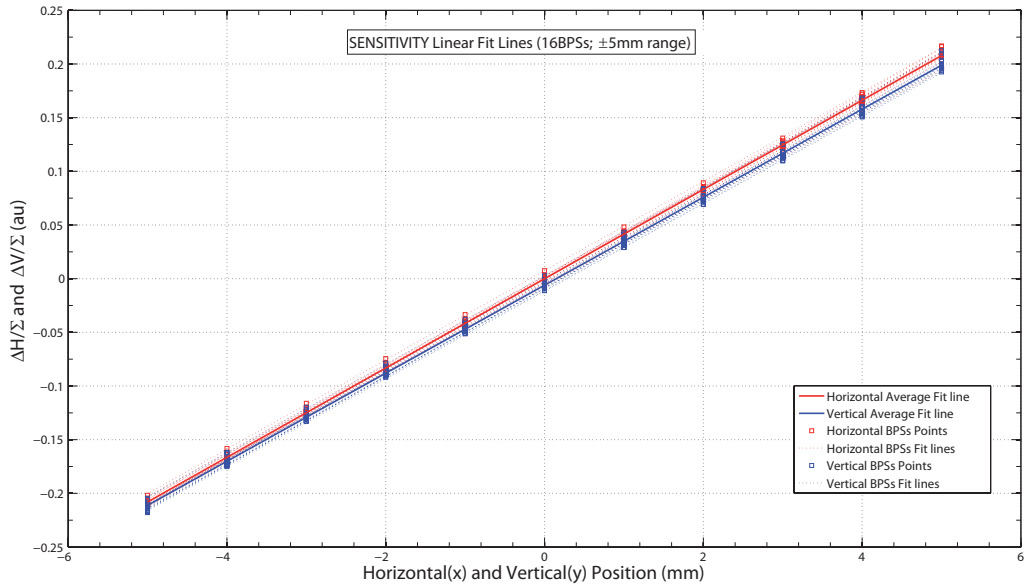

(a)

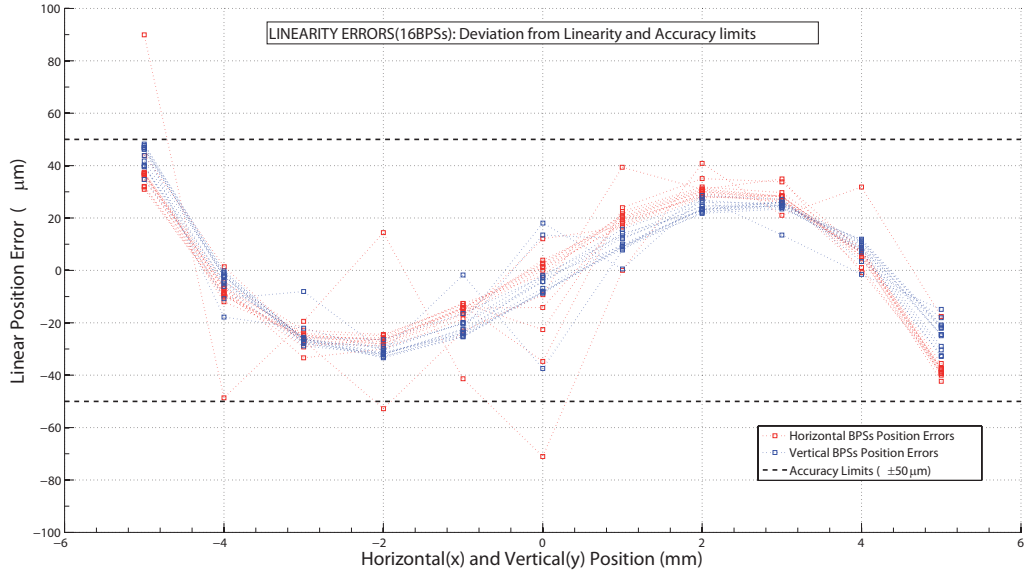

(b)

Figure 5.10: Linear fits results (overlapped) of all the TBL BPS units (16) in the position range of interest ±5 mm. (a) For calculation of the (H, V) sensitivity $S_{x,y}$ and electrical offset $\delta_{x,y}$ of each BPS. (b) For calculation of the (H, V) accuracy $\sigma_{x,y}$ of each BPS.

test configuration of the equipment setup in Sec. 5.2.2 and for several meaningful wire positions at the BPS center and extreme off-center displacements, as well as for the calibration input excitation. The frequency response results are first presented for the BPS electrode outputs ($V_{\pm}$,$H_{\pm}$), and after for the resulting mixed signals: the difference signals for both coordinates (ΔV, ΔH) and the sum signal Σ.

Frequency response of BPS electrode outputs

In Figs. 5.11 and 5.13 are presented the frequency response plots measured for the four electrode outputs of the BPS1s and corresponding respectively to a centered wire and, the equivalent calibration case with balanced signals driving the $Cal_{\pm}$ input ports. From these plots the low cutoff frequencies can be determined at magnitude fall of -3 dB, and then its associated pulse droop time constants, being respectively for (H_+,H_-,V_+,V_-):

$$f_{low} = (2.58, 2.47, 2.78, 2.62) \text{ kHz and } \tau_{droop} = (61.7, 64.4, 57.2, 60.7) \text{ μs};$$

$$f_{low,Cal} = (2.51, 2.54, 2.58, 2.62) \text{ kHz and } \tau_{droop,Cal} = (63.4, 62.7, 61.7, 60.7) \text{ μs}.$$

In Figs. 5.12 and 5.12 the BPS1s electrode outputs frequency response is obtained for an off-center wire at two positions with displacements of +10 mm along the horizontal and vertical coordinates; and, the equivalent calibration case with unbalanced signals driving only the Cal_+ input port. The other cases of negative wire position end of -10 mm and Cal_- were measured for the BPS1s although are not shown since they represent the complementary situation for the electrodes response with negligible difference (under ~10 Hz) of their low cutoff frequencies from the positive cases.

As can be seen in these plots, for both excitation cases the electrodes are not sensitive to the off-center wire positions, or the calibration inputs unbalance, at low frequencies. Only at some point at higher frequencies the electrodes start to detect the wire position, or calibration signal, variation, which will determine the Δ low cutoff frequency as the electrode signals difference. This behavior is explained in Chap. 4 according to the BPS electrical model.

It also must be noted that the magnitude difference of approximately -10 dB for the wire excitation case plots. Both calibration input ports and wire input port were driven by the same power of 10 dBm coming out from the VNA, but finally the wire had lower current caused mainly by the input resistor divider and the wire load, though not affecting the frequency response profile.

Frequency response of Δ and Σ mixed signals

In Fig. 5.15 is presented the frequency response plots measured for the ΔH, ΔV and Σ signals of the BPS1s, and corresponding respectively to a centered wire and, the equivalent calibration case with balanced signals driving the $Cal_{\pm}$ input ports. From these plots only the low cutoff frequencies of Σ signals for both excitation cases, and its associated pulse droop time constants, can be determined, being

$$f_{low\Sigma} = 2.58 \text{ kHz and } \tau_{droop\Sigma} = 61.7 \text{ μs};$$

$$f_{low\Sigma,Cal} = 2.51 \text{ kHz and } \tau_{droop\Sigma,Cal} = 63.4 \text{ μs}.$$

For this case of a center wire, or balanced calibration input, the difference Δ signals are canceled until a magnitude level around -85 dB (within the pass-band), as an approximate floor for the common mode noise rejection of the BPS. Then, in order to measure the low cutoff frequencies for the Δ signals for an approximately centered wire case, there were measured from the frequency response plot in Fig. 5.16 for a wire slightly moved away from the center at two positions with +1 mm displacements along the horizontal

and vertical coordinates. The corresponding low cutoffs, and associated pulse droop time constants, for the ΔH and ΔV signals are

$$f_{low\Delta H} = 226 \text{ kHz and } \tau_{droop\Delta H} = 704 \text{ ns};$$
$$f_{low\Delta V} = 217 \text{ kHz and } \tau_{droop\Delta V} = 733 \text{ ns}.$$

In Fig. 5.17 the BPS1s ΔH, ΔV and Σ signals frequency response is obtained for an off-center wire at two positions with displacements of +10 mm along the horizontal and vertical coordinates; and, the equivalent calibration case with unbalanced signals driving only the Cal_+ input port. The other cases of negative wire position end of -10 mm and Cal_- were measured for the BPS1s although are not shown since, like for the electrode outputs, they represent the complementary situation for the electrodes response with negligible difference (under ~10 Hz) of their low cutoff frequencies from the positive cases.

Then, the low cutoff frequencies and the pulse droop time constants are, for the wire at off-center positions $(x, y) = (10, 0)$ mm and $(x, y) = (0, 10)$ mm:

$$f_{low\Sigma} = 6.22 \text{ kHz and } \tau_{droop\Sigma} = 25.6 \text{ μs};$$
$$f_{low\Delta H} = 267 \text{ kHz and } \tau_{droop\Delta H} = 596 \text{ ns};$$
$$f_{low\Delta V} = 267 \text{ kHz and } \tau_{droop\Delta V} = 596 \text{ ns};$$

and, for the calibration input Cal_+:

$$f_{low\Sigma,Cal} = 2.58 \text{ kHz and } \tau_{droop\Sigma,Cal} = 61.7 \text{ μs};$$
$$f_{low\Delta H,Cal} = 163 \text{ kHz and } \tau_{droop\Delta H,Cal} = 976 \text{ ns};$$
$$f_{low\Delta V,Cal} = 168 \text{ kHz and } \tau_{droop\Delta V,Cal} = 947 \text{ ns}.$$

As explained in the BPS electrodes response, there is a magnitude difference of approximately -10 dB between the wire and calibration cases due to the lower current in the wire than in the calibration inputs. In addition, it must be noted that the Σ signals for both excitation cases have a magnitude decrease of -6 dB due to the factor 2 reduction introduced by the combiners used for the sum at the VNA input ports. Then, in principle the magnitude of $\Delta(H, V)$ signals will coincide with the Σ magnitude, as it is for the calibration case because, as expected, the $\Delta(H, V)$ signals, each one measures only two electrodes, having so a half magnitude (-6 dB) difference with respect the Σ signal magnitude as being the sum of the four electrodes. In the wire case, there still exists a -2 dB difference between $\Delta(H, V)$ and Σ signals, just because the wire is not, and con not be, at the electrodes closest end position, as the calibration excitation case represents.

Theses magnitude level differences are coherent with the BPS expected response and do not affect the frequency response profile or cutoff frequencies measurements. Also the aim of this test was not to precisely measure them since the BPS signal levels will be eventually calibrated in TBL.

Finally, in Fig. 5.18 are plotted the frequency response of all the BPS units installed in the TBL and corresponding to: a center wire position $(x, y) = (0, 0)$ mm and balanced calibration inputs $Cal_\pm$ for the Σ signals; and an an off-center wire positions $(x, y) = (10, 0)$ mm and $(x, y) = (0, 10)$ mm, and unbalanced calibration input Cal_+ for the

Δ signals. In Tab. 5.2 are summarized these low cutoff frequencies and the corresponding pulse droop time constants for Δ and Σ signals, specific to each BPS unit and also including the parameter averages and standard deviations between all of them.

These characteristic parameters in Tab. 5.2 were obtained systematically for all the BPS units considering the cases of positive wire position and calibration excitation, and also obtaining $f_{low\Delta}$ as the mean of the ΔH and ΔV low cutoffs being nearly the same. The complementary case were not systematically measured on all of them since the parameters difference were negligible (under 10 Hz) as observed before. Concerning the BPS electrode outputs low cutoffs, these are practically considered the same as the Σ low cutoff frequency, $f_{lowelec} \equiv f_{low\Sigma}$, since are mainly determined by the BPS ferrite loop surrounding the four electrodes.

High cutoff frequency and pulse edges considerations

Concerning the high cutoff frequency it could not be determined exactly due to the wire test bench limitations at high frequencies, as stated before. As can be seen from the previous frequency response plots for the wire excitation case, a strong signal spiking is produced at frequencies around 100 MHz so it was difficult to precisely and systematically determine the high cutoff frequency for each BPS signal cases. Nevertheless, from Figs. 5.11 of the BPS electrodes outputs, and Fig. 5.17 of the Δ and Σ signals a -3 dB magnitude fall can be approximately located close to 200 MHz, although not being clear the high cutoff points and perhaps this fall being also caused by the wire reflections. At least a lowest bound of 100 MHz could be set common to all of the tested BPS units which was enough to fulfill the specifications for the high cutoffs. Similarly, a highest bound to the pulse rise time constant τ_{rise} are thus obtained from the inverse of the high cutoff lowest bound according to Eq. (3.61).

Therefore, the high cutoff frequency and pulse rise constant for all the BPS units and common to all the BPS signals fulfilled

$$f_{high} > 100 \text{ MHz and } \tau_{rise} < 1.6 \text{ ns.}$$

and, in consequence, also the TBL specifications for the bandwidth upper limit.

In addition, in the calibration cases the frequency response for the different signals exhibit a magnitude increase from the pass-band level, starting at around 100 MHz and with different raising slopes (see Fig. 5.18). After simulating several options using the BPS electric model (in Sec. 4.7), by introducing a series inductance at the PCB circuit outputs a resonance bump is produced with the stray capacitances (introduced mainly due to the transformers windings) and at different frequencies above 200 MHz for different values. The same would happen for the wire excitation case but it would be masked by the strong reflections at those frequencies, which after a small dip seems to follow the raising tendency beyond 200 MHz.

This particular effect would need a deeper study and more test at higher frequencies for the precise measurement of the high cutoffs. Although, there can also be set the same lowest bound to the high cutoff frequency, which would mainly affect to the pulse raising/falling edges of less importance than the pulse top droop, since the position measurements are sampled at the center of the pulses as explained before in Sec. 3.5.3.

Low cutoff frequencies and pulse droop considerations

Because the pulsed beam of TBL will have a maximum pulse period of t_{pulse} = 140 ns, the specification for the $f_{low\Delta}$ was set as low as 10 kHz in order to correspondingly get a droop time constant of τ_{droop_Δ} = 16 μs for the Δ pulse signal, according to Eq. (3.61) and as it was explained in Sec. 3.5.3. Following the rule stated there of $\tau_{droop_\Delta}/t_{pulse} \simeq 10^2$ the Δ pulse droop time will be much larger than its pulse period allowing a good flat-top pulse transmission through the BPS outputs.

The measured Δ signals low cutoffs $f_{low\Delta}$ of all the BPS units, clearly above the specified 10 kHz, were provided by these frequency response tests in order to perform the pulse droop compensation strategy implemented in the external amplifier Δ channels, as described before in Sec. 4.8.1.

The high Δ low cutoffs was an expected consequence from the BPS design, since the one-turn magnetic loop of the ferrite and the electrodes used for extending the BPS frequency response towards lower frequencies, was only effective for individual electrodes and for the sum signal Σ, but not for the Δ signals. This is, basically, because the one-turn loop effect is canceled out when making the difference of the electrode signals, as also stated in previously.

In addition, for the calibration and the wire signal inputs it was found a big difference between their corresponding low cutoff frequencies of Δ signals, with smaller low cutoff for the calibration excitation than for the wire, $f_{low\Delta,Cal} < f_{low\Delta}$, and with a difference between them of about 100 kHz. These low cutoff measured values can be checked in Tab. 5.2.

Focusing just in one BPS electrode channel, the toroidal transformer primary side have, in principle, equivalent single winding turns, one from the input calibration circuit in the PCB and other being the electrode itself with its end screw going through the toroidal transformer (see Figs. 4.9, 4.13). This is the case for the Σ signal, also equivalent to the one-electrode response, with the wire positioned at the BPS center, where the low cutoff frequencies, $f_{low\Sigma,Cal}$ and $f_{low\Sigma}$, for both calibration and wire excitations have the same value, as shown for the BPS1s measurements above. Thus meaning that their respective single-turn inductances of the transformer primary are also the same.

For the Δ frequency response the low cutoff can not be measured at a center wire because the signal is canceled at this position, although the Δ low cutoffs $f_{low\Delta(H,V)}$ could be measured for a small displacement of 1 mm from the wire center, as well as for the 10 mm off-center displacement.

From the Δ frequency response measurements, is also observed that the low cutoffs exhibit a clear position dependency increasing with larger off-center wire displacements with respect the calibration low cutoffs $f_{low\Delta,Cal}$ as the reference value. The Σ frequency response also showed a position dependency in the same way as the Δ signals, although $f_{low\Sigma}$ is still kept below the 10 kHz low cutoff specifications for the largest measured wire off-center displacement at 10 mm.

The low cutoffs frequency shifts at a given maximum wire displacement x_{max} with respect the reference low cutoff at the calibration or wire position center f_{lowCal} are obtained as

$$\delta f_{low}(x_{max}) = f_{low}(x_{max}) - f_{lowCal}, \tag{5.1}$$

which can be particularized for Σ and Δ signals.

Then, from the frequency response test measurements in Tab. 5.2 the shifts of the Δ signal low cutoff frequencies, measured at a maximum wire displacement x_{max} = 10 mm, could be obtained as the average of all the BPS units being

$$\delta f_{low\Delta}(10\ mm) = +(111 \pm 17)\ \text{kHz},$$

where for the horizontal and vertical Δ low cutoffs is taken the average as $f_{low\Delta}$.

For the Σ signal, the measured low cutoffs in Tab. 5.2 for all BPS units correspond to a center position. The shifts at off-center positions were not measured systematically for all the BPS units since there were small and already under specifications. The Σ low cutoff shift for an off-center position x_{max} = 10 mm was particularly measured for the BPS1s being

$$\delta f_{low\Sigma}(10\ mm) = +4\ \text{kHz}\ ;$$

as can be seen in the frequency response plots of the BPS1s unit.

Summarizing from these results, balanced (*Cal+* and *Cal−*) and unbalanced (*Cal+* or *Cal−*) calibration frequency response yield nearly the same low cutoffs for individual electrode channels, Σ and Δ signals, and having also nearly the same low cutoffs values for the wire or beam excitation frequency response at the center of the BPS monitor. Then for this case, the single calibration turn is equivalent to a strip electrode, carrying the wire induced wall current, in the sense of both acting as the primary inductance of each toroidal transformers, so that BPS calibration can be performed with a pulse calibration current experiencing the same droop as a wire or beam current pulse.

But in the case of an off-center wire, the single calibration turn is no longer equivalent since Σ and Δ low cutoffs are shifted upwards. This position dependency appears when the current is not evenly distributed among the four strip electrodes, as it is for the wall current induction of an off-center wire or beam displacement.

Therefore the low cutoff shifts seems to be related to a change of primary inductance of the electrodes and the mechanism of wall current induction on the strip electrodes which would see a different inductance due to the wire or beam proximity to them. This in fact was linearly modeled with the BPS circuital model by coupling inductors between the strip electrodes, as it was explained in Sec. 4.7, reproducing so the low cutoff frequency shift behavior of the electrodes, although this effect would have to be better understood with further studies, for instance, simulating with EM field solver software for the exact geometry of the four strip electrodes and relevant surrounding elements.

As shown above, the sum signal shift $\delta f_{low\Sigma}$ still leave a low cutoff under 10 kHz specification and at double of the position range of interest ±10 mm, so it would not need to be corrected. In the case of the Δ signals, the low cutoff had to be lowered anyway by performing the pulse droop compensation in the external amplifiers Δ channels, but only the same compensation can be applied for both calibration and wire inputs. Then it was decided to compensate for the calibration, so also for the centered wire case, and for off-center displacements although reduced the shift $\delta f_{low\Delta}$ will produce a droop variation with the wire or beam position. In the next section are shown the results of the pulse test performed on the BPS jointly with the external amplifier which were fundamentally made in order to implement the pulse droop compensation in the amplifier.

5.3.3 Pulse response test

In this last section are presented the results of the pulse response test which were performed on the BPS2 unit and the amplifier test unit, which were used to make the fine adjust of the $\Delta(H,V)$ channels amplifier components values for the pulse droop compensation of the Δ signals as explained before in Sec. 4.8.1. After these tests it was set the definitive values of RC filter components in the feedback loop of the Δ channels first stage operational amplifiers which can be found in Tab. 4.10, and eventually they were applied on all the AFE amplifiers installed in the TBL.

In Figs. 5.19 and 5.20 are shown the signal plots of the stand-alone BPS2 pulse response for the wire and calibration respectively, and before droop compensation by the external amplifier. For this test it was used a positive square pulse input of 5 V and 2 μs pulse length.

In the case of a wire pulse input, there are provided the BPS transmitted pulse signals of the four electrode output channels and the Σ for a centered wire, which have the same droop constant $\tau_{droop\Sigma} = 55$ μs; and the $\Delta(H,V)$ pulse output signals at a 10 mm off-center wire position, for the horizontal and vertical coordinates, with a droop constant of $\tau_{droop\Delta} = 587$ ns (as the average of both coordinate planes).

The same pulse is sent to the calibration inputs to get the BPS transmitted pulse signals for this case and to compare with the wire case. Hence the same BPS pulse output signals are plotted, of the four electrode output channels and the Σ for the balanced calibration inputs $Cal_{\pm}$ (equivalent to a centered wire), with a droop constant of $\tau_{droop\Sigma,Cal} = 57$ μs; and the $\Delta(H,V)$ for the horizontal and vertical coordinates of $\tau_{droop\Delta,Cal} = 976$ ns (as the average of both coordinate planes).

Refer to Tab. 5.2 for the the droop constant of all the BPS units corresponding to their respective low cutoff frequencies. Just remark also that for a given positive input pulse, the turns winding orientation in the transformers was chosen to get an inverted polarity pulse (as shown in pulse plots), according to TBL specifications for an electron beam.

Therefore the Σ signal droop is under specification and needs no compensation, as stated before, and it can be taken as a flat-top reference for the wire and calibration input Δ signals, both experiencing a stronger droop which will be compensated by the amplifier.

In this compensation had to be considered the observed difference between the Δ pulse droops at an off-center wire position and the equivalent unbalanced calibration input as explained below. This difference was caused by the wire or beam position dependency which shifted upwards their low cutoffs, so getting smaller (or faster) Δ pulse droops for the wire case.

The pulse droop compensation is performed on the $\Delta(H,V)$ signals regardless of the type of BPS input excitation, from the BPS electrode outputs in the corresponding amplifier channels, as previously described in Sec. 4.8.1. In Fig. 5.21 is shown the BPS2 pulse response after the amplifier compensation on the Δ signals. As can be seen in this plot, it was decided to compensate for the lowest Δ low cutoffs corresponding to the calibration cases and also to a centered wire or beam position. In principle, this is better to avoid a worse effect of pulse bumps due to over-compensation, otherwise produced if the compensation is made for higher low cutoffs. But mainly this is a trade-off solution that yields a correct droop compensation for the calibration input and also around the BPS center positions, where the pulse droop is reduced down to: 4 % for a pulse length of

2 μs, and 1.25 % for the TBL maximum beam pulse length of 140 ns. But due to the strong frequency shift of the Δ signals as the wire or beam moves away from the center, the worst pulse droop case is observed at extreme wire position of 10 mm which would not be enough compensated. This would need further study in order to diminish this low cutoff position dependency shifts for bigger wire or beam displacements.

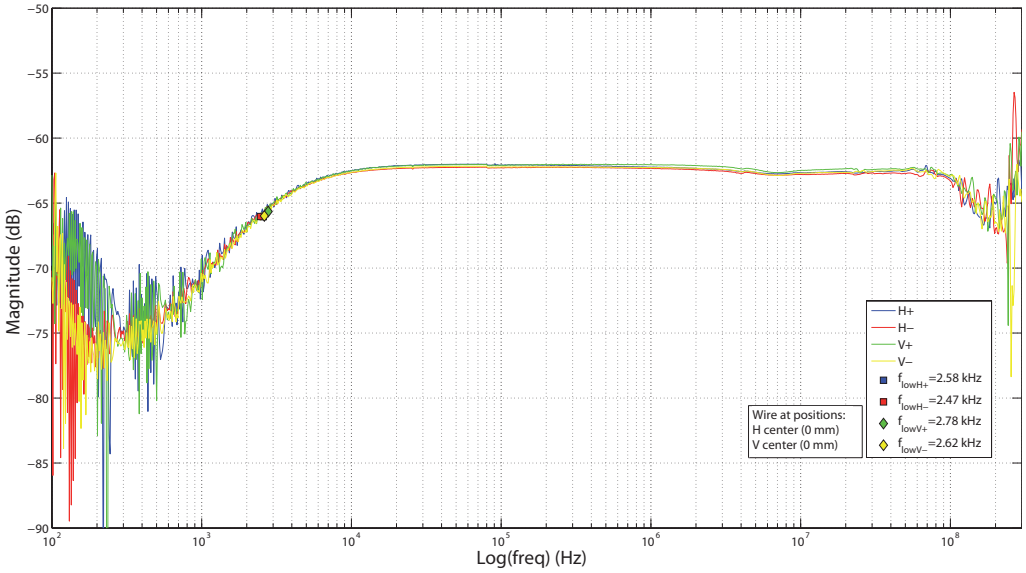

Figure 5.11: Frequency response of BPS1s for the $(H_{\pm}, V_{\pm})$ electrode outputs at the center wire position with $(0, 0)$ mm (H, V) coordinates. The low cutoffs values are shown and are indicated with markers.

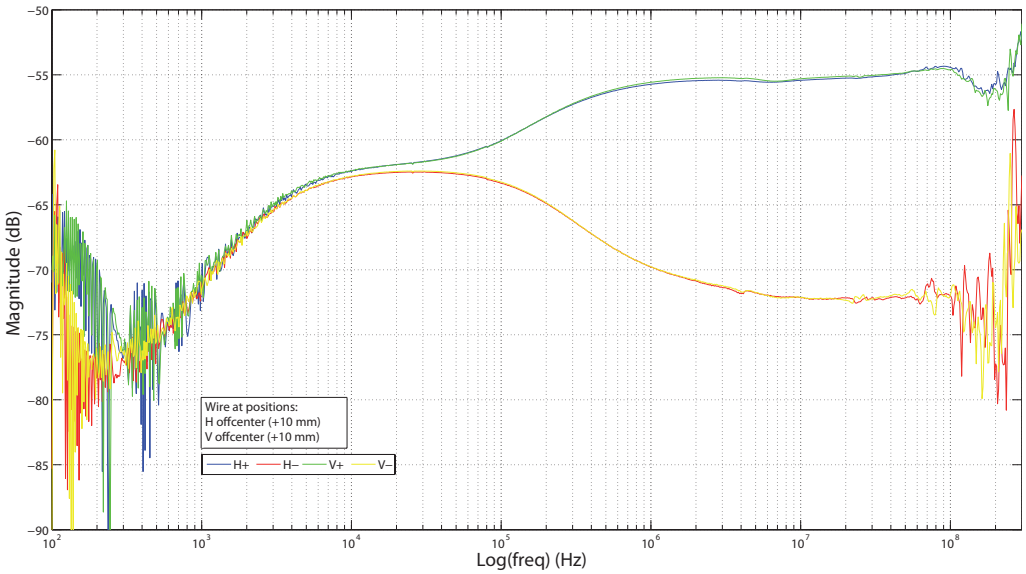

Figure 5.12: Frequency response of BPS1s for the $(H_{\pm}, V_{\pm})$ electrode outputs at two off-center wire positions corresponding to (H, V) coordinates of $(+10, 0)$ mm (H displacement) and $(0, +10)$ mm (V displacement).

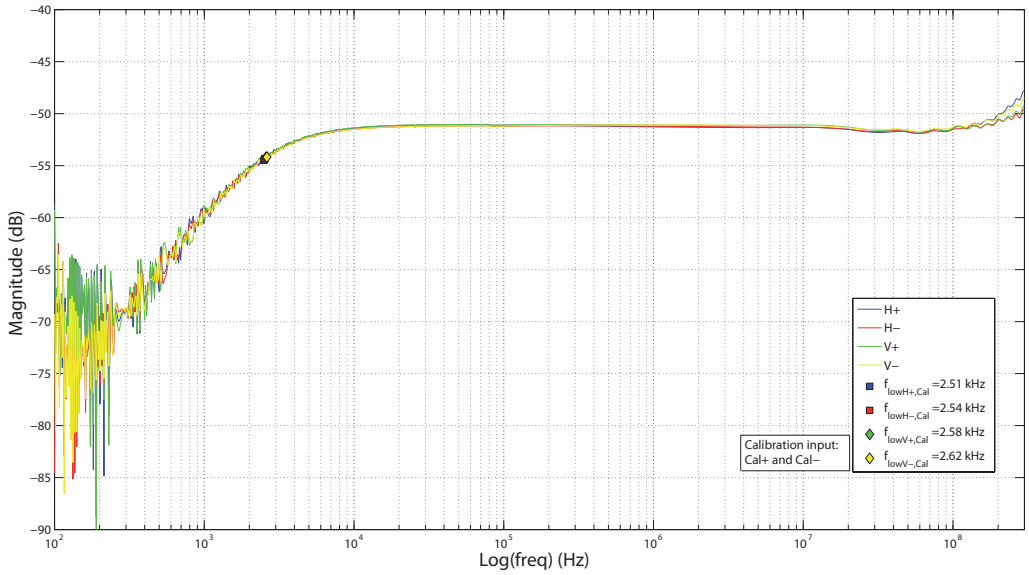

Figure 5.13: Frequency response of BPS1s for the $(H_{\pm}, V_{\pm})$ electrode outputs with balanced excitation at the two calibration inputs $Cal_{\pm}$ (equiv. to a center wire/beam). The low cutoffs values are shown and are indicated with markers.

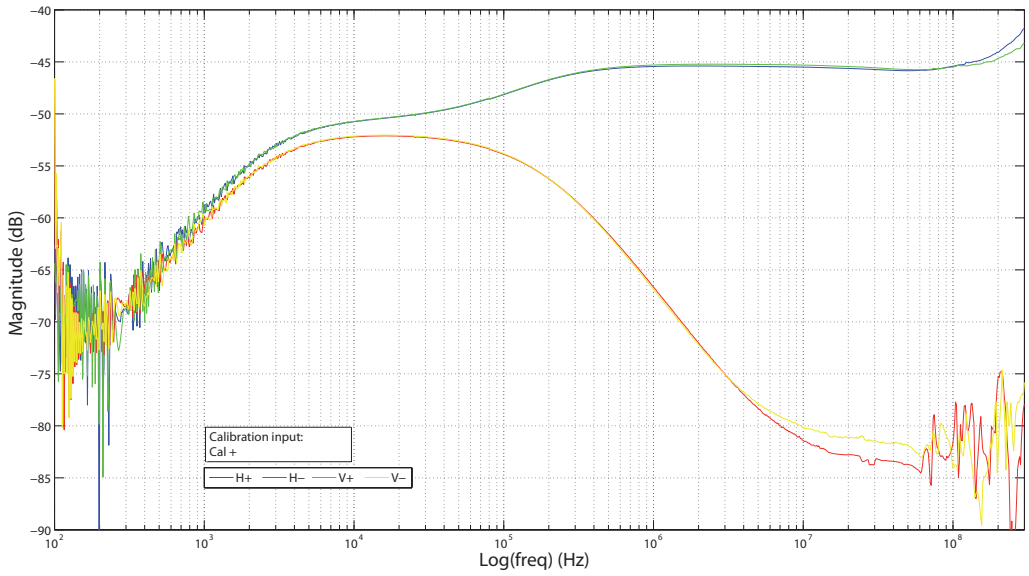

Figure 5.14: Frequency response of BPS1s for the $(H_{\pm}, V_{\pm})$ electrode outputs with unbalanced excitation at only one calibration input Cal_{+} (equiv. to a fully off-center wire/beam).

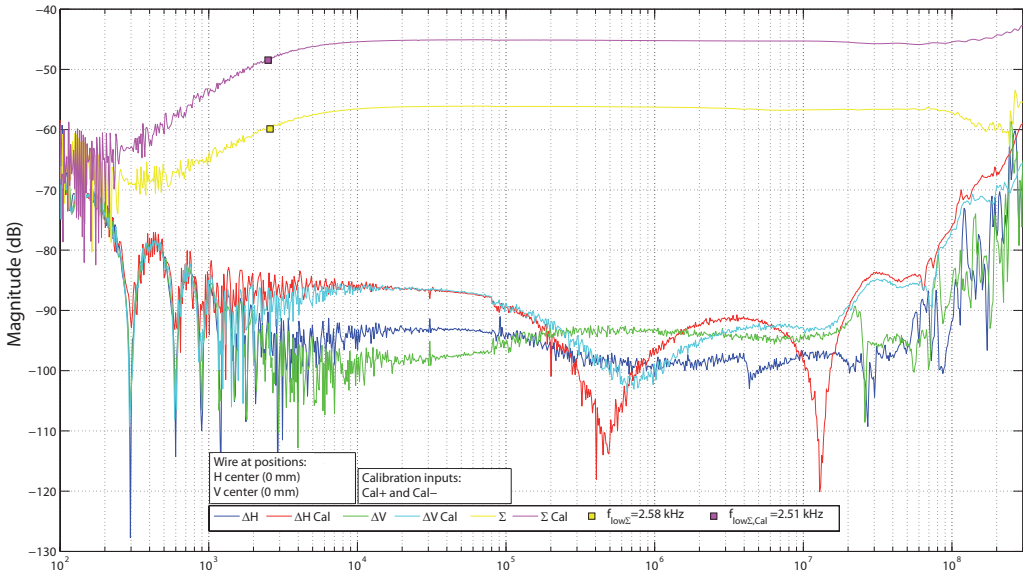

Figure 5.15: Frequency response of BPS1s for the $\Delta(H, V)$ and Σ signals and for a center wire position, with $(0, 0)$ mm (H, V) coordinates, and balanced calibration inputs $Cal_{\pm}$ (equiv. to a center wire/beam). The difference Δ signals are canceled, so only the sum Σ signals low cutoffs values are shown and are indicated with markers.

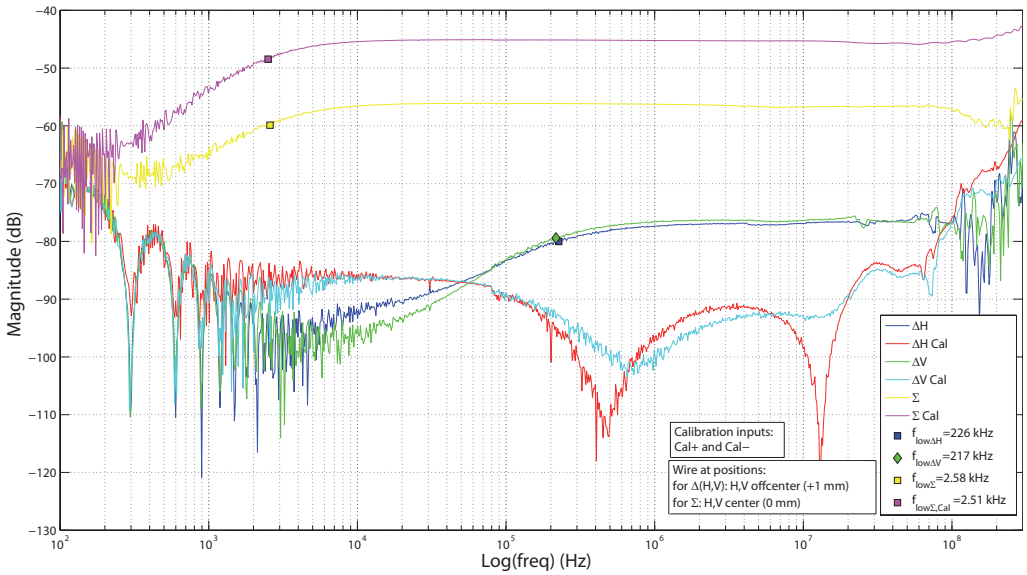

Figure 5.16: Frequency response of BPS1s for the $\Delta(H, V)$ and Σ signals and for small off-center displacements of the wire, corresponding to (H, V) coordinates of $(+1, 0)$ mm (H displacement) and $(0, +1)$ mm (V displacement); and for balanced calibration inputs $Cal_{\pm}$ (equiv. to a center wire/beam). The difference Δ signals are not canceled and can be determined for those wire positions. The low cutoffs values are shown and are indicated with markers.

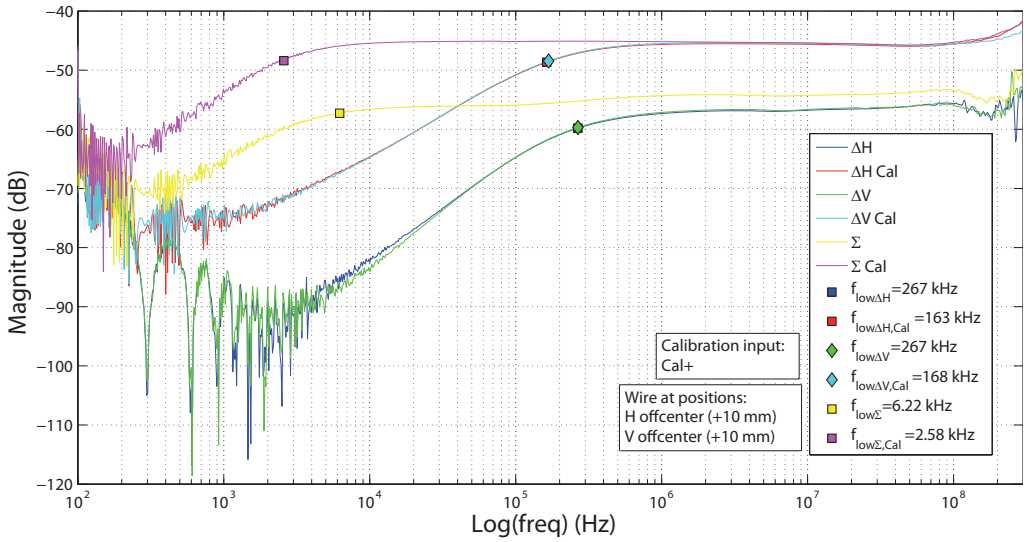

Figure 5.17: Frequency response of BPS1s for the $\Delta(H,V)$ and Σ signals and for two off-center wire positions, corresponding to (H,V) coordinates of $(+10,0)$ mm (H displacement) and $(0,+10)$ mm (V displacement); and for unbalanced calibration input Cal_+ (equiv. to a fully off-center wire/beam). The low cutoffs values are shown and are indicated with markers.

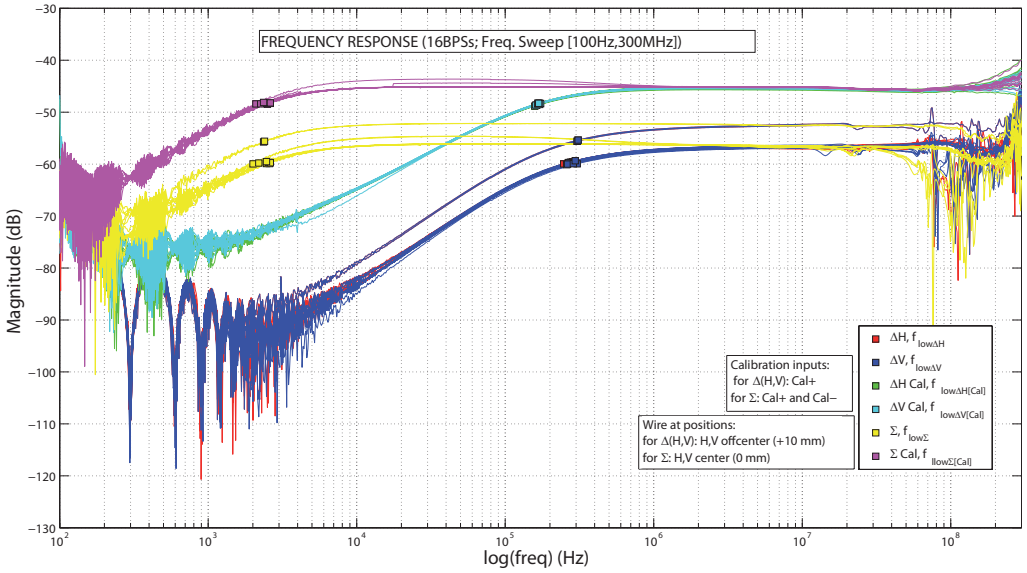

Figure 5.18: Summary plot of the frequency response of all the TBL BPS units for the $\Delta(H,V)$ and Σ signals and for wire and calibration excitation cases. The wire positions and type of input calibration corresponding to the Δ and Σ signals are indicated as well as their respective low cutoffs with markers.

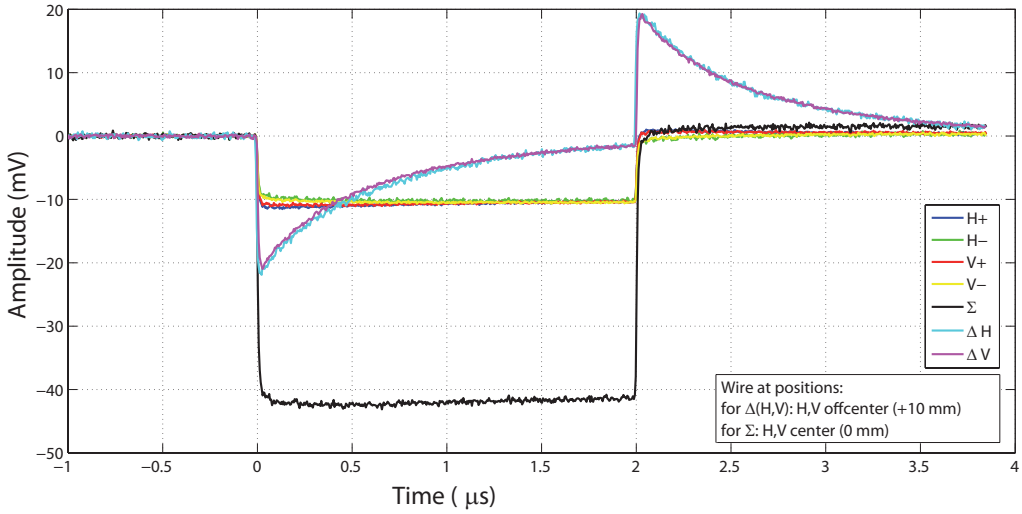

Figure 5.19: Pulse response of BPS2 for the $(H_{\pm}, V_{\pm})$ electrode outputs and Σ signal at a center wire position, and for $\Delta(H, V)$ signals at two off-center wire positions $(H, V) = (+10, 0)$ mm and $(H, V) = (0, +10)$ mm. Positive square pulse of 5 V and 2 μs at the wire input.

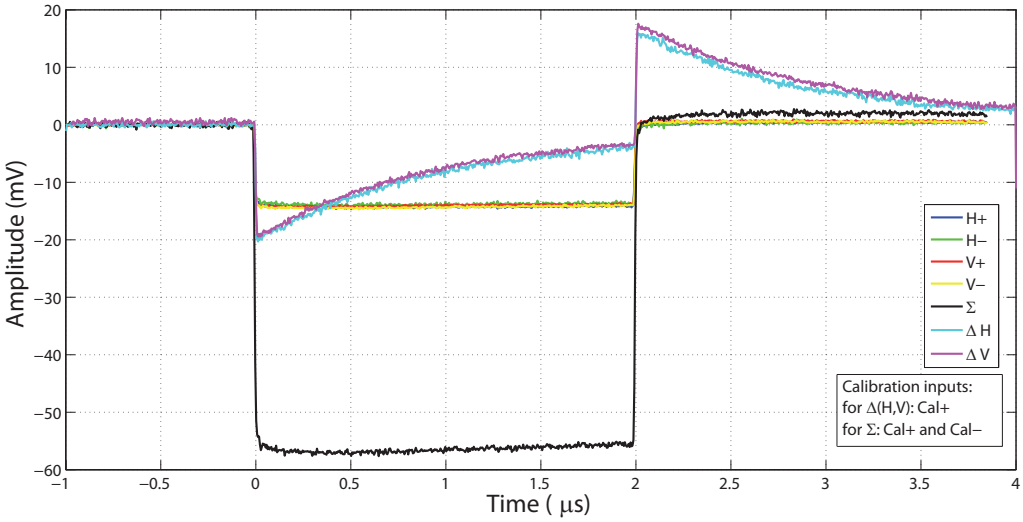

Figure 5.20: Pulse response of BPS2 for the $(H_{\pm}, V_{\pm})$ electrode outputs and Σ signal for balanced calibration input $Cal_{\pm}$, and for $\Delta(H, V)$ signals for unbalanced calibration input Cal_{+}. Positive square pulse of 5 V and 2 μs at the calibration inputs.

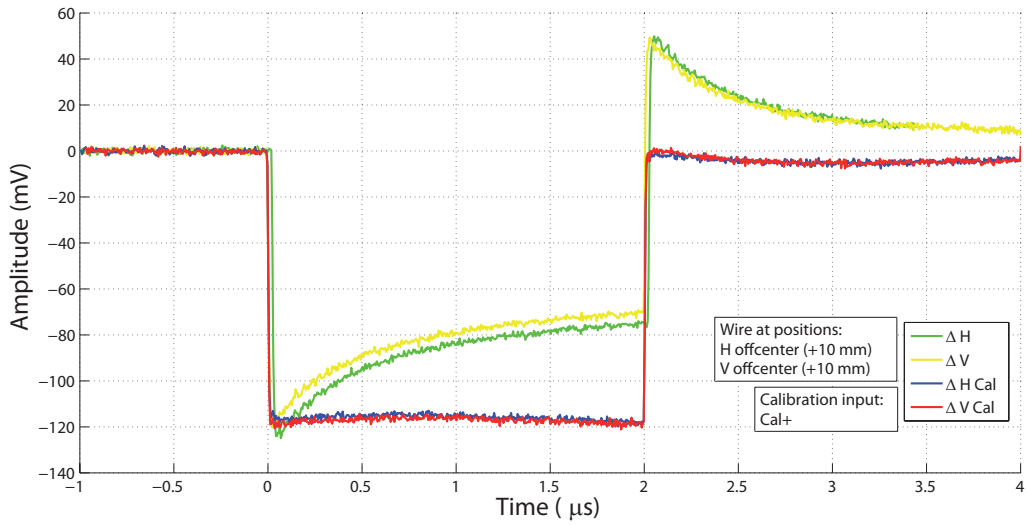

Figure 5.21: Pulse response of BPS2 and the AFE amplifier (in high gain mode) for the $\Delta(H, V)$ signals corresponding to off-center wire positions and unbalanced calibration input Cal_+. Positive square pulse of 5 V and 2 μs at the wire and calibration inputs respectively.

5.4 High frequency test for longitudinal impedance of the BPS

5.4.1 Basic operation mechanism of the BPS monitor

The BPS inner vacuum pipe has a ceramic gap surrounded by gold plated cylinder which is divived along into four orthogonal strip electrodes. The wall current intensity induced by the beam flows through these electrodes at bigger wall diameter, and the beam position is measured by means of the image current distribution among these electrodes that will change according to the beam proximity to them. Thus the current level in each electrode is sensed inductively by their respective transformers, which are mounted on two internal PCB halves as part of the electrode outputs conditioning circuit. In Fig. 4.10 the BPS longitudinal section view shows the vertical plane electrodes, the wall image current flowing through them and the toroidal transformers mounted on the PCBs (same for the horizontal plane). From the PCB circuits, the output SMA connectors give four voltage signals (V_+, H_+, V_-, H_-) that will drive an external amplifier to yield the three voltage signals for determining the beam position and intensity: the sum signal $V_\Sigma = V_{H+} + V_{H-} + V_{V+} + V_{V-}$, to get the beam current intensity proportional to it; and two difference signals $V_{\Delta H} = V_{H+} - V_{H-}$ and $V_{\Delta V} = V_{V+} - V_{V-}$, which are proportional to the horizontal and vertical coordinates of the beam position. Finally, at the digitizer end the coordinates data are obtained from several amplitude samples within the normalized pulse signals respectively as, $(x, y) \propto (V_{\Delta H}/V_\Sigma, V_{\Delta V}/V_\Sigma)$.

Wall image current paths

The beam time structure in TBL is made of pulses between 20-140ns composed of micro-bunches of 83 ps giving a bunching frequency of 12 GHz. The monitor is designed to work in a bandwidth at the beam pulse time scale, from 10 kHz (100 μs) to more than 100 MHz (10 ns), to have a good pulse shape transmission at the electrodes outputs for measuring

the beam position. In principle, the image current, regardless of its frequency components, follows the path through the electrodes for normal operation of the monitor. Nevertheless, the longitudinal impedance, $Z_{\|}$, of the device becomes too large for high frequencies of the image current until the bunching frequency, and higher harmonics extending beyond the microwave X band. This is due to the inductive behavior, which increases linearly with frequency, introduced by the larger diameter step seen by the image current when passing over the electrodes. To avoid this, the inner wall of the ceramics (see Fig. 4.10) was coated with a thin Titanium (Ti) layer deposited by sputtering, giving an alternative path of minimum inductance to the high frequency components of the image current, and limiting so $Z_{\|}$. In consequence, the image current frequency components will follow the electrodes path of minimum resistance for the lower and the Ti coating path of minimum inductance for the higher, having a transition frequency determined by the particular impedances of both paths.

5.4.2 Longitudinal impedance $Z_{\|}$

The resistance value of the coating must be the lowest possible but not too low in order to have a transition frequency above enough the operation bandwidth and to do not reduce it significantly. In the work done in [58] for a previous IPU is determined the coating optimal resistance value around $10\,\Omega$ which is low enough to limit the monitor impedance at the higher frequencies but preserving the BPS operation bandwidth at the lower frequencies that otherwise would be affected by a lower coating resistance. Following that criteria the BPS used the same Ti coating thickness.

The measurement of $Z_{\|}$ is usually performed with the so called wire method where the device under test (DUT), the BPS monitor, is inserted in a test bench of a coaxial transmission line as shown in Fig. 5.22. This method assumes that an ultra-relativistic beam has a closely transverse electromagnetic (TEM) field distribution, what is the case of the 150 MeV TBL electron beam with $\beta \cong 1$, and it can be emulated with a coaxial structure having pure transverse TEM propagation modes to determine $Z_{\|}$. The Scattering matrix parameters (S-parameters) between the two test bench coaxial ports are directly measured from a Vector Network Analyzer (VNA) in the frequency range of interest. Thus $Z_{\|}$ can be obtained from the transmission coefficient, S_{21}, which is the signal drop along the line. But the typical calculation method for lumped impedances is not valid here because the DUT insertion length is already much larger than the main wavelength of the bunching frequency. Instead, the calculation method for distributed impedance proposed in [59] is used as good approximation for the complex longitudinal impedance

$$Z_{\|} = -2Z_L ln\left(\frac{S_{21}}{S_{21R}}\right) \tag{5.2}$$

where Z_L is the impedance of coaxial line test bench, S_{21} is the transmission coefficient of the test bench with DUT, and S_{21R} is the transmission coefficient of the reference measurement, with the DUT replaced by a drift tube to remove the test bench dependency.

5.4.3 The coaxial waveguide test bench simulation and design

The test bench shown in Fig. 5.22 was made of 70/30 brass alloy and built as a coaxial airline of $50\,\Omega$ transverse impedance along the structure, matching with the $50\,\Omega$ output ports of the VNA. The transverse impedance of a coaxial line is written as

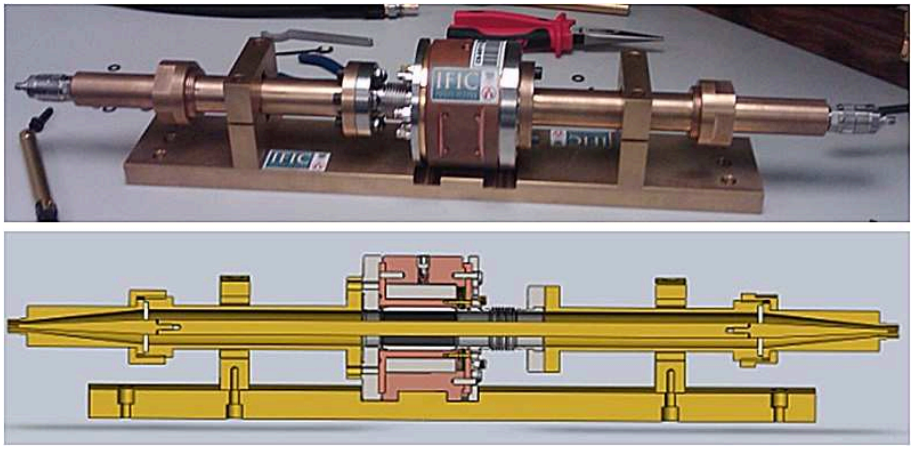

Figure 5.22: High frequency coaxial test bench with the BPS inserted for measuring its longitudinal impedance.

$$Z_{coax} = \frac{c\mu_0}{2\pi\sqrt{\epsilon_r}} ln\left(\frac{r_o}{r_c}\right) \tag{5.3}$$

where c and μ_0 are, respectively, the speed of light and the magnetic permeability in vacuum, it depends on the dielectric permitivity of the medium between conductors and, geometrically, on the radius of the coaxial center conductor, r_c, and the outer conductor, r_o. Since the outer conductor in the test bench straight section must have the same 24 mm aperture diameter of the BPS vacuum pipe, the central conductor is then fixed at 10.422 mm diameter by Eq. (5.3). The test bench input ports are two APC-7mm connectors with screw central conductors what made easier the assembly with the test bench central rod and also with low reflection specifications up to 18 GHz. Thereby a cone geometry was chosen in order to have a 50 Ω smooth transition between the outer diameters of the connector and the test bench straight section, keeping the conductors diameters ratio at constant value. The end connection to the VNA was done via more popular SMA (or 3.5 mm) adaptors with same specifications as the APC-7mm.

The main elements of the coaxial test bench, with the drift tube for reference measurements, was simulated using specialized microwave software FEST3D [60]. The key element in the structure simulation was the transition cones, essentially the cone geometry was loaded into the simulator by linking together short length coaxial waveguides of increasing diameters in a staircase pattern. Cones with several step lengths, l_{step}, were simulated, finally choosing l_{step}=200 µm ensuring small enough steps $l_{step} << \lambda_{max}$ to have no influence due to the staircase discontinuities at maximum simulation frequency, f_{max}=30 GHz. Also the selected cone length was l_{cone}=80mm in a compromise between shortest l_{cone} and lowest S_{11} reflection coefficient to get a smooth enough transition. In Fig. 5.25 are plotted the simulated S-parameters of the full coaxial waveguide with an intermediate section with room to place the BPS and the two symmetric transition cones. This result show a reflection level less than -45 dB in the maximum available bandwidth for the only-TEM modes propagation until 22 GHz where undesired TM modes starts propagating. The theoretical cut-off frequency was calculated being exactly 21.9 GHz [61].

In Fig. 5.24 are shown the S-parameters of the manufactured coaxial test bench, where

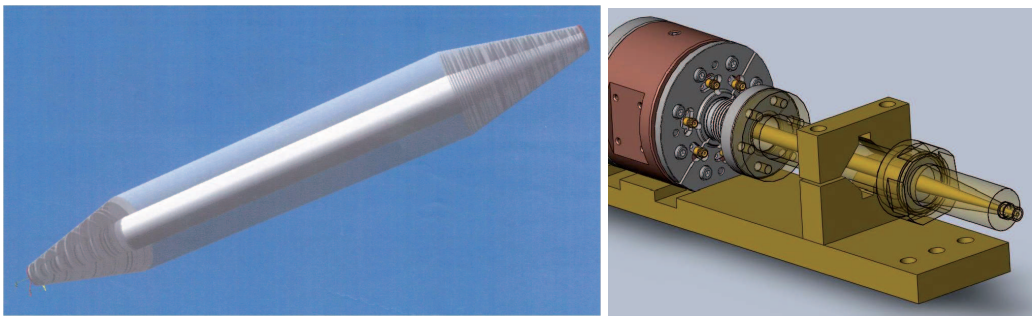

(a) (b)

Figure 5.23: (a) View of the simulated coaxial structure of the high frequency test bench with matching transition cones implemented by adding small coaxial waveguide sections in staircase steps. (b) Detail of test bench mechanical design, zooming on one side to show the matching transition cone implementation.

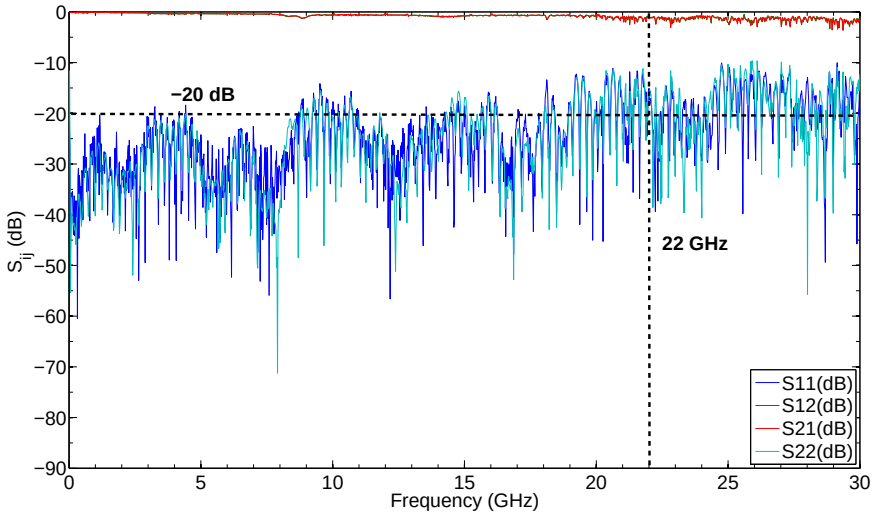

Figure 5.24: S-parameters test results of the manufactured coaxial test bench.

are also indicated the theoretical useful bandwidth at 22 GHz, and the signal reflection level at -20 dB given by S_{11} which was increased, so deteriorated, with respect the simulated one by +25 dB.

Initially, in the test bench design, it was introduced two PTFE washers at the end of the transition cones, keeping the 50 Ω transverse impedance with a diameter step in the outer conductor, to help in the central rod support, but finally they were removed because introduced a resonance around 10 GHz deteriorating too much the test bench bandwidth. Before manufacturing, it was also simulated random mechanical tolerances of the coaxial conductor diameters with 50 μm standard deviations showing a less than 5dB reflection level increase.

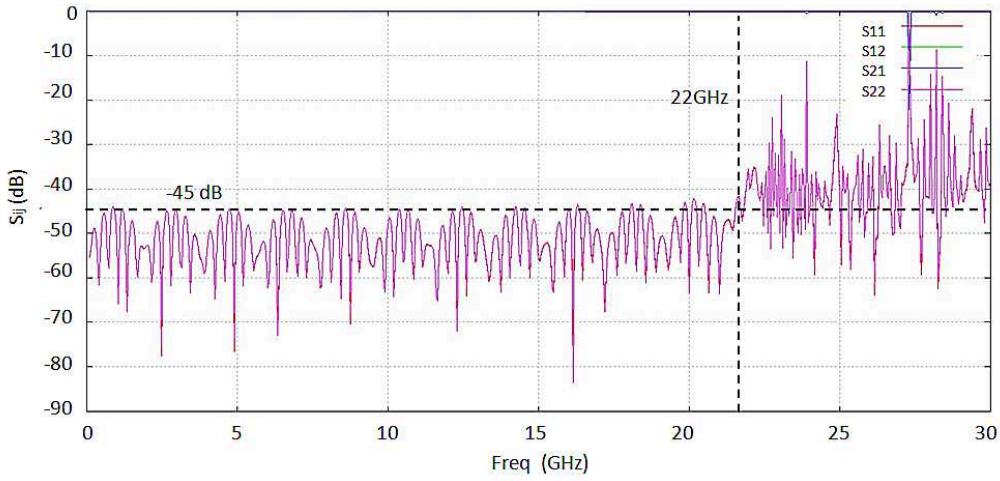

Figure 5.25: S-parameters simulation of the coaxial test bench.

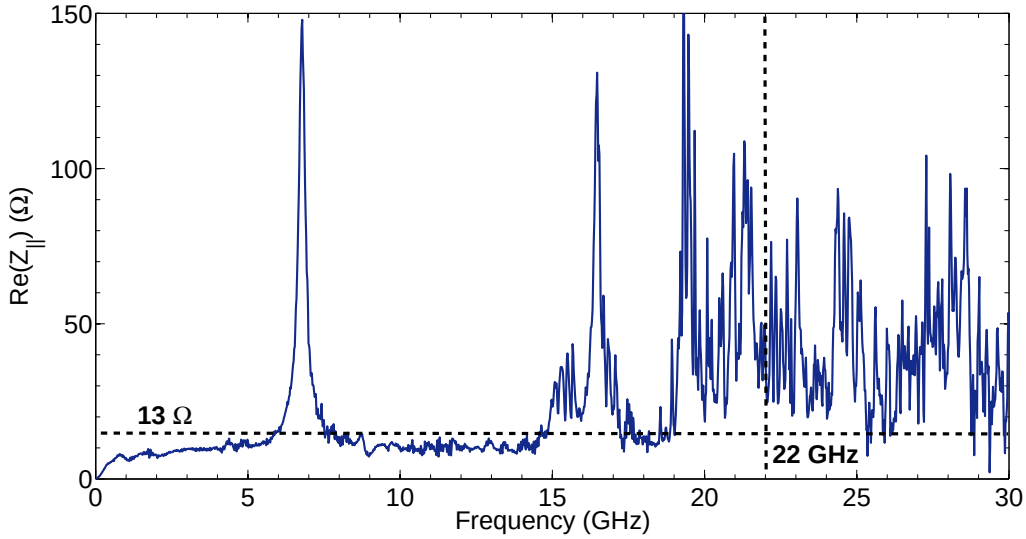

Figure 5.26: Test result plot of BPS longitudinal impedance, $Z_{\|}$.

5.4.4 HF test method and results of the BPS longitudinal impedance

The S-parameters test was carried out using the available VNA equipment at the ESA *European High Power RF Laboratory* in the *Val Space Consortium* (VSC) in Valencia. It was performed on BPS5s unit randomly selected from the series production and according to the method proposed before to determine its $Z_{\|}$ in the 18MHz to 30GHz range. First, the S-parameters between the two ports of the test bench with a drift tube as reference measurement and after, with the drift replaced by the monitor, getting their respective transmission coefficients, S_{21R} and S_{21}. Thus, the plot in Fig. 5.26 shows the real part of the $Z_{\|}$ frequency response calculated from Eq. (5.2). It can be seen here that the $Z_{\|}$ real part exhibit the expected saturation tendency. At low frequencies it increases linearly

until the transition frequency, around 800 MHz, when the Ti layer image current path becomes dominant for these frequency components limiting $Z_{\|}$ below 13 Ω. The limitation is continuously effective up to nearly 6 GHz, then a first resonance occurs at 6.8 GHz with 148 Ω resistive peak to come down again below the 13 Ω. More peaks starting around 15 GHz appears before reaching up to 22 GHz, which was taken as our useful test bench bandwidth due to the theoretical limit imposed by the beginning of TM modes propagation [62], as stated before. Explanation of these resonances needs further study to look for their nature and eventually to check whether the BPS $Z_{\|}$ will show the expected saturation tendency at higher frequencies or these resonances really belong to the BPS design.

5.5 Beam test performance of the BPS

It is essential for CLIC an efficient and stable 12 GHz power production, so the experimental program of TBL is focused on that power production in the X-band microwave frequency range, and the transport of the decelerated beam [63]. In order to insure proper beam transport through the line, the quadrupoles have to be aligned within 10 μm by beam-based alignment demanding to the BPS units a 5 μm position resolution for a beam with 28 A maximum current. Thereby the resolution parameter is considered the BPS figure of merit. Preliminary beam test on BPS resolution were performed in the TBL which are reported in [64]. Here are presented the method and results of the beam test carried out in July 2011 for determining the BPS resolution at different beam currents.

5.5.1 Characterization test benchmark of the resolution parameter

Concerning the position measurement performance there are two main parameters the overall precision or accuracy and the resolution. The accuracy can be seen as the uncertainty in measuring an absolute position with respect to a known reference. In contrast, the resolution represents the uncertainty in measuring a relative position increment being limited by several sources of system noise in the signals used to measure the position.

The accuracy in the BPS is determined as the root mean square of the horizontal and vertical position deviations from the linear fits in the range of interest. The analysis performed on the data from this lab characterization test yield a benchmark accuracy of 32 μm and 28 μm (averaged over all BPS units in TBL) for the horizontal and vertical coordinates which are under the 50 μm specification.

At design phase of BPS on board PCBs its circuit component values were chosen in order to get an output voltage variation with the beam position of 3.5 mV per 5 μm step at 28 A beam current, being at least far above thermal noise.

In order to measure the BPS resolution in the test stand, it has been also analyzed the data for all the BPS units taken before their installation in TBL in the characterization tests at lab. In the Fig. 5.27 are shown the resolution points as the standard deviation of scattered positions at each wire nominal position. The resolution parameter is then given as the standard deviation for all the scattered positions in the full ±10 mm range. The same behavior of the resolution parameter depending on position was observed in the rest of the tested monitors. Resolution improves towards the center of the monitor having the minimum value at the electrical center. This is because the difference signal $\Delta(H, V)$, from which the position is calculated, cancels as it also does the external noise.

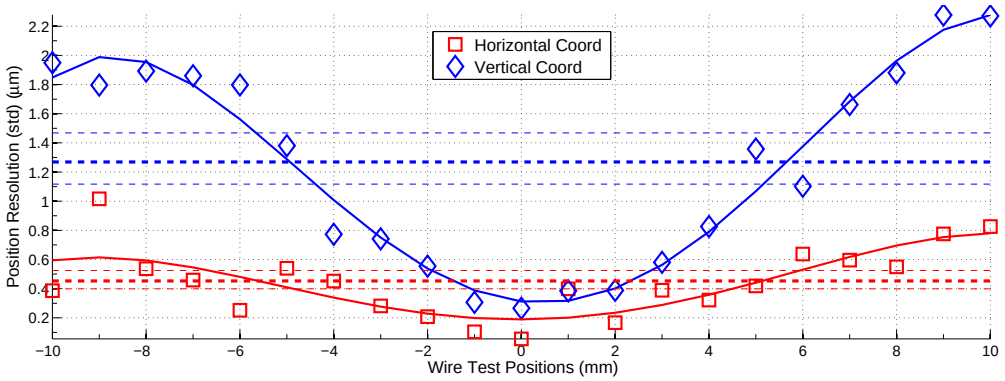

Figure 5.27: Resolution vs. position plot for BPS0510 in the ±10 mm range.

The resolution parameter at wire current of 57 mA, and particularly for the BPS tested with beam, is 0.6 µm and 1.4 µm in the BPS0510, for the horizontal and vertical coordinates respectively (shown in the plot as dashed lines). These resolution levels were obtained for a low noise test stand with a very precise excitation signal of 1 MHz generated with a Vector Network Analyzer. This resolution parameter sets the lowest limit that could be achieved with a BPS, and it can be considered as test benchmark.

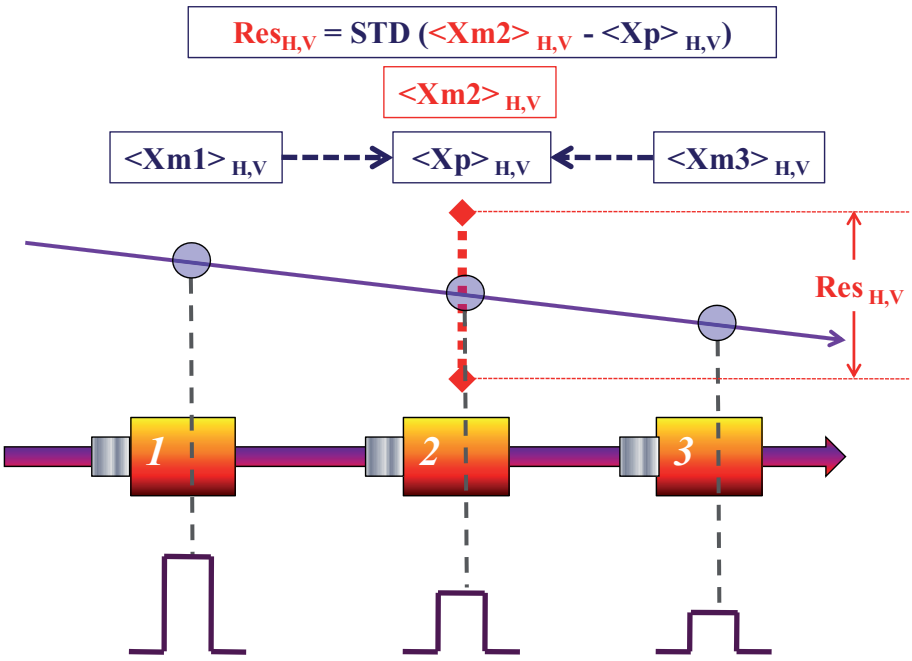

Figure 5.28: Illustration of the 3-BPMs resolution method.

5.5.2 Beam test for the BPS resolution measurement

Since the beam positions have jitter from pulse to pulse shots in a beam line, the BPS resolution can not be determined with measurements taken in a single BPS, in contrast to the resolution measured in the characterization test stand where the wire emulating the beam can be set to a fixed position. For that reason, the resolution beam test method illustrated

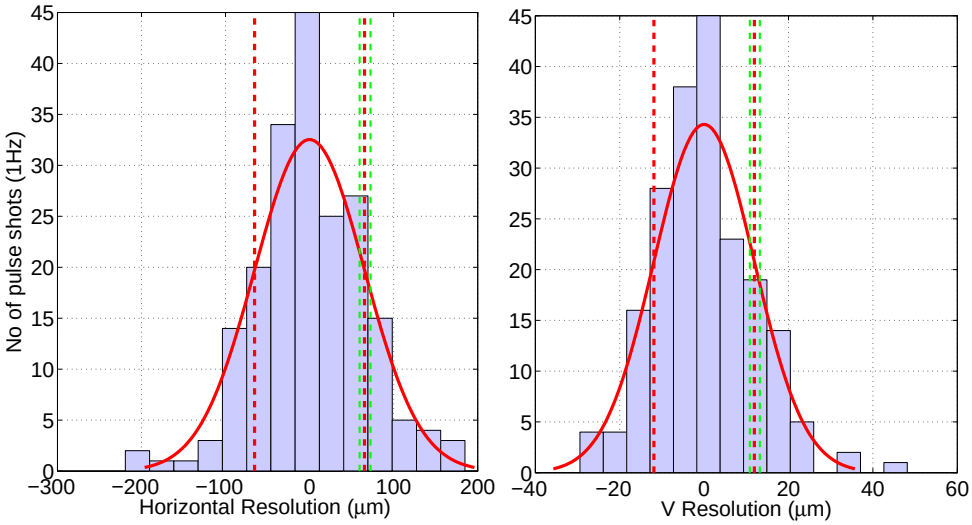

Figure 5.29: Resolution (red dashed) and its 95 % confidence interval (green dashed) for the BPS0510 (BPS13s series naming) position coordinates at 12 A beam current.

in Fig. 5.28 is based on the measurements of beam positions on three consecutive BPS units in order to obtain the position resolution of the central BPS from several beam pulse shots and taking out the beam jitter contribution. A straight beam trajectory, without significant beam current loss, can be set across the three BPSs section by switching-off the steering quadrupoles around this section. Thus, from the position measurements of the two side BPSs the beam position in the central BPS is obtained by interpolating it in the beam straight path and compared to its own reading. The difference of the interpolated and the measured beam positions in this BPS, after substracting the relative mechanical offset, reflects only the system noise uncertainty in the position readings having removed the beam jitter influence. Afterwards the resolution of the central BPS can be obtained as the standard deviation (or the RMS value) of this difference for many beam pulse shots.

The main aim of this beam test was to evaluate the beam position resolution that could be achieved in TBL for different beam currents. At the moment of the beam test four TBL modules in the beginning of the line were fully equipped with their respective PETS tanks. Therefore, the next available BPS units for resolution measurements were located downstream just after these modules to avoid unknown influence of the PETS. It was acquired relevant data from a total tothree consecutive BPS units (labeled as BPS0450, BPS0510 and BPS0550; corresponding to BPS1s, BPS13s, BPS11s for the series naming convention)) being able to evaluate the resolution independently on the central BPS with its respective side monitors, according to the previous method. The present maximum beam current entering in TBL from the CTF3 combiner ring is around 13 A corresponding to a recombination factor four, then it was chosen four beam currents with increasing recombination factor to observe the behavior of the resolution in function of the current.

For each beam current, it was acquired the entire pulsed waveforms of the beam current and the horizontal and vertical positions in the four mentioned monitors for 200 beam pulse shots with a repetition rate of 1Hz and pulse length of 280 ns. The current and coordinate positions were averaged within their pulse signal samples in a time gate of about 230 ns (46 ADC samples at 5 ns per sample) removing the sharp pulse flanges. Then, tak-

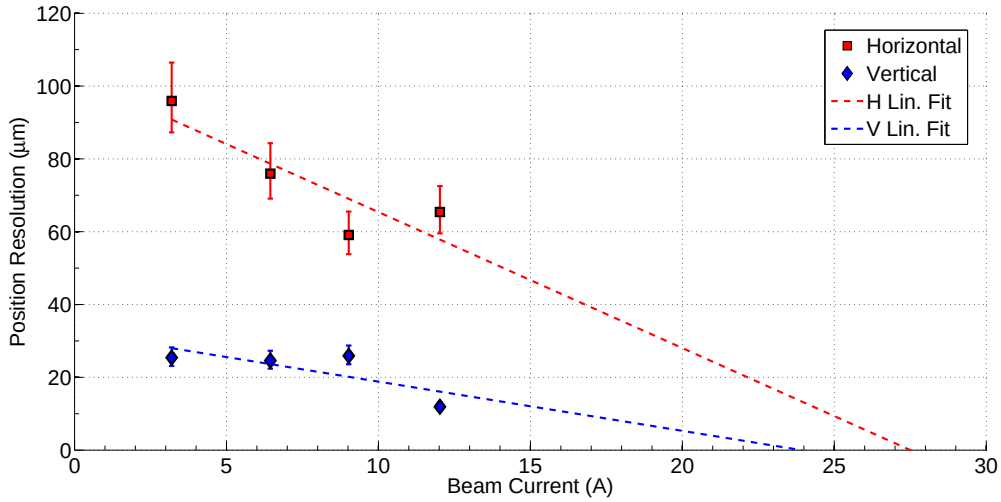

Figure 5.30: Resolution vs. beam current result plot for the BPS0510 (BPS13s series naming).

ing the set of three BPS, the resolution was calculated in the respective central monitor, BPS0510, using their pulse averaged positions as described in the previous method. A gaussian fit was performed on the values of the difference between interpolated and measured positions taking the standard deviation as a measure of resolution, matching up with the rms measure, and calculating also the confidence intervals for that resolution point. In Fig. 5.29 it is shown the resolution histogram and the gaussian fit of the BPS0510 at maximum available current of 12 A, having the best resolution for the vertical coordinate of 11.9 μm in a [10.8, 13.2] μm 95 % confidence interval, while for the horizontal coordinate is 65.4 μm and [59.5, 72.5] μm for the same confidence interval.

Finally, as depicted in Fig. 5.30, each of the resolution points was evaluated like in the analysis shown in Fig. 5.29, and they were obtained for the selected monitor and currents in the horizontal and vertical coordinates.The set of four nominal beam currents was [3.5 A, 7 A, 10 A, 13 A] although arriving lower current levels at the location of the monitors under test due to beam transport losses. As expected, higher beam current improves the resolution leading to lower values because of the better signal to noise ratio. A fit has been performed to these resolution points to show their linear scaling with current for both position coordinates. The 95 % confidence intervals for those resolution points calculated previously are also depicted. The linear fit is used to extrapolate the resolution points to higher currents beyond the measured ones. As a result it can be observed the strong tendency and a good outlook to achieve the 5 μm resolution goal at the nominal maximum beam current of 28 A for both coordinates. The significant difference between the horizontal and vertical coordinates indicates that the resolution levels had also contributions from the additional noise in the BPS signals most likely due to beam losses. Moreover the 10-bits resolution ADC jointly with the BPS signal levels at the ADC input set a quantization step corresponding to a 10 μm beam position step, biasing also the measured position resolution levels. Since the beam quality can still be improved much more, it turns to be in favor to reach the desired BPS resolution.

Linearity test parameters benchmarks of TBL BPS units

TBL label	Ref. name	Sensitivity		Position sensitivity		Electric offset		Accuracy (rms, ±5 mm)		Linear error (max., ±5 mm)	
		Horizontal	Vertical	H	V	H	V	H	V	H	V
		S_x ($\times 10^{-3}$mm^{-1})	S_y ($\times 10^{-3}$mm^{-1})	k_x (mm)	k_y (mm)	δ_x (mm)	δ_y (mm)	σ_x (μm)	σ_y (μm)	ϵ_{xdev} (%)	ϵ_{ydev} (%)
(not inst.)	BPS1–v1	40.26 ± 0.14	40.29 ± 0.09	24.84 ± 0.08	24.82 ± 0.06	0.176 ± 0.011	0.056 ± 0.008	35.3	25.4	0.9	0.9
BPS0210	BPS1–v2	44.03 ± 0.14	44.62 ± 0.08	22.71 ± 0.07	22.41 ± 0.04	0.289 ± 0.011	−0.133 ± 0.006	32.5	19.3	1.1	0.6
BPS0250	BPS2	41.02 ± 0.12	41.61 ± 0.12	24.34 ± 0.07	24.04 ± 0.07	0.066 ± 0.009	0.343 ± 0.011	29.6	31.2	1	1
BPS0310	BPS3	40.48 ± 0.14	42.07 ± 0.14	24.70 ± 0.08	23.77 ± 0.08	0.042 ± 0.011	0.166 ± 0.012	35.3	34.9	1.3	1.1
BPS0350	BPS4s	42.41 ± 0.11	40.40 ± 0.10	24.15 ± 0.06	24.75 ± 0.06	0.115 ± 0.008	0.155 ± 0.009	26.9	26.9	0.8	0.9
BPS0410	BPS2s	41.54 ± 0.11	40.99 ± 0.10	24.07 ± 0.06	24.39 ± 0.06	0.066 ± 0.008	0.219 ± 0.008	26.9	26.6	0.8	0.9
BPS0450	BPS1s	41.56 ± 0.11	41.16 ± 0.10	24.08 ± 0.06	24.29 ± 0.06	−0.003 ± 0.008	−0.065 ± 0.008	27.2	24.9	0.8	0.7
BPS0510	BPS13s	41.63 ± 0.11	40.90 ± 0.11	24.02 ± 0.06	24.45 ± 0.06	−0.063 ± 0.008	0.283 ± 0.009	27.4	27.1	0.8	0.9
BPS0550	BPS11s	41.09 ± 0.11	40.67 ± 0.10	24.33 ± 0.06	24.59 ± 0.06	−0.055 ± 0.008	0.227 ± 0.008	27.2	26.2	0.8	0.9
BPS0610	BPS3s	42.17 ± 0.11	41.38 ± 0.10	23.71 ± 0.06	24.17 ± 0.06	−0.015 ± 0.008	0.204 ± 0.009	26.4	26.5	0.8	0.9
BPS0650	BPS6s	42.11 ± 0.11	41.25 ± 0.10	23.75 ± 0.06	24.24 ± 0.06	0.002 ± 0.009	0.123 ± 0.008	28.6	27.1	0.7	0.8
BPS0710	BPS9s	42.50 ± 0.11	41.34 ± 0.10	23.53 ± 0.06	24.19 ± 0.06	−0.048 ± 0.008	0.104 ± 0.008	26.6	26.1	0.8	0.8
BPS0750	BPS8s	41.79 ± 0.12	41.18 ± 0.11	23.92 ± 0.07	24.28 ± 0.06	−0.011 ± 0.009	0.213 ± 0.009	30.3	27.2	0.8	0.9
BPS0810	BPS12s	41.55 ± 0.11	40.56 ± 0.10	24.07 ± 0.06	24.66 ± 0.06	−0.180 ± 0.009	0.274 ± 0.009	26.9	26.8	0.8	0.9
BPS0850	BPS14s	42.24 ± 0.23	41.11 ± 0.21	23.68 ± 0.13	24.33 ± 0.12	0.028 ± 0.017	0.256 ± 0.017	57.5	52.4	1.9	1.8
BPS0910	BPS10s	41.80 ± 0.19	41.72 ± 0.10	23.93 ± 0.11	24.56 ± 0.06	0.076 ± 0.015	0.147 ± 0.008	48.6	26.0	1.8	0.8
BPS0950	BPS7s	42.12 ± 0.11	42.26 ± 0.10	24.28 ± 0.06	23.66 ± 0.06	−0.017 ± 0.009	0.007 ± 0.008	26.9	27.1	0.7	0.8
BPS-Averages[a]		41.52 ± 0.13	41.12 ± 0.11	24.09 ± 0.07	24.32 ± 0.07	0.011 ± 0.010	0.169 ± 0.009	31.72	28.84	0.97	0.96

[a] Averages of all the BPS units except the BPS1–v2 of different PCB version.

Table 5.1: Summary of the linearity test parameters benchmarks of the TBL BPS units within a ±5 positions range, their parameter averages are given at the table bottom.

Frequency and pulse response test parameters of TBL BPS units

TBL label	Ref. name	Low cutoff frequencies				Pulse droop time constants			
		Wire (Beam)		Calibration		Wire (Beam)		Calibration	
		Σ	$\Delta(H,V)$	Σ	$\Delta(H,V)$	Σ	$\Delta(H,V)$	Σ	$\Delta(H,V)$
		$f_{low\Sigma}$ (kHz)	$f_{low\Delta}$ (kHz)	$f_{low\Sigma,Cal}$ (kHz)	$f_{low\Delta,Cal}$ (kHz)	$\tau_{droop\Sigma}$ (µs)	$\tau_{droop\Delta}$ (ns)	$\tau_{droop\Sigma,Cal}$ (µs)	$\tau_{droop\Delta,Cal}$ (ns)
(not inst.)	BPS1–v1	1.8	282	1.8	180	90	564	90	884
BPS0210	BPS1–v2	1.0	175	0.7	79	159	909	224	2000
BPS0250	BPS2	2.9	271	2.8	163	55	587	57	976
BPS0310	BPS3	1.7	275	1.7	171	93	579	93	931
BPS0350	BPS4s	2.5	279	2.6	166	64	570	61	961
BPS0410	BPS2s	2.0	281	2.6	166	79	566	61	961
BPS0450	BPS1s	2.6	267	2.5	166	62	597	64	920
BPS0510	BPS13s	2.5	292	2.4	168	65	545	67	947
BPS0550	BPS11s	2.5	296	2.6	160	63	537	62	998
BPS0610	BPS3s	2.6	279	2.5	172	61	570	63	926
BPS0650	BPS6s	2.2	267	2.1	167	73	597	76	954
BPS0710	BPS9s	2.4	310	2.3	169	66	512	70	940
BPS0750	BPS8s	2.4	305	2.4	168	67	522	67	947
BPS0810	BPS12s	2.6	273	2.6	166	61	583	61	961
BPS0850	BPS14s	2.7	255	2.6	173	59	624	61	920
BPS0910	BPS10s	2.5	255	2.6	166	63	624	62	961
BPS0950	BPS7s	3.2	280	2.5	171	50	568	64	64
BPS-Averages[a]		2.4 ± 0.3	281 ± 15	2.4 ± 0.3	168 ± 5	69 ± 11	568 ± 30	68 ± 11	951 ± 26

[a] Averages of all the BPS units except the BPS1–v2 of different PCB version.

Table 5.2: Summary of frequency response test parameters, low cutoff frequencies and pulse droop constants, of the TBL BPS units. For all the BPS units: the low cutoffs of the BPS electrode outputs coincide with $f_{low\Sigma}$; with the high cutoff frequency being $f_{high} > 100$ MHz, so that $\tau_{rise} < 1.6$ ns. The parameter averages are given at the table bottom.

Chapter 6

Conclusions

In this thesis has been presented the work carried out on the design, construction and test of the Inductive Pick-Ups (IPU) Beam Position Monitors (BPM), named BPS monitors, for the Test Beam Line (TBL) in the CLIC Test Facility (CTF3) at CERN. The Inductive Pick-Up (IPU) was the BPM technology type selected for the TBL. In spite of its complex mechanics with many parts assembled, an IPU design was fundamentally chosen because of the following main features matching up the TBL needs as presented at the beginning of Chap. 4.

The BPS project was developed in two main phases: the prototyping phase and the BPS series production and testing phase which are summarized as follows.

The *prototyping phase* consisted in the design, construction and characterization test of the BPS-IPU prototypes from 2007 to end of 2008. The first prototype (labeled as BPS1) was tested with two different design options of the on-board PCBs, leading to BPS1–v1 and BPS1–v2 prototype versions. Afterwards, the BPS1-v2 was validated and installed in TBL in July 2008.

The *BPS series production and testing phase* comprised the construction of 15 more units, jointly with its respective mechanical alignment supports, and their corresponding characterization tests for completing the 16 cells of the TBL line. The construction of the series units started at the beginning of 2009. In March 2009 a pre-series of two BPS units, labeled as BPS2 and BPS3, were requested in advance due to TBL beam test needs. After their corresponding characterization tests, these units were delivered and installed in May 2009, having thus 3 fully operational units in the TBL. The BPS parts construction, and follow-up of processes, continued until the final assemblies when there were ready for the characterization test of the full BPS series at IFIC labs made during September 2009. Two specific test benches were also designed and constructed for these BPS tests, at low and high frequencies. The 15 BPS units were finally delivered at the end of September 2009. The installation of all BPS monitors in the TBL finished by mid October 2009.

In total 17 BPS units was constructed which were labeled as BPS1, BPS2, BPS3 for prototype and pre-series; and BPS-1s to BPS-14s for the series. BPS-5s unit remained at IFIC as spare to perform the test for evaluating the BPS response at high frequencies and measuring its longitudinal coupling impedance beyond the bunching frequency (12 GHz) in the X-band microwave region. Finally, the project field work finished at mid 2011 with the BPS beam tests performed in the TBL. This allowed to measure the BPS resolution and its variation with an increasing beam current, showing a linearly decreasing tendency of the resolution to go down below 5 μm at the maximum beam current of 28 A, as

the main measurement goal of the BPS monitor and its figure of merit (see BPS project milestone at Fig. 4.4).

The main work and activities of the author within the BPS monitor development are summarized below:

- Design and implementation of the on-board current sensing PCBs of the BPS monitors, and the follow-up tasks regarding the construction and assembly of the non-vacuum and vacuum mechanical parts of the BPS prototypes and the series.
- Design and implementation of the low frequency wire test bench used to perform the BPS characterization tests (linearity over ±10 mm positions range and frequency response under 100 MHz) on all the BPS units.
- At the time of tests it was also made the study and design of the pulse droop compensation inside the external amplifier, as an important part of the BPS and amplifier joint response characterization and performance.
- A new proposed electric lumped circuit model of the BPS-IPU monitor which came out as a consequence of the analysis of the frequency response measurements and to better understand and simulate its frequency response behavior.
- Afterwards, it was made the simulation study of a coaxial waveguide structure used as the high frequency (RF and microwave) test bench which, after its construction, allowed to perform the S-parameters measurements for the longitudinal impedance determination of the BPS up to 22 GHz.
- Finally, there were performed the beam test on a sample BPS monitor of the TBL line in order to determine and study its achievable position resolution in function of increasing beam current.

This work was mainly carried out at IFIC labs in Valencia but also with several stages at CERN, first for prototypes testing in the BE-BI-PI section and after for the installation and beam tests in TBL of CTF3 with the invaluable help of their respective working teams.

In Tab. 6.1 are listed the BPS main parameters averaged over the full series measured from the characterization tests performed on every BPS unit installed in the TBL line. The BPS characteristic parameters were quite sensitive to the mechanical and electronic components fabrication tolerances, particularly those involved in the beam or wire position determination, as the sensitivity, electrical offsets and overall accuracies at the requested levels. In consequence, the characterization tests provided the benchmarks on each BPS unit in order to fulfill the specification demanded by the TBL line.

The BPS units parameters results showed small relative deviations from the average, and also a good balance between the horizontal and vertical plane parameters, indicating a successful fabrication process of the BPS series, and also as a result of the test data analysis acquired for different BPS orientations inside the test bench made to take into account for the parameters deviations due to test stand misalignments and imperfections.

Concerning the frequency response test results, it is determined the operational bandwidth on all the BPS units (below 10 kHz up to 100 MHz) measuring the low and high cutoff frequencies, and so the corresponding pulse droop and rise time constants, for the

the output electrode signals, their sum Σ signal and the horizontal and vertical difference $\Delta(H, V)$ signals.

The low cutoffs of the Δ signals are in principle at much higher frequencies than the specified 10 kHz, thus producing larger pulse droops. In consequence they were properly compensated in the Δ channels of the external amplifier by the implementation of active RC filters.

The pulse test performed on the BPS2 unit for the $\Delta(H, V)$ signals yield a correct pulse droop compensation for the calibration input and also around the BPS center positions, where the pulse droop is reduced down to: 4 % for a test pulse length of 2 μs, and 1.25 % for the TBL maximum beam pulse length of 140 ns. The worst pulse droop case is observed at a wire position of 10 mm away from the center (over the 12 mm beam pipe radius), due to the observed position dependency of the Δ low cutoffs producing strong frequency shifts of around 111 kHz, which would not be sufficiently compensated. For the Σ, and equivalently for the electrode signals, are also observed smaller low cutoff shifts of around 4 kHz at a 10 mm off-center wire position, still leaving their low cutoffs below 10 kHz, and hence the corresponding pulse droops, under specifications.

The BPS longitudinal impedance was measured in the high frequency tests for one BPS unit sample, showing a low impedance value below 13 Ω almost in all the frequency range up to 22 GHz (test bench bandwidth limit). But unwanted impedance peaks around 140 Ω, most likely caused by resonances of beam EM fields with the monitor geometry, occur at 6.8 GHz and frequencies above 15 GHz that would need further tests and a deeper study.

Finally, the BPS beam test performed in the TBL line shows a linear decreasing tendency of the BPS position resolution measured at four beam current steps increasing from 3.5 to 13 A (nominal values at the beginning of the line). A minimum of 11.9 μm is obtained at an available beam current of 12 A, yielding a good outlook to achieve the goal of 5 μm resolution at the maximum nominal beam current of 28 A.

Modern particle accelerators and in particular future colliders like CLIC require precision beam diagnostics in order to handle the beams which are pushed more and more to their limits either in terms of intensity or beam quality. A critical performance parameter for CLIC is the luminosity which depends directly on the accelerator alignment. The CLIC approach is based on a novel technology of two-beam acceleration scheme (drive and main beams) and requires an extreme alignment and stabilization of the beam which rely heavily on a beam based alignment techniques [65]. In order to perform this beam based alignment, IPU technology based devices like the BPS monitor can play an important role providing enough precision and high resolution for the position measurements of ultra-relativistic beams as shown in this thesis. Besides this, other BPS-IPU features like the beam current measurement and wide dynamic range operation in current and bandwidth can be considered as additional advantages for the CLIC Drive Beam decelerator where new devices will have to cope with beam intensities of 100 A and precisions of 20 μm. It also must be taken into account that the mechanical complexity of these monitors could represent a limitation at the time of manufacturing large number of units, though in principle some device simplifications could be performed being optimized to the specific line needs.

BPS linearity test parameters	
Sensitivity	
Horizontal S_x	$41.5\pm0.6\times10^{-3}\text{mm}^{-1}$
Vertical S_y	$41.1\pm0.5\times10^{-3}\text{mm}^{-1}$
Position sensitivity	
Horizontal k_x	$24.1\pm0.4\,\text{mm}^{-1}$
Vertical k_y	$24.3\pm0.3\,\text{mm}^{-1}$
Electric offset	
Horizontal δ_x	0.01 ± 0.08 mm
Vertical δ_y	0.17 ± 0.11 mm
Overall precision (RMS within ±5 mm)	
Horizontal σ_x	$32\pm8\,\mu$m
Vertical σ_y	$29\pm7\,\mu$m
Linearity error (Max. deviation at ±5 mm)	
Horizontal ϵ_{xdev}	0.9 ± 0.4 %
Vertical ϵ_{ydev}	0.9 ± 0.3 %

BPS frequency response parameters	
Wire/Beam input excitation	
Low cutoff freq. Σ, $f_{low\Sigma}$	2.4 ± 0.4 kHz
Low cutoff freq. Δ, $f_{low\Delta}$	279 ± 16 kHz
High cutoff freq. f_{high}	>100 MHz
Calibration input excitation	
Low cutoff freq. Σ, $f_{low\Sigma,Cal}$	2.4 ± 0.3 kHz
Low cutoff freq. Δ, $f_{low\Delta,Cal}$	168 ± 5 kHz
High cutoff freq., $f_{high,Cal}$	>100 MHz

BPS pulse-time response parameters	
Wire/Beam input excitation	
Droop time const. Σ, $\tau_{droop\Sigma}$	$67\pm12\,\mu$s
Droop time const. Δ, $\tau_{droop\Delta}$	572 ± 32 ns
Rise time const., τ_{rise}	<1.6 ns
Calibration input excitation	
Droop time const. Σ, $\tau_{droop\Sigma,Cal}$	$67\pm10\,\mu$s
Droop time const. Δ, $\tau_{droop\Delta,Cal}$	948 ± 26 ns
Rise time const., $\tau_{rise,Cal}$	<1.6 ns

Table 6.1: BPS full series average performance with errors given as the standard deviations of the main parameters.

Bibliography

[1] *International Linear Collider Reference Design Report*, Aug. 2007. ILC Global Design Effort and World Wide Study Groups. ILC-REPORT-2007-1, see also http://www.linearcollider.org.

[2] *ILC Research and Development Plan for the Technical Design Phase*. ILC Global Design Effort, July 2009.

[3] The CLIC Study Team, *A 3 TeV e^+e^- Linear Collider based on CLIC Technology*. CERN 2000008, 28 July 2000, Proton Synchrotron Division.

[4] G. Geschonke, A. Ghigo et al., *CTF3 Design Report*, CERN/PS 2002-008 (RF). LNF-02/008, 2002. CTF3 Note 047, 2002.

[5] *CLIC Conceptual Design Report*, released soon [to be updated].

[6] S. Döbert, D. Schulte, I. Syratchev, *Status report of the CTF3 Test Beam Line*. CTF3 Note 076, 2006.

[7] F. Toral et al., *Design, Manufacturing and Tests of a Micrometer Precision Mover for CTF3 Quadrupoles*, Proceedings of the 11th biennial European Particle Accelerator Conference, EPAC'08, Genova, 2008.

[8] D. Carrillo et al., *Engineering Design of PETS Tank Prototype for CTF3 Test Beam Line*, Proceedings of the 11th biennial European Particle Accelerator Conference, EPAC'08, Genova, 2008.

[9] M. Gasior, *An inductive pick-up for beam position and current measurement*. CERN-AB-2003-053-BDI.

[10] J.J. García-Garrigós, A. Faus-Golfe, J.V. Civera-Navarrete, *Design and Construction of an Inductive Pick-up for Beam Position Monitoring in the Test Beam Line of The CTF3*. Proceedings of the 11th European Particle Accelerator Conference, EPAC'08, Genova, 2008, JACoW conference proceedings, pp. 1110-1112.

[11] P. Forck, *Lecture Notes on Beam Instrumentation and Diagnostics*. Gesellschaft für Schwerionenforschung (GSI), Joint Universities Accelerator School (JUAS), available at www-bd.gsi.de/conf/juas/juas.html.

[12] P. Strehl, *Beam Instrumentation and Diagnostics*, Springer-Verlag Berlin Heidelberg 2006.

[13] M.G. Minty and F. Zimmermann, *Measurement and Control of Charged Particle Beams*, Springer-Verlag, Berlin 2003.

[14] G. Kube, *Specific Diagnostics for Different Machines*, Beam Diagnostics for Accelerators, Proceedings of CERN Accelerator School (CAS), CERN-2009-005, Dourdan, 2009, pp. 1-64.

[15] V. Smaluk, *Particle Beam Diagnostics for Accelerators: Instruments and Methods*, VDM Verlag Dr. M´uller, Saarbr´ucken 2009.

[16] E. Bravin, *Transverse Beam Profiles*, Beam Diagnostics for Accelerators, Proceedings of CERN Accelerator School (CAS), CERN-2009-005, Dourdan, 2009, pp. 377-406.

[17] J. Alabau-Gonzalvo, C. Blanch Gutierrez, A. Faus-Golfe, J.J. Garcia-Garrigos, IFIC (CSIC-UV), Valencia, Spain; J. Cruz, D. McCormick, G. White, M. Woodley, SLAC, Menlo Park, California, USA, *Multi Optical Transition Radiation System for ATF2*, Proceedings of the 1st International Particle Accelerator Conference, IPAC'10, Kyoto, 2010.

[18] J. Alabau-Gonzalvo, C. Blanch Gutierrez, A. Faus-Golfe, J.J. Garcia-Garrigos, IFIC (CSIC-UV), Valencia, Spain; J. Cruz, D. McCormick, G. White, M. Woodley, SLAC, Menlo Park, California, USA, *Optical Transition Radiation System for ATF2*, Proceedings of the 2nd International Particle Accelerator Conference, IPAC'11, San Sebastián, 2011.

[19] A.H. Lumpkin et al., Proceedings of Particle Accelerator Conference, PAC'97, Vancouver, 1997, p. 874.

[20] R.J. Steinhagen, *Tune and Chromaticity Diagnostics*, Beam Diagnostics for Accelerators, Proceedings of CERN Accelerator School (CAS), CERN-2009-005, Dourdan, 2009, pp. 317-359.

[21] J. Wenninger, *Luminosity Diagnostics*, Beam Diagnostics for Accelerators, Proceedings of CERN Accelerator School (CAS), CERN-2009-005, Dourdan, 2009, pp. 453-466.

[22] A.S. Müller, *Measurements of Beam Energy*, Beam Diagnostics for Accelerators, Proceedings of CERN Accelerator School (CAS), CERN-2009-005, Dourdan, 2009, pp. 427-451.

[23] H. Koziol, *Beam Diagnostics for Accelerators*, Proceedings of CERN Accelerator School (CAS), Uni. Jyvaskyla, Finland, p. 565 CERN 94-01, http://schools.web.cern.ch/Schools/CAS/CAS Proceedings.html (1993). And at CERN 2005-004 p. 154, 2005.

[24] M. Lonza, *Multi-bunch Feedback Systems*, Beam Diagnostics for Accelerators, Proceedings of CERN Accelerator School (CAS), CERN-2009-005, Dourdan, 2009, pp. 467-511.

[25] J. Borer, R. Jung, *Diagnostics*, Course given at CERN Accelerator School (CAS) on Antiprotons for Colliding Beam Facilities, Geneva, CERN/LEP-BI/84-14 (1984).

[26] P. Forck, P. Kowina, D. Liakin, *Beam Position Monitors*, Beam Diagnostics for Accelerators, Proceedings of CERN Accelerator School (CAS), Dourdan, 2009, CERN-2009-005 p. 187.

[27] R.E. Shafer, *Beam position monitoring*. In S.R. Smith, editor, 7th Beam Instrumentation Workshop, 1990, AIP Conference Proceedings vol. 390, pages 2658.

[28] J. Belleman, *From Analog to Digital*, Beam Diagnostics for Accelerators, Proceedings of CERN Accelerator School (CAS), CERN-2009-005, Dourdan, 2009, pp. 281-316.

[29] A. Hofmann, *Dynamics of beam diagnostics*, Beam Diagnostics for Accelerators, Proceedings of CERN Accelerator School (CAS), CERN-2009-005, Dourdan, 2009, pp. 65-139.

[30] J. Bosser (Ed.) *Beam Intrumentation*, E. Schulte, Cap. 5 and G. Gelato, Cap. 7, Services Éducatifs - Enseignement Technique 1994, CERN PE-ED 001-92 Revised November 1994.

[31] S. Battisti, M. Le Gras, J.M. Roux, B. Szeless and D.J. Williams, *Magnetic Beam Position Monitors for LEP Pre-Injector*, Proceedings of the 1987 IEEE PAC, Washington, 1987, pp. 605-607.

[32] E. Durand, *Electrostatique*, Tome II (Masson, Paris, 1966), p. 207.

[33] I.S. Grant and W.R. Phillips, *Electromagnetism*, 2nd ed., The Manchester Physics Series, John Wiley & Sons, Chichester, 1990, pp. 464-469.

[34] J.C. Denard, *Beam current monitors*, Beam Diagnostics for Accelerators, Proceedings of CERN Accelerator School (CAS), CERN-2009-005, Dourdan, 2009, pp. 141-155.

[35] R. E. Shafer, *Characteristics of Directional Coupler Beam Position Monitors*, IEEE Trans. Nucl. Sci. 32, 1985, p. 1933.

[36] K. Satoh, *Beam Position Monitor using Wall Currents*, Rev. Sci. Instr. 4, 1979, p. 450.

[37] I. Podadera, S. Calatroni, L. Søby, *Precision Beam Position Monitor for EUROTeV*. EUROTEV Report 2007-046.

[38] Datasheet of *High Frequency Ni-Zn Ferrite*, C2050, Ceramic Magnetics Inc. NJ, USA.

[39] Datasheet of *VITROVAC - Amorphous Tape-Wound Cores for Digital Interface Transformers and Common Mode Chokes in ISDN - Equipment and Communication Systems*. Part number T60009-E4006-W650. Manufacturer VACUUMSCHMELZE GMBH & Co. KG, P.O. Box 2253, D-63412 Hanau, Germany.

[40] Datasheet of *Coaxial Panel Connector*, 23_SMA-50-0-13/111_N, Huber+Suhner AG, Herisau, Switzerland.

[41] Datasheet of *BalShield™ EMI Spring Gaskets*, BG15H5, Bal Seal Engineering, Foothill ranch, CA, USA.

[42] Datasheet of *Characteristics of Kyocera Technical Ceramics*, A-479SS, Kyocera Corp., Kyoto, Japan.

[43] Heitz GmbH, Metal Bellows Expansion Joints, Rheinstetten, Germany, web: www.heitz-gmbh.de.

[44] S. Turner (Ed.), *Vacuum Technology*, Proceedings of CERN Accelerator School (CAS), CERN-99-05, Snekersten, Denmark, 1999.

[45] J.A. Eichmeier, M. K. Thumm, *Vacuum Electronics. Components and Devices*. Springer-Verlag Berlin Heidelberg 2008.

[46] M. Gasior, *Hardware of the CTF3 beam position measurement system*. CTF3 Note 053, 2003.

[47] G. Montoro. Private communications.

[48] J. Jacquemier, J.M. Nappa, J. Tassan, S. Vilalte, *Acquisition chain for CTF3 pick-ups read-out*. LAPP-TECH-2009-01, in2p3-00412457 version 1, 2009.

[49] Datasheet of *Wideband, low noise, low distortion fully differential amplifier*, THS4508, Texas Instruments Inc., Dallas, Texas, USA.

[50] L. Søby and F. Guillot. Private communications.

[51] Manual of *ILS Series, High-Performance Mid-Range Travel Linear Stages*, M-ILS100CCHA, Newport Corporation, Irvine, California, USA.

[52] Manual of *URS-B Series, Precision Rotation Stages*, URS150BCC, Newport Corporation, Irvine, California, USA.

[53] Manual of *ESP300 Motion Controller/Driver*, Newport Corporation, Irvine, California, USA.

[54] Datasheet of *Coaxial Amplifier Medium High Power*, ZHL-3A, Mini-Circuits, Brooklyn, New York, USA.

[55] Datasheet of *Coaxial Power Splitter/Combiner 2 Way–180°*, ZFSCJ-2-2, Mini-Circuits, Brooklyn, New York, USA.

[56] Datasheet of *Coaxial Power Splitter/Combiner 2 Way–0°*, ZFRSC-2050, Mini-Circuits, Brooklyn, New York, USA.

[57] L. Søby, *Software requirements for CTF3 TL2 and CLEX BPMs using the SIS3320 ADCs*. CERN engineering specification, CERN EDMS Document Information Page, 08/12-2009.

[58] M. Gasior, *Limiting High Frequency Longitudinal Impedance of an Inductive Pick-Up by a Thin Metallic Layer*, EPAC04.

[59] F. Caspers, *Impedance Determination from Bench Measurements*, CERN-PS-2000-004 (RF).

[60] *FEST3D-A Software Tool for the Design of Microwave Passive Components*, Distributed by AURORASAT, www.fest3d.com

[61] N. Marcuvitz, *Waveguide Handbook*, 1st published McGraw-Hill, 1951; Vol. 10 in the MIT Radiation Laboratory series, Dover Publications Inc., 1965; IEEE Electromagnetic Waves Series 21, Peter Peregrinus Ltd., 1993.

[62] D.M. Pozar, *Microwave Engineering*, 3rd ed., John Wiley & Sons Inc., 2005.

[63] E. Adli, et al *Experimental Program for the CLIC Test Facility 3 Test Beam Line*, IPAC2010.

[64] S. Döbert et al., *Commissioning Status of the Decelerator Test Beam Line in CTF3*, LINAC10.

[65] S. Döbert. Private communications.